Experimental Investigation on the Rheology of Fault Rocks

Inauguraldissertation

zur
Erlangung der Würde eines Doktors der Philosophie

vorgelegt der
Philosophisch-Naturwissenschaftlichen Fakultät
der Universität Basel

von

Matěj Peč

aus Prag (Tschechische Republik)

Minneapolis, März 2014

Genehmigt Von der Philosophisch-Naturwissenschaftlichen Fakultät auf Antrag von:

Prof. Dr. R. Heilbronner (Dissertationsleiterin)

Prof. Dr. G. Di Toro (Korreferent)

Basel, den 13. November 2012

Prof. Dr. Jörg Schibler
Dekan der Philosophisch-
Naturwissenschaftlichen Fakultät

Originaldokument gespeichert auf dem Dokumentenserver der Universität Basel **edoc.unibas.ch**

Acknowledgements:

The most exciting phrase to hear in science,
the one that heralds new discoveries,
is not "Eureka!" but "That's funny..."

Isaac Asimov

Abstract

Plate tectonic movement is accommodated on fault zones which operate under a broad range of pressures and temperatures. Depending on the pressure and temperature conditions, the rocks will either flow viscously or fracture. Depending on how much strain is accommodated by the viscous component (mass-transfer processes etc.) and by the frictional component (fracturing, granular flow and frictional sliding) the rheological response will be either more viscous or more frictional. The rheological behavior of rocks under purely viscous and purely frictional conditions is relatively well understood, however this is not the case when both processes interfere.

The aim of this study is to explore and identify physical and chemical processes occurring during deformation of granitoid fault rocks under elevated pressures and temperatures where an interplay between brittle/frictional and viscous processes is expected. The mechanical response of a crushed granitoid rock (grain size ≤ 200 μm) placed between forcing blocks pre-cut at 45° was studied under a broad range of temperatures (T = 300 – 600°C), confining pressures (Pc $\sim$ 300 – 1500 MPa) and displacement rates ($\dot{d}$, of $\sim 10^{-6}$, 10^{-7} and 10^{-8} m s^{-1} inducing strain rates, $\dot{\gamma}$, of $\sim 10^{-3}$, 10^{-4} and 10^{-5} s^{-1}) to different sample bulk shear strains ($\gamma \sim 0 - 5$). Various observation techniques were used to track the microstructural evolution. Based on the microstructural observations and mechanical data interpretation, we attempt to identify physical and chemical processes responsible for the mechanical behavior. Based on the results, an expected rheological behavior of natural fault zones is discussed.

Microstructural observations show, that the crushed fault rock undergoes compaction accommodated by short, closely spaced R$_1$ Riedel shears producing large amounts of fine-grained (< 100 nm) material. This is accompanied by strain hardening in the mechanical record. Compaction is complete around a finite shear strain, γ, of ~ 1.5, well before peak strength and deformation starts to partition into interconnected, anastomozing slip zones (SZ). Around peak strength ($\gamma \sim 2$) a S-C fabric is well developed and the fine grained material (< 100 nm) in the SZ is being transformed into a nanocrystalline (mean grain size ~ 35 nm), partly amorphous material with an intermediate chemical composition between potassium-feldspar and plagioclase. These zones are often initiated by favorably oriented micas (perfect basal slip in the C' direction) and, as a consequence, micas are often incorporated or adjacent to the SZ.

High peak shear strength ($\tau \sim 0.6 - 1.4$ GPa) is reached around a γ, of ~ 2.5 where the SZ form 7-12 % of the fault rock volume. Very fine layering and mostly laminar flow structures are observed in the SZ. Fracturing and grain size reduction continues in lenses of material

viii

---

delimited by individual SZ indicating strain partitioning. Quartz fractures the least and forms rigid inclusions surrounded by a weaker matrix of slip zones and fine grained aggregates of feldspars.

After peak strength, the fault rocks weaken slightly ($\sim 40 - 140$ MPa) and continue to deform at approximately constant and high stress levels ($\tau \sim 0.45 - 1.2$ GPa) up to a finite shear strain of ~ 5. Peak stress as well as the stress level during steady-state deformation exhibits a strong temperature dependence and a weak strain rate dependence indicating a viscous component of deformation.

With increasing strain and temperature, the amount of the slip zones increases (up to ~ 25 %) indicating either strain hardening in the nanocrystalline, partly amorphous material, or that geometrical constraints do not allow continuous operation of the SZ. After peak strength, the SZ form an through going interconnected, anastomozing network. Deformation continues to localize within the SZ and the material changes its microstructure further. Around 90% of this material is amorphous to the TEM beam in zones which accommodated high local strains ($\gamma > 5$). Turbulent flow structures and a very heterogeneous chemical composition develops in the high strain SZ which cover roughly ~ 1% of the sample volume exploiting some of the pre-existing SZ and seem to form a multiply-connected topology, in contrast to SZ which accommodated lower strains. Crystalline fragments and nanocrystalline material is often incorporated into the high strain SZ and at highest stresses and lowest temperatures (300°C), small bubbles (~ 15 nm $- 1$ μm) appear. This material is preferentially observed at high stress sites and shows intrusive relationships with the surrounding fine grained material forming injection veins.

The calculated temperature increase at the fault is small (max ~ 2.5°C) as the displacement rate was slow (experiments take up to several days inducing only ~ 2 mm of displacement) and the heat conduction high. Based on inspection of the microstructures and mechanical data, it is inferred that the fragment loaded, amorphous material exhibited a fluid-like rheology, i.e. shear stress was proportional to shear strain rate. However the microstructural record down to ångstöm scales is not compatible with the material being a liquid (i.e. in the sense of being molten above its liquidus temperature) and indicates that the loss of long-range order was achieved by mechanical work.

Our results indicate, that faults can build up significant stresses at the brittle-viscous transition leading to extreme grain comminution and amorphization. By comparison of the experimentally produced microstructures to microstructures observed in natural pseudotachylites, we conclude that the material produced during the experiments could be identified as a pseudotachylite in nature. However, pseudotachylites are currently being interpreted as high-temperature frictional melts that can form exclusively during earthquakes. Nevertheless, the fragment loaded amorphous material produced during the experiments did form neither fast nor at high temperatures, causing a conundrum. Some natural pseudotachylites are found under conditions which are considered "paradoxical" under the assumption that all pseudotachylites originated as frictional melts. Our observations open new possibilities how to resolve these paradoxes. It is concluded that the use of pseudotachylites as evidence for ancient earthquakes should be reconsidered.

Contents

List of Figures

List of Tables

Introduction

1.1 General aspects

Strain localizes in fault zones in the earth's lithosphere. Faults occur from small-scale fractures which accommodate little displacement to lithosphere scale fault zones accommodating kilometers of displacement between tectonic blocks and plates. Fault zones release accumulated energy with various intensity and at different time scales. Some faults creep steadily (e.g. Thatcher, 2009; Bürgmann et al., 2000) , some slowly and periodically release energy as "slow earthquakes" (e.g. Beroza and Ide, 2011), and some release abruptly large amounts of energy, which is manifested as an "earthquake" (e.g. Kanamori, 1994).

Figure 1.1, shows a synoptic diagram of what an idealized lithosphere-scale strike-slip fault could look like (the Sibson – Scholz fault model). Because faults are the result of strain localization, it is implied that they are weaker than the surrounding country rock. With "weaker" meaning that they accommodate more strain under iso-stress conditions, or deform at lower stresses under iso-strain rate conditions in a rheologically polyphase material (Taylor and Sachs average). Detailed studies of exhumed fault zones document that deformation is accommodated by a zone of foliated mylonites, cataclasites, and gouges, which tend to narrow towards the earths surface (e.g. Imber et al., 2001; Takagi et al., 2012; Chester and Chester, 1998). Lithosphere scale fault zones operate over a broad range of pressure - temperature conditions. Rocks at high-pressure / high-temperature (HP – HT) conditions flow viscously whereas at low-pressure / low-temperature (LP – LT) conditions rocks crack, fracture and loose cohesion. Hence, fault movement is achieved by a complex spatial and temporal interplay between "viscous" and "brittle" processes. The interaction becomes most pronounced around the so called "brittle - viscous transition"[1] where viscous flow cannot

---

[1]The terminology used is confuse - some scientists use "brittle - plastic transition", some "brittle - viscous transition", some "brittle - ductile transition" and some "frictional - viscous transition". Each has its merits and in essence describe similar concepts, i.e. transition from temperature and strain rate dependent flow to normal stress dependent frictional sliding. See Tab. 1.1 for definitions.
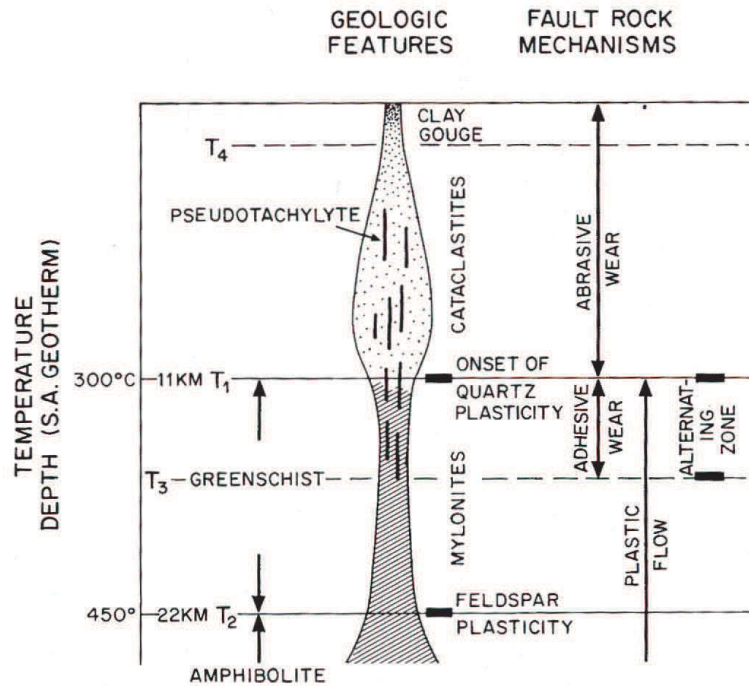
Figure 1.1: Idealized fault zone. After Scholz (2007).

accommodate the displacement and abundant pervasive fracturing occurs (e.g. Kohlstedt et al., 1995). Obviously, complex overprinting relationships may develop during the operation and exhumation of a fault zone, which renders the work with natural fault rocks challenging. Nevertheless, as faults represent zones where energy is dissipated, our understanding of fault rheology presents an important issue for our understanding of the forces driving plate tectonics and the mechanics of earthquakes.

1.2   Fault related rocks

The microstructures connected to fault zones from all crustal depths are ubiquitously showing grain size reduction achieved by, for example, dynamic recrystallization at HP - HT conditions or fracturing at LP - LT conditions. Abundant microstructural evidence suggests that mass-transfer processes exploit these fine-grained zones at all crustal levels (e.g. Gratier et al., 2011; Pennacchioni et al., 2006; Gratier et al., 1999; Faulkner et al., 2010; Chester and Chester, 1998; Evans and Chester, 1995; Chester et al., 1993; Keulen et al., 2007; Fusseis and Handy, 2008; Kilian et al., 2011a; Menegon et al., 2011) and promote metamorphic reactions and authigenic mineral growth. Thus LT-LP fault rocks are not just granulated equivalents of the surrounding country rock but can be viewed as low- to medium-grade metamorphic rocks even in the upper crust (Faulkner et al., 2010).

The work done in fault zones drives the deforming material further away from an equilibrium state through e.g., grain size reduction (increase in surface area), deformation induced lattice defects as dislocations, stacking faults (increase in strain energy) (e.g. Stünitz, 1998) and other

irreversible increases in entropy (e.g. Austin and Evans, 2007). Atomic mobility influenced by temperature and time on the contrary drive the system towards an equilibrium state (e.g. Suryanarayana, 2001) and therefore complex feedback relationships develop. How far from equilibrium can the fault zone material be driven?

The smallest grain sizes reported in natural rocks are as small as few tens of nanometers (e.g. Olgaard and Brace, 1983; Wilson et al., 2005; Viti, 2011) and even amorphous material was observed (e.g. Janssen et al., 2010; Ozawa and Takizawa, 2007). Nevertheless, the most striking far-from-equilibrium structure connected to fault zones is the occurrence of peculiar "glassy" rocks, called pseudotachylites[2], which form at depths from the uppermost mantle to the uppermost crust (e.g. Sibson, 1975; Cowan, 1999; Di Toro and Pennacchioni, 2004; Spray, 2010; White, 2012; Andersen and Austrheim, 2006; Ueda et al., 2008; Austrheim and Boundy, 1994; John et al., 2009). These observations suggest that fault zones are often associated with meta-stable materials. What processes can produce such materials? And how do such features affect the rheological behavior of faults?

1.3 Contribution of rock deformation experiments

The complex interplay between physical, chemical and mechanical effects occurring in a fault zone together with high spatial and temporal variability calls for an interdisciplinary approach (e.g. Niemeijer et al., 2012; Faulkner et al., 2010). Laboratory experiments are offering valuable insights into processes occurring in natural fault zones thanks to a more or less direct control over a series of parameters (confining pressure, temperature, stress, pore fluid and pore fluid pressure, displacement rate inducing strain rates in the sample etc.). This allows us to simulate conditions prevailing at depth in the earths crust (i.e. follow a geothermal gradient). Detailed microstructural observations together with mechanical data interpretation allow, under favorable circumstances, the identification of physical processes responsible for the observed behavior which is a necessary prerequisite for extrapolation of laboratory data to natural conditions.

1.4 Rheology of the lithosphere

The current view on the distribution of strength profile with depth in the lithosphere is based on extrapolation of strength envelopes derived from laboratory experiments. This approach was pioneered in the late 1970s (Byerlee, 1978; Goetze and Evans, 1979; Brace and Kohlstedt, 1980; Kohlstedt et al., 1995) and has been very useful in explaining many observations. The basic idea behind the strength envelopes is that rocks at different depths deform by different deformation processes (Fig. 1.2).

Figure 1.2a shows how the strength of a rock develops with increasing confining pressure at constant temperature and strain rate. If an intact rock is loaded, the maximum differential stress it can support is limited by the fracture envelope. At low confining pressures, the increase of confining pressure results also in an increase of the maximal supported differential stress (Mohr-Coulomb envelope). Nevertheless, as rocks cannot support infinite differential stresses, the slope of the fracture envelope levels off until it becomes independent of the applied

---

[2]alternative spelling: pseudotachylytes

confining pressure (von Mises envelope) where the rocks reach their maximum compressive strength. As fracture strengths are sample size dependent and vary widely depending on the lithology (e.g. Scholz, 2007), they are not useful to constrain the strength of the lithosphere (Kohlstedt et al., 1995).

Term	Definition	Based on
Frictional	τ depends on σ_n	Mechanical data
Viscous	τ depends on $\dot{\gamma}$	Mechanical data
Plastic	τ is constant	Mechanical data
Brittle	fragmentation and fracturing	Observation
Ductile	homogenous deformation on sample scale	Observation

Table 1.1: Definitions. τ - shear stress, σ_n - normal stress, $\dot{\gamma}$ - shear strain rate. Frictional, viscous and plastic are rheological properties accessible only in the laboratory. Viscous and plastic deformation is often temperature dependent and normal stress independent, frictional deformation is often temperature independent. Brittle and ductile are based on observation and therefore are observation scale dependent. They do not imply specific rheological behavior nor physical processes. Plastic is also used synonymous to "crystal-plastic" deformation, or permanent deformation without loss of cohesion (observation based). Frictional processes are often brittle, viscous and plastic processes are often ductile. However this is not a neccesity.

However, once a fault surface is created, strength of rocks seems to follow the so-called "Byerlee's rule" for frictional sliding (Byerlee, 1978). Frictional sliding is treated in terms of a friction coefficient, μ, which is the ratio of shear stress, τ, to normal stress, σ_n, resolved on the pre-existing fault with a certain orientation with respect to the applied stress tensor. This ratio was found to be remarkably constant ($\mu \sim 0.6 - 0.8$) over a wide range of rock types, temperatures and displacement rates and is thus in the first order dependent only on the resolved normal stress. Furthermore as the resolved shear stress needed to slide on a pre-existing fracture is lower than the critical resolved shear stress for fracturing an intact rock at low confining pressures, it is implied that the strength of a pre-fractured sample will be limited by frictional sliding on favorably oriented faults. It is therefore more useful for predicting rock strength at low confining pressures than fracture envelopes (Kohlstedt et al., 1995).

Nevertheless, with increasing confining pressure, the resolved shear stress needed to slide a pre-existing fracture will be higher than the critical resolved shear stress for fracturing of the surrounding country rocks (so called "brittle-ductile transition", B-D in Fig. 1.2a) which results in pervasive microfracturing leading to cataclastic or semi-brittle flow.

Further increase in confining pressure leads to the intersection of the Von Mises envelope with the "Goetze's criterion" which is an experimentalists rule of thumb stating that rocks will deform by crystal-plastic deformation processes if the supported differential stress is lower or equal to the confining pressure. This is referred to as the "brittle - plastic transition" (B-P in Fig. 1.2a). Crystal-plastic deformation is described by various flow laws which relate the strain rate tensor (i.e. how fast the material flows) to the applied stress tensor. Viscous flow of rocks is in the first order normal stress independent and strongly strain rate and temperature dependent.

If we want to apply these concepts to the lithosphere we have to replace the pressure-axis with "depth". An increase in depth implies the increase of temperature, confining pressure and various chemical effects (e.g. water fugacity which facilitate mass-transfer and hence viscous flow). Then, *if* we choose a constant strain rate, we can predict at what differential stress the lithosphere should flow at different depths. With this step, we impose an iso-strain rate

boundary condition (i.e. the stress varies with depth, strain rate stays constant). However, we could equally well impose an iso-stress boundary condition (i.e. the strain rate varies with depth, stress is constant) (e.g. Platt and Behr, 2011). Both represent end member possibilities, with natural faults lying somewhere in-between. I will take the original constant strain rate rate approach for now (see Chapter 5 for more discussion).
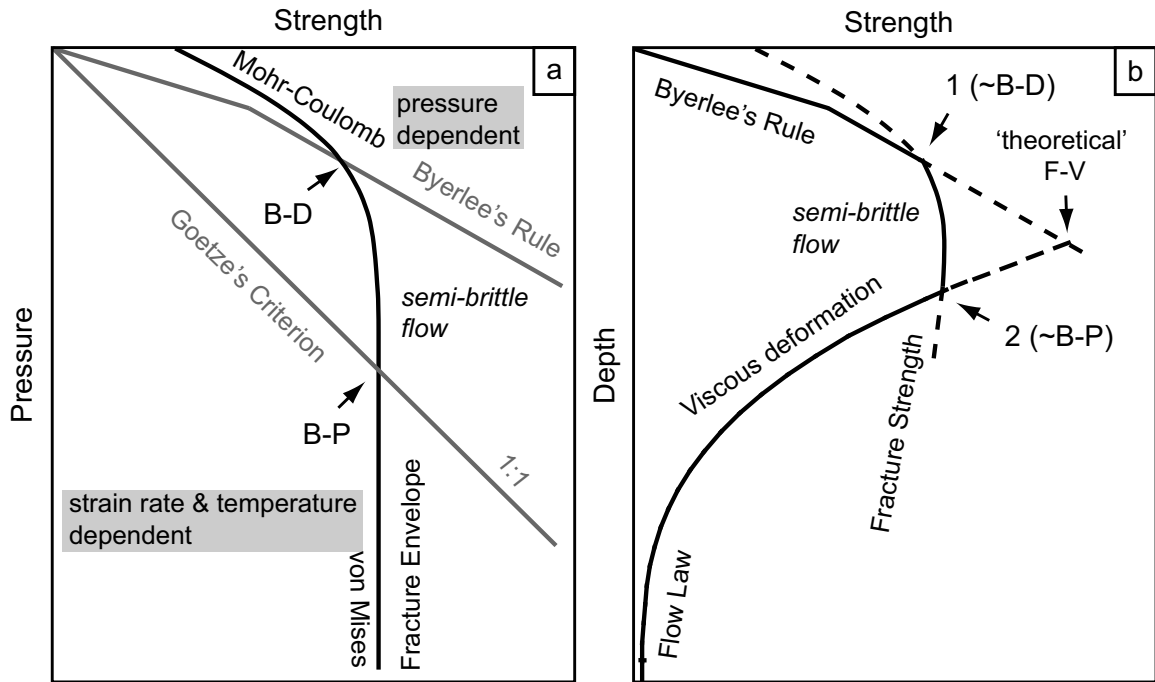
Figure 1.2: Strength of the crust. a) Strength envelopes. Fracture envelope encompasses Mohr-Coulomb and von Mises envelopes. B-D - brittle–ductile tranistion, B-P - brittle–plastic transition b) a rheological profile through an idealized lithosphere (modified after Kohlstedt et al., 1995 and Shimada, 1993). F-V - frictional–viscous transition

Figure 1.2b shows a rheological profile for constant strain rate. Full lines represent strength-limiting envelopes as a function of depth and we can define three regions. In the shallow crust strength is dependent only on normal stress resolved on optimally oriented pre-existing faults. If we neglect the semi-brittle field, we find an intersection of the "Byerlee's rule" for frictional sliding with a flow law for viscous flow at a certain depth (dictated by the assumed strain rate and geothermal gradient). This is marked as the "theoretical F-V" in Fig. 1.2b. From this point on it is expected that the strength will decrease dramatically with increasing depth as the viscous flow is strongly temperature dependent. This "theoretical" frictional - viscous transition is however the result of extrapolating both steady-state flow laws as well as Byerlee's rule outside the range of their applicability (e.g. Carter and Tsenn, 1987; Shimada, 1993; Ohnaka, 1995; Blanpied et al., 1995). If we take into account the field of semi-brittle flow, we can remedy this problem and define the "brittle – ductile transition" (point 1 in Fig. 1.2b) and the "brittle – viscous" as point 2 in Fig. 1.2b.

As mentioned above, the position of the "brittle - viscous" transition depends on the strain rate and temperature and the position of the "brittle – ductile" transition will depend on the fracture strength which is poorly constrained for earths crust. Nevertheless, these profiles imply that the strength of the lithosphere will be the highest around the "brittle – ductile" and "brittle – viscous" transitions. It is likely that the region around the "brittle - viscous transition" presents a load bearing layer with the highest potential for nucleating large earthquakes if the stored energy is abruptly released.

Despite the acknowledged importance of semi-brittle flow, few experimental studies explore this region due to the difficulty to deform crustal rocks at relevant confining pressures and temperatures (e.g. Tullis and Yund, 1977, 1980; Kronenberg and Shelton, 1980; Blanpied et al., 1991; Chester and Higgs, 1992; Hirth and Tullis, 1994; Blanpied et al., 1995, 1998; Keulen et al., 2007; Trepmann et al., 2007; Keulen et al., 2008; Druiventak et al., 2011; Brantut et al., 2011; Pec et al., 2012a,b; Violay et al., 2012).

Useful insights are gained by deforming fault rock analogue materials (e.g. Noda and Shimamoto, 2012, 2010; Niemeijer et al., 2009, 2008b; Niemeijer and Spiers, 2007, 2006; Bos and Spiers, 2000; Bos et al., 2000a,b; Bos and Spiers, 2001, 2002a,b; Shimamoto, 1986) which exhibit a "frictional – viscous" transition at better accessible conditions in the laboratory. Nevertheless, despite advances made in this field, no widely acknowledged theoretical framework which would be useful to in the semi-brittle regime exists as this region is difficult to treat due to the normal stress, temperature and strain rate dependence. In fact, the rock deformation community is mostly split into experimentalists working on friction and experimentalist working on viscous flow with little overlap between the fields.

During this thesis I have conducted deformation experiments on crushed granitoids (as an analogue for a fault zone in the continental crust) and explored a broad range of confining pressures (300 MPa – 1500 MPa), temperatures (300 – 600°C), displacement rates (10^{-6} – 10^{-8} m s^{-1}, inducing shear strain rates of 10^{-3} – 10^{-5} s^{-1}) and finite bulk shear strains (γ_{bulk} = 0 – 5) where the material deforms by semi-brittle flow. Based on detailed microstructural observations down to ångstöm scales it is attempted to identify physical processes responsible for the observed mechanical response. Based on the experimental results, an expected rheological behavior of natural fault zones is discussed.

1.5   Organization of this thesis

Individual chapters of this thesis were written in the form of papers, and therefore a certain amount of repetition is unavoidable. The thesis is organized as follows:

- Second chapter describes the experimental procedure, data treatment and the deformation apparatuses used during this study in detail. Part of this data was published in:

  *Tarantola, A., Diamond, L., Stünitz, H., Thust, A. and **Pec, M.** (2012). Modification of fluid inclusions in quartz by deviatoric stress. III: Influence of principal stresses on inclusion density and orientation. **Contributions to Mineralogy and Petrology**, 164, 537-550. doi: 10.1007/s00410-012-0749-1.*

  where the mechanical data was compared to stress estimates and estimates of orientation of the stress field based on fluid inclusion analysis of deformed quartz crystals. This independent gage provided an opportunity to better understand the deformation apparatus.

- Third chapter reports the microstructural and mechanical development in granitoid fault rocks deformed in semi-brittle flow to low finite strains. Strain partitioning and localization occurs and amorphous material is described in slip zones which accommodate large amounts of displacement. The experimental procedure is being optimized

to obtain reliable mechanical data. Microstructural features which lend themselves to quantification are identified and a quantitative method to track comminution is being developed (Vs/Va ratio). This chapter was published as:

Pec, M., *Stünitz, H.,Heilbronner, R. (2012). Semi-brittle deformation of granitoid gouges in shear experiments at elevated pressures and temperature.* **Journal of Structural Geology**, *38, 200-221. doi: 10.1016/j.jsg.2011.09.001.*

- Fourth chapter focuses on the microstructural development of the nanocrystalline, partly amorphous material described in the previous chapter to fragment-loaded amorphous material with increasing finite strain. Detailed microstructural observations in SEM-BSE and Cathodoluminescence are complemented with nanostructural observations in TEM. Based on the mechanical data, the temperature increase during the formation of the amorphous material is being estimated. Microstructural data is compared to mechanical data and a possible explanation is discussed. Possible natural analogues for this material are being proposed. This chapter was published as:

  Pec, M., *Stünitz, H.,Heilbronner, R., Drury, M.R., De Capitani, C. (2012). Origin of pseudotachylites in slow creep experiments.* **Earth and Planetary Science Letters**. *doi: 10.1016/j.epsl.2012.09.004.*

- Fifth chapter explores the microstructural and mechanical behavior of granitoid fault rocks over a broad range of pressures, temperatures and displacement rates. The observations are compared to current theories and a possible approach to treat the "frictional – viscous" transition is being discussed. Processes responsible for amorphization are being discussed in more detail and their rheological implications are explored. This chapter will be submitted to *Journal of Geophysical Research.*

- The sixth chapter presents a summary, conclusions and opportunities for future work.

- Appendix A contains a manual which introduces a MATLAB program written for the evaluation of data from rock deformation apparatuses. It documents all necessary assumptions taken when recalculating the raw data to stress, strain etc. The source code for the program is available at: *http://www.sites.google.com/site/rigprogram*

- Appendix B contains a list of performed experiments.

Experimental methods

2.1 Introduction

In this chapter, the deformation apparatus as well as the experimental procedure and its development will be described in detail. The experiments were performed in the rock deformation laboratory at the University of Tromsø in Norway. Most of the experiments were performed in "Rig 2" (see Appendix B for a list of experiments and used conditions), which was in the course of this project expanded with a digital recording system and a digital linear transformation measurement (DLT) system. The added experimental facility motivated the development of a MATLAB program described in the Appendix for convenient data processing. The availability of digital data from the whole duration of the experiment (pressurization and heating, deformation, quenching and depressurization) adds the opportunity to analyze the behaviour of the deformation machine itself. The procedures for that are treated in this chapter. At last I will discuss the stress conditions during an experiment and the detection limit, accuracy, precision, and resolution of the apparatus.

2.2 Deformation apparatus and pressure vessels

2.2.1 Solid medium deformation apparatus

Two modified Griggs-type solid medium deformation apparatus ("Rig 1" and "Rig 2") were used in this study (Figs. 2.1, 2.2, 2.3). The main differences between the two apparatus are thinner tie bars to allow the use of an internally cooled pressure vessel ("Hercules") on "Rig 1" and the DLT measurement system installed on "Rig 2". Otherwise, apart from some other minor differences in the electric circuiting and the connection of the automatic pumping system, the rigs are very similar. The fact that the derived stress – strain curves
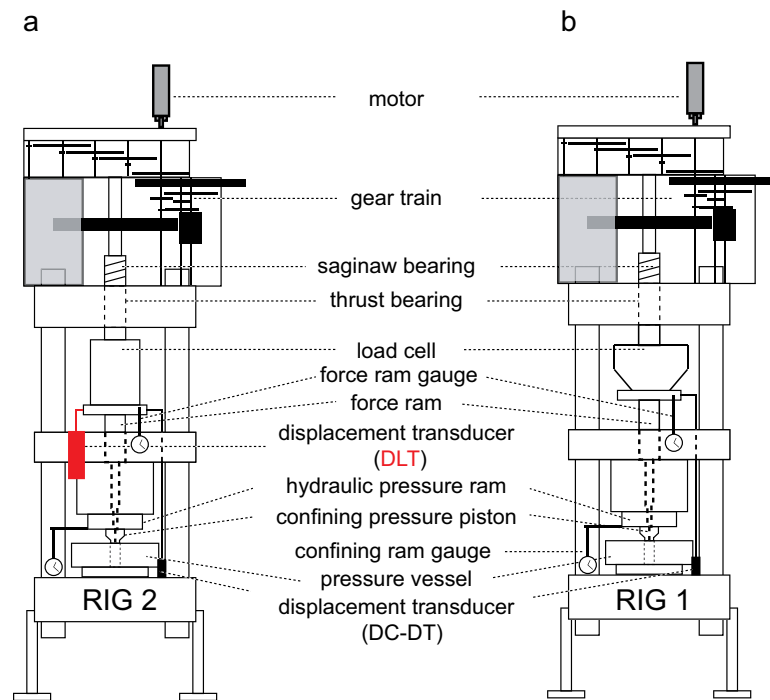
Figure 2.1: Deformation apparatuses. a) rig 2 b) rig 1. Modified after Holyoke and Kronenberg (2010).

show good reproducibility irrespective of the deformation apparatus used shows that the load cells and displacement transducers are well calibrated. The apparatus consists of a steel frame with bottom, middle and upper steel plates connected by steel bars (Fig. 2.2c). One of the electrical poles is connected to the steel frame. The hydraulic ram and the confining pressure piston are attached to the middle steel plate. Water cools the hydraulic cylinder as well as the pressure vessel and minimizes the confining pressure variations due to room temperature variations.
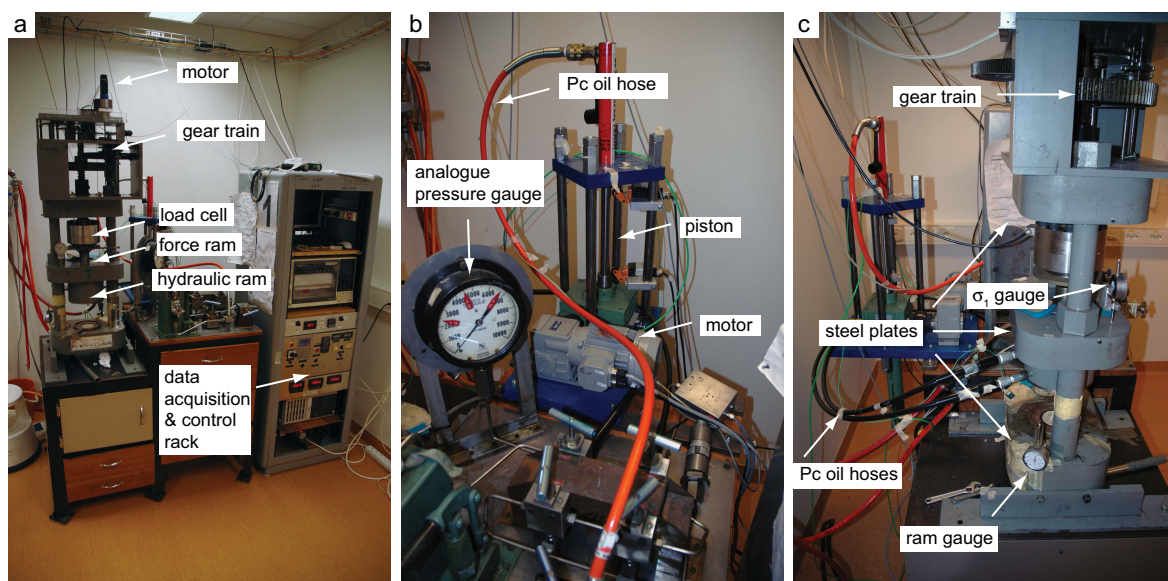
Figure 2.2: Rig 1. a) front view of the deformation apparatus b) automatic pumping system c) back view of the apparatus.

The oil pressure in the hydraulic ram is recorded with an external pressure transducer and is used to calculate the confining pressure (Fig. 2.3b).

The oil can be either pressurized with a hand-pump or a motorized linear drive and hydraulic cylinder, which acts as an oil reservoir and increases/decreases the oil pressure (Figs. 2.2, 2.3). The advancement of the confining pressure ram moves the σ_3 piston (diameter ~ 25.4 mm) into the pressure vessel (Fig. 2.4). Salt collapse around the sample builds up the confining pressure. An external load cell, which is attached to the gear train by a Saginaw bearing, is used to measure the load on the sample (Figs. 2.1, 2.2, 2.3). The gear train on top of the upper steel plate allows for changes in the displacement rate by up to 6 orders in magnitude. In addition, a digitally adjustable motor is used with a potentiometer control allowing a range of r.p.m. between 0 and 1000. The force ram pushes on the tungsten carbide σ_1 piston (diameter 6.3 mm, Fig. 2.4) which advances through the upper Pb-disc until it hits the sample. All the interfaces, rods, and parts below the load cell contribute to the processes in the sample assembly and affect the measured sample strength (see 2.4).
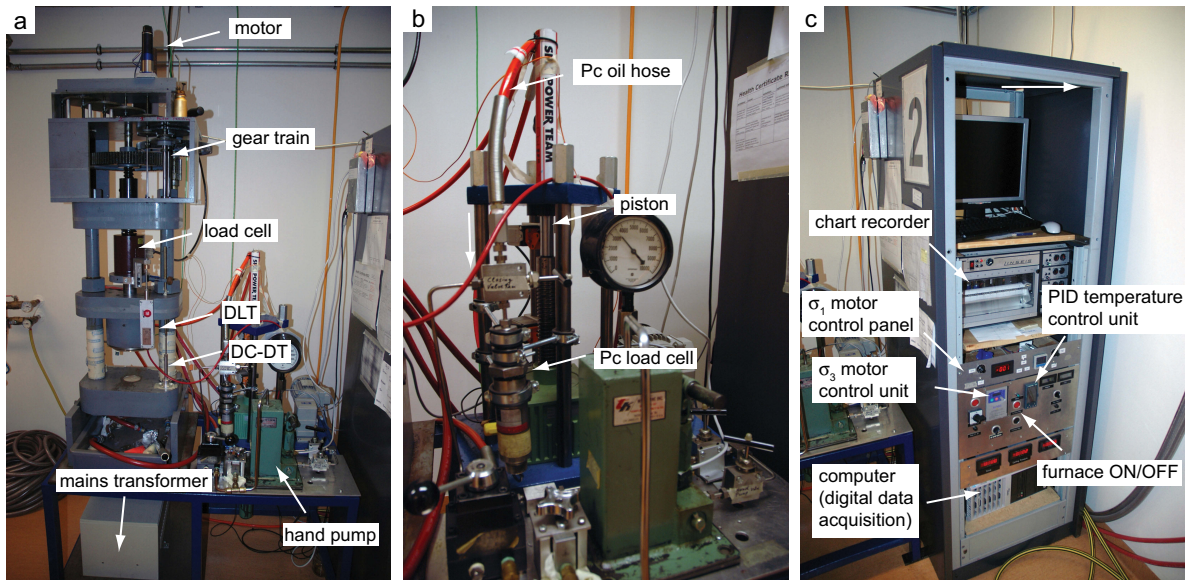
Figure 2.3: Rig 2. a) front view of the deformation apparatus b) automatic pumping system c) data acquisition and control rack.

2.2.2 Pressure Vessels

Three different types of pressure vessels were used (see Appendix B and Fig. 2.5): "old" (conventional Griggs-type), "new" (strip-wound container manufactured by STRECON), and "Hercules" (an internally cooled pressure vessel manufactured by STRECON). Most experiments were performed in the "old" pressure vessels. All the pressure vessels have a 1-inch (25.4 mm) diameter bore. The pre-pressed insert is made of tungsten carbide (WC) or steel. The pressure vessel is placed on top of the base plate, which consists of a steel disc surrounded by a non-conducting Teflon or plastic ring. In the base steel disc, a hole for the WC base plug and thermocouple inserted from the sample assembly is present. It contains a copper rod where one electrical pole is attached to lead the current into the water-cooled base plate.
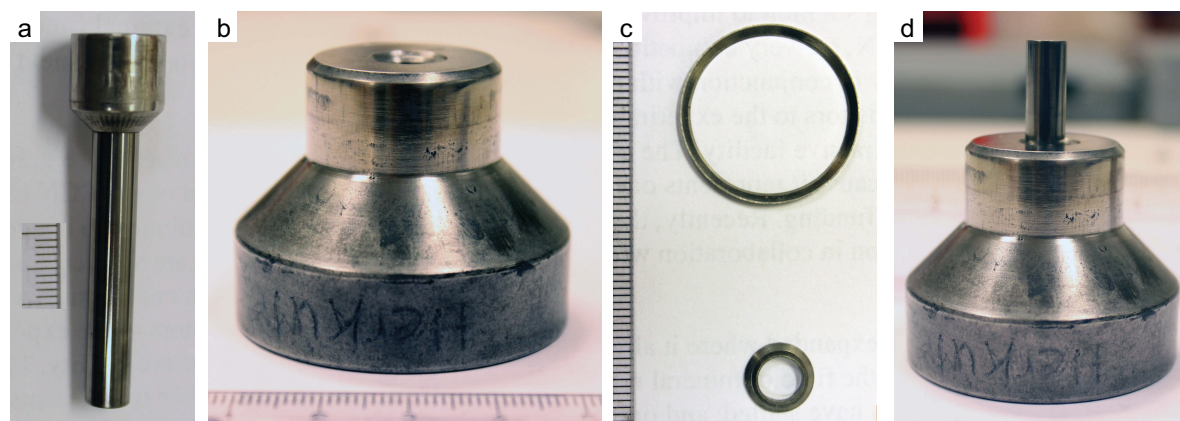
Figure 2.4: Pistons and packing rings. a) WC σ_1 piston b) steel σ_3 piston c) σ_1 and σ_3 piston packing rings d) σ_1 and σ_3 pistons

The contact between the pressure vessel and the base plate is electrically insulated from the load frame and the pressure vessel by thin cardboard discs. The main difference between the individual types of pressure vessels is in the path of the cooling water through the pressure vessel. In the "old" pressure thin copper tubes (4.5 mm inner diameter) are placed on top of the pressure vessel and the base plate. Cooling water travels on the outer perimeter of the pressure vessel. In the "new" pressure vessel an aluminium upper plate is screwed to the top of the pressure vessel and allows circulation of water in direct contact with the pressure vessel. The base plate and pressure vessel cooling is identical to the "old" pressure vessel, however the tubes have a larger diameter (6.5 mm inner diameter) leading to higher water fluxes and more efficient cooling. Steel plates are attached to the top and bottom of the "Hercules" pressure vessel to allow direct cooling. Twelve holes allow water to pass through the outer steel ring around the WC insert from the bottom to the top steel plate. In both "new" and "Hercules" pressure vessels the base plate is attached to the pressure vessel with two brass screws. Despite the different efficiency in cooling and thus probably a different temperature gradient in the sample assembly, no mechanical or microstructural variations were observed which could be connected to the use of the different pressure vessels.
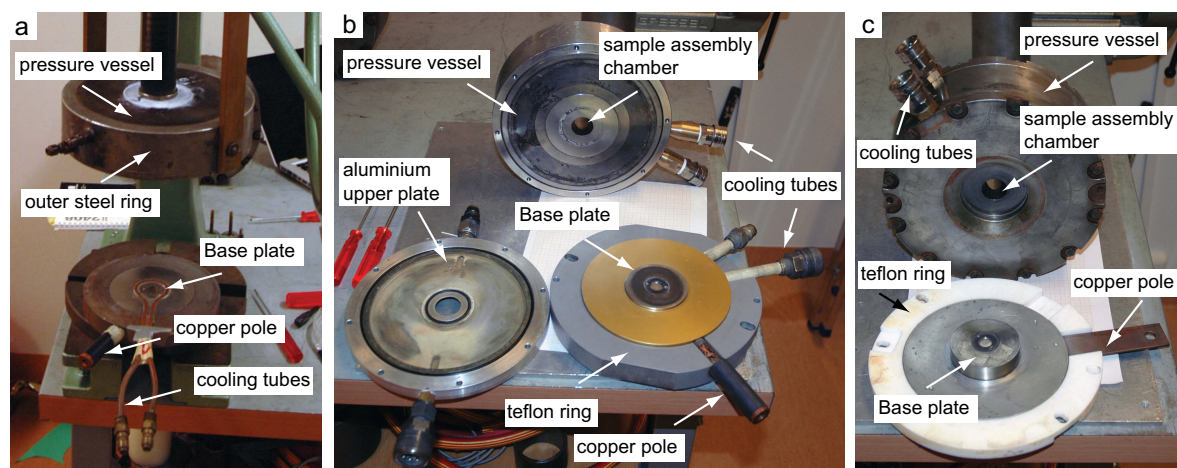
Figure 2.5: Used pressure vessels. a) old b) new c) Hercules
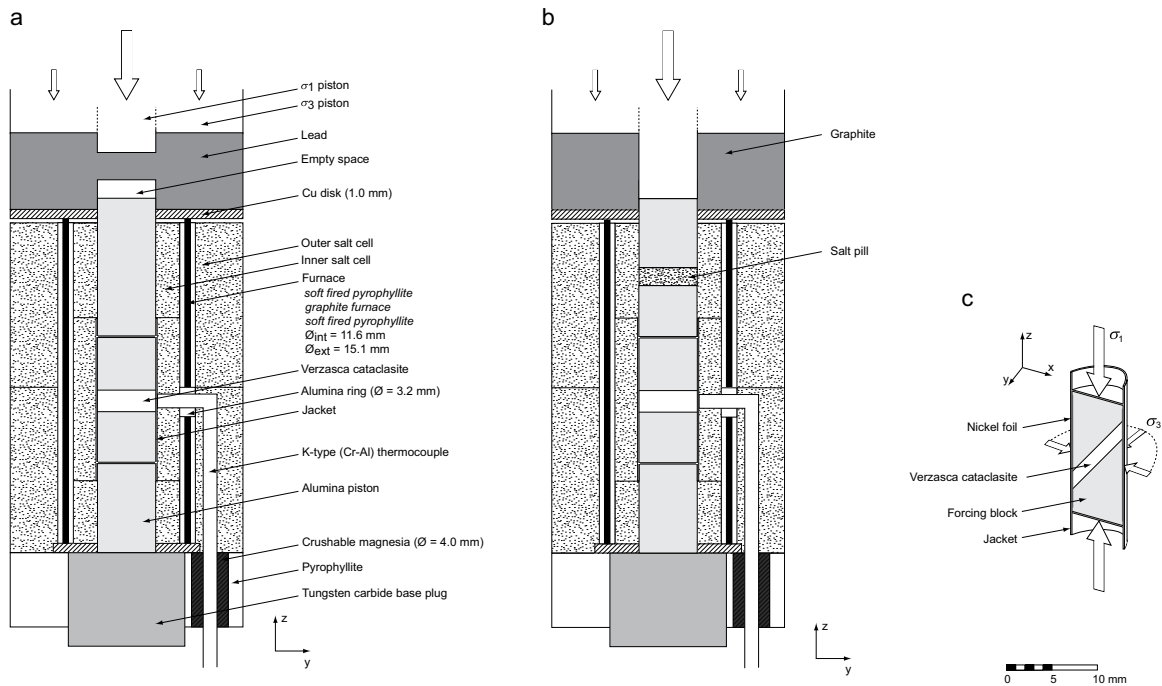
Figure 2.6: Sample assembly and sample. a) sample assembly used in most experiments b) sample assembly used with the graphite upper plug c) sample (modified after Tarantola et al., 2010).

2.3 Sample assembly

A solid salt sample assembly (Figs. 2.6, 2.7) is used to transmit the confining pressure. Various modifications were tried out, especially regarding the salt material used for the inner salt cell and the upper plug material (see Appendix B). The sample is placed in between two alumina pistons which are ground flat, orthogonal, and plane-parallel. The correct position of the thermocouple (Tc) is achieved by dimensioning the bottom piston to a calculated length with respect to a defined lower salt cell height (fixing the Tc-position) and assuming the salt compaction during building up of the pressure (1.5, 1.7 and 1.8 mm compaction for 500, 1000 and 1500 MPa experiments, respectively). Around the sample and pistons the inner salt pieces are fitted, together forming the inner salt cell. The inner salt cell consists of 3 pieces: The lower and upper salt pieces have an inner diameter of ~ 6.5 mm providing a tight fit for the alumina pistons. The middle inner salt piece has an inner diameter of ~ 7 mm providing a tight fit for the sample. A hole for the thermocouple is drilled into the middle inner salt piece (Figs. 2.6, 2.7) and furnace assembly. In the early experiments, sodium chloride (NaCl) and in the later experiments potassium iodide (KI) was used for the inner salt cell (see Appendix B). KI has a lower flow stress and melting point (Inoue, 1957; $T_{melt} = 681\,°C$ at ambient pressures), so that it is a more suitable pressure medium at low temperature. Around the inner salt cell a resistivity furnace consisting of an inner and outer pyrophyllite tube and a central graphite tube is placed. The hole for the Tc through the furnace holds an alumina ring inside to insulate the K-type thermocouple electrically from the furnace. On top and bottom of the furnace two 1 mm thick copper discs are placed to allow the transmission of the current through the furnace. The outer salt cell consists of an upper and lower salt piece made of NaCl. The outer salt cell is wrapped with a Teflon tape to reduce friction on the salt / pressure vessel interface and to reduce friction and corrosion of the pressure vessel walls,

and for easier pressing-out of the sample assembly after the experiment. In the lower outer
salt piece a hole is drilled vertically and a u-shaped hole is cut with a scalpel to seat the
thermocouple. A chromel-alumel thermocouple (K – type) was used for all experiments. The
bottom of the sample assembly is made of a tungsten carbide (WC) plug on which the sample
and alumina pistons are seated. A base pyrophyllite with the same outer diameter as the
outer salt cell surrounds the WC plug. The thermocouple is prevented from extrusion at high
pressure by a crushable magnesia sleeve within the base pyrophyllite (Figs. 2.6, 2.7). The
load from the piston is transmitted through an upper soft metal disc. Lead (Pb), lead – zinc
(Pb – Sn), graphite (C) and indium (In) were tested as upper disc material (see Appendix
B). Indium gave a superior detection limit compared to lead. However, it started extruding
around 500 MPa confining pressure and T = 300 °C. Graphite caused high "friction" at the
experimental conditions used showing a high increase in the load as the piston was advanced
(see section 2.6). Furthermore, large elastic compaction occurs during building up of the
pressure rendering the use of Graphite plugs difficult at higher confining pressures. Lead
turned out to be the most useful material for the upper metal disc as it is reasonably soft
if re-molten before every experiment and does not extrude from the pressure vessel even at
1500 MPa confining pressures and temperatures of 1000 °C.
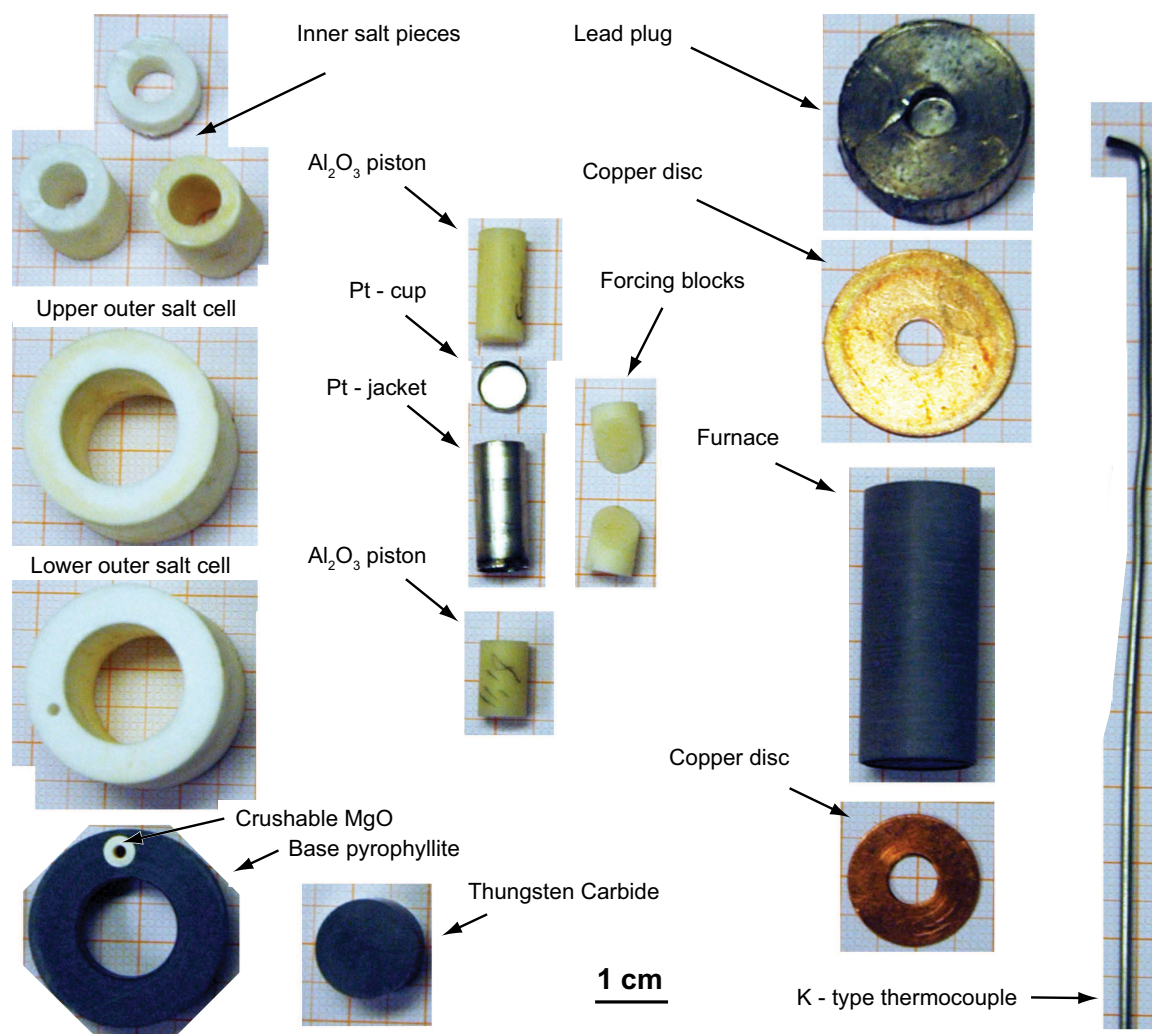
Figure 2.7: Individual pieces used to prepare the sample assembly. Nickel foil, alumina ring and Verzasca
powder are not shown.

2.4 Sample preparation

2.4.1 Powder

To obtain the fault rock material, a fine-grained granitoid gneiss sample (P2) from the Val Verzasca (see Keulen (2006) for coordinates) was crushed to powder by pounding on it once or twice with a hammer in a steel container. After each hit, the powder was sieved through a sieve with a 200 μm mesh. The fragments, which did not pass through the mesh, were crushed again. This procedure was repeated until enough powder was produced with a grain size $\leqq$ 200 μm (Fig. 2.8). The amount of material produced was sufficient to be used for all experiments.
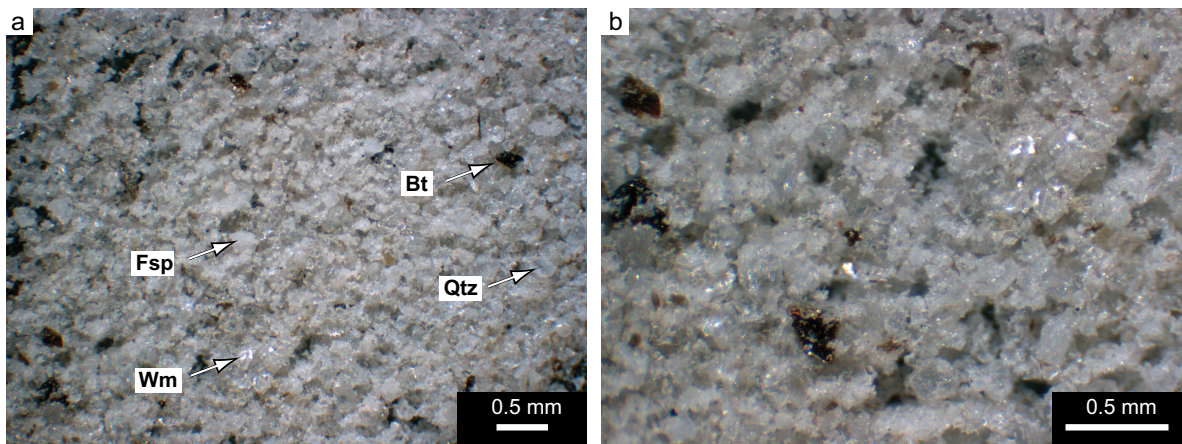
Figure 2.8: Starting material powder. Bt – biotite, Wm – white mica, Fsp – feldspars, Qtz – quartz. a) lower magnification image b) high magnification image

2.4.2 Forcing blocks

Two types of forcing blocks were used: Verzasca forcing blocks in the early experiments (176MP – 194MP, 237MP and 239MP) and alumina forcing blocks in the later experiments (195MP – 330MP). The use of Verzasca gneiss blocks was stopped because at the high peak differential stresses the strength of the intact Verzasca gneiss turned out to be equal or lower than that of the Verzasca powder after reaching a finite shear strain, γ , of $\sim$ 1.5 (Fig. 2.9). Essentially, coaxial sample deformation started then. The considerably stronger alumina forcing blocks did not deform during the experiments and a good correlation between the amount of finite shear strain calculated from the machine data and the amount of finite shear strain measured on thin-sections was achieved (Fig. 2.9).Verzasca forcing blocks were prepared from an intact boulder (P2). Cores were drilled using a diamond drill with an inner diameter of 6.55 mm. The used alumina forcing blocks (diameter of 6.33 mm) were manufactured commercially from fine- grained alumina (grain size $\sim$ 5 μm, Figs. 2.7,2.10). The pistons were cut to a length of 11.5 – 14 mm and ends ground flat, orthogonal, and plane parallel (to an accuracy of $\sim$ 0.005 mm). These pistons were cut in the middle at an angle of 45° with a Buehler diamond wafer saw. The pre-cut surfaces were ground flat with silica carbide (grain size $\sim$ 150 μm) to assure good grip. No grooves were cut into the forcing blocks. After this procedure the forcing blocks were cleaned with ethanol and left to dry before an experiment.
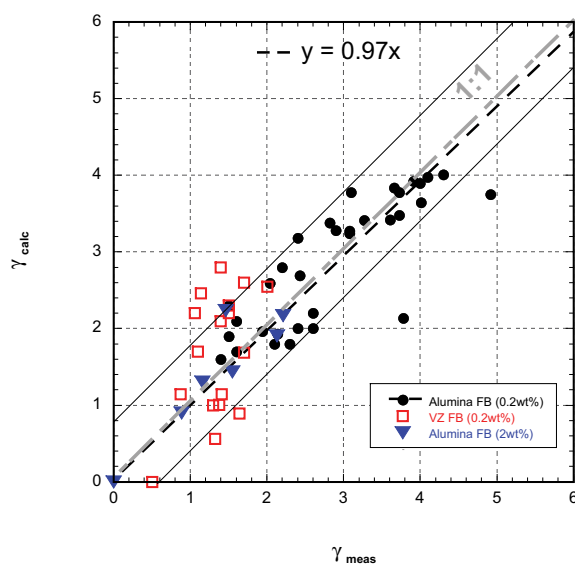
Figure 2.9: Shear strain calculated from the apparatus record compared to shear strain measured in thin sections. FB – forcing blocks. VZ – Verzasca gneiss. Black dashed line – best fit for alumina forcing blocks experiments, Black solid lines – maximal variability neglecting two outliers. Note that Verzasca gneiss forcing blocks experiments do not accommodate more than a shear strain of ~ 1.5
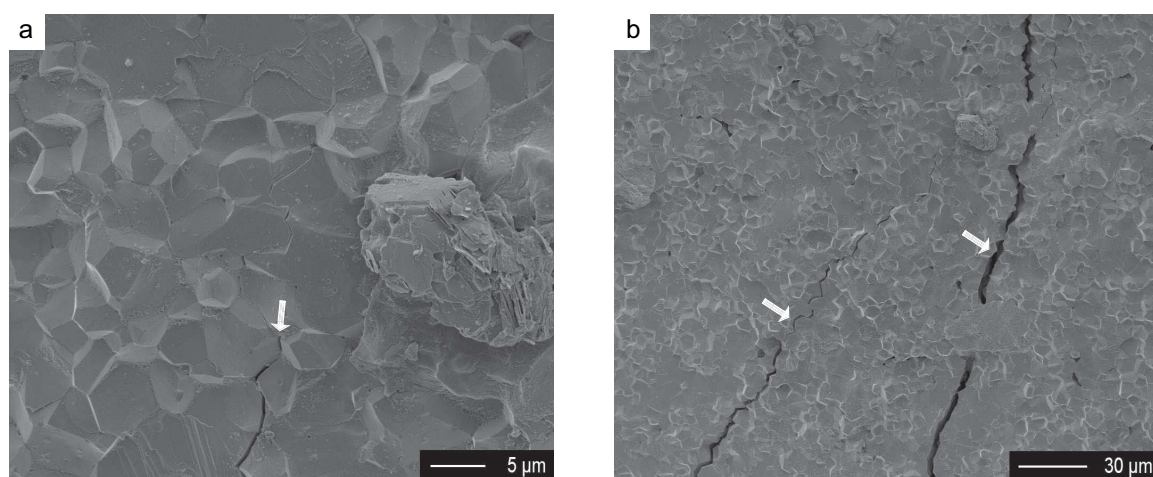
Figure 2.10: Alumina forcing blocks. Broken surface SEM-SE (secondary electron) images of an alumina forcing block. White arrows show unloading cracks.

2.4.3   Jacketing

A gold or platinum jacket (roughly 16 mm long) was cut from a prefabricated metal tube with an outer diameter of 6.9 mm, inner diameter 6.6 mm and wall thickness of 0.15 mm (see Appendix B for jacketing used for individual experiments). Two cups of the same metal as the jacket were prepared from a foil of 0.15 mm thickness. In later experiments this jacket material (from 245MP onwards) was annealed at 900 °C for at least 2 hours. The lower cup was fit into the tube and weld sealed with a graphite welding arc in the early experiments and with a Lampert precision welding apparatus in the later experiments. A mark on the metal tube was made with a scalpel to assure good orientation of the forcing blocks in the jacket with respect to the thermocouple.
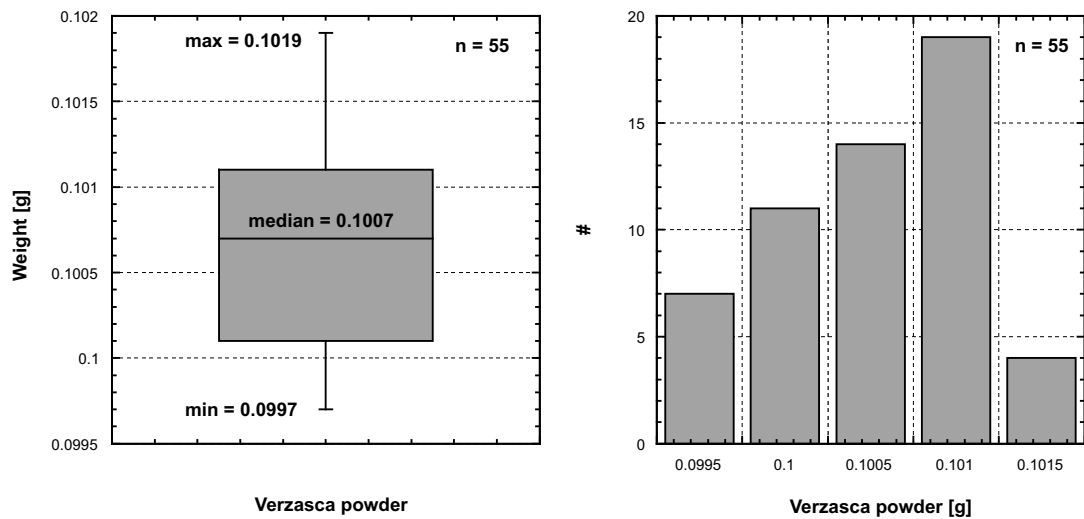
Figure 2.11: Statistical distribution of the measured weight of Verzasca gneiss powder put into the sample without one outlier (powder weight = 0.1076 g).

2.4.4 Sample fabrication

The lower forcing block was inserted into the prepared jacket. In the experiments performed with alumina forcing blocks, a thin Nickel foil (thickness = 0.025 mm) was wrapped around the forcing blocks. ~ 0.1 g of the crushed powder (see Appendix B and Fig. 2.11 for exact amount) was placed on top of this lower forcing block and compacted with a flat brass tool cut at 45 degrees to the sample long axis. A small amount of water (2 or 0.2 μl, see Appendix B for amounts) was placed on the top tip of the upper forcing block with a micro-syringe or a micro-pipette (from experiment 279MP onwards).
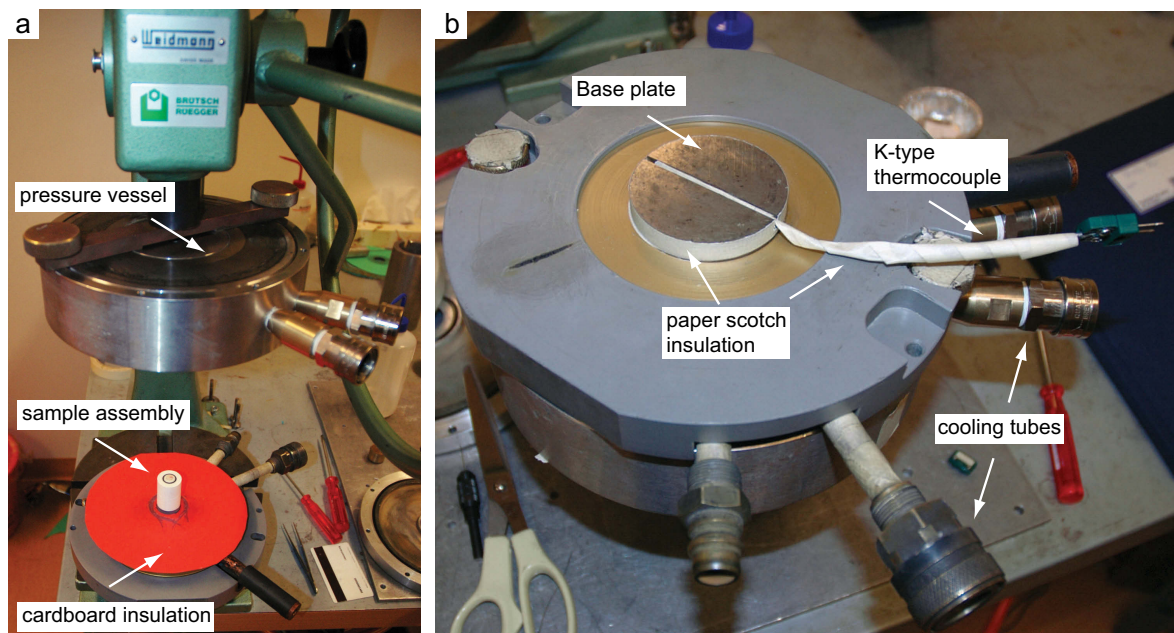
Figure 2.12: Putting the sample assembly into the pressure vessel. a) pressure vessel and base plate centred in the hand press. b) View from the bottom of the pressure vessel after insulation of all potential contact sites with the rig itself.

The upper forcing block with the drop of water was then lowered on top of the pre-compacted powder. The upper cup was placed on top of the upper forcing block and weld sealed as fast as possible (usually within $\sim$ 10 minutes) to avoid water evaporation. Various cooling methods were tried out – liquid nitrogen cooling, water-cooling and finally a cooled brass heat sink was used. No differences in the mechanical or microstructural record were detected which could be assigned to different H_2O contents due to the different cooling methods.

2.5   Experimental procedure

After the sample assembly is fit together, it is placed on the centred base plate in an arbor press. The cardboard disc is placed around the sample assembly on the base plate (Fig. 2.12a).

The pressure vessel is attached to the arbor press piston and is carefully lowered onto the sample assembly. Once the sample assembly is in the pressure vessel, the base plate and thermocouple are insulated with a paper scotch tape (Fig. 2.12b), and the pressure vessel is placed below the hydraulic ram. The water hoses for cooling and electricity cable for heating are attached to the pressure vessel (Fig. 2.13). The σ_1 and σ_3 pistons are placed on top of the upper plug, and the hydraulic ram is lowered. Care is taken that no contact between the σ_1 piston and hydraulic ram occurs and that all interfaces are orthogonal to each other (Fig. 2.13). Load, pressure, and the displacement of the σ_1-piston are recorded by an analogue chart recorder as well as a digital chart recording system from the beginning of the pressure increase by slow manual pumping.

At $\sim$ 25 MPa confining pressure an audible cracking is usually heard, which indicates that the graphite furnace is in full contact with the copper discs. Around 50 MPa confining pressure, the furnace is turned on and the temperature is manually raised with a Eurotherm proportional-integral- derivative (PID) controller to the set point (30 °C). If no contact in the furnace is yet established the confining pressure is further raised to approx. 100 MPa and the heating sequence is repeated. Once at the set point the temperature is raised to 100 °C in a rate of 20 °C / min for all experimental temperatures. At $\sim$ 100 MPa confining pressure the automatic pumping system is started.
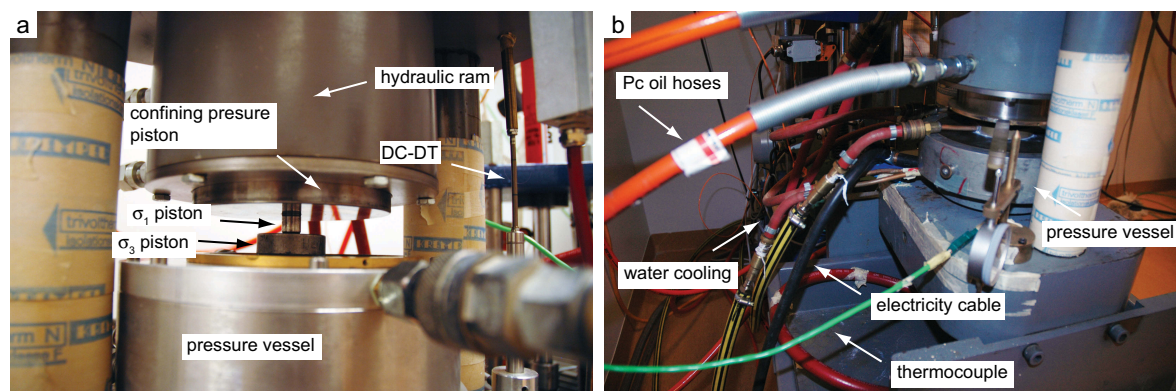
Figure 2.13: Loading the pressure vessel into the deformation apparatus. a) position before lowering the confining pressure piston. b) rear view of the attachment of the water cooling, electricity and thermocouple to the "old" pressure vessel
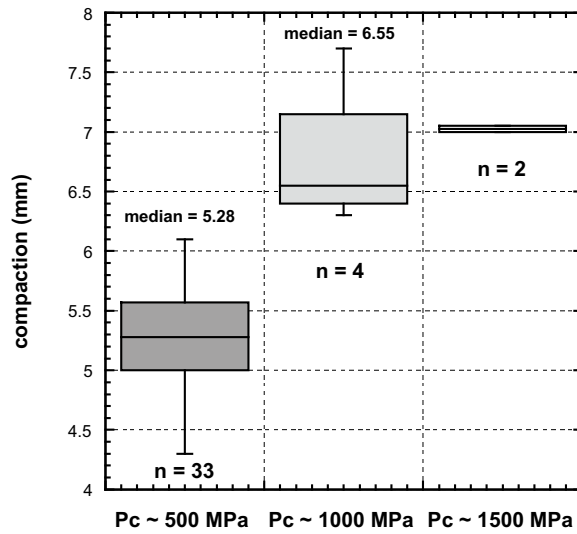
Figure 2.14: Total compaction of the whole sample assembly vs. confining pressure. Note that those values differ from the values used for the calculation of the correct TC position as they include also the compaction of the whole assembly from the lower salt cell upwards.

The movement of the confining pressure piston as well as that of the σ_1 piston is monitored with two manual gauges (Fig.2.2c).

During the building up of the confining pressure and temperature the salt cell compacts (typical compaction values are given in Fig. 2.14). The temperature is raised in $100\,°C$ steps to the desired value at progressively increasing confining pressure (typical output values are given for given temperature in both rigs, Fig. 2.15). The last heating step is performed just below the desired confining pressure. The whole pressurization procedure takes between 4 to 8 hours. Double thermocouple measurements indicate a vertical temperature gradient of $\sim 10\%$ from the centre of the shear zone to its tips (~ 3.165 mm). The vertical temperature gradient in the solid medium deformation apparatus is very high ($\sim 5 \times 10^3 - 1 \times 10^4\;°Cm^{-1}$) and slightly non-linear (Fig.2.16) due to the short furnaces relative to sample length (35.7 mm furnace length, sample including forcing blocks length ~ 13 mm). Further indication of the high heat fluxes in the sample assembly is the fact that switching off the furnace (for example during a failed experiment) causes the temperature to drop rapidly to room temperature in much less than 30 seconds.

After the experimental P-T conditions are reached the motor driving the σ_1 piston is started at a constant displacement rate. The σ_1 piston hits the sample after ~ 30 minutes to ~ 8 hours, depending on the amount of upper plug material between the upper alumina piston and σ_1 piston and the applied displacement rate. The sample deforms until the desired amount of vertical piston displacement was reached. Then the temperature is lowered to $200\,°C$ within 1.5 minutes (resulting in different quenching rates for different temperatures: $300\,°C = 1.1$ $°Cs^{-1}$, $400\,°C = 2.2\;°Cs^{-1}$, $500\,°C = 3.3\;°Cs^{-1}$, $600\,°C = 4.4\;°Cs^{-1}$). Simultaneously with the quenching, the load is removed as fast as possible by reversing the motor. The goal is to reach a $\Delta\sigma$ of ~ 100 MPa at the end of quenching. However, it is difficult to reach the exact value, especially at low temperatures, due to the very high differential stresses. If the load is too high during this period, the sample can audibly crack and fail – this happened in two experiments (191MP and 286MP). This failure during unloading is easy to identify in thin
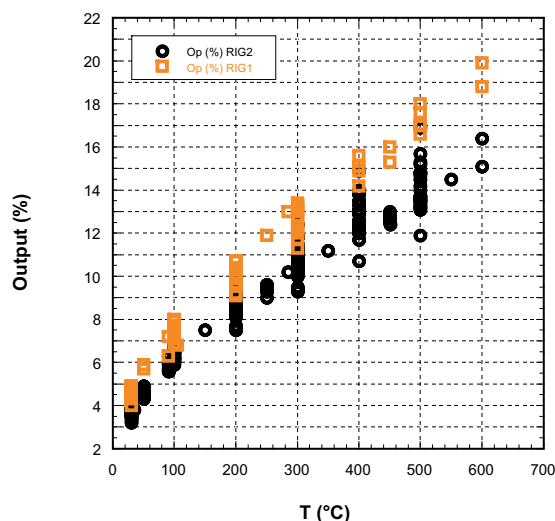
Figure 2.15: Typical output values of the Eurotherm PID controller.
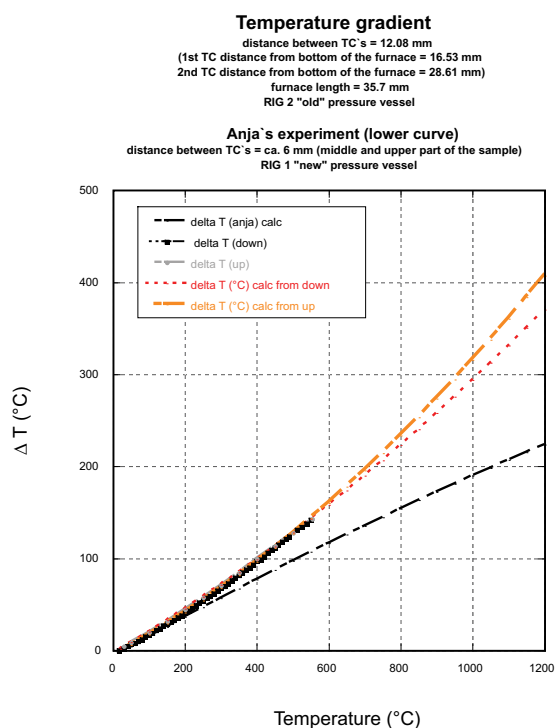
Figure 2.16: Double thermocouple experiments measuring the temperature gradient in the "old" and "new" pressure vessel at different distances.

section from microstructural cross-cutting relationships and further, the fracture cutting the fault rock as well as forcing blocks has a different orientation ($\sim 30°$ to σ_1) than features connected with the controlled part of the experiment. The $\Delta\sigma$ of ~ 100 MPa should approximate hydrostatic conditions, taking into account the forces acting on the piston in the pressure vessel (see section 2.6) and avoid excessive formation of unloading cracks (always sub perpendicular to σ_1). After reaching the cooling water temperature ($\sim 14\,°C$) and room pressure, the sample is pressed out from the pressure vessel. The sample is then carefully removed from the salt cell using a scalpel (Fig.2.17).
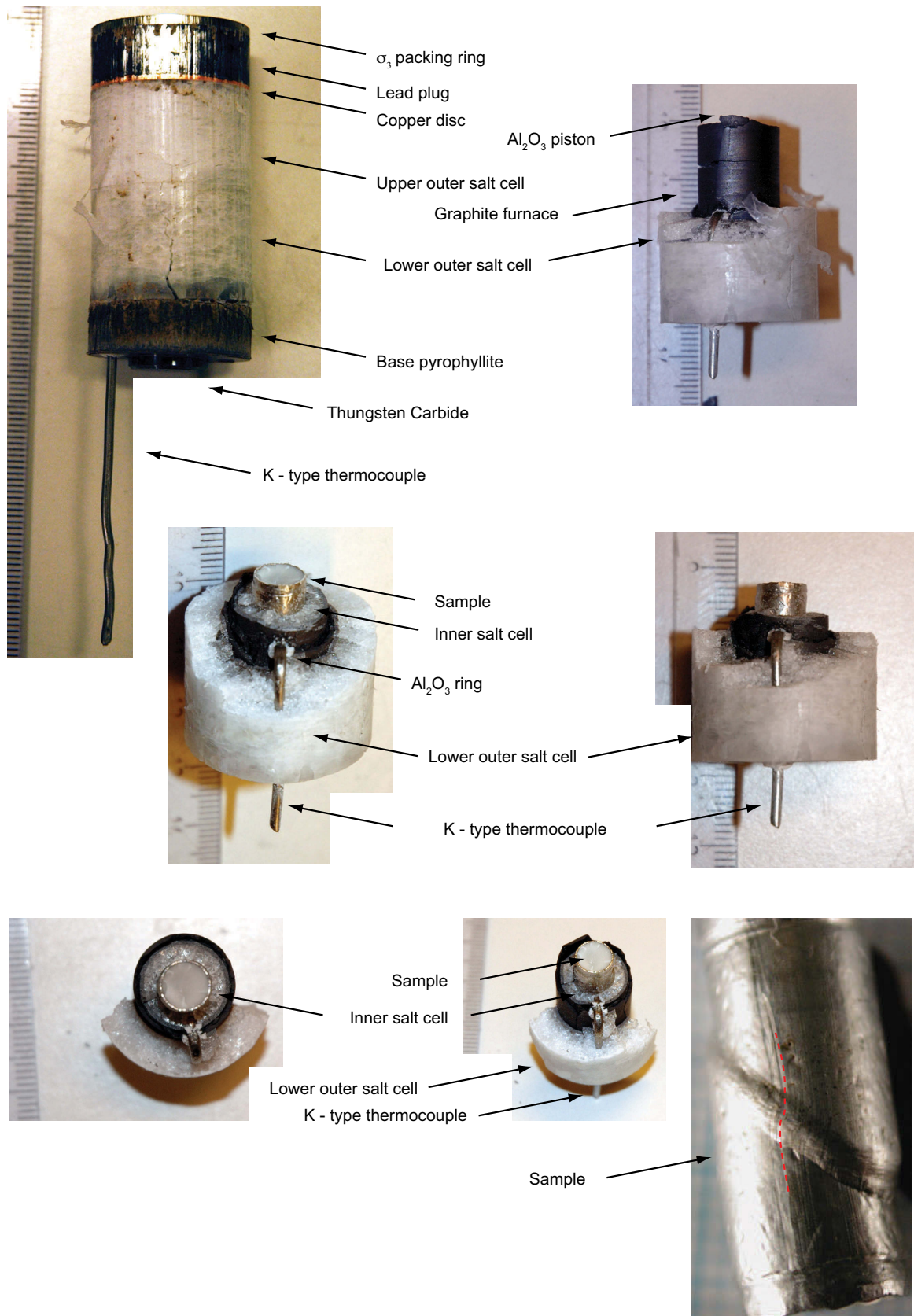
Figure 2.17: Sample and sample assembly after the experiment.

2.6 Characterization of the experimental parameters

The digital recording system allows to record the whole experiment at a sampling frequency of 2 – 0.1 Hz and provides a wealth of data about the apparatus and experimental conditions and parameters. In this section the data is analyzed and discussed.

2.6.1 General evolution of the recorded parameters during an experiment

2.6.1.1 Pressurization

During pressurization the confining pressure is increased, first with the hand pump and later with the automatic pumping system. The load cell (σ_1) starts to record the first load around a confining pressure of $\sim$ 100 MPa (the load cell assembly hangs on the force ram by its own weight, which is not supported at lower pressures and thus is not recorded). During the pumping, the σ_1 piston is advanced from time to time to avoid stripping off the packing ring of the σ_1 piston. Advancing the σ_1 piston with the motor causes a sharp increase in the force curve when the piston is pushed into the Pb (this increase is also referred to as "friction" in the literature), accompanied by a slight confining pressure decrease (Fig. 2.18b). After the yield point of the Pb the force increase diminishes and becomes linear at a low angle slope (Fig. 2.18a). The slope is steeper (Fig. 2.18) the more the σ_1 piston is pushed into the pressure vessel. The same correlation is seen with confining pressure, as these two processes (advancement of the σ_1 piston and the increase of confining pressure) are not separable, however the fact that the slope of the run-in curves scales only with the distance to hit point and not confining pressure shows that the steepness of the run-in slope is indeed controlled by the increasing contact area of the σ_1 piston with the pressurized sample assembly (see section 2.6.1.2 for further discussion and section 2.6.3 for more information on piston forces). A well-defined point can be derived from the intersection of two linear fits in the displacement – force space which approx. corresponds to the "yield point" of the metal plug (inset in Fig. 2.18b). Comparing the stresses at this point with the confining pressure we find a 1:1 agreement with hydrostatic pressures shifted by $\sim$ 90 MPa (Fig. 2.19) indicating that at the Pb "yield point" during advancement of the σ_1 piston the sample is already subjected to differential stress (see section 2.6.3).

Leaving the experiment to equilibrate over an extended period of time, we find that the stresses recorded by the σ_1 piston always are 65 – 165 MPa lower than the stresses recorded by the σ_3 piston (Figs. 2.20). Two end-member possibilities (and all combinations of these) exist: either the σ_1 piston records the "correct" pressure and the lower values of 65 – 165 MPa result from "friction" of the σ_3 piston at the pressure vessel, or the σ_3 piston records the "correct" pressure and the lower values of 65 – 165 MPa result from "friction" of the σ_1 piston inside the σ_3 piston, inside the apparatus, or the sample assembly. If we assume that the stresses in the sample assembly should tend towards hydrostatic pressures (i.e. $\sigma_1 = \sigma_{2,3}$) during longer equilibration periods, we can estimate the "friction" of the interfaces acting against both pistons in the apparatus and the sample assembly.

a

b
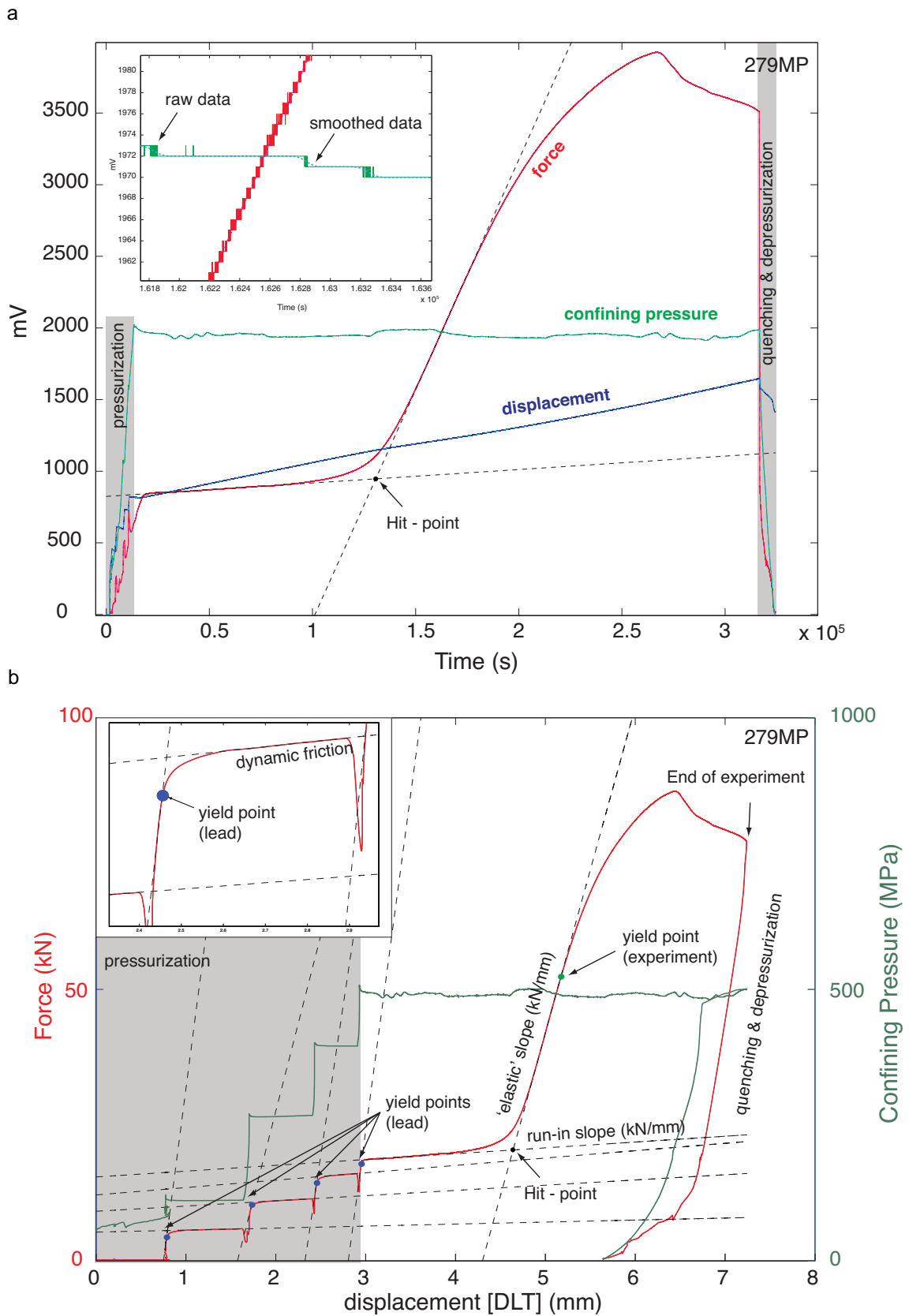
Figure 2.18: Chart records of an example experiment. a) time vs. input. Inset shows the smoothed and raw data (see Appendix B for details). b) Force and confining pressure vs. piston displacement of the same experiment as in a.
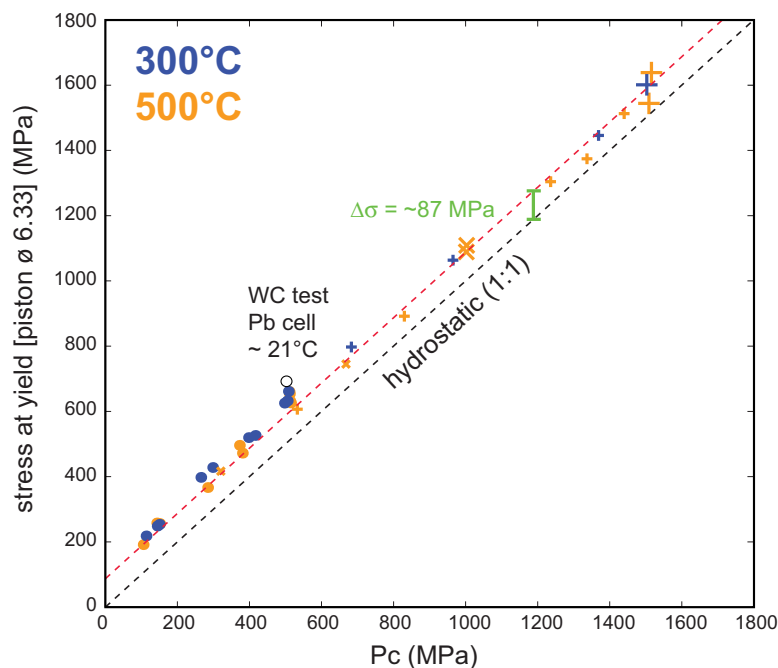
Figure 2.19: Stress at σ_1-piston at the "yield point" vs. confining pressure recorded by the oil pressure in the pumping system. Black dashed lines shows a 1:1 correlation.
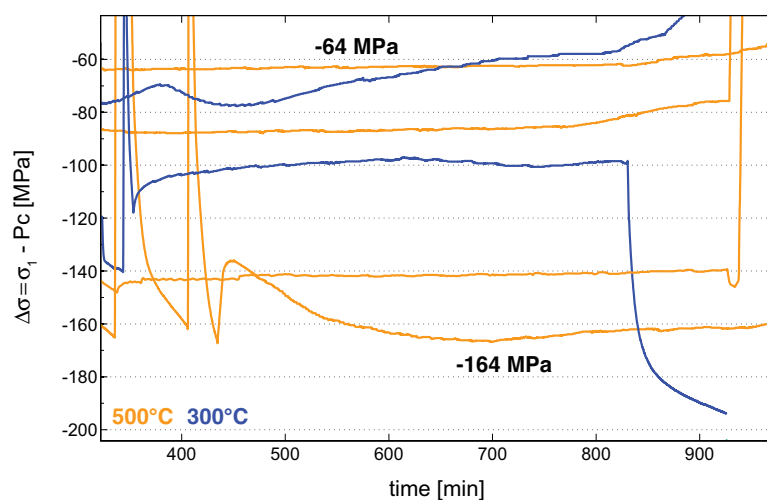
Figure 2.20: Sample assembly equilibration. Difference between the pressures recorded from the confining pressure and force load cells. Abrupt changes reflect the driving in of the σ_1 piston into the pressure vessel.

2.6.1.2   Deformation

At the beginning of every deformation experiment, once the desired P-T conditions are reached, the σ_1-piston is advanced at a pre-set displacement rate. First, the force increases sharply up to the "yield point" of the Pb (Fig. 2.18). After the Pb "yield point", the force curve records the constant-rate movement of the σ_1 piston through the top Pb disc (run-in curve) (Fig. 2.18). The touching of the σ_1 piston with the inner alumina piston marks the point where direct sample loading commences, and is called the "hit point" (Fig. 2.18). Unfortunately, this event is not marked by a single point in time, but instead, the direct loading of the sample takes place over a time interval and it produces a gradual increase in the force

curve (Fig. 2.18). Conventionally, a discrete hit-point is constructed by fitting, extrapolating, and intersecting the two linear slopes of the "run-in" and the steeply increasing segment of the force curve (Fig. 2.18). The confining pressure shows slight variations due to changes in the room temperature (night / day) and extension of the apparatus during loading (see section 2.6.2). These variations are on the order of +5 to -20 MPa with respect to the confining pressure at the hit point (i.e. $1 - 4$ % at Pc $\sim$ 500 MPa). Upon close inspection, it can be seen that also the displacement rate (blue line, Fig. 2.18a) is not entirely constant during the whole experiment and a small slope change can be detected at the hit-point. If we plot the first derivatives by time of the force ($\partial F/\partial t$), displacement ($\partial Dx/\partial t$) and confining pressure curves ($\partial Pc/\partial t$), the changes in trends become more visible (Fig. 2.21). The slope of the force curve increases in the beginning ("friction") and then quickly decreases (yield point of Pb) to a level close to zero (2×10^{-5} kN/s, see section 2.6.3) during the "run-in" stage of the experiment. During this stage the displacement rate of the σ_1-piston is roughly constant (Fig.2.21b). As the σ_1-piston approaches closer to the hit-point (gray vertical line in Fig. 2.21) the force slope progressively increases and the displacement rate decreases (by $\sim 0.4 \times 10^{-5}$ mm s^{-1} i.e. $\sim 27\%$). This change in both slopes stops at the yield-point of the experiment (Fig.2.18 and 2.21). At this inflexion point, the slope of the force curve starts decreasing monotonically towards 0 whereas the displacement rate increases monotonically as the peak strength is approached. The weakening is accompanied by an abrupt change of the force slope towards negative values after which again a steady slow decrease is observed until the end of the experiment. The weakening is accompanied by a transient displacement rate increase (0.25×10^{-5} mm s^{-1} i.e. $\sim 14\%$) after which the displacement rate stabilizes. The changes of confining pressure are less clear in the $\partial Pc/\partial t$ space as they are much less ($< 5\%$) than the changes in $\partial F/\partial t$ and $\partial Dx/\partial t$. Nevertheless, the strongest increase in the slope of the confining pressure is right before the hit point (Fig.2.21c) followed by a decrease during loading of the sample to its peak strength. After the weakening the confining pressure starts to rise again (Figs. 2.18 and 2.21c).
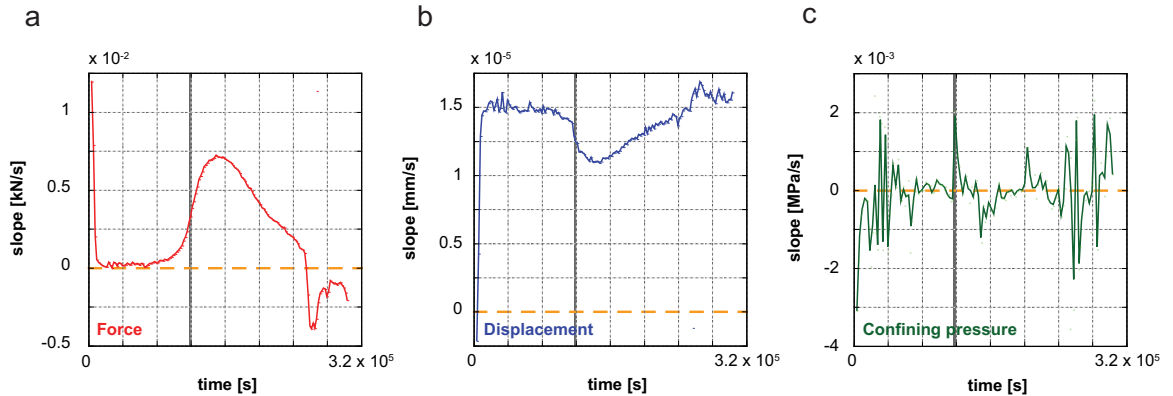
Figure 2.21: first derivatives by time of the a) force b) displacement c) confining pressure curves from experiment 279MP. Gray vertical bar indicates the position of the hit-point obtained by linear extrapolation of the run-in and "elastic" curves (see Fig.2.18). Orange dashed line shows a slope of 0 (i.e. no parameter change).

2.6.1.3 Quenching and depressurization

Once the desired vertical displacement rate is reached, the sample is quenched to 200 °C in 1.5 minutes. During quenching the load on the σ_1-piston is lowered as fast as possible by reversing the motor. The abrupt decrease in temperature causes the confining pressure and

load to decrease as the sample assembly shrinks (Salts have a high thermal expansion). After quenching, the force and confining pressure are lowered together by reducing oil pressure and moving the force ram until the sample reaches room pressure and temperature conditions.

2.6.2   Rig extension between the lower and middle steel plates

Mounting of the DLT displacement gauge (installed in March 2010) to the middle steel plate allows comparing the differences in the displacement recorded by the DLT and the DC-DT (mounted to the lower steel plate) with respect to the load cell in "Rig 2" (Fig.2.22). Unfortunately, the position of the independent two gauges does not measure the whole rig extension (a gauge would have to be placed on the top steel plate as well) so these measurements cannot be used to assess the complete apparatus stiffness.
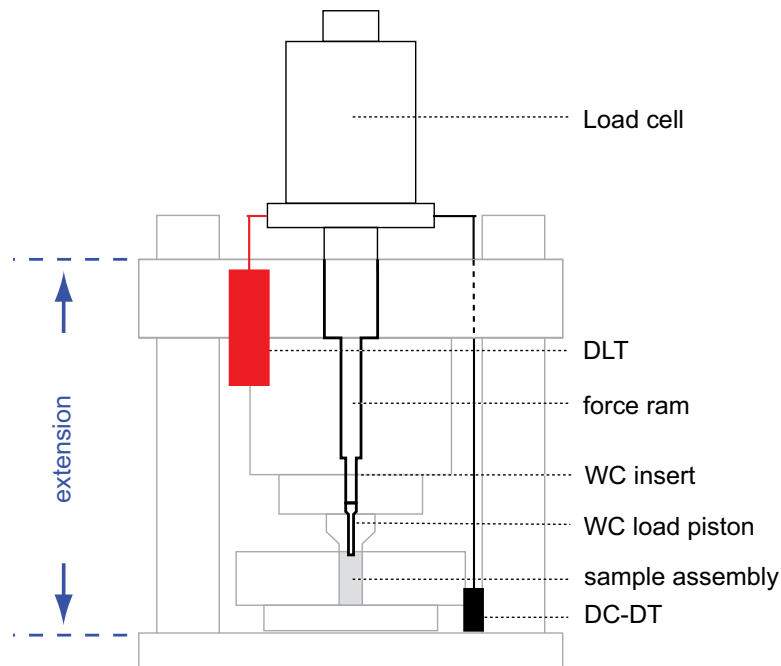
Figure 2.22: Position of displacement gauges which allows quantification of extension between the lower and middle steel plates. Every interface below the load cell contributes to the recorded force. (Modified after Holyoke and Kronenberg, 2010)

During increasing confining pressure, the displacement measured relative to the middle steel plate (DLT) shows first a very slight increase (Fig.2.23) which levels off to an approximately stable position (Fig. 2.23, field II). This probably reflects the settling of the σ_1 piston accommodated by creep processes in the upper Pb disc after the advancement of the piston with the motor. The displacement recorded relative to the lower steel plate decreases with increasing confining pressure and the difference, or extension (Δmm), recorded by the two displacement gauges increases (Fig. 2.24).

This behaviour is interpreted to be the result of advancement of the σ_3 piston into the pressure vessel. Increasing the oil pressure in the confining pressure piston exerts a force acting on the base plate and a force of the same magnitude but opposite direction on the middle steel plate and therefore leads to absolute extension of the frame bars connecting the bottom and middle plates (Fig. 2.24). The middle steal plate moves further away from the lower steel plate together with the σ_1 piston (therefore no relative displacement is recorded with the
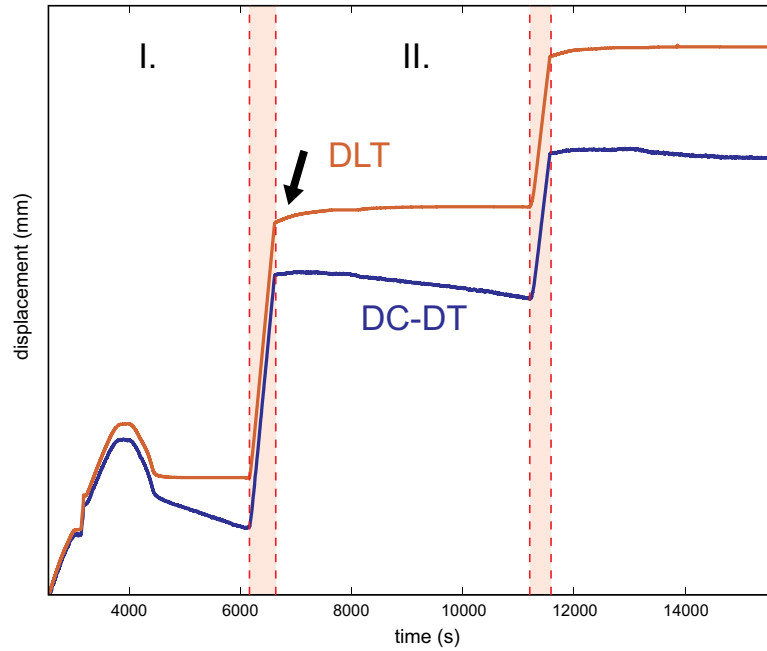
Figure 2.23: Record of the σ_1 piston displacement relative to the middle steel plate (DLT) and lower steel plate (DC-DT). I. shows the region right after the load is transmitted to the load cell (around Pc $\sim$ 100 MPa). Areas between dashed lines show the advancement of the piston into the pressure vessel. II. Increasing of confining pressure with no movement of the σ_1 motor. Arrow shows the region where DLT records small creep movement.

DLT). Two clear trends can be distinguished in figure 2.24. Up to a confining pressure of $\sim$ 180 MPa the increase in confining pressure causes more extension between the two steel plates ($\sim 10^{-3}$ mm MPa^{-1}) than at confining pressures $>$ 180 MPa where the extension is by one order of magnitude lower ($\sim 10^{-4}$ mm MPa^{-1}). Both trends are linearly elastic in the examined pressure range (Fig. 2.24). Once the desired confining pressure is reached the deformation part of the experiment is started which leads to further rig extension due to the increasing load on the σ_1 piston. The amount of extension during the deformation experiment decreases with increasing pressure despite the fact that absolute loads are higher (Figs. 2.24 and 2.25). The response of the apparatus to the applied force is shown in figure 2.25. The extension between the two steel plates decreases with increasing load on the σ_1 piston, i.e. the apparatus gets progressively stiffer at higher loads (by a factor of $\sim$ 1.8). The extension differs for a salt cell assembly with a Verzasca cataclasite sample compared to a all-lead assembly with a WC rod used to asses the apparatus stiffness by a factor of $\sim$ 2.25 (Fig. 2.25). This behavior is interpreted to be a result of different material properties of the two assemblies on which the force is exerted. Furthermore, it is interesting to note that at confining pressures $>$ 500 MPa the extension is fully elastic (i.e. during the weakening of the sample the extension decreases following the same slope as during strengthening). At 500 MPa confining pressure the extension of the two steel plates actually continues despite the weakening of the sample and the slope during weakening differs from the one during strengthening (Fig. 2.25).

This observed extension behaviour corresponds well to the recorded variations in confining pressure and displacement rates (see section 2.6.1). From this analysis, it can be concluded that the deformation apparatus should not be operated at confining pressures lower than $\sim$ 200 MPa as its elastic response strongly differs from the response at higher confining pressures. At $\sim$ 500 MPa confining pressure the elastic response of the apparatus due to the force exerted by the confining pressure ram is identical to that at the highest explored confining pressures.
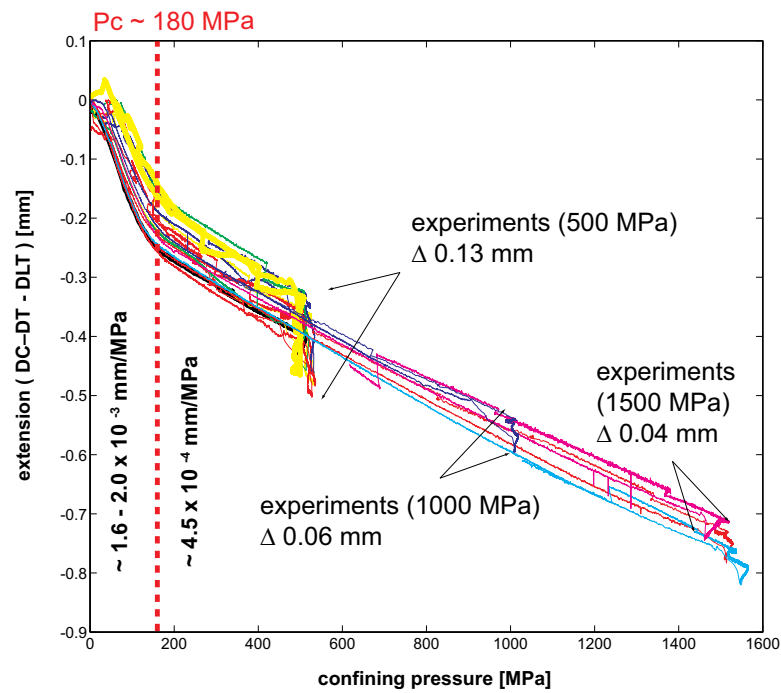
Figure 2.24: Extension between the middle and lower steel plate relative to the σ_1 piston vs. confining pressure. Black thick line = WC rod experiment.
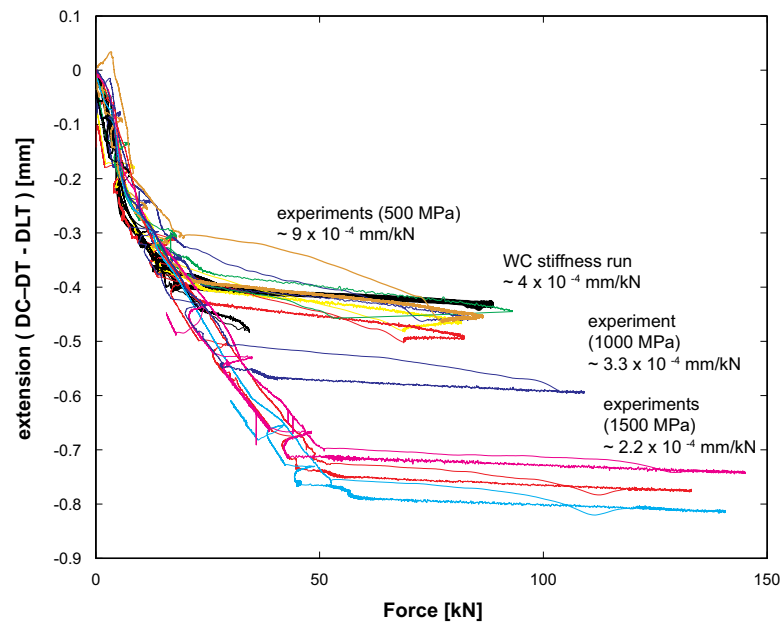
Figure 2.25: Extension between the middle and lower steel plate relative to the σ_1 piston vs. force. Black thick line = WC rod experiment.

Nevertheless, the response of the apparatus due to the force exerted by the σ_1 piston is not fully elastic. This response becomes fully elastic at confining pressures above of 500 MPa. However, it should be kept in mind that the deforming sample itself (Verzasca cataclasite in general shear) will affect the measured apparatus properties reported in Fig. 2.25. The above-discussed results suggest that a complex rig stiffness correction should be ideally performed at different confining pressures as the elastic properties of the rig could change with increasing

confining pressure to fully characterize the rig stiffness. Nevertheless the stiffness assessed here varies only by a factor of ~ 1.8 so the introduced artefact by neglecting this effect is expected to be small. The apparatus performs best at confining pressures > 500 MPa.

2.6.3 Forces acting on the σ_1 piston in the apparatus and pressure vessel during an experiment
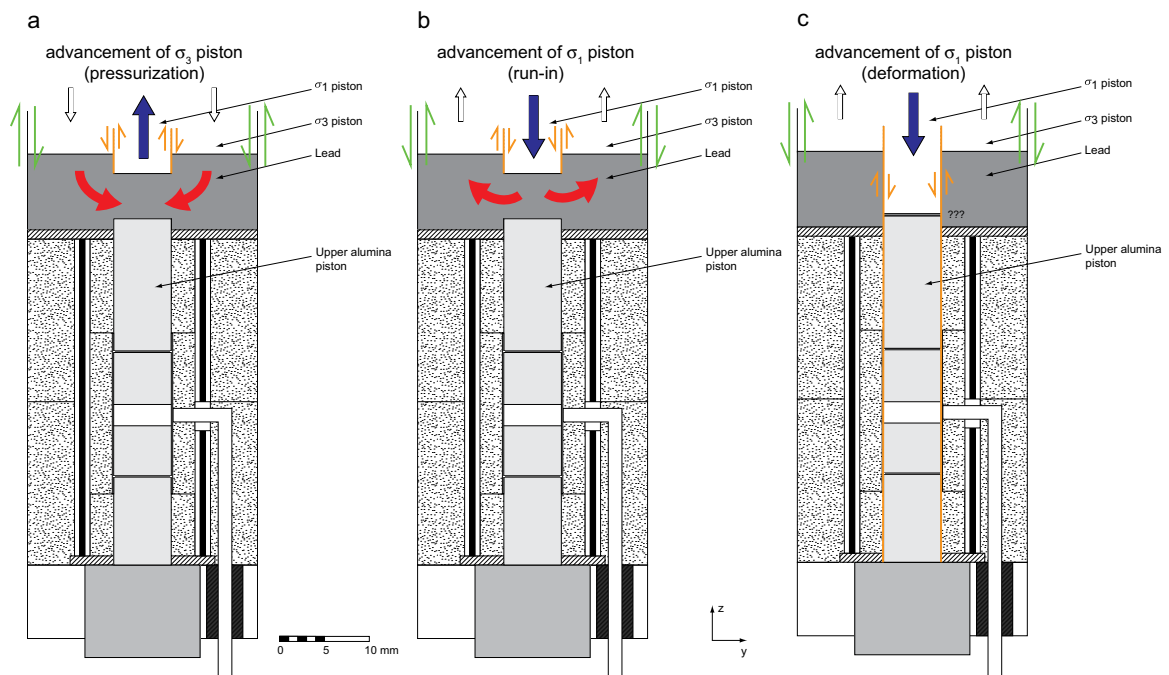
Figure 2.26: Forces acting on the pistons and sample during an experiment. a) pressurization b) run-in segment c) after hit-point (modified after Tarantola et al., 2010). Green arrows - drag on the pressure vessel walls, orange arrows - drag on the piston / sample and lead / salt cell interfaces, red arrows - movement of lead

It was stated above, that all the forces acting on the σ_1 piston below the load cell will contribute to the measured load. Two types of forces act against the movement of the σ_1 piston (Fig. 2.26):

1. Drag forces act on the σ_1 piston/packing ring, on the σ_1 piston/lead, and on the alumina piston/salt interfaces. The σ_1 piston/packing ring and alumina/salt interfaces do not change in length whereas the σ_1 piston/lead interface increases in length as the σ_1 piston advances into the sample assembly. As drag forces act parallel to the sample throughout the whole experiment, they do not have to be subtracted from the recorded total strength of the sample, i.e. they constitute the background "friction" of the apparatus (Renner, 1996; Holyoke and Kronenberg, 2010).

2. Displacement forces act on the lead disc between the σ_1 piston and the alumina piston and on the inner salt sleeves as the sample is being deformed. These forces have to be subtracted from the total recorded strength of the sample because the load is transmitted through the lead to the sample and the strength of the confining medium has to be overcome during the sample deformation (Renner, 1996; Holyoke and Kronenberg, 2010).

In addition to these forces acting in the pressure vessel, all interfaces outside the pressure vessel below the load cell (Fig. 2.1) will also contribute to the measured load. Furthermore, a force will be exerted on the σ_3 piston and the pressure vessel walls.

2.6.3.1   Run-in curves

First, we analyze the general behaviour of experiments before reaching the hit-point. In Figs. 2.26 and 2.27 we show a compilation of 77 run-in curves for which digital data records are available from experiments performed in two different deformation apparatuses (at Tromsø University). The data cover different sample materials (Verzasca gneiss, Milky Quartz, K-feldspar, Black Hills Quartzite, NaCl and KI), different solid confining media (NaCl and KI) in both shear and co-axial configurations, and a large range of experimental conditions (Pc $\sim$ 500 – 1500 MPa, T = 300 – 1000 °C, displacement rates of $\sim 10^{-3}$ - 10^{-5} mm s^{-1}). Each data point represents the slope of the run- in curve obtained by a linear curve fit. Two distinct parts of the curve can be identified: 1) The region further away from the hit-point (> 1.5 mm). 2) The region close to the hit-point (< 1.5 mm away). These regions are characterized by systematic differences:

1. Far away from the hit-point the slope of the run-in curve ($\partial\mathrm{F}/\partial\mathrm{dx}$) is independent of confining pressure, temperature and displacement rate (Fig. 2.27). The curve can be fitted with a linear slope of ~ 1.3 kNmm^{-1} for distances > 1.5 mm (Fig. 2.27). The differential stress ($\Delta\sigma = \sigma_1 - \sigma_3$) at the yield-point is not systematically dependent on the applied experimental conditions (Fig. 2.28) and scatters between $\sim 48 – 120$ MPa (with a mean of 80.95 MPa).

2. Closer to the hit point the slope of the run-in-curve ($\partial\mathrm{F}/\partial\mathrm{dx}$) increases (Fig. 2.27) as the sample is being loaded. The differential stress at the yield point increases in both magnitude and scatter ($\sim 63 – 230$ MPa, mean = 110 MPa), (Fig. 2.28).

The fact that the slope of the run-in curve ($\partial\mathrm{F}/\partial\mathrm{dx}$) further away from the hit-point is independent of the applied experimental conditions indicates that drag forces between σ_1 piston/lead, and friction between σ_1 piston/packing ring and other rig parts dominate this behaviour. The drag forces between alumina piston/salt should not be important, because the alumina piston probably does not move at this point of the experiment, and no temperature or displacement rate dependence can be observed (the salt strength will change dramatically with temperature). The temperature of the upper lead plug varies considerably less than the temperature in the inner salt sleeves due to the temperature gradient in the sample assembly. Therefore, we conclude that the slope of the run-in curve ($\partial\mathrm{F}/\partial\mathrm{dx}$) is primarily dependent on the σ_1 piston/lead interfaces and friction at the σ_1 piston/packing ring and other rig interfaces. As mentioned above, the σ_1 piston/packing ring interface as well as the other rig interfaces have a constant size during the experiment, whereas the size of the σ_1 piston/lead interface increases as the σ_1 piston is being advanced into the pressure vessel.
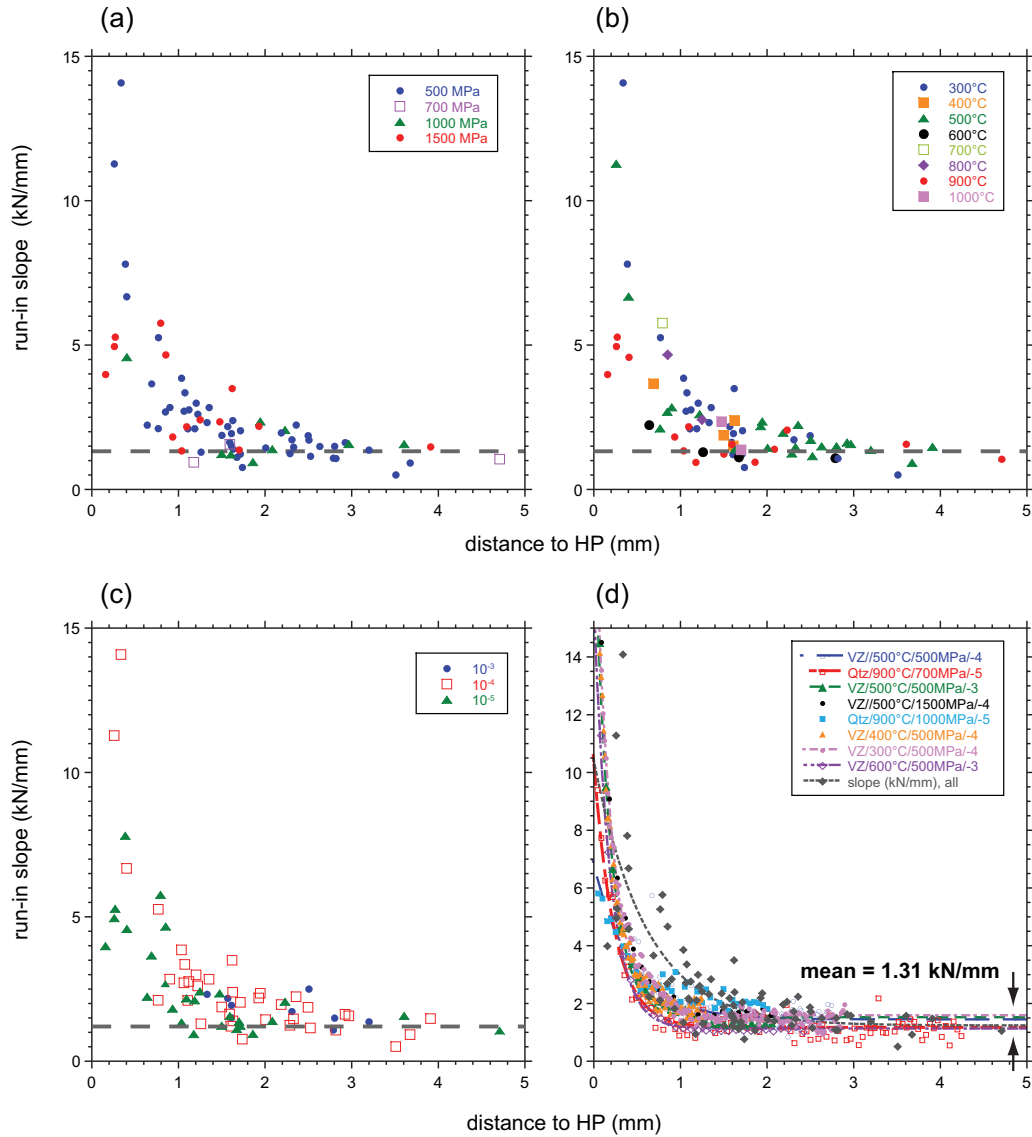
Figure 2.27: (a-c) Every data point shows the slope of a linear best-fit curve (via least-squares method) through the run-in segment of one individual experiment. The gray dashed line shows a slope of $1.3\,\mathrm{kN}\times\mathrm{mm}^{-1}$. The data are grouped by confining pressure (a), temperature (b), and displacement rate (c). Note the good correlation between the slope of the run-in curve and the distance to the hit-point, and the lack of a correlation with the experimental conditions. (d) Data from a-c (black lozenges) and the derivative $\partial\mathrm{F}/\partial\mathrm{dx}$ of selected individual experiments with long run-in segments. VZ – Verzasca gneiss shear experiments, Qtz – milky quartz co-axial experiments. The legend for the individual experiments is material/ temperature (°C) /confining pressure (MPa) /displacement rate (10^x). Notice that the general trend seen in a-c follows the evolution of the run-in slopes of each individual experiment. Furthermore, at distances far away from the hit-point, the slope of the run in curve is roughly constant (e.g. red squares and pink dots). after Tarantola et al. (2012).
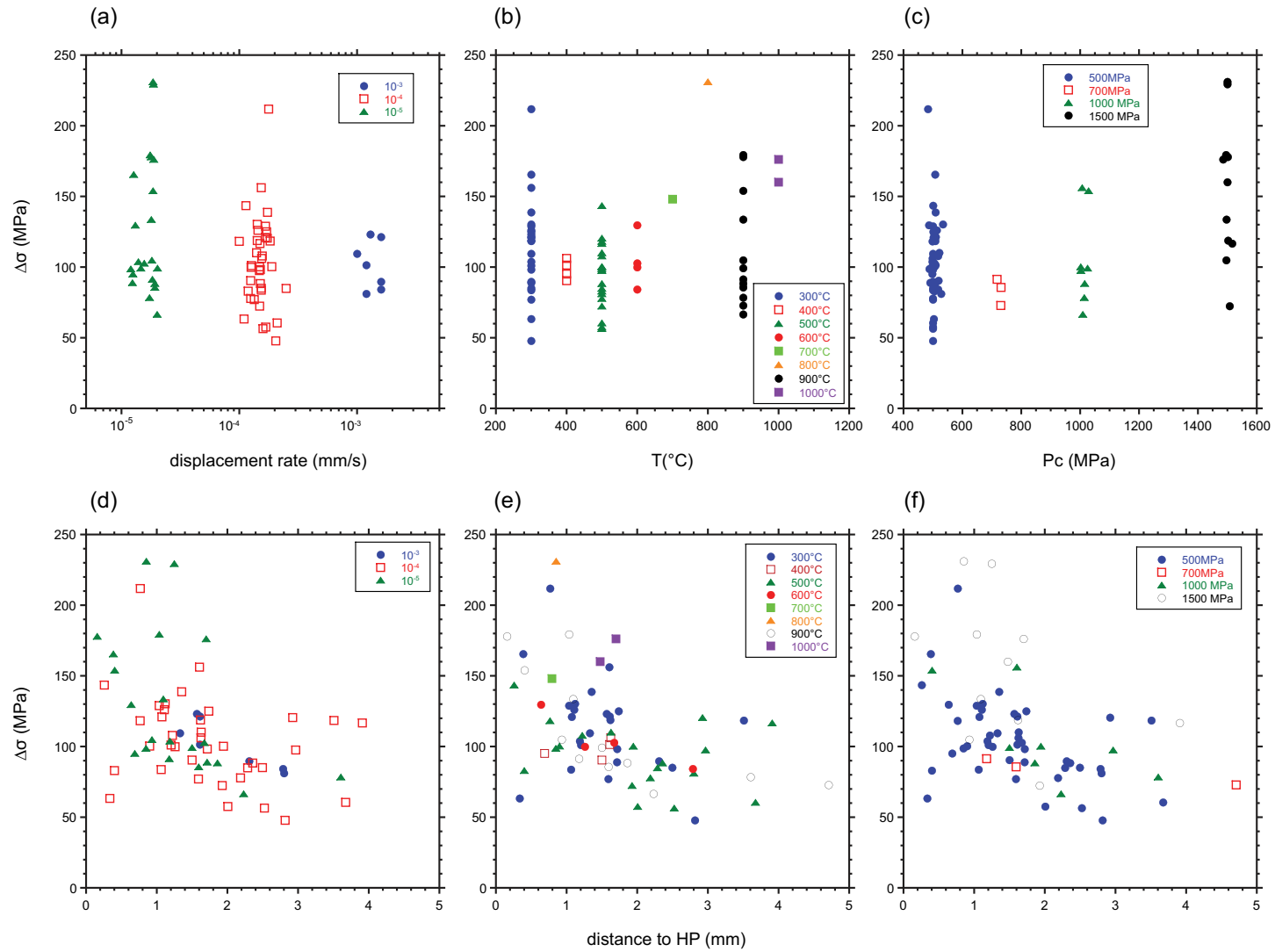
Figure 2.28: Each data point represents the differential stress ($\Delta\sigma$) at the "bend-point" from one individual experiment. (a-c) $\Delta\sigma$ versus displacement rate (a), temperature (b), and confining pressure (c). There is no systematic variation in $\Delta\sigma$ with the applied experimental conditions. (d-e) $\Delta\sigma$ versus distance to hit point grouped for displacement rate (d), temperature (e), and confining pressure (f). The $\Delta\sigma$ value increases in scatter and magnitude as the σ_1 piston approaches the hit-point. after Tarantola et al. (2012)).

The drag forces on the σ_1 piston/lead interface are neither purely frictional (they do not depend on normal stress) nor purely viscous (they do not depend on the displacement rate or temperature). Nevertheless, movement along these interfaces requires a force of ~ 1.31 kN per driven millimeter (or 41.6 MPa $\times$ mm^{-1} for a piston with a diameter of 6.3 mm), regardless of the given experimental conditions (Fig. 2.27). Closer to the hit-point we observe that the slope ($\partial F/\partial dx$) increases strongly (Fig. 2.27). The differential stress at the yield point also increases both in scatter and magnitude (Fig. 2.28). The sharpness of the hit point is determined by the viscosity (or strength) contrast between the sample, the confining media and the lead disc. If the contrast is low, the hit point is marked by a gradual increase in force over a distance of more than 1 mm, whereas if the contrast is high, the hit-point is sharper, on the order of hundreds of μm. It is most likely that the change in slope ($\partial F/\partial dx$) in this region is caused by hardening in the lead disc for geometric reasons: When the lead layer becomes very thin between the pistons, there is an enormous increase in strain rate as the material is pushed out over a distance of up to $1/2$ of the σ_1 piston diameter.

The commonly observed fact that the slope ($\partial F/\partial dx$) scales with peak sample strength (e.g. Renner, 1996; Holyoke and Kronenberg, 2010) indicates that probably the lead cannot be entirely pressed out between the σ_1 and alumina piston and a thin layer remains there during the deformation. After disassembling the experiments a thin ($\sim 300~\mu$m) foil of lead usually can be observed between the σ_1 and alumina piston however it is hard to tell whether this layer was present during the whole experiment or whether it got squeezed in during the unloading procedure. If this layer is present during the whole experiment than this layer should get thinner with increasing load on the σ_1 piston and obscure less the deformation of the sample itself. This could explain why strong samples have a better defined hit-point (i.e. steeper $\partial F/\partial dx$ curves after the hit-point) than weak samples. It should be noted that over the whole period of the "run-in-curve" and hit point, the sample is already subjected to a differential stress.

The behaviour of a single experiment is shown in figure 2.29. The force-displacement – time curves of experiment 284MP are marked as 3 different stages (I to III). During stage I, the σ_1 piston was driven into the lead at a rate of 1.5×10^{-4} mm s^{-1} (run-in curve). When the piston starts to move into the lead, the force curve increases abruptly to the yield point at $\Delta\sigma \sim$ 48 MPa while the advancement of the piston remains constant. Conventionally, the abrupt increase in force before the yield point is attributed to friction in the rig before the σ_1 piston starts to move into the lead. The σ_1 motor was stopped for about 2 hours (stage II). During this period, the force decreased non-linearly, in different stages (by ~ 2 kN; corresponding to 63.5 MPa for a 6.3 mm piston); Fig. 2.29a) and the σ_1 piston advanced very slowly at a displacement rate of 7.62×10^{-7} mm s^{-1} under the applied load (creep deformation). In stage III, the motor for the σ_1 piston was turned on again but at a faster displacement rate (one order of magnitude higher than during stage I). At a $\Delta\sigma$ of ~ 61 MPa the yield point was reached, a remarkably similar value to the relaxed value during the 2 h hold period (Fig. 2.29b). The slope of the curve of stage III is identical to the slope of stage II, although the velocity of the σ_1 piston was one order of magnitude faster, consistent with the results discussed above. The force-displacement-time curves of experiment 318MP (Fig. 2.29c) show the effect of force relaxation after the hit-point during a change to a very slow displacement rate. In stage I, the σ_1 piston is advanced at a fast velocity $\sim 1.5 \times 10^{-3}$ mm s^{-1}, and then, after the hit-point, the gears in part II are changed to a velocity 3 orders of magnitude slower at $\sim 9.9 \times 10^{-7}$ mm s^{-1}. The onset of a slow movement resulted in a clear relaxation of the force values by 0.68 kN (or 20.5 MPa).
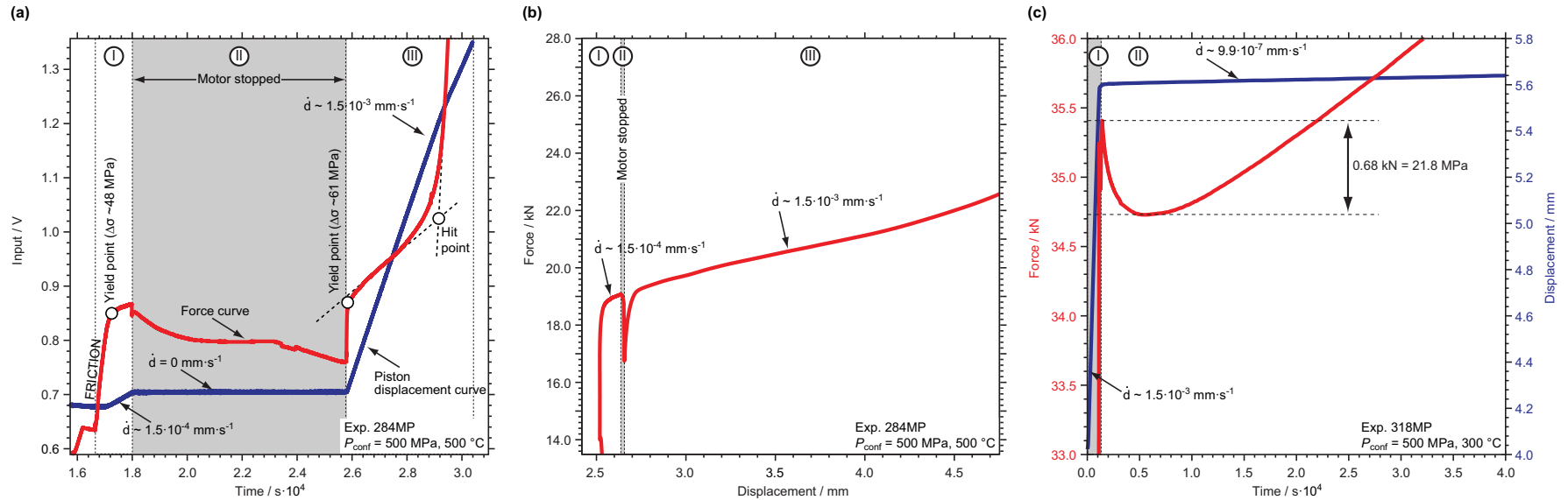
Figure 2.29: Mechanical data of the run-in part. Red curves = force; Blue curves = displacement. (a) Exp. 284MP. Chart record (time vs. input). Region I: The σ_1 piston advances at a displacement rate of 1.5×10^{-4} mm s^{-1}. The force increases abruptly to the yield point and then steadily increases due to work hardening in the lead and – probably more importantly – to increase in drag forces (area increase) as the σ_1 piston is pushed into the lead. Zone II: σ_1 motor is stopped and the force relaxes. Zone III: The σ_1 motor is started at one order of magnitude faster displacement rate than in zone I to the hit-point and beyond. (b) Exp. 284MP. Displacement vs. force for the experiment shown in (a). Regions I, II and III correspond to the same as in (a). Note that during the stop period (Zone II) the σ_1 piston advances slightly (~ 0.02 mm) into the pressure vessel. An increase in displacement rate by one order of magnitude (Zone III) does not affect the "run-in" slope. (c) Exp. 318MP. Time vs. force and displacement of an experiment where the displacement rate was lowered by ~ 3 orders of magnitude during the deformation. Note the relaxation of force by 0.68 kN (or 21.8 MPa for a sample with 6.3 mm diameter) after the decrease of the displacement rate (Zone II). after Tarantola et al. (2012).

Three major conclusions can be drawn from the results discussed above:

1. The run-in-curve slope ($\partial F/\partial dx$) is independent of the applied experimental conditions (pressure, temperature, strain rate) within the tested range.

2. The first segment of abrupt force increase of the run-in-curve up to the yield point is reversible when the motor is stopped and started again - independent of applied experimental conditions.

3. The fact that the σ_1 piston advances at a very slow rate under an applied load without the motor advancing it (stage II, Fig. 2.29a) indicates that creep processes in the lead control this movement.

It seams that the run-in curve of the experiments is mainly controlled by processes in the lead disc as the σ_1 piston advances. Based on the above-mentioned arguments we conclude that it is of little importance at which conditions the σ_1 piston is advanced during the run-in stage. A reliable hit-point can be constructed as long as the σ_1 piston starts at ~ 2 mm away from the hit-point.

2.7 Detection limit, accuracy, precision and resolution of the deformation apparatus

The solid medium deformation apparatus have a bad reputation among parts of the rock deformation community, despite hundreds of studies published since the 1950'. This may possibly be caused by early studies, which have attempted to derive flow laws from solid medium mechanical data, which does not reach the sufficient accuracy needed for flow laws (see Holyoke and Kronenberg, 2010). Furthermore, in the early experiments, talc was used as a confining medium and as the strength of the dehydrated talc is high, and the measured stress strain curves were afflicted with large errors (Caleb Holyoke, pers. comm.). The development of solid and later liquid salt cells in the 90' considerably improved both, the precision and the detection limit of the apparatus (Borch and Green, 1989). In the last years systematic studies of the apparatus appeared (Holyoke and Kronenberg, 2010; Renner, 1996; Tarantola et al., 2012). In the following, it will be attempted to summarize and discuss the probable confidence limits of the apparatus.

2.7.1 Definitions

The detection limit defines the lowest measured quantity, which can be reliably distinguished from background noise. Accuracy (systematic error) defines how close the measured value to a known reference value is. Precision (random error) defines how large the scatter on the measured value is in repeated measurements (Fig. 2.30). Resolution defines the smallest change in the measured quantity that can be detected by the measurement system.

2.7.2   Detection limit

As discussed in section 2.6.1.1 a background "friction" of approx. 100 MPa could be present in the load column and confining pressure piston/pressure vessel interface. However, it should be noted that (a) this is probably an upper limit, and (b) it is uncertain how much "friction" is located in the load column and how much in the confining pressure piston and the pressure vessel walls. Holyoke and Kronenberg (2010) report that a reasonable stress- strain curve can be obtained for samples as weak as 30 MPa. This values appears reasonable. Nevertheless, samples weaker than ~ 100 MPa will have a poorly defined hit-point and the recorded load will be a result of processes occurring in the top metal disc, salt cell and the sample itself. This detection limit (i.e. no weaker samples can be measured) is often referred to as "resolution" in the literature, which, however, leads to confusion (see section 2.7.4).
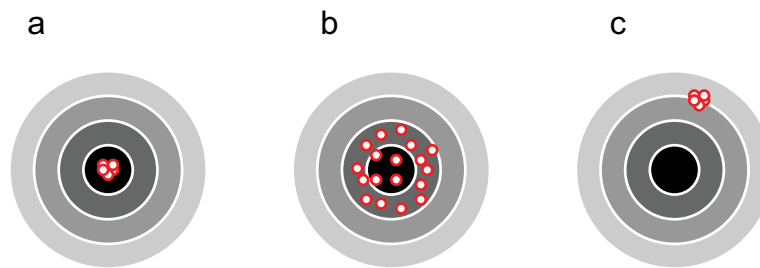
Figure 2.30: Accuracy and precision. Centre represents the "true" value, red circles are individual measurements. a) accurate as well as a precise measurements b) accurate but not precise measurements c) precise but not accurate measurements

2.7.3   Accuracy

The accuracy of the apparatus was recently compared to the gas rig (Holyoke and Kronenberg, 2010) at 300 MPa confining pressure (i.e. unfavorable conditions for the operation of the modified Griggs apparatus, however highest possible pressures of the gas apparatus). Results show that the stresses measured in the solid medium apparatus are by approx. 30% higher compared to those in the gas apparatus. However, they vary systematically and reproducibly. Therefore, it should be possible to correct the recorded data. Another complication with the estimation of the absolute stress values is the necessity of a "dynamic friction" correction (see section 2.6.3.1) and assessment of the "background friction" level (Fig. 2.31). The uncertainty of the best-fit line through the run-in curve leads to variations in the recorded peak strength by 20 MPa (i.e. $\sim 1.5\%$). If the dynamic force increase (during the advancement of the σ_1 piston into the pressure vessel) is neglected, a difference of 100 MPa (i.e. $\sim 7\%$) arises between the two methods of hit-point definition. These relative differences are comparatively minor for strong samples, however they will be more pronounced for weak samples. A further uncertainty arises from calculation of various correction parameters for the evolving shape of the deformed sample to derive stresses from the recorded loads (see Appendix B). These issues complicate the assessment of the absolute values of the measured stress in the sample.

2.7.4   Reproducibility (precision)

The reproducibility of experiments performed in the solid medium deformation apparatus is usually lower compared to experiments performed in a gas deformation apparatus. This is
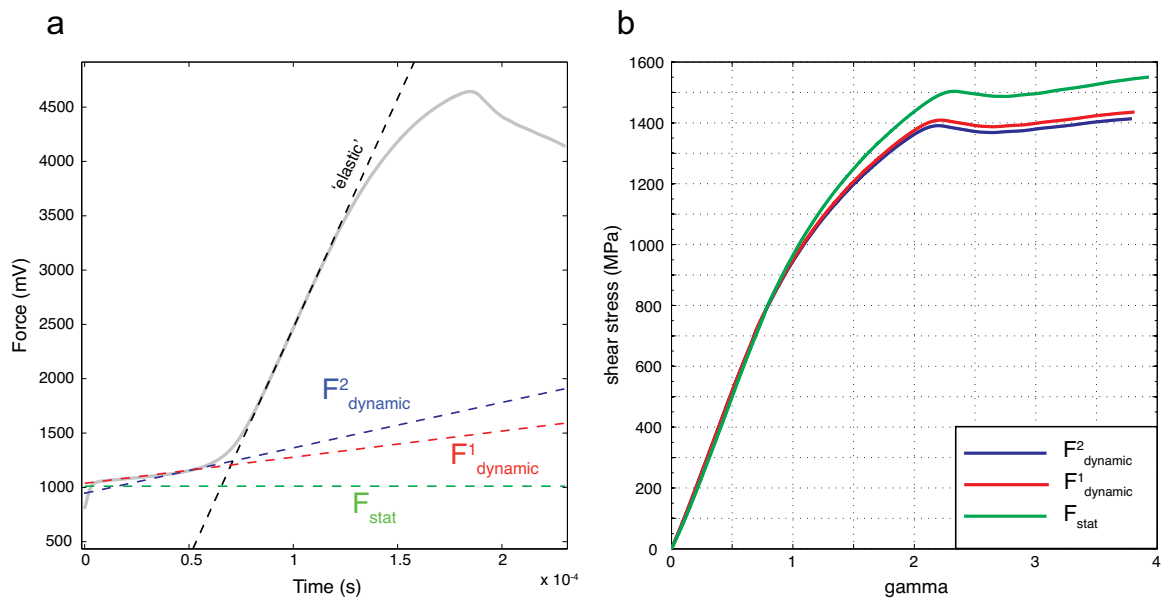
Figure 2.31: Influence of the chosen background "friction" level on the resulting hit-point. a) raw chart record with different fits through the run-in curve b) resulting stress-strain curves.
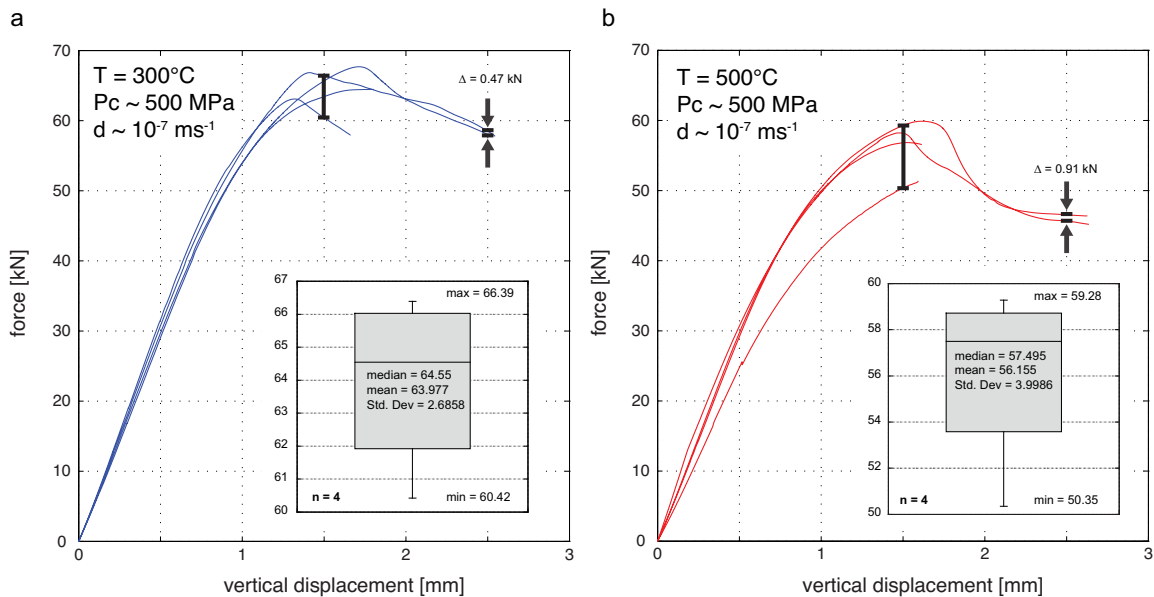
Figure 2.32: Experiments performed on verzasca gneiss under identical conditions. Inset shows the maximum, minimum, mean and standard deviation of the recorded values at 1.5 mm vertical displacement. Note that the range in steady state is much smaller than the range in peak strength a) $300°$C b) $500°$C

caused by the fact that for a solid medium experiment all the pieces constituting the sample assembly have to be machined and fitted together. Clearly, in such a case, the variability from one experiment to another is necessarily higher than in the case of gas deformation apparatus where only the deforming sample is replaced from one experiment to the other. It is therefore desirable to establish an experimental routine which is followed during every experiment and to take special care that all pieces used in the sample assembly have dimensions as similar as possible. Figure 2.32 shows the results of repeated experiments under the same experimental conditions performed on Verzasca gneiss in force vs. piston displacement space (i.e. raw recorded data without any further corrections). The standard deviation at 1.5 mm vertical

displacement (i.e. around peak strength) is 2.7 kN (i.e. $\sim 4.2\%$) for 300 °C experiments and 4 kN (i.e. $\sim 7.1\%$) for 500 °C experiments. Note that 1 kN ~ 32 MPa stress on a piston of 6.3 mm diameter. Comparing just the peak strength, which is a well-defined quantity, we find a standard deviation of 2.12 kN (i.e. $\sim 3.2\%$) for 300 °C experiments and 1.53 kN (i.e. $\sim 2.6\%$) for 500°C experiments (Fig. 2.33). At steady-state a range of 0.47 kN (i.e. $\sim 0.8\%$) at 300 °C and 0.91 kN (i.e. $\sim 2\%$) at 500 °C is observed. This translates into ~ 15.1 MPa and ~ 29.2 MPa difference in the recorded differential stress for a piston of 6.3 mm diameter. Holyoke and Kronenberg, 2010 report a ± 30 MPa precision of stress measurements performed in a solid salt cell at 300 MPa confining pressure which is slightly higher than the values reported here.
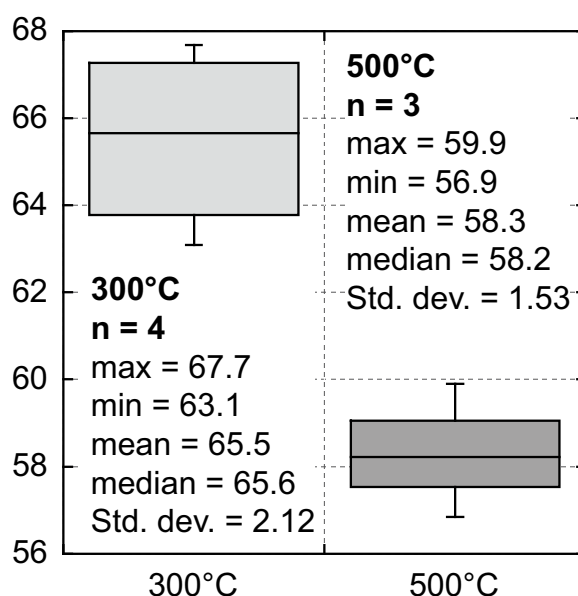
Figure 2.33: Evaluation of precision at peak strength

2.7.5   Resolution

Resolution of the apparatus is difficult to assess quantitatively. Once the mating surfaces in the load column are in good contact (> 15 kN according to Holyoke and Kronenberg, 2010) the load cell is capable of recording tiny variations in the load (e.g. stick slip events on the order of $\sim 2 - 5$ MPa i.e. $\sim 0.5\%$). Deformation of samples with high water contents also lead to the appearance of "trembling" (high-frequency variations of about 5 MPa) after the peak strength. These events can be interpreted as the result of high pore pressures. Further, variations in temperature by a couple of °C (for example due to a unstable control thermocouple) are clearly visible in the force record. A rough estimate of the resolution of the measured values is ± 5 MPa, i.e. relative changes in the stress record within a single experiment of such magnitude can be reliably detected and interpreted.

2.8   Concluding remarks

The data presented above show that the modified Griggs rig is mainly an apparatus of strength (or viscosity) contrasts. If the strength of the deforming sample is much higher than the "background friction" of the machine and the strength of the sample assembly itself, the hit-points are well defined and good coupling between the interfaces in the load column assures good force resolution at high loads. However, if the sample is very weak, the measured stress evolution will be obscured by the deformation of the sample assembly itself leading to poorly defined hit points and questionable stress-strain curves.

Semi-brittle deformation of granitoid gouges in shear experiments at elevated pressures and temperatures

Abstract:

The physical and chemical processes acting in the "brittle-to-plastic" transition are of great interest for a better understanding of fault rheology. We performed a series of experiments on granitoid gouge material under high confining pressures (Pc = 500 – 1500 MPa), temperatures (T = 300°C and 500°C) and fast shear strain rates ($\sim 1.8 \times 10^{-4}$ s^{-1}) where the material deforms by semi-brittle flow. Samples deformed at 500°C are systematically weaker than samples deformed at 300°C over the whole examined confining pressure range indicating a non-frictional component of the deformation. All samples develop a S-C' fabrics and deformation localizes in slip zones containing "amorphous" feldspar material with an intermediate composition (Na,Ca and K rich). Further, we observe changes in composition of feldspars (enrichment in the albite component) in the highly fragmented – but crystalline – regions with increasing finite shear strain. Our results indicate that mass-transfer processes keep pace with frictional deformation even at high strain rates and together with viscous flow of the "amorphous" material are responsible for the observed strength difference.

3.1 Introduction

Many of the largest earthquakes in the continental crust nucleate at the bottom of the seismogenic layer in depths between 10 – 20 km (i.e., Scholz, 2007) indicating that the stresses can be released by brittle failure under high confining pressures and temperatures. The physical and chemical processes acting under these conditions are of great interest for a better understanding of fault rheology in the broad so- called "brittle-to-plastic transition" region, which is poorly approximated by current strength profiles of the lithosphere (Fig. 3.1).
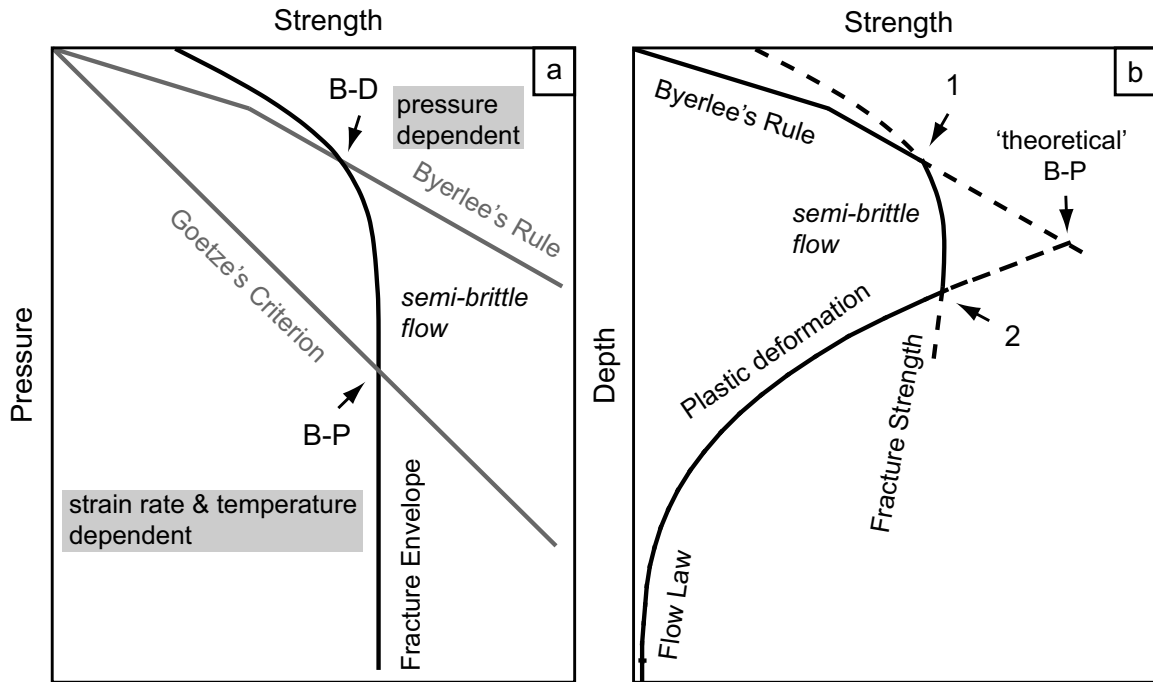
Figure 3.1: Schematic diagram in a strength – pressure space showing the transition from localized brittle deformation to pervasive brittle (semi-brittle) deformation (B-D, "brittle-ductile" transition) which eventually gives way to fully plastic flow for fixed temperature and strain rate conditions. Friction is controlled by normal stress and plastic flow is controlled by temperature and strain rate (modified after Kohlstedt et al., 1995). b) Schematic diagram of a crustal strength profile in strength vs. depth space. Depth includes temperature, confining pressure, water fugacity and other controlling parameters. Point 1 corresponds to the "brittle – ductile" transition but point 2 does not necessarily correspond to the "brittle-plastic" transition from a). For a given depth the black curve indicates the rheological behavior that controls the maximum supported stress. As the fracture strength of rocks depends on temperature, the maximum supported stress decreases with increasing depth. The "theoretical" brittle-plastic transition does not take into account the maximum compressive stress of rocks, hence the depth at which it occurs strongly depends on the strain rate and temperature gradient (modified after Kohlstedt et al., 1995 and Shimada, 1993).

Numerous variations of the classical strength profiles were proposed taking into account the maximum compressive strength of rocks (e.g., Shimada, 1993; Ohnaka et al., 1997; Ohnaka, 1995, 2003 and references therein) as well as "frictional-viscous" behavior (Bos and Spiers, 2002b).

Fracturing is one of the most efficient mechanisms to reduce grain size, and it occurs under a wide range of conditions. It also appears to be important (maybe even a pre-requisite) for the onset of viscous deformation in the crust (Menegon and Pennacchioni, 2010; Fusseis and Handy, 2008; Menegon et al., 2008; Pennacchioni and Mancktelow, 2007 and references therein; Trepmann et al., 2007; Fusseis et al., 2006; Pennacchioni et al., 2006; Mancktelow and Pennacchioni, 2005; Trepmann and Stöckhert, 2002, 2003; Handy and Stunitz, 2002;

Imber et al., 2001; White, 2001; Stewart et al., 2000; van Daalen et al., 1999; Fitz Gerald and Stünitz, 1993). Furthermore, the reduction of grain size causes an increased surface to mass ratio, which promotes fluid/rock interactions and thus accelerates possible mineral reactions and mass-transfer processes.

At upper crustal levels, frictional sliding is described by Byerlee's rule, which states that the strength of the rocks depends only on normal stress and is largely independent of lithology (Byerlee, 1978). The differential stress required to cause sliding on a pre-existing fault is lower than that required to fracture an intact rock thus it is commonly assumed that friction controls rock deformation at shallow depths. With increasing confining pressure, the intersection of the Mohr-Coulomb / Von Mises failure envelope with Byerlee's rule marks the so-called "brittle-ductile" transition (Fig. 3.1) where the amount of stored elastic energy in the rock reaches a critical value (maximum compressive strength of rocks). From this point onwards the differential stress required to slide on a pre-existing fault is greater than that required to create new fractures (e.g., Kohlstedt et al., 1995) (Fig. 3.1). The result is a pervasive comminution of the rock. Eventually, with increasing temperature and water fugacity, semi-brittle deformation gives way to fully crystal plastic deformation at the so-called "brittle-plastic" ("frictional-viscous") transition.

Despite the acknowledged importance of semi-brittle flow, only few experimental studies exist to date at pressure and temperature conditions relevant to semi-brittle flow in natural rocks (e.g., Tullis and Yund, 1977, 1980; Kronenberg and Shelton, 1980; Hirth and Tullis, 1994; Blanpied et al., 1991, 1995, 1998; Keulen et al., 2007, 2008).

We present the mechanical and microstructural data from a series of experiments performed in a solid medium tri-axial deformation apparatus (modified Griggs rig) at elevated pressures and temperatures. Our results indicate that mass-transfer processes keep pace with fracturing even at high strain rates in the "semi-brittle" flow regime.

3.2   Experimental methods

3.2.1   Starting material

Experiments were performed on granular material produced from a fine-grained granitoid rock collected in the Val Verzasca in Switzerland (for sample location see Keulen et al., 2007). The intact rock is composed of 35% quartz, 29% plagioclase, 27% potassium-feldspar and 7% micas (Keulen et al., 2007) and contains almost no alteration minerals (e.g. clay minerals). Samples were prepared by repeatedly pounding once or twice on the solid material inside a steel container. After each crushing the material was sieved through a 200 μm mesh. The coarser fraction was repeatedly crushed again until the whole sample consisted of a powder with a grain size d $\leq$ 200 μm. XRF analysis yielded a composition of $\sim$ 77.04 wt% SiO_2, 13.31 wt% Al_2O_3, 4.63 wt% K_2O, 3.16 wt% Na_2O, 1.01 wt% CaO, 0.64 wt% Fe_2O_3 and trace amounts of MgO and TiO_2. Weight loss after heating for 1 hour at 1000°C was $\sim$ 0.1 wt%. This material was used in previous studies (Heilbronner and Keulen, 2006; Keulen, 2006; Keulen et al., 2007, 2008; Stünitz et al., 2010) so that there is mechanical data already available.
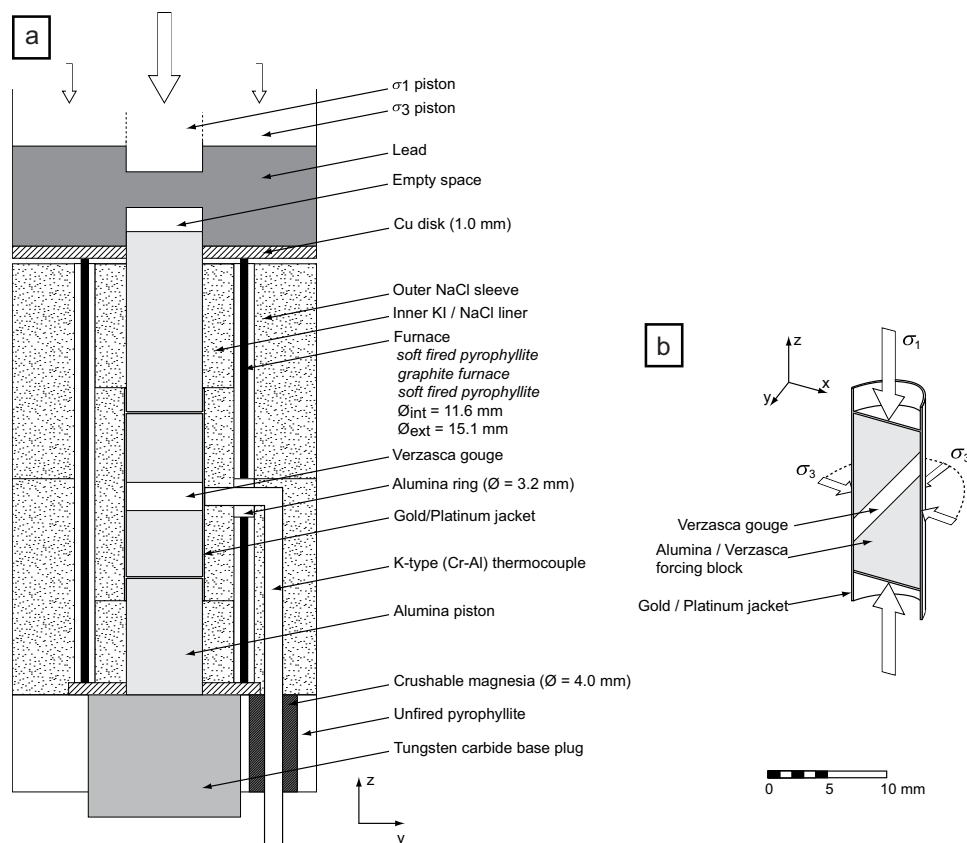
Figure 3.2: Drawing of the assembly and sample. a) Assembly inside the pressure vessel, y-z section. b) Sample geometry in a 3D view. In some experiments an inner Ni foil (thickness = 0.0025 mm) was inserted between the outer jacket and the forcing blocks (see table 3.1). Modified after Tarantola et al. (2010)

3.2.2   Sample preparation

Samples of Verzasca gneiss powder (0.1 g, grain size $\leq$ 200 μm), either with $\sim$ 0.2 wt% H_2O water added or dried at 200°C for 24 hours ("dried"; Table 3.1) were placed between alumina or Verzasca gneiss forcing blocks pre-cut at 45° and roughened with silicon carbide powder (grain size of 150 μm). Samples were weld-sealed in gold jackets (0.15 mm wall thickness), or platinum jackets (same wall thickness) with a 0.025 mm nickel foil insert (Fig. 3.2) (see table 3.1 for a summary of material and experimental conditions). During welding, the samples where either cooled in liquid nitrogen or in a cooled brass heat sink. A Lampert welding apparatus was used (minimizing the warming up of the jacket) to assure good control of the water content.

3.2.3   Experimental set-up

Inner liners of sodium chloride (NaCl) and potassium iodide (KI) were used as confining medium (Fig. 3.2). Experiments using salt samples placed in-between alumina forcing blocks pre-cut at 45° in Au and Pt jackets were performed with NaCl and KI at displacement rates of $\sim$ 1.5 $\times$ 10^{-4} mm $\times$ s^{-1} to obtain the bulk strength of the confining media, jacket, and to determine any frictional resistance of the apparatus itself. The supported shear stresses of the NaCl salt runs are $\sim$ 180 MPa at 300°C and $\sim$ 80 MPa at 500°C. Thus, a strength

difference between 300°C and 500°C experiments is expected because of a non-negligible strength of the NaCl confining medium. The strain rate in the salt samples is higher than that in the surrounding confining medium during the experiments, so that these values (180 MPa and ~80 MPa for 300°C and 500°C, respectively) represent an upper bound for the NaCl confining medium strength. KI is a much weaker salt than NaCl (Inoue, 1957). Its strength is not measurable in experiments on jacketed salt samples, neither at 300°C nor at 500°C and hence its influence on the recorded sample strength can be neglected.

The samples were pressurized to desired experimental conditions while the temperature was raised by 20°C/min in 100°C steps within 4 - 8 hours. Then, the σ_1 motor was advanced at a constant displacement rate of $\sim 1.5 \times 10^{-4}$ mm $\times$ s^{-1} hitting the sample within 1 - 5 hours. Some samples where left over night ($\sim$ 8 - 15 h) in the apparatus before the motor was started. During the experiments, confining pressure variations were in the range of $\pm$ 10 MPa or less and temperature was held constant with a proportional-integral- derivative (PID) controller. Double thermocouple experiments indicate a temperature gradient of 10% from the center to the top end of the shear zone (i.e. 30°C and 50°C for 300°C and 500°C experiments, respectively). After reaching the desired displacement the samples were quenched to 200°C in 2 minutes and the temperature was lowered to cooling water temperature within $\sim$ 30 minutes after quenching. During depressurization an initial differential load of $\sim$ 100 MPa was kept on the sample which was then reduced together with the reduction of the confining pressure to minimize unloading cracks.

3.2.4 Data processing

An external load cell was used to measure the force applied to the sample; the displacement of the σ_1 piston was measured using a direct current displacement transducer (DC-DT, resolution ~ 1 μm) and, in later experiments, using a digital linear transformation measurement (LTM) system (resolution = 0.1 μm). Experimental data were digitally recorded in 0.5 or 1 second intervals and evaluated using a newly developed open source MATLAB program RIG (http://sites.google.com/site/rigprogram/). The displacement was corrected for apparatus compliance and force was corrected for friction using a set of calibration experiments, run-in curves, and salt samples experiments. Differential stress was corrected for any changes in confining pressure during the run ($\pm$ 10 MPa). We assume that the shear zone thickness decreases during the run as gouge material is pushed out at the ends of the forcing blocks with increasing displacement, resulting in increasing shear strain rates within the shear zone while maintaining a constant displacement rate. Furthermore, forcing blocks do not change their diameter and the contact area of the shear zone on which the force acts becomes smaller with increasing slip. The calculated finite shear strain from the chart record was compared to the finite shear strain measured on thin sections because the amount of finite shear strain may vary slightly depending on the amount of pre-deformation compaction of the gouge during building up of the confining pressure. Thus, all reported finite shear strains were corrected using the following equation:

$$\gamma_{(t)} = \frac{\gamma_{rigData(t)}}{max(\gamma_{rigData})} \times \gamma_{measured} \tag{3.1}$$

where $\gamma_{(t)}$ = shear strain at t record time, $\gamma_{rigData}$ = shear strain calculated from machine data and $\gamma_{measured}$ = shear strain measured on thin sections.

exp. #	T (°C)	Pc (MPa)	mean $\dot{\gamma}$ (s^{-1})	inner sleeves	water added (wt%)	jacket	forcing blocks	sample $\varnothing$ (mm)	γ^1_{meas}	γ^2_{calc}	max. F (kN)	max. τ (MPa)	max. τ^c (MPa)	max. $\Delta\sigma$ (MPa)	max $\Delta\sigma^c$ (MPa)	max μ	max μ^c	duration (h)
138JO	300	500	N/A	NaCl	0.2	Au	VZ	6.5	0.1	0.0	N/A	N/A	N/A	N/A	N/A	N/A	N/A	N/A
147JO	300	500	9.31×10^{-5}	NaCl	0.2	Au	VZ	6.5	1.3	1.0	31.3	511	N/A	950	N/A	N/A	N/A	1.35
156JO	500	500	1.20×10^{-4}	NaCl	0.2	Au	VZ	6.5	1.1	1.7	34.5	569	N/A	1055	N/A	N/A	N/A	1.79
176MP	500	590	2.28×10^{-4}	NaCl	0.2	Au	VZ	6.5	1.5	2.3	46.2	869	610	1395	970	0.73	0.62	2.49
177MP	300	560	2.25×10^{-4}	NaCl	0.2	Au	VZ	6.5	1.4	2.1	54.2	1015	717	1641	1150	0.77	0.67	2.46
180MP^a	500	540	2.99×10^{-4}	NaCl	0.2	Au	VZ	6.5	1.5	2.2	47.6	898	632	1438	1002	0.74	0.63	2.02
188MP^a	500	535	1.91×10^{-4}	NaCl	0.2	Pt	VZ	6.5	1.4	2.8	51.8	992	700	1562	1092	0.75	0.65	3.40
194MP^a	300	510	1.96×10^{-4}	NaCl	0.2	Pt	VZ	6.5	1.7	2.6	56.2	1098	778	1713	1202	0.82	0.71	3.25
245MP	500	510	1.44×10^{-4}	KI	dried	Pt*+Ni	Al$_2$O$_3$	6.33	1.4	1.6	56.9	1076	762	1822	1282	0.76	0.66	3.10
247MP	500	495	1.28×10^{-4}	KI	0.2	Pt*+Ni	Al$_2$O$_3$	6.33	2.3	1.8	50.2	972	686	1607	1125	0.75	0.65	3.94
251MP	300	515	2.04×10^{-4}	KI	0.2	Pt*+Ni	Al$_2$O$_3$	6.33	1.5	2.3	64.5	1333	950	2064	1459	0.86	0.76	3.20
253MP^a	500	530	1.86×10^{-4}	KI	0.2	Pt*+Ni	Al$_2$O$_3$	6.33	2.1	1.8	56.8	1094	775	1815	1277	0.76	0.66	2.73
255MP	500	1010	1.69×10^{-4}	KI	0.2	Pt*+Ni	Al$_2$O$_3$	6.33	1.6	1.7	69.9	1287	916	2231	1580	0.61	0.51	2.69
256MP^a	500	1020	1.99×10^{-4}	KI	0.2	Pt*+Ni	Al$_2$O$_3$	6.33	2.6	2.2	70.7	1305	929	2259	1601	0.61	0.51	3.01
257MP	300	495	2.12×10^{-4}	KI	dried	Pt*+Ni	Al$_2$O$_3$	6.33	2.2	2.8	61.9	1333	950	1979	1397	0.90	0.80	3.64
260MP	300	1010	1.92×10^{-4}	KI	0.2	Pt*+Ni	Al$_2$O$_3$	6.33	1.6	2.1	83.3	1594	1140	2663	1896	0.68	0.58	3.06
261MP	300	515	1.94×10^{-4}	KI	0.2	Pt*+Ni	Al$_2$O$_3$	6.33	2.6	2.0	63.1	1166	827	2016	1424	0.77	0.67	2.74
262MP	300	1475	1.67×10^{-4}	KI	0.2	Pt*+Ni	Al$_2$O$_3$	6.33	1.5	1.9	88.3	1632	1168	2834	2021	0.56	0.47	3.20
263MP	500	1555	2.11×10^{-4}	KI	0.2	Pt*+Ni	Al$_2$O$_3$	6.33	N/A	2.4	81.4	1466	1046	2604	1853	0.51	0.42	3.16
266MP	500	1515	1.89×10^{-4}	KI	0.2	Pt*+Ni	Al$_2$O$_3$	6.33	2.4	2.0	79.2	1419	1011	2534	1802	0.51	0.42	2.93

Table 3.1: Summary of experimental conditions. Mind that the reported stresses have an $\pm$ 30 MPa error inherited in the solid salt assembly. [1] - measured on thin sections, [2] - calculated from apparatus data, [a] - experiments used only for mechanical data, [c] - corrected after Holyoke and Kronenberg (2010), τ - shear stress, $\Delta\sigma$ - differential stress, μ - friction coefficient resolved on 45° pre-cut, $\dot{\gamma}$ - shear strain rate, VZ - verzasca gneiss, * - annealed
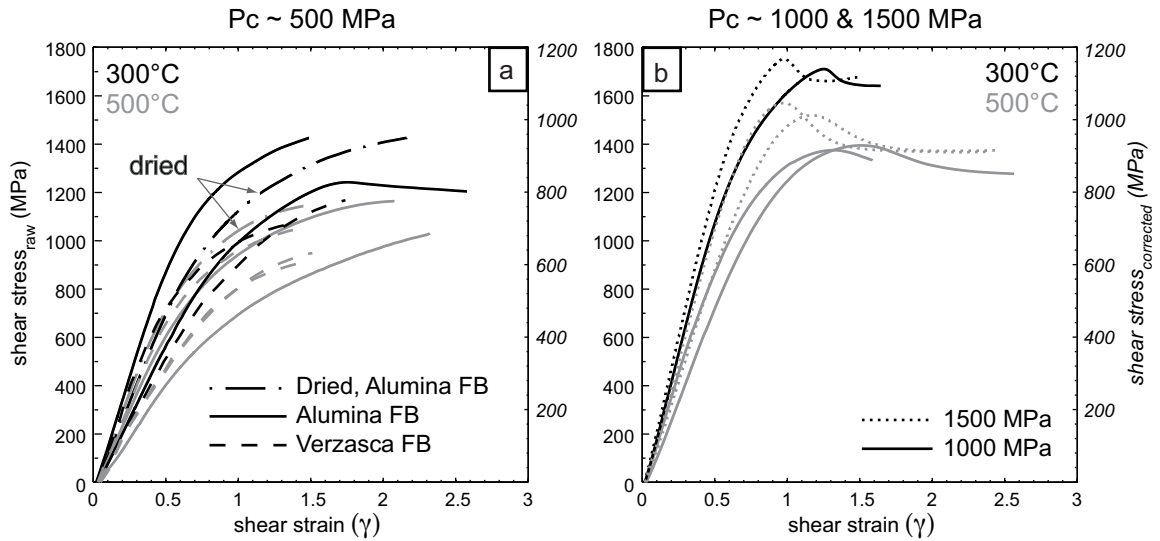
Figure 3.3: Shear strain vs. shear stress curves for a mean shear strain rate of $\sim 1.8 \times 10^{-4}$ s^{-1}. Dried samples were placed in an oven at 200°C for 24 hours before the experiment, to all other experiments 0.2 wt% H_2O has been added. In both plots, the left y-axis shows raw uncorrected data and the right y-axis is corrected after Holyoke and Kronenberg (2010). a) Experiments at $\sim$ 500 MPa confining pressure with Verzasca gneiss and alumina forcing blocks (FB). b) High confining pressure experiments with alumina forcing blocks.

The differential stress was corrected using the calibration by Holyoke and Kronenberg (2010) for the Griggs apparatus (see table 3.1) to obtain stress values for comparison with other laboratories using the following equation:

$$\sigma_{(GasApparatus)} = 0.73 \times \sigma_{(GriggsApparatus)} - 48 MPa \qquad (3.2)$$

All reported stresses contain a $\pm$ 30 MPa error inherited in the solid salt cell assembly (Holyoke and Kronenberg, 2010). A summary of experimental data (corrected and uncorrected) is in table 3.1.

3.3 Experimental Results

We report the results from 20 experiments, which were performed at 500 MPa, 1000 MPa and 1500 MPa confining pressure, temperatures of 300°C and 500°C and mean displacement rates of $\sim 9.3 \times 10^{-5}$ to 2×10^{-4} mm $\times$ s^{-1} translating into mean shear strain rates of 1.2 x 10^{-4} to 3 x 10^{-4} s^{-1}.

3.3.1 Experiments at 500 MPa confining pressure

All but one sample deformed at 500 MPa confining pressure show strain hardening over the whole of the examined finite shear strain range (up to γ of $\sim$ 2.6; Fig. 3.3). The experiments conducted with Verzasca gneiss forcing blocks at 300°C show consistently lower stresses compared to those with alumina forcing blocks. At 500°C, there is no systematic difference between the different forcing block experiments (Fig. 3.3). The samples with
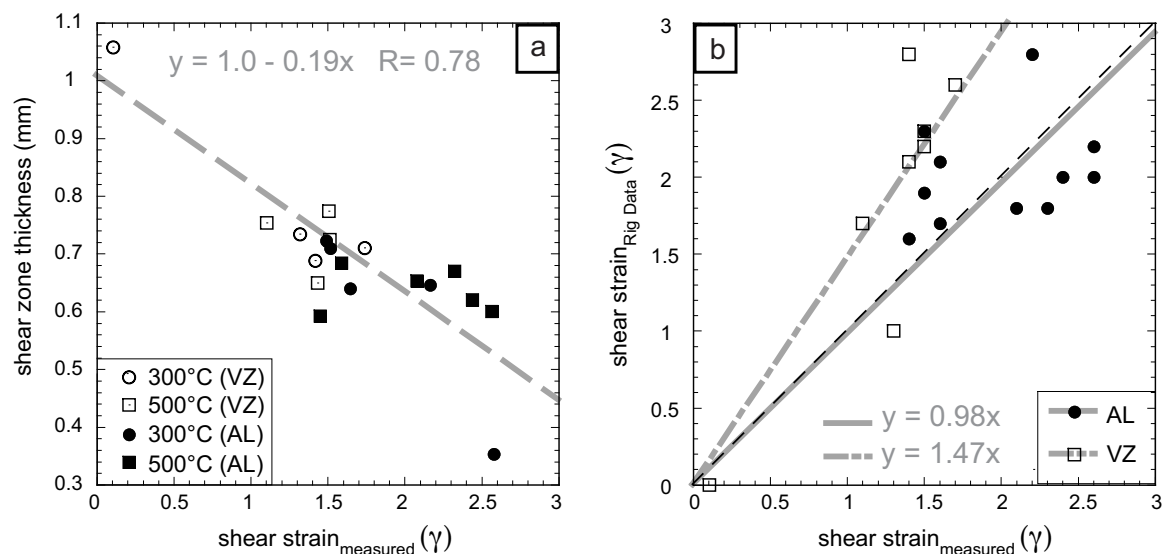
Figure 3.4: Mechanical data a) Shear strain measured on thin sections vs. shear zone thickness for both temperatures and alumina (AL) and Verzasca (VZ) forcing blocks. b) Shear strain measured on thin sections of the deformed sample vs. shear strain calculated from the rig data. Note that samples deformed with Verzasca gneiss forcing blocks (VZ) accommodate less shear strain than those with alumina forcing blocks (AL). Black dashed line shows measured shear strain = calculated shear strain. Best-fit lines are forced through zero.

Verzasca gneiss forcing blocks reach lower finite shear strains measured in thin section at a given apparatus-recorded shear strain (corresponding to piston displacement) compared to alumina forcing blocks experiments (Fig. 3.4). At high stresses piston displacement does not increase the shear strain in the gouge zone, because deformation is transferred into the Verzasca forcing blocks (Fig. 3.5), indicating that the frictional strength of the gouge is equal or higher to the strength of the intact Verzasca forcing block. Samples deformed at 500°C are systematically weaker than those deformed at 300°C, irrespective of the forcing blocks and inner confining salt medium used (min ∼ 100 MPa, max ∼ 500MPa, Fig. 3.3a). The reproducibility of the experiments is within ∼ 200 MPa shear stress at levels of 1000 - 1400 MPa (Fig. 3.3). Dried samples are stronger than wet ones (0.2 wt% H_2O added) at 500°C, whereas the strength is similar in 300°C experiments (Fig. 3.3; strength difference between 300°C and 500°C: ∼ 150 MPa).

3.3.2 Experiments at confining pressures greater than 500 MPa

Additional experiments at higher confining pressure were conducted to gain insight into the processes responsible for the observed strength difference. All samples deformed at higher confining pressures (1000 and 1500 MPa) strain weaken after reaching a peak stress around a γ-value of 1 – 1.5 (Fig. 3.3). Typically samples attain a quasi steady state stress level 60-130 MPa lower than peak strength (Fig. 3.3). The reproducibility of experiments conducted at higher confining pressures is far better (∼ 15 MPa at stress levels of 1400 – 1800 MPa) than that of those conducted at 500 MPa (Fig. 3.3). The increase of sample strength with an increase in confining pressure from 1000 MPa to 1500 MPa is considerably smaller compared to that of the 500 MPa to 1000 MPa increase (Fig. 3.6). The strength difference between the 500°C and 300°C experiments is 200 – 300 MPa at 1000 MPa and 1500 MPa confining pressure and does not systematically increase with increasing confining pressure.
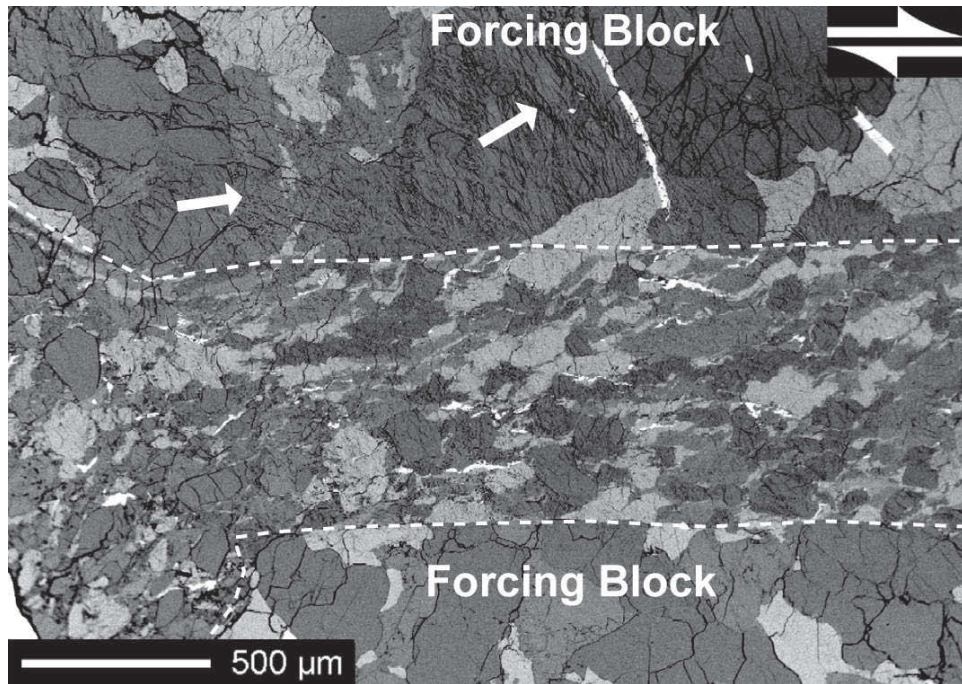
Figure 3.5: Deformed Verzasca gneiss forcing block. White dashed lines delimit the gouge zone. Note the closely spaced fractures in the forcing block (white arrows).
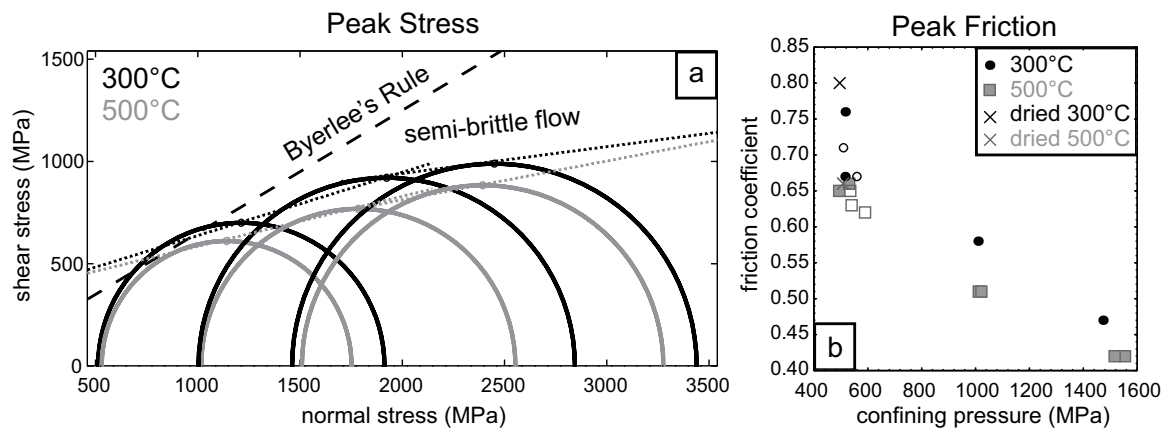
Figure 3.6: a) Mohr diagram for selected 500 MPa, 1000 MPa and 1500 MPa confining pressure experiments. Black and gray dotted lines are envelopes for peak strength. All data corrected after Holyoke and Kronenberg (2010) b) Bulk peak friction coefficient calculated for the 45° pre-cut. Full symbols – alumina forcing blocks, empty symbols – Verzasca forcing blocks. Note that the friction coefficients for the 500MPa experiments are a lower estimate as peak strength was not reached with the exception of one experiment.

3.4   Microstructural Observations

3.4.1   Analytical methods

After the experiment, samples were vacuum-impregnated with low viscosity epoxy and double-polished thin sections parallel to the displacement direction were prepared for microstructural analysis. One sample was cut perpendicular to the main displacement direction to help resolve the strain distribution within the samples.

The thin sections were carbon coated and analyzed in a field emission Philips XL 30 ESEM with an EDX detector. An acceleration voltage of 20 kV was used for high contrast images and 15 or 10 kV was used for high-resolution imaging. EDX maps were collected on a Jeol JXA 8600 superprobe with an EDX detector at 15kV acceleration voltage. The samples were further analyzed with a polarizing light microscope and a cold cathodoluminescence source (Technosys 8200 MkII) at 20 kV acceleration voltage.

3.4.2   Microstructure and image analysis

For the shear zone description, the angles are measured counterclockwise from 0° (positive x- direction) to 180° and samples were consistently analyzed with dextral shear sense. The shear zone boundary is always horizontal, i.e., at 0°.

Orientations up to 90° will be called "synthetic" and orientations > 90° "antithetic" to the shear. We use the term "survivor grains" for grains that can be well identified as porphyroclasts at a given magnification and the term "fragmented mantle" for finely crushed material (e.g. Fig. 3.7) which typically surrounds a survivor grain. In the fragmented mantle individual grains or porosity can still be resolved at high magnifications. We describe survivor grains together with the fragmented mantle as "aggregates", they are monomineralic and delimited by phase boundaries.

With increasing shear strain so-called "slip zones" are observed. We use the term slip zone to describe a through going zone of localized deformation where probably amorphous material is present. By the term "amorphous" we refer to visually homogenous material with "flow" structures where unloading cracks concentrate and no grains or porosity can be resolved up to a magnification of 20 000x (spatial resolution of 4 nm) by backscattered and secondary electrons in a field emission SEM. The physical nature of the feldspar-derived material in slip zones is difficult to assess. In cases where a well identifiable marker is displaced by the slip zone (i.e., biotite) the amount of accommodated shear strain within the local slip zones is high ($\gamma \geq 10$). The reasoning for using the term "amorphous" is given in the discussion (see section 5.5). The microstructure development of the slip zones was assessed only qualitatively, they were primarily analyzed for the associated chemical and inferred material properties.
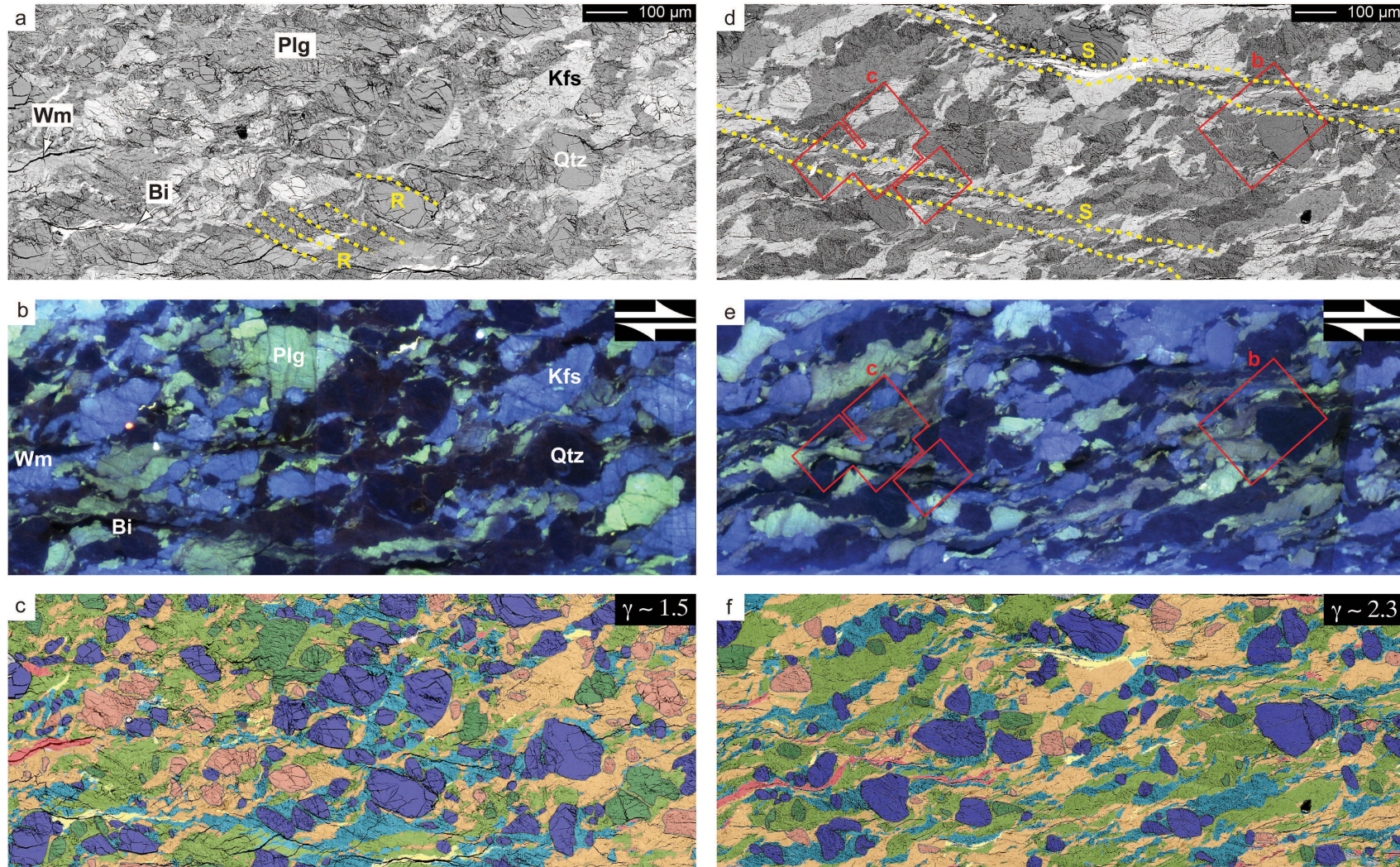
Figure 3.7: Microstructure at low ($\gamma \sim 1.5$) and high shear strains ($\gamma \sim 2.3$), scale and dextral sense of shear apply to all images. a) and d) SEM backscatter (BSE) images. Minerals in order of increasing brightness: quartz (Qtz), plagioclase (Plg), white mica (Wm), potassium-feldspar (Kfs) and biotite (Bi). Yellow dashed lines labeled R indicate R_1 Riedel shears and yellow dashed lines labeled S indicate slip zones. Note decrease in density and change in orientation with increasing shear strain. b) and e) CL images of a) and d). Black – micas, dark blue/black – Qtz, light blue – Kfs, green – Plg. c) and f) colour coded images used for quantitative microstructural analysis. Dark blue – Qtz survivor grains, cyan – Qtz fragmented mantle, dark green – Plg survivor grains, light green – Plg fragmented mantle, dark orange –Kfs survivor grains, orange – Kfs fragmented mantle, red – Wm, yellow – Bi. Note the higher amount of Qtz survivor grains compared to feldspar survivor grains. Red frames indicate areas where EDX maps were collected (Fig. 3.16).

1. Individual survivor grains from all three major phases - quartz (Qtz), potassium-feldspar (Kfs) and plagioclase (Plg) were digitized manually at a magnification of 100x from the whole shear zone until a statistically representative number was attained (where possible around 200 grains). Preferred orientation of surface elements (i.e. grain boundaries) of the survivor grains for each major phase was analyzed using the SURFOR method (Panozzo, 1984) and the shape preferred orientation (i.e. grain orientation) was analyzed using the PAROR method (Panozzo, 1983) (software at: http://pages.unibas.ch/earth/micro/).

2. The described analyses were carried out using representative regions from the centre of the shear zones at a magnification of 100x resulting in an image size of 1666 x 833 μm ($\sim$ 22 % of the total sample area) (e.g. Fig. 3.7). SEM and CL images were combined to separate the mineral phases via gray level thresholding in ImageSXM (http://www.liv.ac.uk/$\sim$sdb/ImageSXM/) and manual digitalization.

3. The ratio between areas with survivor grains and aggregate area which is equal to the volume ratio Vs/Va is a measure for the amount of comminution of the individual phases and was calculated by the following equation:

$$V_s/V_a = \frac{A_s}{A_a} \times 100; (\%) \tag{3.3}$$

where V_s = volume of survivor grains, V_a = volume of aggregates, A_s = area of survivor grains and A_a = area of aggregates. It ranges from 0 % (aggregate formed entirely by fragmented mantle) to 100% (aggregate formed entirely by survivor grains).

4. For the quantitative analysis of shape preferred orientation of the aggregates, the autocorrelation function (ACF) was used because it does not require segmentation of the individual aggregates, which is often difficult (Fig. 3.7). The ACFs were thresholded at two different levels, one corresponding to an area of $\sim$ 8000 μm^2 and one corresponding to an area of $\sim$ 400 μm^2. These areas roughly correspond to the typical cross-sectional area of aggregates including survivor grains and to the more comminuted aggregates formed of fragmented mantle, respectively. The orientation of the ACF sections and the anisotropy were measured by the striking, ϕ, and the axial ratio, b/a, of the best fit ellipse to the ACF (Fig. 3.8) (for details of the technique see Heilbronner, 1992, 2002; De Ronde et al., 2004).

5. Selected areas with typical SEM and CL microstructures were mapped with EDX analyses in the staring material as well as in high and low strain samples (300°C and 500°C) to obtain semi- quantitative information about chemical changes coupled with deformation.

3.4.3   Microstructure development with increasing strain

The development of the microstructure with increasing shear strain was analyzed using a set of experiments deformed at Pc = 500 MPa with 0.2 wt% H$_2$O added using both types of forcing blocks, from a shear strain of $\gamma \sim 0.1$ to $\gamma \sim 2.6$. Additional observations were performed on dried samples and samples deformed at higher confining pressures (1000 MPa and 1500 MPa).
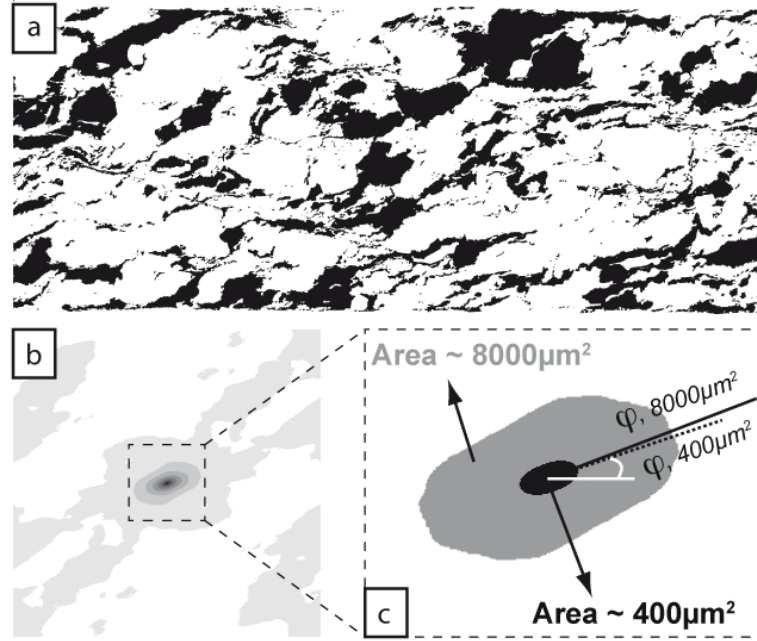
Figure 3.8: a) Binary image showing aggregates (survivor grains and fragmented mantle combined) of Kfs, long edge of image = 1666 μm. b) Bulk ACF of a). c) ACF calculated for two 1024 × 1024 pixel matrix thresholded at two different levels: gray; corresponding to the size of the aggregates with survivor grains. Black; corresponding to the size of aggregates formed of fragmented mantle (for procedure see Heilbronner, 1992). ϕ – long axis orientation derived from best fit ellipses. Anisotropy of the ACF; short axis / long axis (b/a) of the best-fit ellipses (0.51 for aggregates with survivor grains, 0.49 for fragmented mantle).

3.4.3.1 Starting material ($\gamma \sim 0.1$)

The starting material was characterized in an experiment where the sample was pressurized to 500 MPa confining pressure and the temperature was increased to 300°C but no differential stress was applied. From SEM images the composition was determined as: 32% quartz (Qtz), 29% k-feldspar (Kfs), 21% plagioclase (Plg), 3% biotite (Bi) and 0.5% white mica (Wm). The average thickness of the shear zone is ~ 1 mm and the porosity estimated by image analysis is $\sim 10\%$. All three major phases (Qtz, Kfs and Plg) deform by fracturing on grain-to-grain contacts (Hertzian fractures) (Fig. 3.9) and have a similar axial ratio of ~ 0.53. Micas deform mainly by kinking and fracturing and are randomly distributed within the sample. The anisotropy of the ACF ellipses is ~ 0.8 for all analyzed phases and the orientation varies between 10° for feldspars to 15° for quartz with respect to shear zone boundary (Fig. 3.10). There is a weak shape preferred orientation of the grains sub-perpendicular to the direction of compaction (Fig. 3.11). No fragmented mantle is formed in the starting material, thus the volume ratio V_s/V_a is 100% (Fig. 3.12). In CL images, the luminescence within Kfs and Qtz grains is homogeneous, Plg grains show variations in luminescence depending on the Ca or Albite content.

3.4.3.2 Low strain samples ($\gamma \sim 1.5$)

The gouge zone is pervasively cut by closely spaced (10 – 50 μm), short R_1-Riedel shears ($\sim$ 160 μm) with an en-echelon geometry (Fig. 3.13a,b). Adjacent to the R_1-Riedel shears the smallest detectable grain size is < 0.05 μm (Fig. 3.13c). R_1-Riedel shears form at an angle
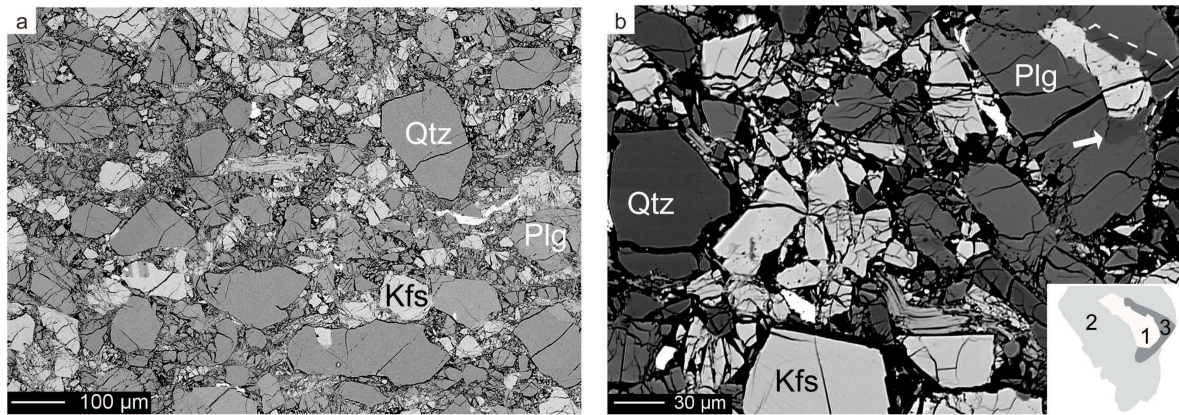
Figure 3.9: a) Microstructure of starting material, SEM backscatter images (BSE). Grains fracture on grain-to-grain contacts. b) High contrast image of starting material. Note that some grains are not necessarily monomineralic and furthermore, a Plg grain shows a more albitic rim (white arrow and white dashed line). Inset shows a drawing of the polymineralic grain (1 – Kfs, 2 – Plg, 3 – more albitic Plg)
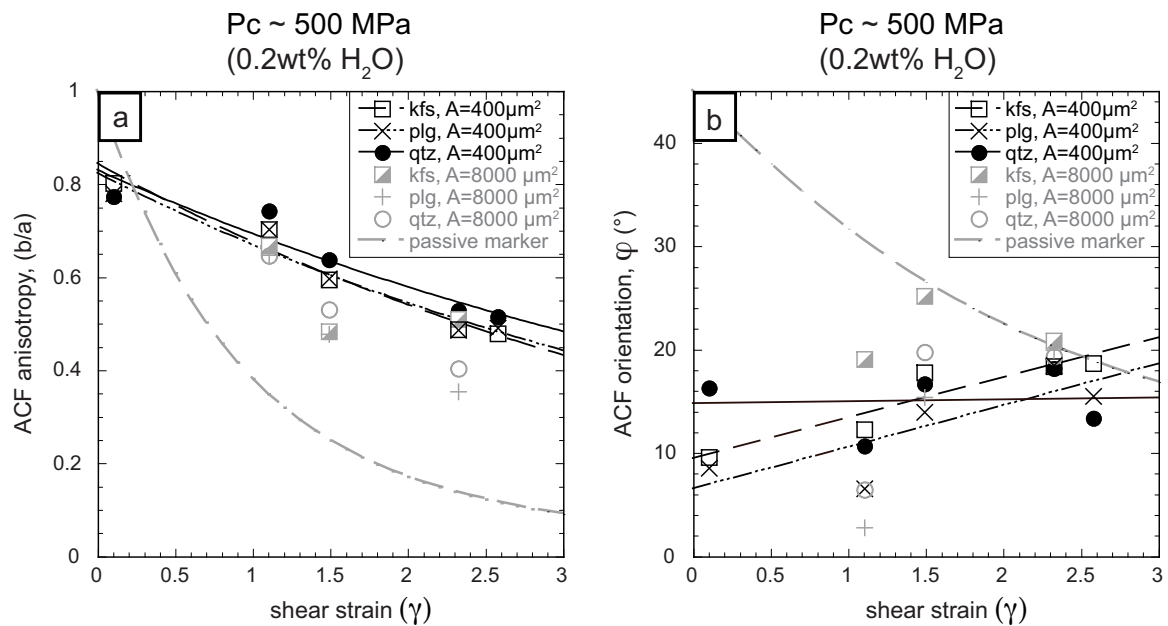
Figure 3.10: Microstructural data for aggregates. a) Anisotropy of the ACF ellipses vs. shear strain. b) Orientation of long axis of the ACF vs. shear strain. Gray dashed line in a) and b) show the development of anisotropy and orientation of a passive marker in pure simple shear. Other lines show the trends for Kfs, Plg and Qtz. Black symbols; aggregates formed of fragmented mantle (area $= 400~\mu m^2$), gray symbols; aggregates with survivor grains (area $= 8000~\mu m^2$).
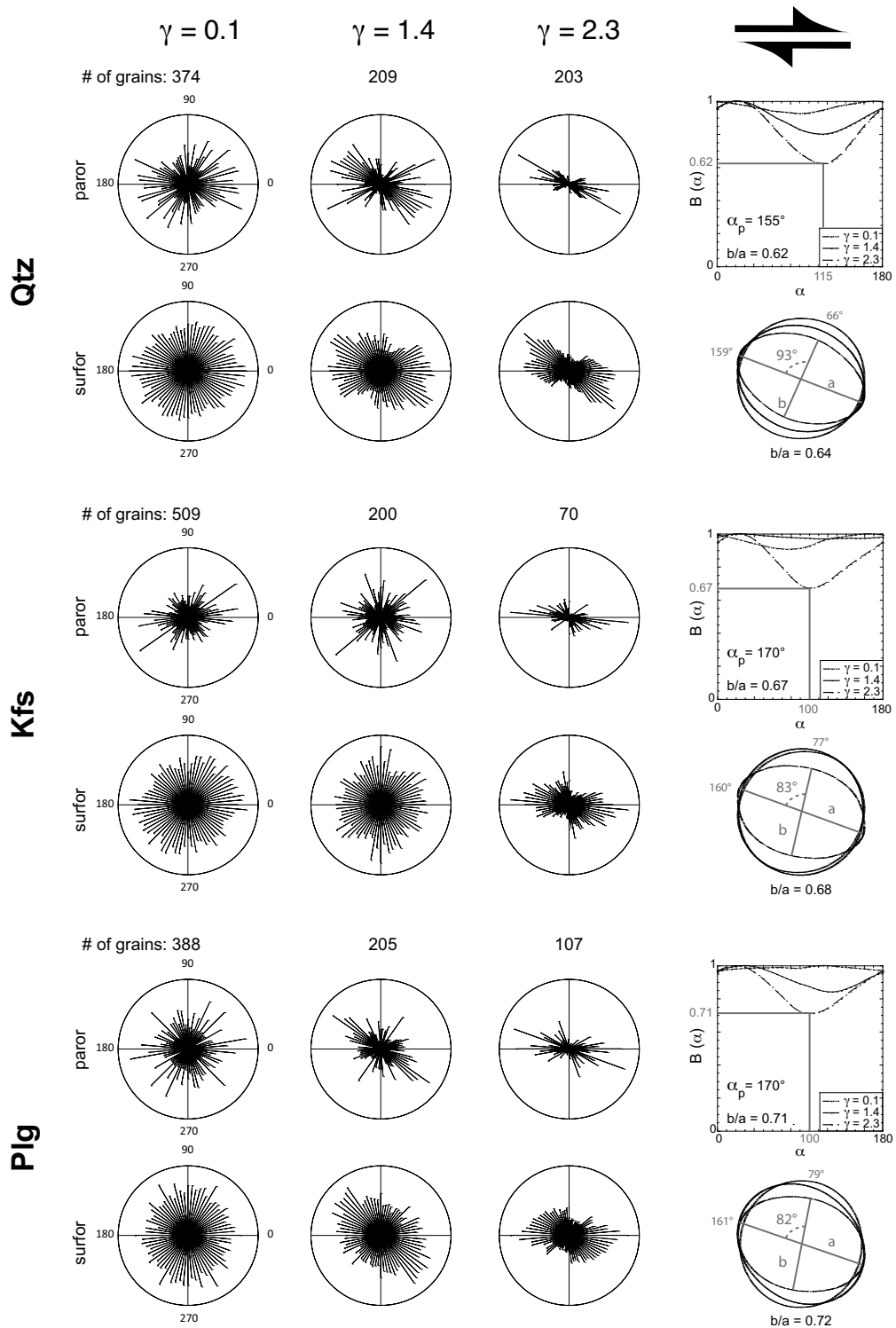
Figure 3.11: Particle and surface orientation distribution functions (ODFs) of survivor grains for samples at different shear strains for Qtz, Kfs and Plg. Dextral sense of shear for all. On the right, B(α) curves (particle analysis) and characteristic shapes (surface analysis) are shown for increasing shear strain. The fabric anisotropy (b/a) and orientation (α_p) is shown for the maximum shear strain of 2.3. The orientation of the short and long axis, b and a, the angle between the two axes and the anisotropy (b/a) of the characteristic shape is shown for the maximum shear strain of 2.3.
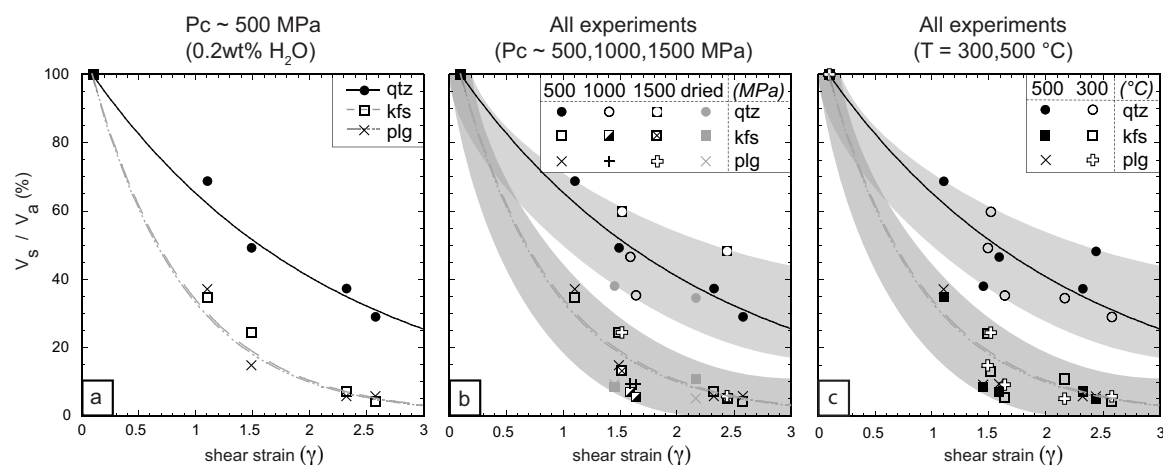
Figure 3.12: Volume ratio of survivor grains to aggregate. Lines show approximate trends. a) Vs/Va for experiments conducted at 500 MPa confining pressure with 0.2 wt% H_2O added. Note that quartz has always more survivor grains than feldspars and that both feldspars follow the same trend. b) Vs/Va for all experiments grouped by confining pressure. c) Vs/Va for same experiments grouped by temperature. Shaded areas highlight the trend for feldspars (Kfs and Plg) and quartz survivor grains in both b) and c). Note the only systematic dependence of the amount of survivor grains is on strain.
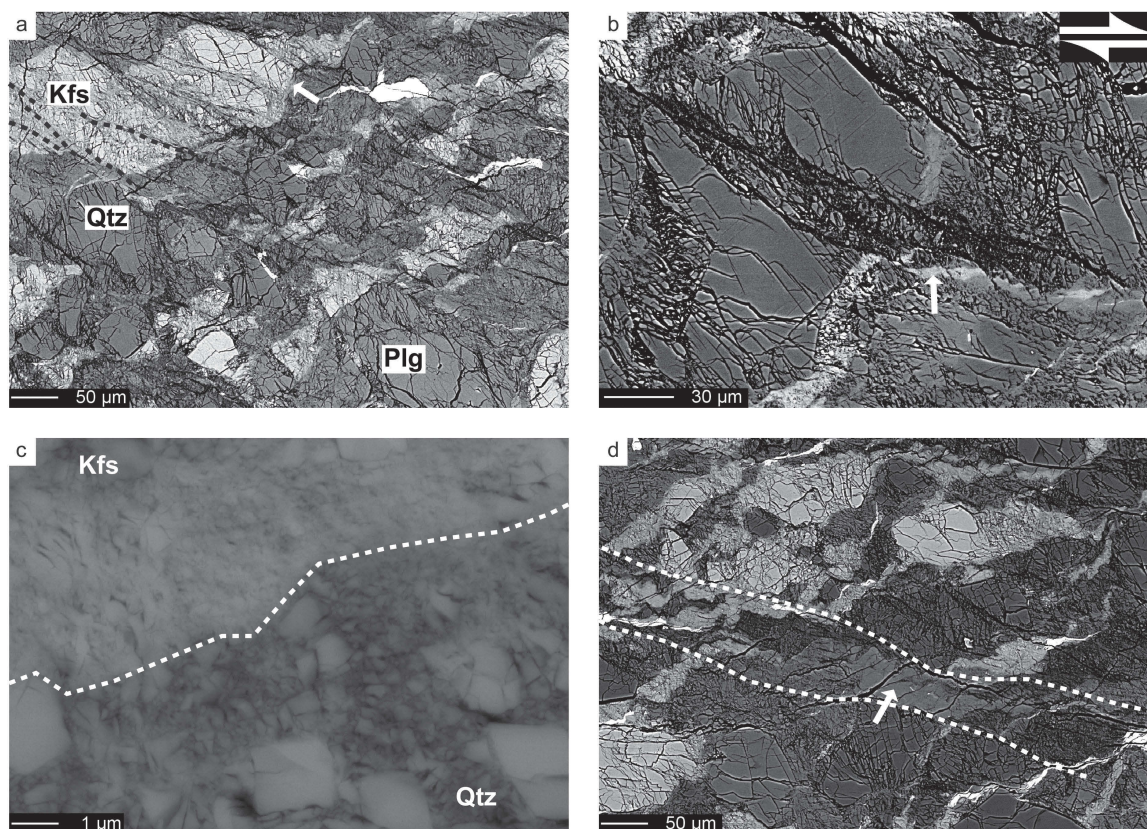
Figure 3.13: SEM backscatter images (BSE) of typical microstructures at low shear strains. All images have a dextral sense of shear and the long edge is parallel to shear zone boundary. a) Closely spaced R_1 Riedel shears (dashed lines) pervasively crosscut the grains producing large amounts of fine-grained material. b) Qtz grain crosscut by a R_1 Riedel shear – note the en-echelon geometry and the fine seam of Kfs (white arrow) c) Smallest resolvable grains in BSE ($\leq$ 50 nm). d) Incipient slip zone (between white dashed lines) at low shear strain ($\gamma \sim 1.6$). Note the absence of larger survivor grains in this region and the more homogenous appearance of the Plg (white arrow).

of $\sim 153°$ or $18°$ to σ_1 which is oriented at $135°$ (shear zone boundary $= 0°$). Locally, we can observe incipient slip zone formation where the amount of fine grains is very high (Fig. 3.13d). In CL images we observe a change in luminescence in feldspar aggregates within the highly fragmented regions, corresponding to chemical changes in these aggregates in both, $300°C$ and $500°C$ experiments.

The aggregates (survivor grains together with the fragmented mantle) are elongated along the R_1- Riedel shears and show a strong shape preferred orientation (SPO) synthetic with the induced sense of shear. The anisotropy of the ACF increases steadily with b/a decreasing from 0.8 (starting material) to ~ 0.6 and ~ 0.5 for small (400 μm^2) and large (8000 μm^2) ACF sections, respectively. Quartz has usually a slightly lower anisotropy than feldspars for both aggregate sizes. The orientations of the ACFs show large scatter and tend to rotate antithetically with increasing shear strain (Fig. 3.10).

The SPO of the individual survivor grains is antithetic to the induced sense of shear and is best developed in Qtz grains (Fig. 3.12). The fractured Qtz survivor grains have a slightly higher average axial ration (0.52) than the feldspar survivor grains (0.50) and the survivor grain to aggregate ratio is higher for Qtz (Vs/Va = 70%) than for feldspars (Vs/Va = 40%) (Fig. 3.12).

The porosity estimates by image analysis are around 5%. However, porosity certainly was lower during the experiment because extension cracks and the thin section making process increase the apparent porosity in the samples. The average thickness of the shear zones after experiment is ~ 0.7 mm, compared to 1 mm in the starting material (Fig. 3.4a). The thinning of the shear zones is accommodated by compaction and by the development of Reidel R_1 shears. There is no systematic difference of the microstructure for different temperatures.

3.4.3.3   High strain samples ($\gamma \sim 2.5$)

With increasing shear strain, deformation localizes into a few anastomozing slip zones with a spacing of $1000 - 1500$ μm (usually around 6 in the whole sample) which accommodate most of the displacement (Fig. 14a,b). The slip zones contain "amorphous" material and develop predominantly in feldspars. Unloading cracks ($\sim 45°$, sub-perpendicular to σ_1) concentrate in the "amorphous" material and typically terminate at its boundaries (Fig. 3.14). Incipient Y-shears (shear zone boundary parallel) develop in the most strained samples at the gouge – forcing block interface. The slip zones often contain micas. However, micas do not form an interconnected layer within the slip zones. If a quartz aggregate is present within the slip zone it usually develops a σ-clast geometry (Fig. 3.14b), indicating that Qtz has the highest strength of all phases also on the slip zone scale. On phase-to-phase contacts fine Fe-rich seams (thickness ~ 0.1 μm) in feldspars develop (Fig. 3.14c,d).

The orientation of the slip zones progressively rotates with increasing shear strain and thinning of the shear zone to $\sim 162°$ (resp. $27°$ to σ_1). Especially in quartz aggregates, original R_1- Riedel shears are preserved with a steeper orientation ($\sim 145°$) than the through-going slip zones. The only sample showing strain weakening (261MP) has a considerably thinner shear zone than usual (0.4 mm) and well developed slip zones with a Y-shear orientation. Thus, the development of Y-shears appears to be responsible for the observed weakening.

CL images show that luminescence of Plg and Kfs varies significantly within the sample
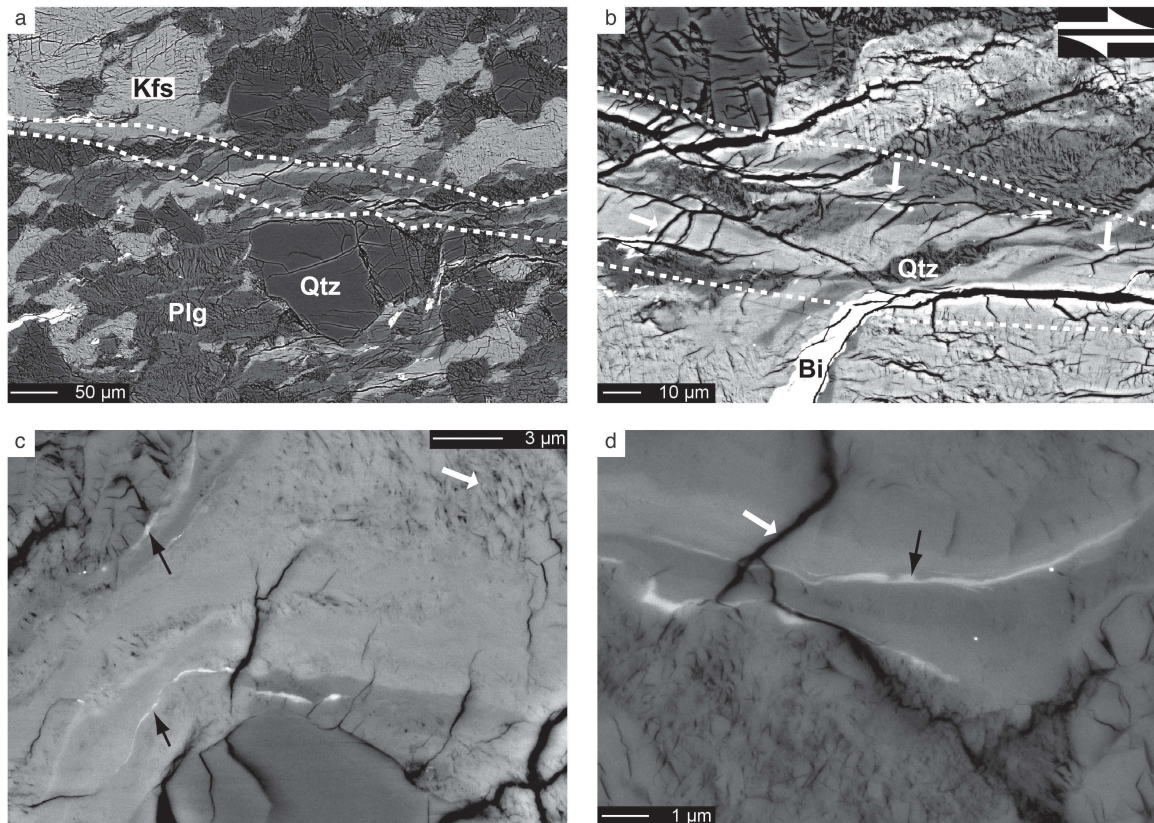
Figure 3.14: SEM backscatter images (BSE) of typical microstructures at high shear strains. All images have a dextral sense of shear and the long edge is parallel to shear zone boundary. a) Deformation localizes into slip zones containing "flowing" material derived from Kfs and Plg material (between white dashed lines). b) Qtz aggregate surrounded by feldspar material with "flow" structures (between dashed lines) showing a σ-clast geometry. Note that unloading cracks concentrate in "flowing" zones (white arrows) c) Dried sample deformed at $T = 500°C$. Note the fine-grained fragmented mantle where individual grains can still be resolved (white arrow) and the "flow" of the irresolvable feldspar material around a quartz porphyroclast outlined by a bright Fe-rich seam (black arrows). Note also the unloading crack. f) Higher magnification view of feldspar with "flow" structures (upper part of image) that is impossible to resolve in the field emission SEM. Note a bright Fe-rich seam (black arrow) and an extension crack (white arrow) which terminates at the interface between "flowing" feldspar and fine-grained fragmented mantle.

depending on the amount of strain accommodated within an individual aggregate for both examined temperatures. The anisotropy of the ACF further increases with b/a decreasing to ~ 0.5 and ~ 0.4 for small and large aggregates, respectively (Fig. 3.10). The orientation of the ACF further rotate antithetically compared to the starting material and low strain samples (Fig. 3.10). The Vs/Va ratio of survivor grains to aggregate decreases for quartz and both feldspars (30% and $< 10\%$, respectively) with increasing shear strain (Fig. 3.12). There is no dependence on temperature, neither for the survivor grain to aggregate ratio nor for the anisotropy of the ACF ellipses (Figs. 3.10, 3.12). The porosity estimated from SEM images is $< 5\%$.

3.4.3.4   Samples deformed to $\gamma \sim$ 1.5 - 2.5 at high confining pressures

Due to the small number of experiments performed at higher confining pressures (1000 and 1500 MPa) we will describe only the main differences to the lower confining pressure samples. In general, the high confining pressure experiments show similar microstructures with increasing shear strain like experiments performed at 500 MPa confining pressure.

At high confining pressures the slip zones are more shear zone boundary parallel ($\sim 164°$) and are well developed even at low shear strains ($\gamma \sim 1.6$) at the interface between gouge and forcing block as well as in the middle of the shear zone (Fig. 3.15a,b). The slip zones are surrounded by large amounts of "amorphous" material (Fig. 3.15c,d). A sample cut perpendicular to the main displacement direction (Y-Z section) shows that the slip zones cross-cut at an angle of $\sim 120°$ with the acute angle bisected by Y. Thus, the slip zones form a complex anastomosing network.

R_1 Riedel shears are less common (possibly due to more compaction during pressurization) and do not develop an en-echelon geometry. The Vs/Va ratio shows similar characteristics for quartz as for both feldspars to the experiments performed at 500 MPa confining pressure (Fig. 3.12). However, due to the very homogenous appearance of, especially, feldspars it is more difficult to identify survivor grains in the high confining pressure experiments. In CL we observe a large variability in luminescence in both Kfs and Plg in the highly strained regions.

3.4.3.5   Chemical analysis

3.4.3.6   Starting Material

In the starting material we observe a homogenous CL signal in Kfs (blue) and Qtz (black) and a slightly variable CL signal in Plg (green) (Fig. 3.16). Individual grains are not necessarily monomineralic. EDX maps show that some Plg grains in the starting material change their CL signal according to different Ca/Na ratios (Fig. 3.16a). Plg in the starting material consists of oligoclase ($\sim 93\%$) and albite ($\sim 7\%$). Few Plg grains show perthite lamellae. Kfs grains have very low contents of Na and Ca. Plg never incorporates K in the starting material. Biotite and white mica do not yield any CL signal and have a homogenous composition within one grain even if they are kinked and fragmented.
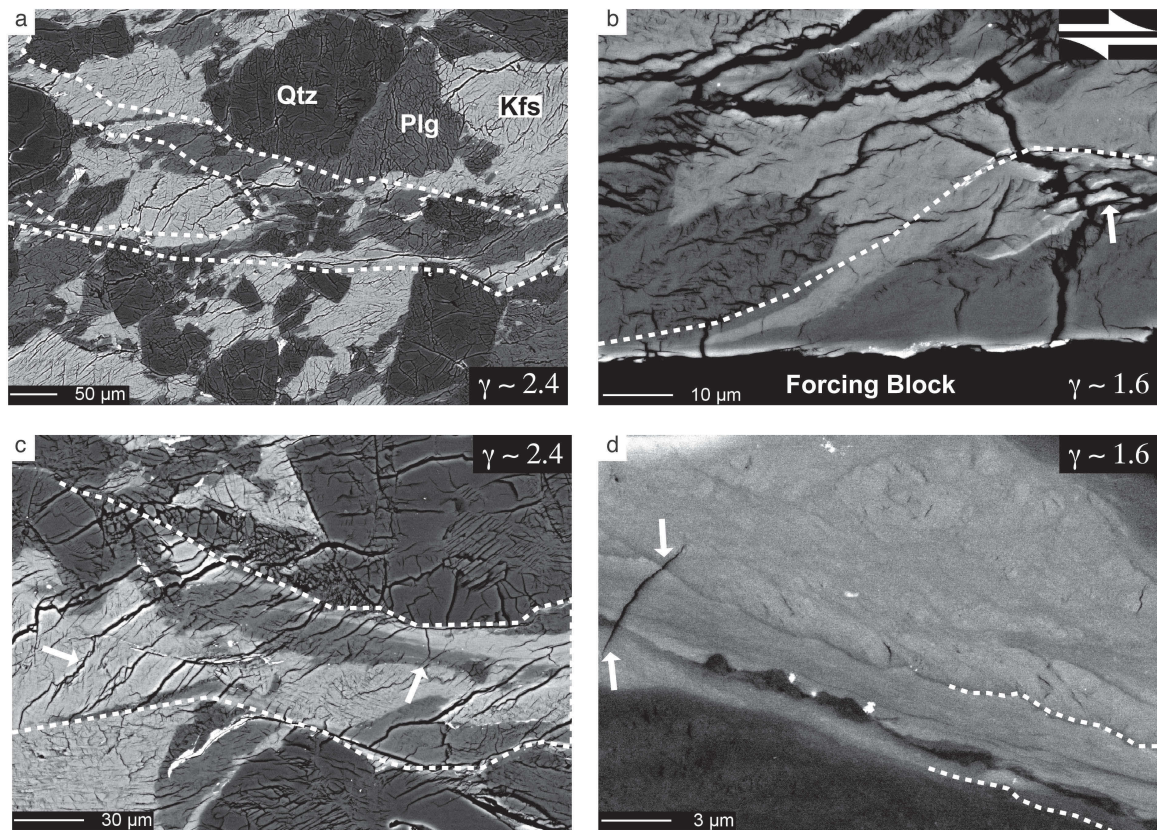
Figure 3.15: SEM backscatter images (BSE) of typical microstructures at high confining pressures. All images have a dextral sense of shear and the long edge is parallel to shear zone boundary. a) Slip zone crosscutting the whole image (between dashed lines). Note the more homogenous appearance compared to 500 MPa samples and the absence of finely fractured Qtz grains compared to Fig. 3.14a and b at similar shear strain. b) Slip zone (white dashed line) developed at the gouge – forcing block boundary. White arrow indicates a mica grain. c) Slip zone (between dashed lines) developed within feldspars showing "flow" structures. Note the large area affected by unloading cracks (white arrows) d) High-contrast detail of a slip zone at Pc ~ 1000 MPa and T = 500°C. Note the main slip zone delimited by darker seams (between white dashed lines) where an unloading crack (white arrows) developed.

3.4.3.7 Deformed samples

After deformation, the Ca/Na and Al/Si ratios of plagioclase (Fig. 3.16b,c,e) change in all samples, irrespective of temperature conditions and water contents. Albite is often observed in strain shadows in the fine-grained fragmented mantle preferentially on aggregate-to-aggregate contacts (Fig. 3.16b,c). The area affected by these changes seems to increases with increasing finite shear strain (oligoclase $\sim$ 91%, albite $\sim$ 9% at $\gamma \sim 2.5$) (compare Fig. 3.15a and d). The change of the feldspar composition in the fragmented mantle seems to be stoichiometric (Na/Ca ratio is coupled with Al/Si ratio) however; precise analysis was not possible because of the fine-grained nature of the material and the topography of the samples. Both Kfs and Plg fragmented mantles tend to incorporate Na/Ca or K, respectively, indicating either intimate mechanical mixing of the deformed feldspars or a high mobility of these elements within the gouge.

The slip zones containing "amorphous" feldspar material show the most significant changes in chemistry (in Plg a relative enrichment in K and Ca and loss of Na, resulting in a green color in the color composite images), (Fig. 3.16b,c,e). Repeated EDX measurements of the same locality show that Na preferentially evaporates from the "amorphous" slip zones whereas it does not evaporate from the adjacent less deformed fragmented mantles and survivor grains. Heavier elements (K and Ca) are not affected by evaporation and are clearly enriched in the "amorphous" material compared to survivor grains and fragmented mantles (Fig. 3.16b).

Compared to the starting material, the phases in the deformed gouge display complex changes in mineral chemistry, especially with respect to the alkali content. The chemical changes are more pronounced in the experiments conducted at 500°C compared to those at 300°C and increase with increasing amount of finite shear strain. In absence of further detailed study these remain qualitative observations.

3.4.4 Summary of microstructural observations

The development of the microstructure at the "large scale" of the whole shear zone is primarily controlled by the imposed shear strain and we did not detect major microstructural differences between the samples deformed at 300°C and 500°C for the monitored quantitative parameters. Quartz is always the strongest rheological phase and fractures least. Both K-feldspar and plagioclase deform in a similar manner and are the weakest phases, together with micas at our experimental conditions. All samples display a microstructure similar to S-C' mylonites (Berthé et al., 1979) or cataclasites (Lin, 2001, 1999). At higher finite strains, the development of through going slip zones containing "amorphous" material is observed.

3.5 Discussion

3.5.1 Influence of starting material porosity

The starting material gouge has a porosity of $\sim$ 10% in this study. Keulen (2006) and Keulen et al. (2007, 2008) deformed intact cores of Verzasca gneiss (porosity $< 1\%$) in coaxial compression at identical temperatures and similar strain rates and confining pressures as in
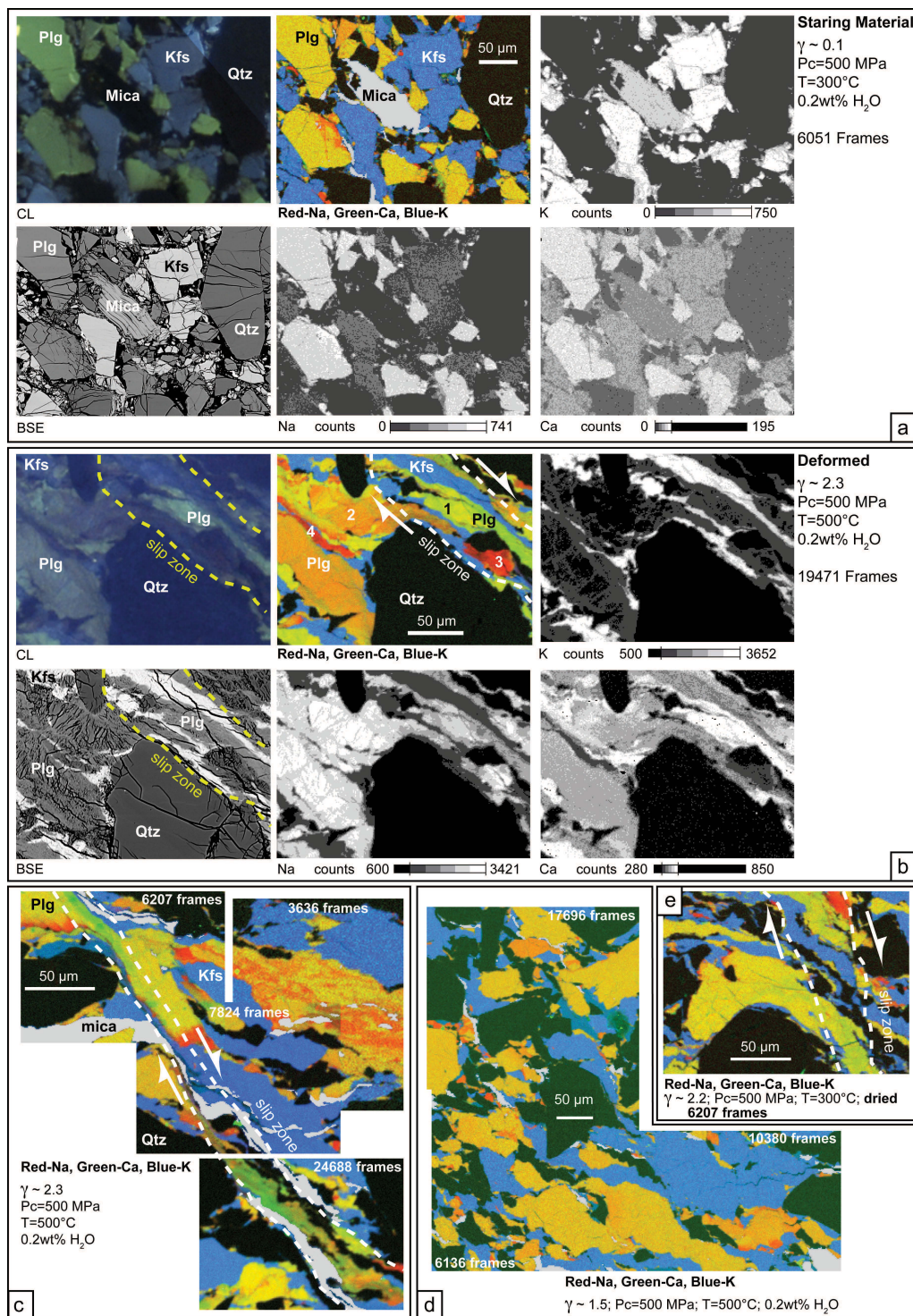
Figure 3.16: EDX maps showing chemical changes during deformation. Long edges of the images are sub-perpendicular to σ_1 (see Fig. 3.7 for location and orientation). CL -cathodoluminescence image, BSE - backscattered electrons image, colour composite images are made by combining RGB channels where Na = Red, Ca = Green and K = Blue. Micas are set to gray. Concentrations of individual elements are shown as contoured gray scale images in a) and b). a) Starting material. Note homogenous CL signal within individual grains. In colour composite image Plg is yellowish/orange (Na/Ca ratio) with minor reddish (albitic) regions, Qtz is black, Kfs is blue. b) Deformed sample. Note the large variability of CL signal. In colour composite image, note the greenish colour (relative enrichment in K and Ca and loss of Na, see text for discussion) of Plg in the slip zone (1). Note the change in colour from yellowish to dark orange in the strained Plg aggregate (2) adjacent to the slip zone and the presence of albite (red) in a strain shadow within the slip zone (3) and on the boundary between two Plg aggregates (4). Furthermore, notice the relative enrichment in K and Ca of the 'flowing' Plg (1) and depletion in Na (due to evaporation) compared to Plg survivor grains (2). c) High magnification color composite image of a slip zone. Greenish color (feldspar containing K, Na and Ca) clearly correlates with the presence of slip zones (between dashed lines). Reddish rims indicate more albitic regions that affect larger areas than in the low strain samples and starting material. d) Color composite image of low strain sample. Plg has a uniform orange/yellowish color on large areas. Note the relatively small area with albitic (reddish) grains compared to b) and c). e) Color composite image of a dried high strain sample deformed at 300°C. Note the greenish and reddish colors in the slip zone.
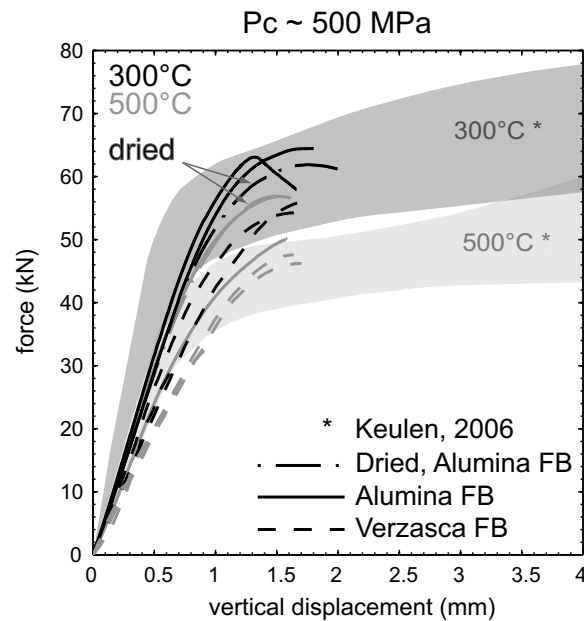
Figure 3.17: Comparison of mechanical data from axial shortening experiments on intact Verzsca gneiss of Keulen (2006) (shaded areas) and on gouge experiments (this study). Force vs. vertical displacement was used to allow comparison of the different experimental set-ups.

this study. The slope to maximum strength in stress-strain curves in a Griggs apparatus is the result of several processes acting in parallel, so that it is impossible to separate compaction from other deformation processes in our experiments. However, during deformation and compaction to <5% porosity of gouge the load supported is remarkably similar to that of the same intact Verzasca Gneiss samples deformed by Keulen (2006) (Fig. 3.17).

Keulen et al. (2007) carried out experiments with two loading cycles. The supported load was always the same, regardless of the applied hold/healing period between cycles. Microstructural analysis showed that each deformation cycle had produced new faults. Thus, deformation did not reactivate the previously formed faults. All of these observations provide further evidence that 500 MPa confining pressure is sufficient to inhibit sliding on pre-existing fault planes (Keulen et al., 2007). Furthermore, the initial porosity of $\sim 10\%$ of the gouge does not seem to affect its maximum strength. Compaction occurs at the beginning of our experiments where the pore space is filled by fractured grains which are spalling from larger grains along Hertzian fractures. Thus, compaction does not change maximum strength but it will strongly affect the work hardening and strain localization processes. Microstructures show that extremely small grains ($< 0.1 \, \mu$m) already form at very low shear strains – so the whole range of grain sizes is formed instantaneously during fracturing of a single individual grain (Keulen et al., 2007; Stünitz et al., 2010).

Dilatancy is negative during the first stage of the experiment because the positive dilatancy during cracking is compensated by a greater volume decrease during pore space collapse. Porosity is reduced to near zero at $\gamma \sim 1.5$ (maximum amount of shear strain in the experiments conducted with Verzasca forcing blocks; Fig. 3.14). Once the porosity is eliminated, fracturing of grains will do work against the confining pressure (Davies and McSaveney, 2009).

The varying rate of compaction from one experiment to another may explain the scatter in the slopes at 500 MPa confining pressure (Fig. 3a). The porosity reduction to near zero values should occur at lower shear strains in experiments conducted at higher confining pressures.

The peak strength reached in these experiments is observed around $\gamma \sim 1$ (Fig. 3.13b) which probably indicates the end of the compaction stage, which occurs at considerably lower strains at higher confining pressure than at 500 MPa (Fig. 3.13). Furthermore, the initial slopes of the higher confining pressure experiments are more reproducible and the slopes are steeper with increasing confining pressure (Fig. 3.13b) supporting this interpretation. Another explanation of the scatter in initial slopes is that it may be caused by the mating surfaces in the load column of the deformation apparatus. At confining pressures greater than 800 MPa, the misfit of these surfaces is eliminated and the elastic behavior of the load column becomes linear (a discussion of the phenomena is given by Holyoke and Kronenberg, 2010).

3.5.2 Development of the S - C' fabric

Increasing amount of finite simple shear leads to further formation of R_1-Riedel shears which cut through the gouge zone, offset survivor grains, and produce more fine-grained material. Among the fine-grained gouge material, the best detectable individual grains are quartz. The amount of very fine-grained but still detectable fragments (e.g. Fig. 3.13c) decreases with increasing confining pressure and increasing shear strain. It is important to point out that fine but well resolvable grains (~ 500 nm) always have angular shapes and we never observe grains with indenting, lobate grain boundaries which are thought to be typical for dissolution-precipitation creep (i.e Keulen et al., 2008; Tenthorey and Cox, 2006). However, it is impossible to resolve the grain shapes of extremely fine-grained fragmented mantles where only porosity is visible (e.g. Fig. 3.14c, d).

The elongation of this finely fractured material ("fragmented mantle") around survivor grains leads to the formation of aggregates, which have a SPO synthetic with the induced sense of shear (Fig. 3.10) and usually have a monoclinic shape asymmetry. The anisotropy of the fabric increases with increasing finite shear strain and the orientation of the aggregates rotates antithetically in feldspars (from $\sim 10°$ to $\sim 20°$) but remains stationary in quartz ($\sim 15°$), but a large scatter is present in the data (Fig. 3.10b). In the less fractured domains between individual R_1-Riedels larger survivor grains can be identified with an antithetic SPO to the induced sense of shear. With progressive shear deformation, the amount of the survivor grains decreases steadily, their orientation becomes more shear zone boundary parallel (especially for feldspars), and their SPO becomes stronger (Fig. 3.11). Both feldspars always have a similar Vs / Va ratio which is systematically lower that the ratio in quartz (Fig. 3.12), probably due to the excellent cleavages in feldspars which promote fracturing (Yund et al., 1990; Tullis and Yund, 1992, 1987).

The development of incipient slip zones can be observed in low shear strain ($\gamma \sim 1.5$) samples in regions with high amounts of fine-grained material. The slip zones always cut original R_1-Riedel shears at a more shear zone boundary parallel orientation. The development of slip zones is probably caused by the fact that R_1-Riedel shears are thought to be short-lived, either due to strain hardening or because they are poorly oriented for continued slip (Byerlee, 1978).

In our samples, there is porosity collapse and thus a thinning of the shear zones from ~ 1 to 0.7 mm. R_1-Riedel shears accommodate part of the shear zone thinning, and in fully compacted shear zones, the more shear zone boundary-parallel orientation of the slip zones is a geometrically more compatible way for the imposed sample kinematics, so that the slip zones overprint R_1- Riedels after compaction. At shear strains $\gamma > 2$ slip zones are well developed

and deformation localizes in these slip zones which accommodate larger amounts of shear strain ($\gamma \geq 10$). At higher confining pressures the dominant slip zone orientation is generally more shear zone boundary parallel compared to the lower confining pressure experiments, which is consistent with the lower observed coefficient of friction (Fig. 3.6) and is probably caused by the enhancement of mode II/III cracks relative to mode I cracks during slip zone formation.

The material in the slip zones has a very homogenous appearance even at the highest magnifications in both BSE and SE images, shows changes in chemical composition of feldspars (enrichment in K and Ca) and has a lower atomic bonding strength (evaporation of Na). The amount of this material, in which individual particles or porosity cannot be resolved in the field emission SEM, increases with increasing shear strain and confining pressure (e.g. Figs. 3.13b,c,d and 3.14). Thus, it shows an opposite trend as the fine-grained but resolvable material. A sketch of the development of the S-C' fabric is shown in Fig. 3.18.

Previous studies performed on fine-grained gneiss in the viscous regime show that strain localization in C' shears is favored if stress concentrations are caused by adjacent weak phases (i.e. on mica tips favorably oriented for the easy slip (001)) and the contrast between the weak and strong phases remains high (Holyoke and Tullis, 2006b,a). Further, micas enhance diffusion rates (Farver and Yund, 1999; Wheeler, 1992), which may contribute further to weaken the slip zones. Such diffusion-accommodated processes indicate a contribution of non-frictional processes to deformation. The origin of the observed changes in chemical composition in the slip zones as well as fragmented mantles is discussed in section 3.5.4.

3.5.3 Effect of added water

Previous studies of frictional strength of granitoid gouges under lower confining pressures (250 – 400 MPa) (Lockner et al., 1986; Blanpied et al., 1991, 1995, 1998) defined two distinct sliding regimes. In the first regime the coefficient of friction is high ($\mu \sim 0.7 - 0.8$) and depends only modestly on temperature, slip rate, or pore pressure. This regime comprises "dry" granite in the temperature range between 22°C to at least 845°C and "wet" granite up to ~ 300°C. A second regime was observed only in samples of "wet" granite (pore pressure of 100 MPa) at temperatures above ~ 350°C where μ markedly decreased with increasing temperature and decreasing slip rate showing "viscous" behavior (i.e., dependent on slip rate and temperature). However, as the effective normal stress was held constant (300 MPa) by adjustment of the confining pressure in experiments performed by Blanpied et al. (1995), it is unclear whether the samples would display a "frictional-viscous" behavior (dependent both on normal stress as well as slip rate and temperature). Blanpied et al. (1995) speculate that the observed strength dependence on temperature is caused by dissolution-precipitation creep, but they did not report any observational evidence for it.

In our experiments, drying of the samples at 200°C for 24 hours (and welding the jacket within 10 min after removing them from the furnace) is expected to remove free water. However, the dried gouge shows a similar behaviour as samples with 0.2wt% H_2O added (Fig. 3.3). This observation indicates that the addition of 0.2wt% water to the gouge does not introduce pore pressure. We did not detect any systematic changes on the resulting microstructure in the monitored quantitative parameters, which could be related to the amount of added water. Keulen et al. (2007) point out that the effect of added water on grain size distributions (GSD) is either unsystematic or not existent, which is in accord with our observations. Thus, the
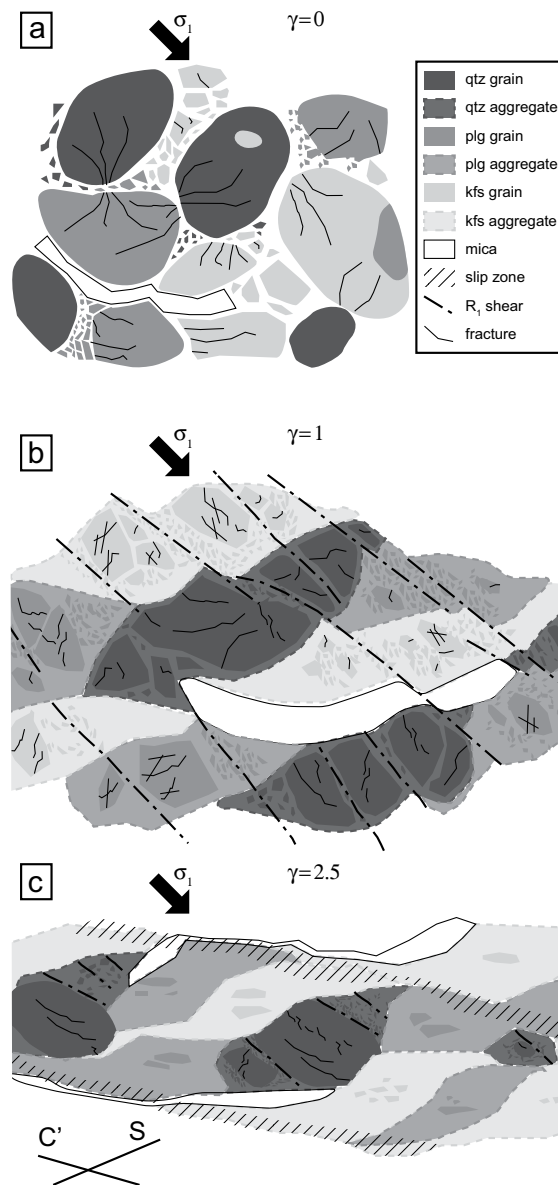
Figure 3.18: Schematic drawing of S-C' fabric development in the experiments. a) Starting material. Grains fracture along Hertzian fractures producing finer grain size and reducing porosity. b) Low shear strain. The sample is pervasively cross-cut by closely spaced R_1 Riedel shears offsetting initial grains. c) High shear strain. Aggregates of feldspars rotate antithetically, have a higher anisotropy and a monoclinic asymmetry. Almost no survivor grains or R_1 Riedel shears can be identified in feldspars. Through going slip zones develop predominantly in the feldspar material and often contain micas.

amount of water necessary for the temperature weakening mechanism must be small and is contained in the starting material in the form of fluid inclusions, micas, and adsorbed H_2O not removed by drying at $200°C$.

3.5.4   Changes of chemical composition

3.5.4.1   Chemical changes in the fragmented mantles

EDX maps show that fragmented feldspar mantles undergo chemical changes in the Ca-, Na- and K- content. Plagioclase in the starting material is mostly oligoclase (93%) with minor albite grains and rims (7%). More anorthite-rich and pure albite compositions are usually separated by sharp boundaries within single grains (Fig. 3.9b). Most grains in the starting material show a homogenous oligoclase composition (Figs. 3.9, 3.15). The plagioclase in the starting material does not contain K and the K-feldspar does contain only trace amounts of Na and Ca. In the high strain samples, albite is observed preferentially in strain shadows (low pressure sites) and we observe gradual changes in Ca/Na and Al/Si ratios within an aggregate derived from a single grain (Fig. 16b,c). These changes affect larger areas compared to the starting material and low strain samples.

Three possible explanations arise; a) either the feldspar mantles mechanically mix or b) they change their chemical composition by diffusion or c) dissolution-precipitation. Mechanical mixing on the aggregate-to-aggregate contacts was never observed in the BSE images due to the low relative displacements. Coupled diffusion of NaSi $\leftrightarrow$ CaAl in feldspar is extremely slow (Yund, 1986) and will not produce the observed compositional differences on a several μm-scale at $300°C$ to $500°C$ within the short duration of the experiments (~ 3 hrs). Therefore, dissolution-precipitation seems to be the most likely process to cause the change in the Na/Ca ratios (Dolejs and Wagner, 2008) of strained feldspar mantles. The regions containing more albitic feldspar (redish colors in Fig. 3.16) correlate with highly fragmented regions. The area affected by these changes increases with increasing finite shear strain (oligoclase $\sim 91\%$, albite $\sim 9\%$ at $\gamma \sim 2.5$ compared to oligoclase $\sim 93\%$, albite $\sim 7\%$ in the starting material) and temperature and the change in composition seems to be somewhat more gradual compared to the starting material. However, the small change in the relative percentage might reflect variations in the starting material composition from one experiment to another.

Despite the changes in mineral composition, it is interesting to note that "healing microstructures" (Keulen et al., 2008; Tenthorey and Cox, 2006) which are thought to be typical for dissolution- precipitation creep (i.e., lobate, interconnected grain boundaries) were not observed in the fragmented mantles. However, as mentioned above, grain shapes are impossible to resolve in large volumes of extremely fine-grained fragmented mantles. Clear evidence for the operation of dissolution-precipitation processes are fine Fe-rich seams (thickness of ~ 0.1 μm), which are found preferentially on contacts between feldspars or quartz-feldspar contacts in the gouge, adjacent to as well as in the slip zones (Fig. 3.14c,d). These observations suggest that incongruent pressure solution of feldspars takes place in the fine-grained fragmented mantle because feldspars contain trace amounts of Fe which is immobile (e.g. Dolejs and Wagner, 2008) and will be left behind at high-pressure sites.

3.5.4.2 Chemical changes in the "amorphous" slip zones

The "amorphous" feldspar material has a clearly different composition (enrichment in Ca and K) than survivor grains or fragmented mantles providing evidence that the changes in chemistry are coupled to deformation (Fig. 3.16b,c,e). Furthermore, the preferential evaporation of Na from this material suggests a lower bonding energy of Na atoms in the "amorphous" material compared to still crystalline material.

3.5.5 Nature of the material with "flow" structures

One of the most peculiar features is the presence of material showing "flow" structures (Figs. 3.14 and 3.15) in the slip zones, irrespective of the confining pressure, temperature, or added water. The material is mostly formed of both feldspars. Unloading cracks concentrate in this material and terminate at their boundaries (Figs. 3.14b,c,d and 3.15c,d). Fitz Gerald et al. (1991) and Stünitz et al. (2003) have shown that if permanent plastic deformation has occurred in a material adjacent to the same material which is only elastically deformed, then unloading of the samples forms unloading cracks in the permanently deformed material, because it becomes extended by the release of elastic strain in the neighboring material. As we can resolve grain sizes of ~ 50 to 100 nm (ca. $100 - 200$ unit cells in diameter) in fine-grained fragmented matles but such grains are absent in the "flow" structures, we are left with three possible explanations for the origin of the "flowing" material in the slip zones: (1) the material in these zones is still composed of individual grains with a smaller grain size than $50 - 100$ nm, (2) the material formed due to frictional melting and represents a pseudotachylite senso stricto, and (3) the material has lost its long-range order, i.e. is amorphous

We consider the first possibility unlikely because of the homogeneous appearance of the flowing material in both BSE (Figs. 3.14c,d and 3.15c,d) and SE images. The second possibility is also unlikely because the melting of granite at the experimental conditions would require a significant increase in temperature to $\sim 700°$C. In addition, the shear strain rates estimated in the slip zones are at the very most $\sim 10^{-3}$ s^{-1}, which is not a seismic deformation rate. We strongly favor the last possibility because amorphous material is expected to behave as a single, permanently deformed volume of material and unloading of the fragmented gouge is expected to cause unloading cracks to form in the "flow" structures, if these are amorphous (Figs. 3.13b,c,d and 3.14c,d).

The presence of silica "gel" in fast, "room-dry" friction experiments on quartzite has been described by Goldsby and Tullis (2002) and Di Toro et al. (2004). They propose that the gel forms due to "solid state amorphization" in the presence of moisture. Another, more relevant, study for our work is by Yund et al. (1990), who performed an extensive TEM study on Westerly granite gouges from high strain ($\gamma \sim 120 - 4800$) rotary friction experiments under low normal stresses ($50 - 75$ MPa) (and isotropic confining pressures of ~ 21 MPa) at room temperature, with and without water added. They observed large amounts of amorphous material ($\sim 5 - 60\%$) in all experiments with a composition commonly between K-rich and Na,Ca-rich feldspars even though some portions were silica rich. The amount of the amorphous material in their experiments increased with increasing average shear strain and at higher shear strains, only quartz formed crystalline fragments embedded in an amorphous matrix of feldspar composition. Yund et al. (1990) convincingly argued that the amorphous material did not form by frictional melting but by comminution of mostly feldspar grains. Furthermore,

they detected large amounts of amorphous material in both water added as well as dried samples arguing that if water is necessary for the formation of the "gel" its concentration must be low (for an extensive discussion and review about this amorphous material refer to Yund et al., 1990 and Ozawa and Takizawa, 2007).

The above-described observations are strikingly similar to our observations on the SEM scale (i.e., variable feldspar composition of the "flowing" material, its formation in both dried as well as water added experiments, a distinct trend in comminution (Vs/Va ratio) between feldspars and quartz (Fig. 12), lower bonding energy of Na in the "flowing" material). Yund et al. (1990) as well as Goldsby and Tullis (2002) further suggest that large displacements are necessary before the amorphous material can be detected ($\gamma \sim 120$). However, in our experiments the possibly amorphous slip zones form at bulk shear strains of $\gamma \sim 2$ and the estimated shear strains accommodated within the slip zones is roughly $\gamma \sim 10$. The amount of the "flowing" material seems to increase with increasing confining pressure as well as temperature.

Ozawa and Takizawa (2007) have identified amorphous material in natural fault rocks, indicating that amorphization is not only a lab peculiarity but may have important implications for the behaviour of natural fault rocks. Intergranular fracturing of grains requires by definition the breakage of atomic bonds and becomes increasingly difficult with the decreasing size of the grains due to smaller flaw sizes, flaw densities (Prasher, 1987) and due to the difficulty to built up large enough deviatoric stresses to break atomic bonds in small grains. This is thought to cause the so-called "grinding limit" which was estimated from grain size distribution (GSD) kink by Keulen et al. (2007) to be ~ 1 μm for quartz and ~ 2 μm in feldspars. These values are in good agreement with our qualitative observation that smaller grains than 1-2 μm never have transgranular cracks (e.g. Fig. 13c). Further grain size reduction to nanometric grains is thought to be achieved by shearing and attrition (Keulen et al., 2007). The smallest observable grains in experimentally produced as well as natural fault rocks are on the order of 10-100 nm (roughly 20-200 unit cells in diameter) (i.e., Ozawa and Takizawa, 2007; Keulen et al., 2007; Wilson et al., 2005; Yund et al., 1990; Olgaard and Brace, 1983; this study). We do not have the data so far to speculate whether a continuous decrease in grain size leads to amorphization or whether amorphization takes place at some threshold grain size. The processes responsible for amorphization are not well understood.

3.5.6 Cause of strength dependence on temperature

Samples deformed at 500°C are systematically weaker than those deformed at 300°C over a range of confining pressures (500, 1000 and 1500 MPa). A similar strength dependence on temperature is observed in experimental studies performed on granites in a gas deformation apparatus (Blanpied et al., 1995, 1998) as well as a solid medium apparatus with different confining media (NaCl – Keulen et al., 2007; NaCl and pyrophyllite – Tullis and Yund, 1980; NaCl and KI – this study). These results clearly demonstrate that the strength dependence on temperature is material dependent and is not caused by the different apparatus used (i.e., different strength of the confining media at different temperature).

More recent work on analogue materials (halite / kaolinite mixtures and halite / muscovite mixtures), (Niemeijer and Spiers, 2006; Bos and Spiers, 2001, 2000; Bos et al., 2000a) has documented the operation of pressure solution in concomitance with cataclasis leading to a "frictional-viscous" behavior (i.e., normal stress as well as rate dependence) which changes to purely frictional behavior (only normal stress dependent) if an inert fluid (oil instead of brine)

or inert solid (Qtz instead of halite) are used. They further demonstrate the necessary presence of phyllosilicates for the frictional- viscous behavior and argue that phyllosilicates inhibit healing of halite-halite contacts (thus re-strengthening of the gouge) and form a through-going zone of easy slip.

"Viscous" mechanical behavior was documented by Blanpied et al. (1995) for "wet" granites under lower normal stresses ($\sigma_{eff} = 300$MPa) above $\sim 350°$C, indicating that possibly these mechanisms operate in granitoids. However, the reached shear strains are low in the experiments conducted by Blanpied et al. (1995) and Blanpied et al. (1998). Judging from the published optical microstructures, no through going zone of phyllosilicates has developed, similarly to our experiments. Furthermore, in experiments using granitoids at higher confining pressures (> 500MPa) where the temperature effect can be observed, varying of the bulk shortening rate between 10^{-4} s^{-1} and 10^{-6} s^{-1} shows "no mechanical effect" on the strength of granites (Keulen et al., 2007). However, the reproducibility of these experiments is not as good as in shear experiments on gouge because of the variable orientation and number of fault surfaces.

Here, we summarize the main characteristics of the samples and put some constrains on the possible mechanism(s) responsible for the temperature effect.

1. Similar amounts of comminution between samples deformed at 300°C and 500°C (V_s / V_a ratio)

2. The strength difference between 300°C and 500°C samples does not systematically increase with increasing confining pressure (it is $\sim$ 200-300 MPa shear stress for all confining pressures).

3. The strength difference between 300°C and 500°C samples is not affected by the amount of water added (dried experiments at 200°C for 24 hours vs. up to 0.2 wt% H_2O added)

4. A positive dependence of the peak strength on confining pressure can be detected.

Blanpied et al. (1998) point out the lack of understanding of underlying physical and chemical processes responsible for the strength dependence on temperature and presumes that the underlying processes include subcritical crack growth, crystal plasticity, diffusion and/or fluid-mineral interactions. We will discuss these points and indicate some additional possible mechanisms below.

3.5.6.1 Subcritical crack growth

As we did not detect any systematic differences in the amount of comminution between 300°C and 500°C in the monitored parameters, we conclude that subcritical crack growth is not responsible for the observed strength dependence on temperature. Fracturing occurs in all experiments and frictional behaviour will be an important factor influencing the mechanical data due to the necessity to slide newly formed grains past each other.

3.5.6.2 Crystal plasticity

Tullis and Yund (1977) have found that crystal plasticity is very limited in "dry" Westerly granite at $300°C$ and 1000 MPa confining pressure and axial strain rates of 10^{-6} s^{-1} and Tullis and Yund (1980) found that the same is true for "wet" Westerly granite deformed at identical temperatures and strain rates but at 1500 MPa confining pressure. Tullis and Yund (1992) have not found any evidence for dislocation multiplication or glide in anorthosites deformed between 300-500°C at 1000MPa confining pressure and axial strain rates of 10^{-6} s^{-1}. Hirth and Tullis (1994) have documented the increase in dislocation activity in non-porous quarzites crossing the brittle-plastic transition at similar experimental conditions to ours. As quartz is always the strongest phase in all samples and because feldspars do not deform by purely crystal plastic processes at $900°C$ and axial strain rates of 10^{-6} s^{-1} (Stünitz et al., 2003), we infer that crystal plastic processes are not responsible for the observed strength dependence at the low temperatures and high strain rates of the experiments. Furthermore, purely crystal plastic deformation in quartz shows a negative strength dependence on confining pressure in the presence of H_2O (Stünitz et al., 2003; Kronenberg and Tullis, 1984) due to the inferred increase in water fugacity (e.g., Tullis and Yund, 1992; Hirth et al., 2001). There is a small positive strength dependence with increasing confining pressure observed in our experiments (Fig. 3.3).

3.5.6.3 Dissolution-precipitation creep

We have observed changes in feldspar composition, which are related to deformation, affecting relatively large areas of the fragmented mantles and fine Fe-rich seams (e.g. Fig. 3.14c,d) on phase contacts in feldspars. Feldspars are the weaker phase than quartz, and we believe that differences in chemical reaction and solution/precipitation rates at $300°C$ and $500°C$ are a likely reason to explain a part of the observed strength dependence on temperature. It has been noted above that material transport in dissolution-precipitation creep is inferred to have been active on a small scale but it affects large areas. It is interesting to note that the chemical changes occur also in dried samples, indicating that the amount of water necessary to enable dissolution-precipitation must be small. Given the extremely small grain size of the fragmented mantles (< 100 nm) it is likely that dissolution- precipitation creep is active.

The short duration of the experiments (~ 3 hrs) makes extensive solution/precipitation creep unlikely, as demonstrated by the absence of typical microstructures. It is more likely that the effect of reaction rates at the different temperatures takes place on a small scale and its effect is limited. Dissolution-precipitation creep, together with fracturing, will help to accommodate geometrical incompabilities imposed by the sample geometry in the less deformed lenses delimited by through going slip zones. The more important effect is to be expected from the formation of the amorphous material in the slip zones, which will be considered below.

3.5.6.4 Influence of "amorphous" material

It is inferred above that the material with "flowing" structures is probably amorphous and constitutes the weakest phase of the deforming gouge, because deformation localizes in the slip zones, which cross-cut the whole sample and where this material is abundant. Thus, it will have a pronounced effect on the mechanical behavior as an interconnected weak layer

(Holyoke and Tullis, 2006a; Handy, 1994). One of the fundamental properties of amorphous material is that it shows elastic resistance to shearing stress and intrinsically has an elastic-plastic behaviour. Thus, when shear stress is applied to amorphous material, it responds with macroscopic viscous flow. Viscous flow of, e.g., glass shows a strong temperature dependence (Hess et al., 2001, 2008; Dingwell et al., 1998) which may explain the observed strength difference over the range of confining pressures. Furthermore, amorphous material is very reactive (i.e., Yund et al., 1990) which is documented by the high mobility of alkalis in this material (Fig. 3.16b,c), and lower atomic-bond energies. It has been noted above that intermixing of fine grains might cause the change of the composition, however we find this possibility unlikely because a) in high- resolution BSE images we observe fine layering of individual mineral phases (e.g. Figs. 3.14d and 3.15d), but never find any evidence for intimate intermixing and b) we observe a homogenous chemical composition within the slip zones. The change in composition is evidence for either solution/precipitation, or other diffusion-accommodated mass-transfer process in the "flowing", probably amorphous, material.

3.5.7 Implications for natural fault zones

Byerlee's rule (Byerlee, 1978) is widely used for estimating crustal strength in the brittle regime because of its independence on material parameters and exclusive dependence on normal stress (e.g. Kohlstedt et al., 1995). Further studies lead to the development of rate-and-state dependent friction laws (i.e., Dieterich, 1978, 1979; Ruina, 1983) which explain the apparent stick-slip behaviour in laboratory and are thought to model the nucleation and propagation of earthquakes in nature as well. However, many of the largest earthquakes on continental faults occur at the bottom of the seismogenic layer between 10-20 km in the "brittle-to-plastic" transition zone. It is widely acknowledged that rocks under these conditions deform by semi-brittle flow where the displacement is not accommodated on a single sliding fault plane, but is achieved by repeated distributed fracturing of the country rocks and gouge. Byerlee's rule, by definition, will no longer be valid at the brittle-ductile transition where the strength of the country rocks equals the strength of pre-existing faults. This occurs in laboratory conditions below 500 MPa confining pressure (< 14 km depth) (e.g., Keulen et al., 2007; this study). However, scaling problems arise because it is widely known that mm to cm-scale laboratory samples have a significantly higher fracture strength than m to km-sized samples (i.e., Shimada, 1993; Ohnaka, 1995, 2003; Kohlstedt et al., 1995).

It is difficult to extrapolate laboratory data on maximum compressive strength of rocks to natural faults. However, the transition to semi-brittle flow in granites must take place at the very deepest around ~ 14 km depth (500 MPa confining pressure), where, e.g., quartz will deform by dislocation creep at $\sim 300°C$ (e.g. Stipp et al., 2002a,b; Jerabek et al., 2007). Friction as a contact property requires a fracture plane, which has to be formed by shear fracture. Thus, unifying of frictional strength with shear fracture strength (Ohnaka, 1995, 2003; Ohnaka et al., 1997; Odedra et al., 2001; Kato et al., 2003) truncates the sharp brittle-plastic transition assumed in traditional rheological profiles, providing a more realistic model for the strength of the lithosphere in the brittle-to-plastic transition zone (e.g. Fig. 3.1b)

Furthermore, dissolution-precipitation processes play an important role under the "hydrothermal" conditions occurring at the hypocentral conditions of large earthquakes and in experiments (Niemeijer et al., 2009, 2008b,a; Niemeijer and Spiers, 2007, 2006; Bos and Spiers, 2001, 2000; Bos et al., 2000a; Blanpied et al., 1995, 1998; Keulen et al., 2008; Chester and Higgs, 1992; Evans and Chester, 1995; Chester et al., 1993; Chester and Chester, 1998; Chester and

Logan, 1987; Imber et al., 2001; Stewart et al., 2000; White, 2001). The effect of dissolution-precipitation processes on fault strength is critical – it may lead to re-strengthening of fault rocks on a time scale of a couple years to a couple of tens of years (Keulen et al., 2008) or it may accommodate significant displacements and weaken the fault by low temperature viscous creep processes. These will be enhanced by the intermixing of minerals and by the amount of available fine-grained material (Wheeler, 1992; Gratier et al., 1999; Renard et al., 2000), as we see in natural samples (e.g. Keulen et al., 2007). Our study demonstrates that even at fast rates of displacement, the strength of granitoid gouge is temperature dependent, probably as the result of dissolution-precipitation and - more importantly - flow processes in feldspar material, which most likely is amorphous.

The development of rheological profiles which take into account "frictional-viscous" behavior in the depths between 5-20 km (Bos and Spiers, 2002b) combined with rheological profiles taking into account the maximal compressive strength of rocks at the "brittle-to-plastic" transition regime is necessary in order to develop more realistic rheological profiles. In the light of the above-mentioned arguments, it is questionable whether rate-and-state dependent friction laws as well as Byerlee's rule can be extrapolated to the semi-brittle regime. Models which extrapolate Byerlee's rule to depths > 15 km therefore seem unrealistic.

3.6   Conclusions

We performed a series of general shear experiments on granitoid rocks under high confining pressures (500 MPa, 1000 MPa and 1500 MPa) and temperatures (300°C and 500°C) at mean shear strain rates of $1.2 - 3 \times 10^{-4}$ s^{-1}. Under the chosen experimental conditions feldspars constitute the weak phase and quartz is the strongest phase. All samples develop a S-C' fabric and we observe the development of most likely amorphous material, consisting mostly of feldspar with an intermediate composition (containing Na,Ca and K) in the C' slip zones. These zones develop even at low bulk finite strains ($\gamma \sim 2$). The formation of this material is favored by higher confining pressures and it always constitutes the weakest phase forming an interconnected weak layer. All samples, irrespective of temperature show changes in feldspar compositions that can be clearly related to deformation. We infer that dissolution-precipitation processes must have been active in the fine grained fragmented mantles thus providing further evidence that fracturing enhances reaction rates and promotes viscous deformation processes even at short laboratory timescales (~ 3 hours). We observe a systematic strength dependence on temperature and infer two most probable mechanisms, which act simultaneously with fracturing: (1) viscous flow accompanied by mass-transfer processes of probably amorphous material in the slip zones (2) dissolution-precipitation in the fragmented mantles. Both contribute to frictional deformation causing semi-brittle flow of granitoid gouge.

Origin of Pseudotachylites in Slow Creep Experiments

Abstract:

We conducted a series of experiments on granitoid cataclasites under mid-crustal conditions (Pc $\sim$ 500 MPa, T = 300°C) and slow displacement rates (10^{-8} ms^{-1} < $\dot{d}$ < 10^{-7} ms^{-1}) i.e. within an order of magnitude of plate tectonic velocities. The samples reach high peak strength (1250 < τ < 1375 MPa) then weaken slightly (by $\sim$ 40 MPa) and continue to deform without any abrupt stress drops up to a γ of $\sim$ 4. Microstructural observations show, that at peak strength nanocrystalline (mean grain size $\sim$ 34 nm, smallest crystalline particles $\sim$ 8 nm) to partly-amorphous material develops. Weakening occurs once this material is abundant enough to form through going anastomozing slip zones where the strain partitions. During higher strain deformation, deformation localizes further and 1 to 2 multiply connected layers of fragment loaded amorphous material develop. This material shares many similarities with naturally occurring pseudotachylites, however was formed at velocities up to 9 orders of magnitude slower than those calculated for earthquakes ($\sim$ 1 ms^{-1}). We conclude that the use of pseudotachylites as indicators for paleoseismic events should be reconsidered.

4.1 Introduction

Natural pseudotachylites are dark, aphanitic rocks which occur as fragment-loaded dikes and networks and are associated with large landslides, impact craters (impact pseudotachylites) (Reimold, 1995; Melosh, 2005) and exhumed fault zones from the uppermost crust to the uppermost mantle (tectonic pseudotachylites) (e.g Sibson, 1975; Cowan, 1999; Spray, 2010; White, 2012; Andersen and Austrheim, 2006; Ueda et al., 2008; Austrheim and Boundy, 1994; John et al., 2009).

On the microstructural scale, pseudotachylites consist of a more or less amorphous matrix (often devitrified) which supports clasts from the host rock. The matrix typically has a non-equilibrium composition which usually is more ferromagnesian and less silicic than the country rock (e.g. Di Toro and Pennacchioni, 2004; Ferré et al., 2012). Further microstructural characteristics used to identify natural pseudotachylites are flow structures, amygdales (bubbles), injection veins, color banding ("quenched margins") and embayed clasts surrounded by a thin layer of different material ("corroded clasts") (e.g. Kirkpatrick et al., 2009; Price et al., 2012). Pseudotachylites are associated with intense comminution, which seems to be a necessary precursor for their formation (Spray, 1995, 2010). Detailed studies also reveal the presence of both extremely fine grained as well as fully amorphous matrix within one pseudotachylite system (Wenk et al., 2000) and characteristic crystal-plastic deformation associated with mid- to lower-crustal pseudotachylites (Wenk, 1978; Bestmann et al., 2011, 2012; White, 2012).

Today, a majority of geologists agree with the interpretation that pseudotachylites represent frictional melts despite a long-standing controversy whether pseudotachylites are the product of comminution (Weiss and Wenk, 1983; Wenk, 1978; Janssen et al., 2010) or frictional melting (Spray, 1987, 1995, 2010). Therefore, it is believed that tectonic pseudotachylites can form exclusively as high temperature friction-induced melts during earthquakes (e.g. Cowan, 1999).

In the laboratory, frictional melting is successfully produced in high velocity friction experiments (HVFE) which involve high velocity motion (on the order of 1 ms^{-1}) on a surface (e.g., Hirose and Shimamoto, 2005; Di Toro et al., 2006, 2011; Niemeijer et al., 2011; Spray, 1987, 1995, 2010). HVFE are typically performed unconfined at ambient temperatures, low uniaxial normal stresses ($\leq$ 50 MPa), and to large displacements (typically $>$ 0.5 m).

A fundamental pre-requisite for the production of frictional melts is thought to be a large mechanical work rate, q = τ V, where τ is the shear stress and V is the sliding velocity, so that the work exchanged on the surface results in a temperature increase and is not buffered by dissipative processes (Di Toro et al., 2011). Results from these experiments suggest that frictional melting is a self-limiting process (i.e. the thickness of the frictional melt layer reaches a steady state) and the presence of frictional melt "lubricates" the fault causing very low friction resistance. Frictional melts have been reported in a few studies carried out using a triaxial apparatus and high confining pressures (Koizumi et al., 2004; Onuma et al., 2011; Beeler et al., 2011). They are associated with stick-slip events which are characterized by abrupt displacements accompanied by significant stress drops which, however, recover promptly. The amount of "melt" generated under these conditions seems to be correlated to the magnitude of both, the stress drop and the displacement. Direct measurements of the temperature increase in stick-slip experiments are lacking due to technical difficulties.

Points of argument among geologists discussing the significance of pseudotachylites found along faults are (a) whether the amorphous material in the pseudotachylite has been formed

by a melting process and (b) how the necessary melting temperature can be achieved and maintained in the fault.

One of the fundamental parameters needed to constrain the shear stress during an earthquake from the volumes of pseudotachylites is the temperature of the melt, T_{melt} (e.g. Di Toro and Pennacchioni, 2004). As the amorphous matrix does not have a eutectic melt composition it is believed that the melt forms from a local chemical environment within seconds so that the heat is not conducted away from the fault (e.g. Spray, 2010). To estimate the T_{melt}, bulk equilibrium melting temperatures of individual minerals forming the amorphous matrix are commonly used (melting point of biotite $\sim 850°C$, feldspars $\sim 1100 - 1500°C$, quartz $\sim 1730°C$). If natural pseudotachylites represent frictional melts, they can be used to constrain the seismic source properties not accessible by geophysical methods (e.g. Wenk et al., 2000; Di Toro et al., 2005; Niemeijer et al., 2012).

In this contribution, we report the formation of amorphous material during slow creep experiments at mid-crustal conditions, discuss the similarity of this material to naturally occurring pseudotachylites and discuss possible mechanisms responsible for their formation.

4.2 Experimental and analytical methods

4.2.1 Experimental strategy and set-up

In order to investigate the processes occurring at the base of the seismogenic layer we have designed our experiments such that they simulate conditions in the earth's crust where: 1) ambient temperature rises with increasing depth, 2) isotropic confining pressure rises with increasing depth, and 3) geological displacement rates are slow (plate tectonic velocities $\sim 1 - 10$ cm/year). We have used a tri-axial solid medium deformation apparatus (modified Griggs rig) to carry out general shear experiments on granitoid fault rocks. Samples were deformed at confining pressures of Pc ~ 500 MPa, corresponding to a depth of $15 - 20$ km, at elevated temperatures of T = $300°C$ over extended periods of time (hours to days) at displacement rates of $\sim 10^{-8}$ ms$^{-1} < \dot{d} < 10^{-7}$ ms^{-1} corresponding approximately to $30 - 300$ cm/year.

4.2.2 Sample preparation and experiment execution

To produce the fault rock material, a fine-grained granitoid sample from the Val Verzasca (for coordinates see Keulen et al., 2007) is crushed and sieved. 0.1 g of the size fraction ≤ 200 μm in diameter (composition see Tab. 4.1), with 0.2 μl (0.2 wt%) H_2O added is placed between alumina forcing blocks pre-cut at $45°$. This assembly is then weld-sealed in a platinum jacket with an inner nickel foil insert (Fig. 4.1). The Val Verzasca granitoid has been used in previous studies, the mechanical data as well as the microstructural characteristics of both intact and fragmented material are well known (Heilbronner and Keulen, 2006; Keulen et al., 2007, 2008; Stünitz et al., 2010; Pec et al., 2012a).

To start the experiment, the confining pressure piston is advanced leading to salt collapse around the sample building up the confining pressure. Heating is achieved using a graphite resistance furnace in $100°C$ steps at a rate of $20°C$/min. Temperature is controlled by a

proportional-integral-derivative controller (Eurotherm) attached to a K-type thermocouple touching the centre of the shear zone (Fig. 4.1). Potassium Iodide with a melting point of 681°C at atmospheric pressure was used as a confining medium because its flow stress is $\sim 3\times$ lower (at room temperatures) than that of the commonly used NaCl (Inoue, 1957) giving a superior stress resolution. Using two thermocouples, a temperature gradient of ~ 20 °C from the center of the shear zone to its tips is measured. Heat conduction in the sample assembly is high ($\sim 5 \times 10^3$ °Cm^{-1}): turning off the furnace causes a temperature decrease from 300°C to ~ 30°C in less than 30 seconds.

After reaching the desired experimental conditions (Pc ~ 500 MPa, T $= 300$°C, typically after ~ 5 hours), the sample has reached a starting thickness, th$_0$, of ~ 1 mm (measured in post-run thin-sections). The σ_1 piston is advanced with a displacement rate of $\sim 10^{-8}$ ms^{-1} $< \dot{d} < \sim 10^{-7}$ ms^{-1}. Vertical displacement of the σ_1 piston is measured with two external devices: a direct current displacement transducer (DC-DT, resolution ~ 1 μm) and a noiseless digital linear transformation measurement (LTM) system (resolution $= 0.1$ μm). The axial force is measured with an external force cell, and the confining pressure is measured via the oil pressure in the hydraulic pumping system.

At the end of the experiment, the samples are quenched to 200°C in 1.5 minutes (1.1°C s^{-1}) while simultaneously removing the load. The temperature is then lowered to the temperature of the cooling water (~ 14°C) within $\sim 10 - 30$ minutes after quenching. During depressurization an axial stress of ~ 100 MPa is kept on the sample to minimize unloading cracks.
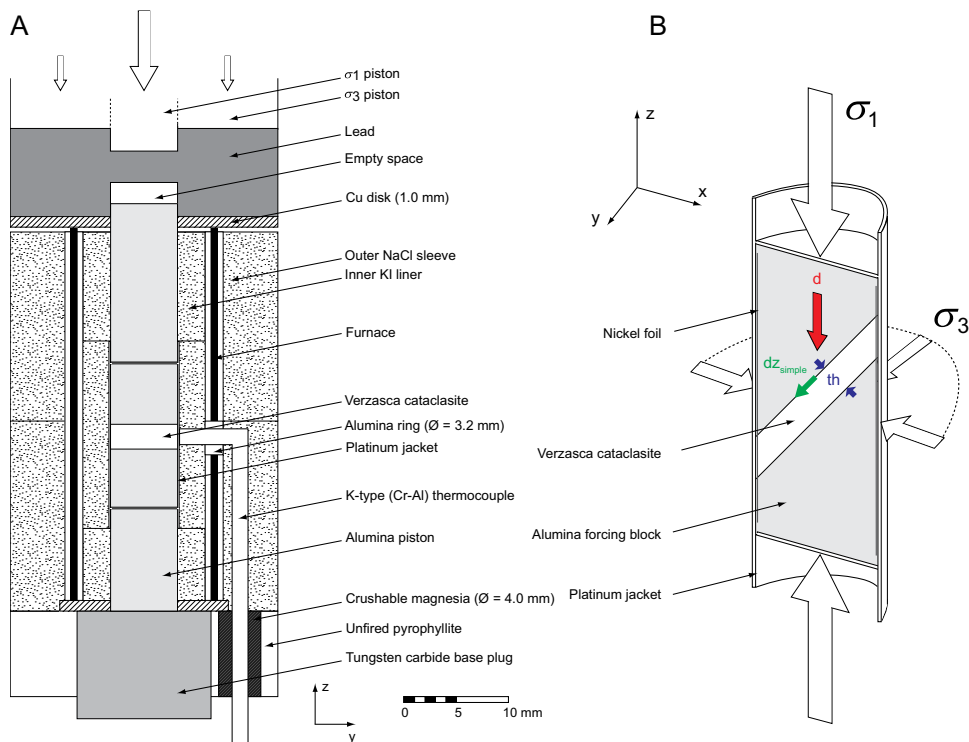
Figure 4.1: Sample assembly. A) Sample assembly and B) sample used for experiments, d = vertical displacement, th = shear zone thickness, dz$_{simple}$ = simple shear component. (Modified after Tarantola et al., 2010)

(wt%)	starting material	Bt	Kfs	Plg	Wm	Bt-AM	Fsp-AM	Wm(?)-AM
SiO_2	77	40.6	65.0	63.8	53.5	51.3	67.7	63.9
Al_2O_3	13.3	17.7	18.5	22.6	30.9	22.1	20.2	20.9
Na_2O	3.2	3.1	1.1	10.9	0.6	2.1	5.5	1.3
K_2O	4.6	7.3	15.4	0.0	10.4	7.4	2.8	8.7
CaO	1	0.0	0.0	2.7	0.0	0.7	2.3	0.5
MgO	< 0.1	8.3	0.0	0.0	1.0	3.5	0.6	1.1
Fe_2O_3	0.64	21.0	0.0	0.0	3.1	11.8	0.4	3.2
TiO_2	0.1	2.0	0.0	0.0	0.0	1.1	0.4	0.5

Table 4.1: Bulk chemical composition of the starting material powder (obtained by XRF), and typical compositions of individual constituent minerals of the Verzasca Gneiss and AM (obtained by EDS). Bt – biotite, Kfs – potassium feldspar, Plg – plagioclase, Wm – white mica, AM – amorphous material.

4.2.3   Data acquisition and treatment

Confining pressure, force, and displacement are recorded in parallel with an analogue chart recorder (sampling frequency 50 Hz) and a digital data-logging system (LabView 7.1) with a sampling frequency of 1 Hz (1 record point equals 0.1 or 0.01 μm of vertical piston displacement depending on the applied displacement rate). The data are evaluated with a MATLAB program ("rig", http://sites.google.com/site/rigprogram), a representative record of a complete experiment is shown in Fig. 4.2. The mechanical data are then corrected for decreasing forcing block overlap with increasing slip, for apparatus compliance (5.0486×10^{-3} mm/kN), changes in the confining pressure relative to hit-point (± 10 MPa, i.e. $\sim 4\%$) and for "friction" associated with driving the tungsten carbide piston into the sample assembly (1.3 kN/mm) (Tarantola et al., 2012).
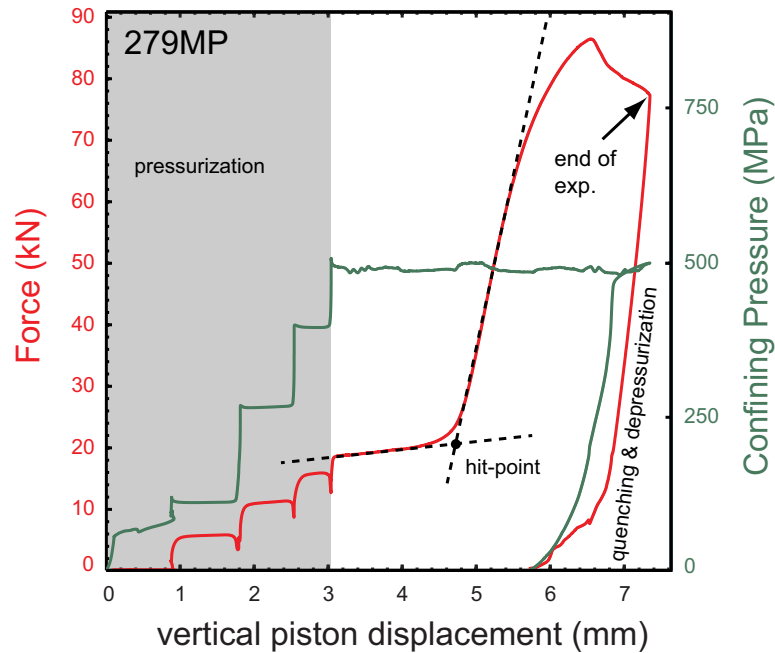
Figure 4.2: Mechanical data. Representative force (red) and confining pressure (green) vs. vertical piston displacement record from one experiment. The small stick-slip events (< 0.4%) cannot be resolved at this scale.

During deformation, the thickness, th, of the cataclasite layer decreases continuously down to $\sim 50\%$ of its original thickness, th_0 (as measured in thin section of over 70 experiments quenched at different finite strains). Therefore, the recorded vertical displacement is resolved into a thinning component, Δth, (normal to the sample-forcing block interface) and a simple shear component, Δdz_{simple}, (parallel to the shearing direction, see Fig. 4.1B). As no lateral escape (perpendicular to the shearing direction) of material is observed, we conclude that thinning occurs by the material being pushed out at the ends of the forcing blocks (parallel to the shearing direction, e.g. Figs. 4.4 and 4.6). Thinning cannot be recorded during the experiment but is known to continue progressively at least to a shear strain of $\gamma = 5$. To simplify the calculation of the shear strain, we assume that the thinning rate is constant, and that the total amount of Δth ($= th_0$ - th_{final}) is distributed linearly over the entire duration of the experiment. The progressive thinning causes an increase in bulk shear strain and bulk shear strain rate of $\sim 2\times$. In effect, in most experiments, the strain rate increases progressively, so that mean bulk shear strain rates of $\dot{\gamma} \sim 2.3 \times 10^{-5}$ s^{-1} and $\dot{\gamma} \sim 2.3 \times 10^{-4}$ s^{-1} (depending on the applied displacement rate) are reached.

4.2.4   Analytical methods

For microstructural analysis, samples deformed to different finite strains are vacuum impregnated with low viscosity epoxy and doubly polished thin sections (30 μm thick) parallel to the compression axis, z, and the displacement direction, dz_{simple}, are prepared. Backscattered electron z-contrast images are obtained using field-emission gun (FEG) SEMs equipped with EDS detectors (Phillips XL30 ESEM and FEI Nova Nano SEM 230) operating at acceleration voltages of 20, 15 and 10 kV. At selected sites, TEM sections are prepared with a FEI NanoLab 600 FIB-SEM using a Ga-ion beam for milling. TEM sections (~ 50 nm thick) are analyzed in a FEI Technai 20 FEG TEM with an EDS detector under 200 kV acceleration voltage. SEM-cathodoluminescence (CL) images were obtained with a Zeiss EVO 50 SEM with a Gatan Mono CL 3 system under 20 kV acceleration voltage. XRF analyses of the starting material powder were obtained using a Siemens SRS 3000 sequential x-ray spectrometer.

4.3   Results

4.3.1   Mechanical data

The samples reach a peak shear strength of (~ 1250 MPa $< \tau < \sim 1375$ MPa) at bulk sample shear strains of ($1.7 < \gamma < 2.1$) (4.3A). Shortly before reaching the peak strength, tiny stick-slip events appear in the force record (stress drop of $2-5$ MPa, i.e. $< 0.5\%$). After a slight weakening (by ~ 40 MPa) the samples continue to deform at approximately constant shear stress without any sudden stress drops. No stick-slip events can be detected either in the force or in the displacement record. The weakening is accompanied by a transient increase of the measured displacement rate of the forcing piston (4.3B). The friction coefficient, μ, of the sample on the 45° pre-cut is ~ 0.7 (Tab. 4.2), which is in the range of values typical of intact rock materials (Byerlee, 1978).
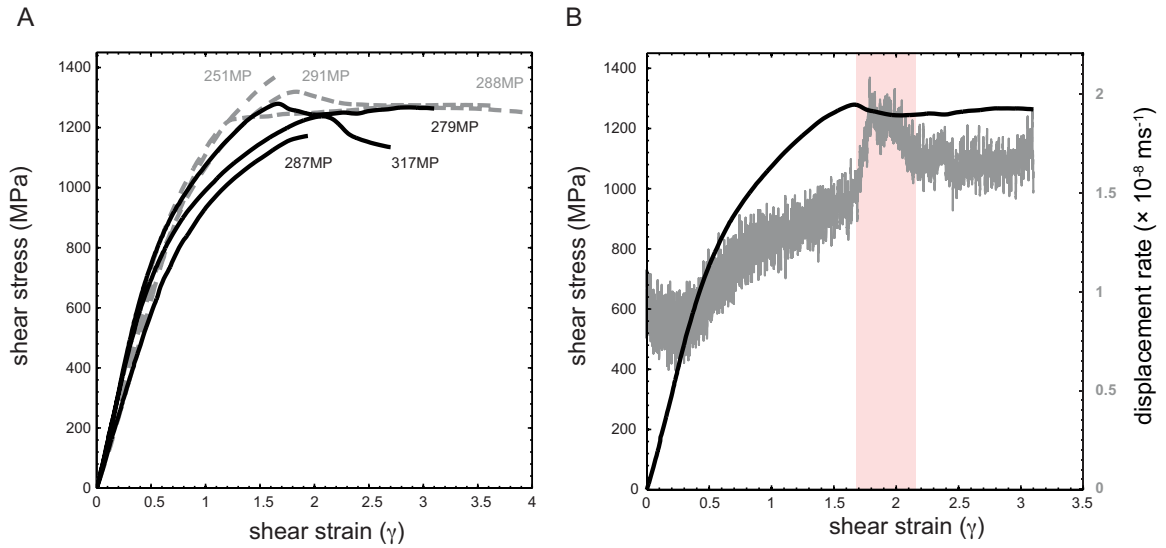
Figure 4.3: Stress – strain curves. A) Experiments conducted at T = 300°C and Pc ∼ 500 MPa: bulk shear strain, γ, versus shear stress, τ. Gray dashed lines: $\dot{d} \sim 10^{-7}$ m s^{-1}, black lines: $\dot{d} \sim 10^{-8}$ m s^{-1}. Note absence of abrupt stress drops. B) Record of the piston displacement rate corrected for apparatus stiffness (gray) and the corresponding stress - strain curve (black). Note the transient increase of the displacement rate during the slight weakening (red zone). No faster movement than 2.1×10^{-8} m s^{-1} is recorded.

4.3.2   Microstructural evolution

Pec et al. (2012a) report that during early stages of the deformation ($0 \leq \gamma \leq 1.5$), the fault rock layer is compacted from ∼ 1 mm to ∼ 0.7 mm. Comminution is achieved mainly along pervasive, closely spaced Riedel shears (length ∼ 160 μm, spacing ∼ 50 μm). Between the shears, the grains are comminuted, forming survivor grains with tails of extremely fine-grained material (grain size < 100 nm) which grades into the shear bands. Together, the survivor grains and the shear bands form an S-C' fabric.

At peak strength, typically 4 to 6 slip zones of nanocrystalline to partly amorphous material (PAM) (mean grain size of ∼ 34 nm, smallest crystalline particles ∼ 8 nm) develop, forming through-going anastomozing and interconnected shear bands in a C' orientation (Figs. 4.4 and 4.5). No individual fragments can be identified in the slip zones by FEG-SEM (Figs. 4.4 and 4.5), and all observations of small particles had to be made by TEM (Fig.4.5). The diffraction pattern with weak spots and arcs as well as a broader band of diffuse intensity is consistent with nanocrystalline to partly amorphous material (Viti, 2011).

The slip zones are 5 to 20 μm thick and accommodate local shear strains often in excess of $\gamma \sim 5$ (if a mineral grain is cut by the slip zone it acts as a strain marker). Compared to the bulk strain across the entire sample, the localization of strain in the slip zones implies an increase of the shear strain and shear strain rate by a factor of ∼ 2.5.

With increasing finite strain, comminution continues and, on account of their low fracture strength, mostly feldspars are affected. Within the slip zones feldspars change their composition and contain Na, Ca and K (Pec et al., 2012a) indicating high mobility of these elements in the PAM (Yund et al., 1990). Micas get entangled in the slip zones, however they do not form through-going layers (Fig. 4.4C,D,F). Quartz grains are always the strongest phase and fracture the least. (see Pec et al. (2012a) for a detailed description of microstructural evolution up to peak strength).
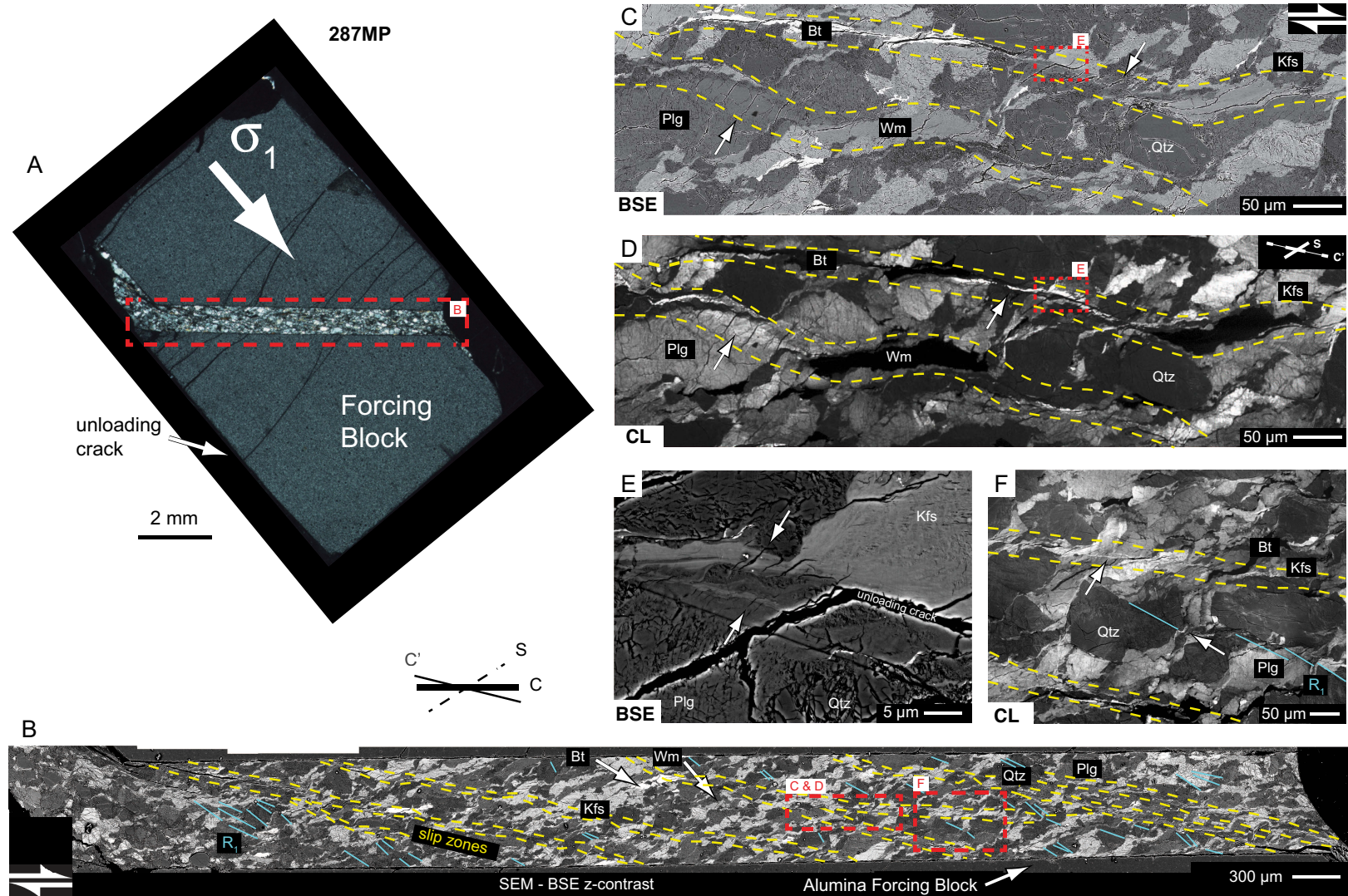
Figure 4.4: Overview of the microstructures at peak strength. Kfs – potassium feldspar, Plg – plagioclase, Qtz – quartz, Bt – biotite, Wm – white mica. A) Crossed polarized light image of the sample. B) BSE image of the whole shear zone. Note the S-C' fabric. C) BSE image showing the anastomozing nature of the slip zones. Note the concentration of unloading cracks in the cohesive material within slip zones (between dashed lines, arrows). D) SEM-Cathodoluminescence (CL) image of the same region as C. Black are both micas. Note the bright luminescence within the slip zones and on high stress and/or high strain sites (arrows). E) High-magnification image of a slip zone (frame indicated in C and D). Note the porosity in the Kfs-aggregate (black, upper right) which progressively disappears towards the cohesive slip zone where unloading cracks concentrate (arrows). This material has a bright CL signal and contains Si, Al, Na, K and Ca. F) SEM-CL image. Bright luminescence highlights zones of high strain and/or high stress within feldspars (arrows).
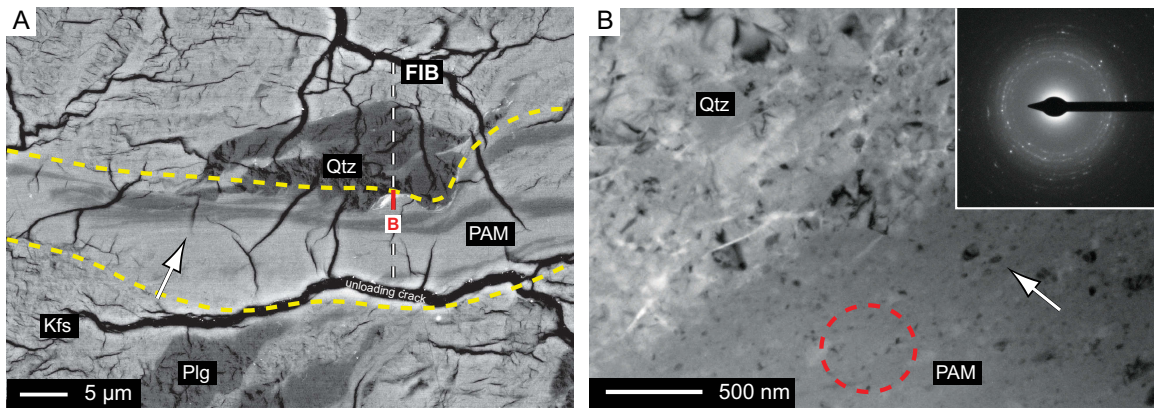
Figure 4.5: Micro- and nanostructures of slip zones. Qtz – quartz, Kfs – potassium feldspar, Plg – plagioclase, PAM – nanocrystalline to partly amorphous alumosilicate containing Na, Ca, and K. A) BSE image of a slip zone (between dashed lines), red line shows the field of view in (B). Note the unloading cracks (arrow) and flow structures. B) TEM bright field image of the PAM. Inset shows the diffraction pattern collected in the red dashed circle. In the Qtz region, bright seams are porosity and black are diffracting crystals. Note no porosity in PAM region and tiny diffracting crystals (arrow, $d_{mean} \sim 34$ nm) embedded in a uniform gray matrix (either not diffracting crystals and/or amorphous material).

At higher strains, the deformation localizes even further implying a further shear strain rate increase within the slip zones. One or two through-going zones of completely amorphous material (AM) (Figs. 4.6E,F, 4.7D) are formed along the pre-existing slip zones with a thickness varying from ~ 100 nm to ~ 30 μm (Figs. 4.6 and 4.7). This material percolates the entire sample from one end to the other (Fig. 4.6B,C) and probably forms a multiply connected layer with gaps across which the fault rocks are continuous. Judging from the 2D tracings (manually traced from mosaics of high-magnification images), we estimate that the area coverage of the film is $\sim 70\%$ leaving approximately 30 area% of gaps (Fig. 4.4C).

To compare the amorphous layer to a pseudotachylite, detailed micro-scale analyses were carried out that confirmed the presence of flow structures (Figs. 4.6E,F, 4.7A-C), injection veins (Fig. 4.7B) and embayed clasts surrounded by a different z-contrast material ("corroded clasts") (Fig. 4.6F). Deformed Bubbles and bubble trains follow the local flow pattern in some of the thicker parts of the amorphous layers (Figs. 4.6F, 4.7A,C,D,E,F). At the nano-scale the presence of amorphous material is confirmed by the lack of electron diffraction spots (Fig. 4.7D,F). Semi-quantitative SEM– and TEM–EDS analyses show that the chemical composition of the AM varies strongly depending on the precursor material, does not have a eutectic melt composition, but is more ferromagnesian and less silicic compared to the bulk rock (Tab. 4.1, Fig. 4.8). High compositional contrasts (expressed by different z-contrast in BSE images) within the AM are observed and indicate a limited amount of mixing and/or atomic mobility (Figs. 4.6D,E, 4.7A,B and 4.8). Due to the highly heterogeneous nature of the AM quantitative electron microprobe WDS analyses were not performed.
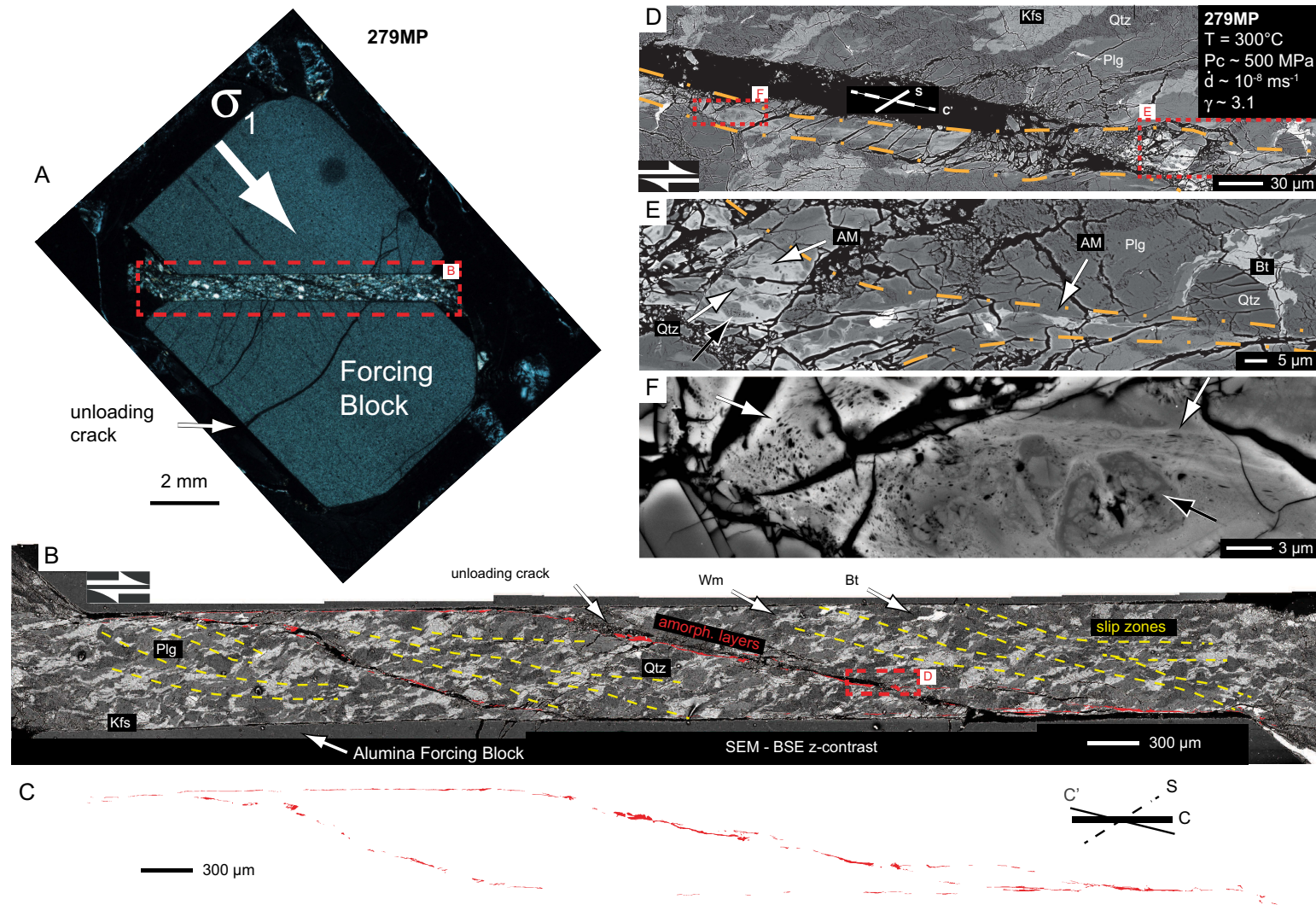
Figure 4.6: Overview of the microstructures after quasi steady-state. Kfs – potassium feldspar, Plg – plagioclase, Qtz – quartz, Bt – biotite, Wm – white mica, AM – amorphous material. A) crossed polarized light image of the sample, B) BSE image of the whole shear zone. Note the S-C-C' fabric. AM was manually traced on high magnification images and is shown in red. C) AM without background image highlighting its percolating nature suggesting a multiply-connected topology. D) AM layer (between dash-dotted lines) cross-cut by an unloading crack (black). Note the high variability in z-contrast on small scale (e.g. area E and F). E) Biotite-derived AM with flow structures, bubbles (black arrow) and qtz clasts. F) Feldspar-derived AM. Note the bubbles (white arrows) and bubble trains following the local flow pattern and the "corroded" appearance of the qtz clast (black arrow).
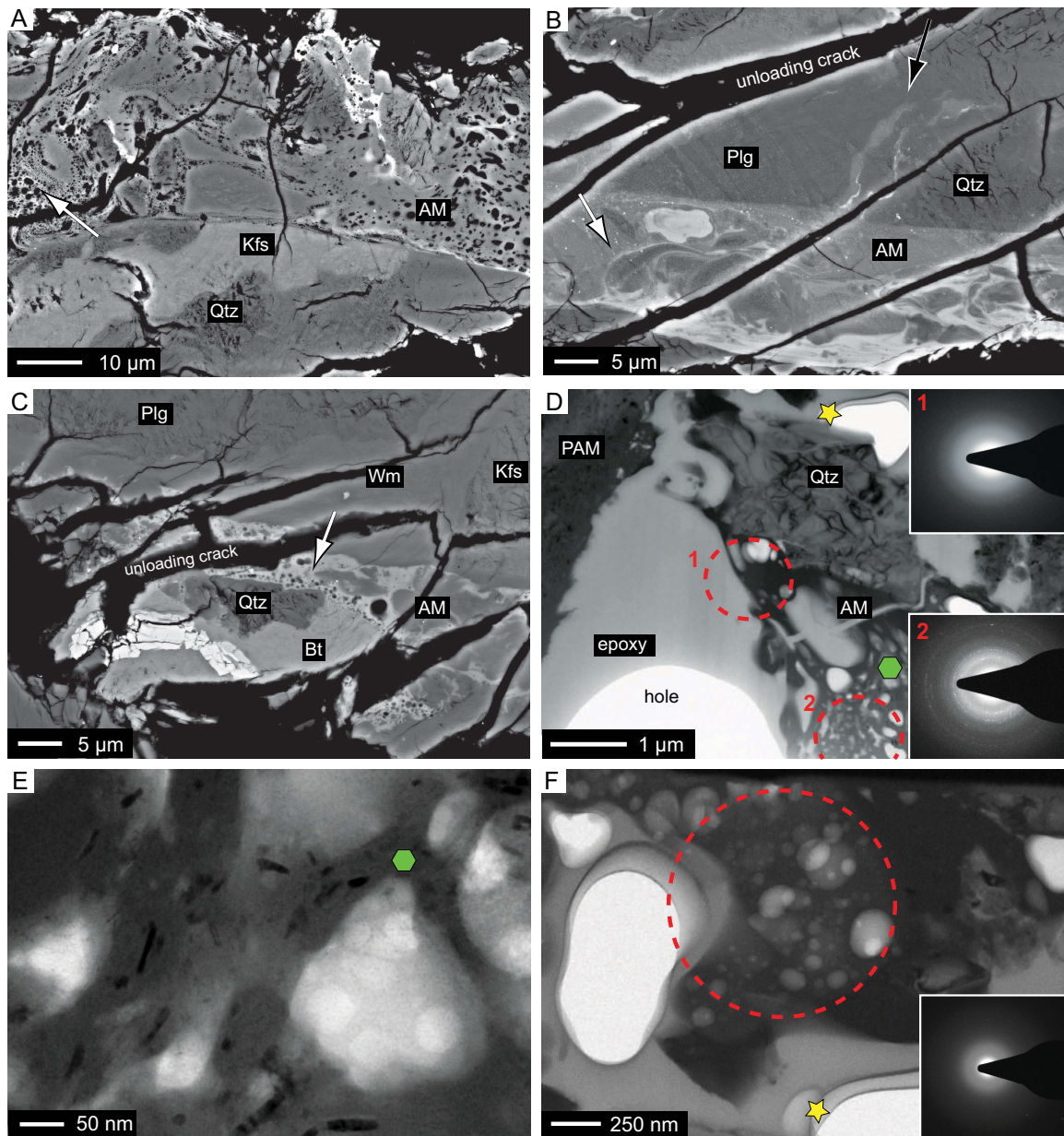
Figure 4.7: Micro- and nanostructures of the amorphous layers. Kfs – potassium feldspar, Plg – plagioclase, Qtz – quartz, Bt – biotite, Wm – white mica, AM – amorphous material, PAM – nanocrystalline partly amorphous material. (A-C) SEM-BSE z-contrast images. A) large bubbles (arrow) following the local flow pattern. Note the changes in brightness (hence composition) within the material B) turbulent flow structures and "schlieren" of quartz (white arrow) within the AM. Note the injection vein (black arrow) and the sharp boundary to the wall rock C) crystalline biotite transforming into an AM containing bubbles (arrow). (D-F) TEM bright field images. D) Amorphous material. Star and hexagon show the position of (E) and (F). Diffraction patterns were collected in the dashed circles. Note the presence of fully amorphous (1) as well as amorphous nanocrystalline (2) and PAM material (upper left) just a micron away. Further, note the high dislocation density and bent crystal planes in the quartz clast. E) Amorphous nanocrystalline material. Note the tiny bent diffracting crystals (arrow, $d_{mean} \sim 15$ nm) within the amorphous matrix. F) fully amorphous region within the bubbly matrix).

4.4   Summary and discussion

4.4.1   Summary and implications of microstructural observations

Throughout the experiments, the deformation in the fault rock sample is increasingly local-ized; first strain partitions into multiple slip zones (thickness $\sim 5 - 20$ μm) made of partially amorphous material (PAM) and later into one or two thin layers (thickness $\sim 0.1 - 30$ μm) made of completely amorphous matetrial (AM). Localization around peak strength occurs due to high phase strength contrast (Holyoke and Tullis, 2006b,a), where favorably oriented micas (slip along weak basal planes) in the C' direction act as stress concentrators and pro-mote fracturing and amorphization of feldspars. Quartz acts as a stress raiser and further contributes to the wide-spread comminution. At peak strength, a nano-crystalline, partly amorphous material (sharing similarities with geopolymers, e.g. Duxson et al., 2007 and references therein) forms a through-going anastomozing network, which is weaker than the surrounding crystalline material (as it accommodates more strain). Many of the slip zones are initiated by mica flakes, and, as a consequence, mica is often present in and adjacent to the slip zones.

A   Biotite-derived amorphous material
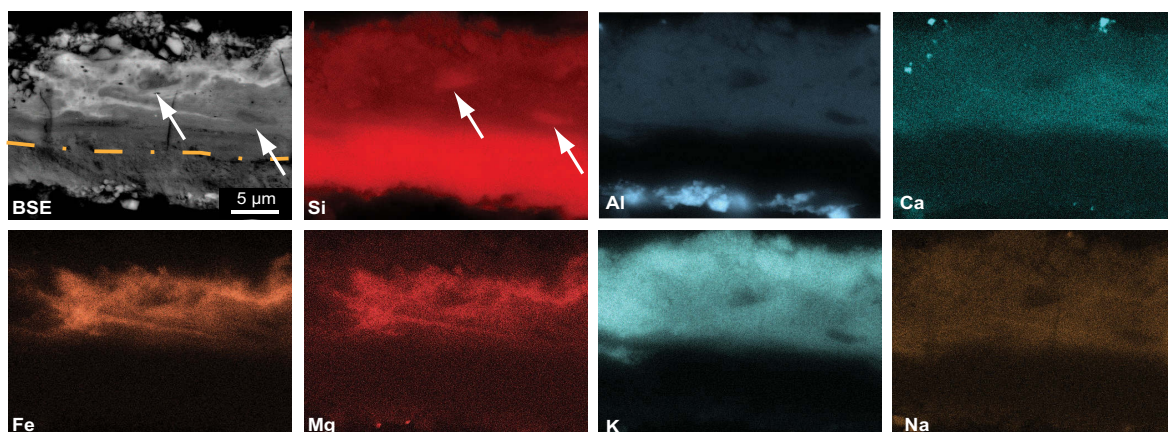
B   Feldspar-derived amorphous material
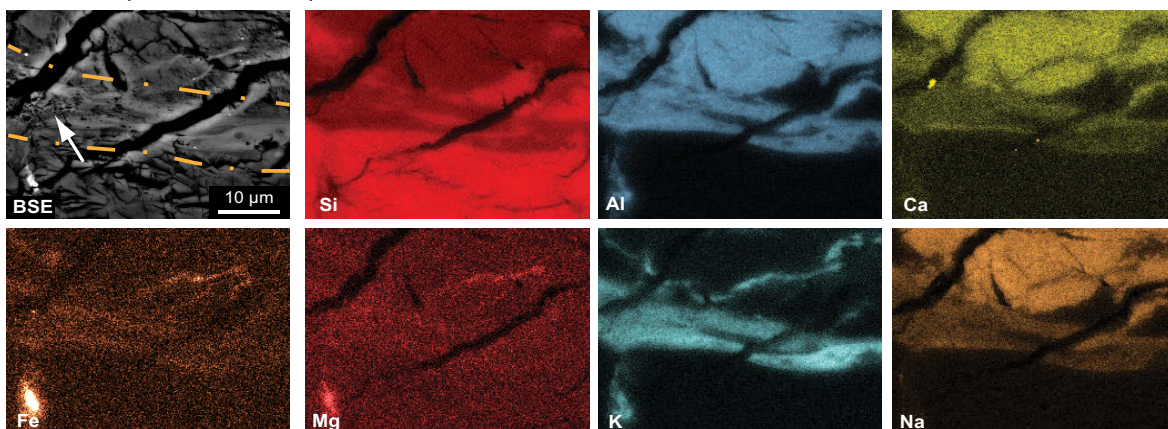
Figure 4.8: EDS maps of the AM. Note the enrichment in Fe and Mg and the presence of Na, Ca as well as K within the AM. Further note the heterogeneity of element distribution (expressed by brightness) within the AM. A) Bitotite-derived AM, note the presence of quartz clasts in the AM (arrows) B) Feldspar derived AM (between dash-dotted lines), arrow shows bubbles. Note the absence of K in the larger Plg clast above the AM.

During the quasi steady-state part of the experiment, deformation further localizes into the amorphous thin layers within the slip zones. This material is characterized by: intense comminution, presence of nano-crystalline to TEM-amorphous material, flow structures, injection veins, deformed bubbles and "corroded clasts", and thus shares many characteristics of a natural pseudotachylite. Microstructural observations show that the amorphous material (AM) forms from the nanocrystalline partly amorphous material (Fig. 4.5). This AM is discordantly cut by the unloading cracks (Fig. 4.6D), and thus, it must have developed before the quenching and unloading procedure.

The AM behaves as a viscous, fragment loaded, turbulent fluid with a lower viscosity than the surrounding crystalline material (as it accommodates more strain). The microstructures of the AM cannot be explained by accumulation of many successive events because the continuity of turbulent flow structures (Figs. 4.6E,F and 4.7B) and deformed bubbles (Figs. 4.6F and 4.7A) indicates that the observed deformation is continuous.

These amorphous layers were formed under Pc $\sim$ 500 MPa and T = 300°C, i.e., at conditions that correspond to mid crustal levels (15-20 km depth). They maintained high and constant stress levels (1150 MPa $< \tau <$ 1275 MPa) and did not produce any substantial weakening or lubrication of the fault. The applied displacement rate, $\dot{d}$, of the piston is within an order of magnitude of natural plate velocities. Thus, the maximum slip velocities in our experiments are at least seven orders of magnitude below those calculated for seismic slip ($\sim$ 1 m s^{-1}).

Localization increases the shear strain rate ($\dot{\gamma} = \dot{d}/w$ where $\dot{d}$ is the displacement rate in ms^{-1} and w is the width of the deforming layer in m) but does not imply an increase in slip velocity. In other words, high strain rates can be produced at low displacement rates (plate velocities) provided the deforming layer is very thin.

In our experiments, the formation of AM did not cause any substantial weakening of the fault, as is commonly observed during frictional melt production in HVFE (Di Toro et al., 2006, 2011; Niemeijer et al., 2011). This may imply that the 3-D network of the amorphous layer is not load bearing. Microstructural observations suggest that gaps exist in the amorphous layers, where the adjacent sides of solid fault rock are in contact and most likely maintain high shear strength (Hirose and Shimamoto, 2005). Alternatively, as the thin layers are deforming at high shear strain rates, they can support high stresses.

4.4.2 Estimating the temperature during the experiment

How can the amorphous material be produced? There are two possibilities: one is by melting at the thermodynamic melting temperature, T_m, the other are non-equilibrium amorphization processes below T_m. We will first examine the possibility of raising the temperature by shear heating from 300°C to the melting temperature of the bulk rock ($\sim$ 750°C) or to that of individual minerals present in the AM (bulk equilibrium melting temperatures of micas, feldspars and quartz (Figs. 4.6 and 4.7, i.e. 850°C – 1730°C).

The temperature increase on the fault of finite width due to shear heating (Mair et al., 2006; Mair and Marone, 2000) can be calculated by the following equation (Cardwell et al., 1978):

$$\Delta T = \frac{\tau D}{\varrho c_p \sqrt{\pi \kappa t_{slip}}} \tag{4.1}$$

Where τ is the shear stress, D is the fault displacement, ϱ is the density, c_p is the specific heat, κ is the thermal diffusivity and t_{slip} is the duration of slip. Using the data from our experiments, the resulting maximum temperature increase in the shear zone is $\sim 2.5°$C (see appendix for details of the calculation) while a ΔT of $\sim 350°$C would be needed to reach eutectic melting of the granitoid rock or a ΔT of $\sim 1430°$C for the melting of quartz. Note that the main reason why the calculated ΔT is small here is that the time over which the slip occurs, t_{slip}, is large. Breaking the displacement D up into n smaller displacements D/n which each take 1/n of the time to complete (keeping the overall displacement rate and all other factors constant) will result in ΔT growing in proportion to $\sqrt{n}$. In the limit, for extremely small slip distances D and extremely short times t_{slip}, ΔT approaches ∞ indicating that the equation is used outside the region of its applicability. In addition to microstructural arguments (see section 4.4.1), comparing the apparatus-recorded displacement to the displacement measured in thin sections at different finite strains show a good agreement (Fig. 4.9) and micro stick slips are not observed during the quasi steady state deformation in our experiments; at a resolution of 50 Hz and 0.1 μm displacement, the deformation is continuous.

Considering (a) the effective way by which the Griggs apparatus conducts heat away from the sample (see section 4.2.2), (b) the presence of high dislocation defects and bent crystal planes in quartz grains surrounded by the amorphous material (Fig. 4.7D), (c) the presence of nano-crystalline material (Fig. 4.7D,E), and (d) the highly heterogeneous chemical composition within a micron range in the AM (all of which would be expected to anneal quickly at high temperatures), combined with the long time during which the experiments remain at elevated temperatures, we conclude that a significant T increase seems very unlikely.
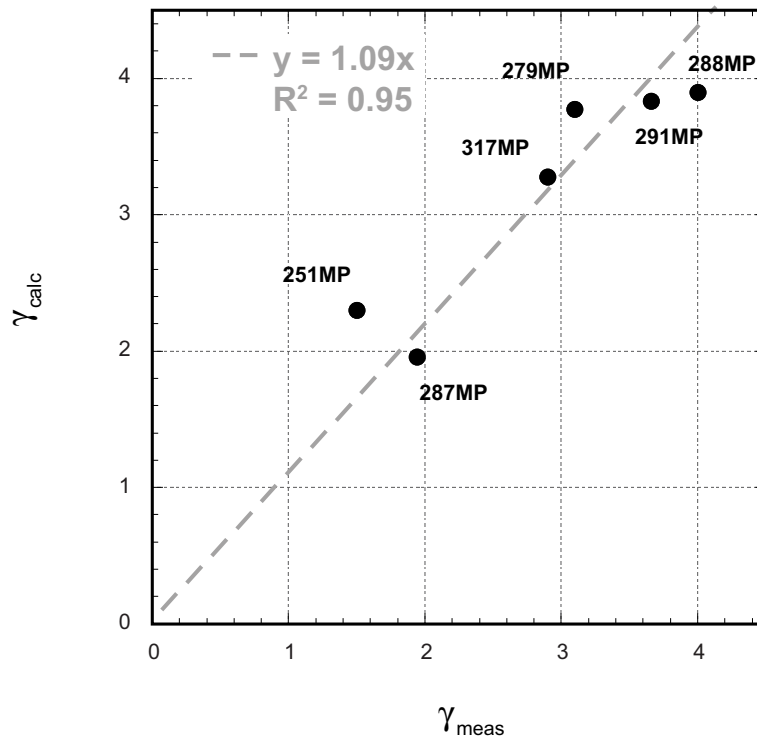
Figure 4.9: Calculated vs. measured finite strain. Comparison of apparatus recorded strain (γ_{calc}) with strain measured in thin sections (γ_{meas}) showing a good correlation.

4.4.3   Amorphization below bulk thermodynamic melting temperatures

A possible explanation for the observed microstructures are non-equilibrium processes, which lead to the destruction of the crystal lattice. Both, melting as well as amorphization, seem to have a common physical cause which is volume expansion leading to a "rigidity catastrophe" where the crystal lattice progressively looses its ability to resist shear stress (see Wolf et al., 1990; Yip et al., 2005; Suryanarayana, 2001; Fecht, 1992 and Angell et al., 2000 for an in-depth discussion). Amorphization occurs by a variety of processes as irradiation damage (e.g. Lumpkin et al., 2012; Gieré et al., 2009; Cherns et al., 1980), deformation (e.g. Suryanarayana, 2001; Nakayama et al., 2001; Lund and Schuh, 2003; Reichelt et al., 2010), application of pressure (e.g. Hemley et al., 1988; Mishima, 1996) or chemical reactions (e.g. Duxson et al., 2007; Rahier et al., 1996, 1997).

Amorphous materials can exhibit a wide range of rheological behavior from solid-like to fluid-like depending on that amount of short- and long-range order, presence of second-phase particles and observation timescales (Malkin, 2009; Haw, 2004) and are therefore usually described in terms of visco-elastic rheology.

4.4.4   Processes leading to the production of the amorphous material

High stresses induce high lattice defect densities and cause pervasive comminution down to the nanometer scale (Figs. 4.5B, 4.7E). Pronounced chemical changes take place in the slip zones as well as in the amorphous layers on a very fine scale (shown by highly heterogeneous z-contrast BSE images (Figs. 4.6 and 4.7) and EDS-maps (Fig. 4.8) further increasing the chemical disorder of this material.

The granitoid rock used in our experiments consists of quartz, micas and feldspars, and the individual minerals can undergo different crystal-lattice destruction processes. A variable and non-equilibrium chemical composition of the amorphous material can be explained in terms of non-equilibrium processes where the comminution, build-up of defects, and amorphization below bulk T_m (i.e. below the solidus of individual minerals or eutectic melting point of the bulk rock) affect weaker minerals (micas and feldspars) more and stronger minerals (quartz) less. Bubbles and flow structures commonly occur in amorphous materials, too (e.g. gels and geopolymers), and "corroded clasts" can be the result of heterogeneous amorphization (Jones and Santana, 1999; Yamasaki et al., 2002). In other words, we argue that the presence of XRD and TEM amorphous material (interpreted as glass) in natural pseudotachylites is not an argument for their frictional melting origin, as the crystalline-to-amorphous transition is not uniquely achieved by temperature increase and thermodynamic melting.

Volume expansion in the amorphous material and cracking in the adjacent wall rock lead to injection veins and characteristic intrusive aspects observed in natural pseudotachylites as well as fluidized cataclasites (e.g. Rowe et al., 2005; Kirkpatrick and Shipton, 2009). The high variability in amount of nano-crystaline material within the micrometer range in our experimental samples (Fig. 4.7D,E,F), the limited amount of mixing (Figs. 4.6D,E and 4.7A,B), and the high supported shear stresses (Fig. 4.3) provide further evidence that the temperatures during formation of the amorphous layers were not necessarily high. The diffusivity of elements is high in high temperature equilibrium melts (as they require the T of self diffusion to be reached) and quickly homogenize the chemical composition unless unmixing occurs.

Comparing the amorphous layers produced in our experiments to BSE micrographs of frictional melts from HVFE experiments on granites (Spray, 2010, G. Di Toro, pers. comm.), it appears that the molten material produced during frictional melting has a homogenous z-contrast, contrary to the amorphous material in our experiments. This may be a consequence of the much higher strains accommodated in the frictional melt and more detailed microstructural studies could point out further differences between frictional melts produced in HVFE and amorphous materials produced during continuous creep.

4.5   Conclusions

With respect to the overall 3-D geometry, the microstructure and nano-structure, many natural pseudotachylites are very similar to the amorphous layers that we have produced in our experiments (e.g. Spray, 2010; Lin, 2007; Wenk et al., 2000). We would therefore argue that pseudotachylites may be produced not only by frictional heating but also under conditions which approximate tectonic plate velocities and mid crustal pressures and temperatures. In other words, not all of the naturally occurring pseudotachylites have to be caused by frictional melting at seismic slip velocities. Rather, we suggest that many natural pseudotachylites may be the ultimate products of rock comminution, intense damage, and amorphization at high stresses and strain rates.

Appendix:

To calculate the temperature increase due to shear heating we use the calculation of Cardwell et al. (1978) which was experimentally validated by the work of Mair and Marone (2000) using a similar experimental setup (shearing of granular material). First the heat production equation can be written as:

$$q = \tau V \tag{4.2}$$

where τ is the shear stress and V is the sliding velocity. The equation governing 1-D unsteady transport of heat can be written as:

$$\frac{\partial T}{\partial t} = \frac{Q(x,t)}{\varrho c_p} + \kappa \frac{\partial^2 T}{\partial x^2} \tag{4.3}$$

where T is the temperature, t is time, ϱ is the density, c_p is specific heat, Q is the rate of heat generation per unit volume and time ($Q = q/w$) where w is the fault width, $\kappa = k/\varrho c_p$ is the thermal diffusivity where k is the thermal conductivity and x is the distance. Thus the rate of temperature increase is a balance between a heat production and heat conduction term (Cardwell et al., 1978). The solution for temperature given by Cardwell et al. (1978) assuming that $T = T_0$ and $Q = 0$ for $t < 0$ prior to faulting is:

$$T(x,t) = T_0 + \frac{1}{2\varrho c_p \sqrt{\pi \kappa}} \int_0^t \int_{-\infty}^{\infty} exp\left[\frac{-(x-x_0)^2}{4\kappa(t-t_0)}\right] \frac{Q(x_0,t_0)}{(t-t_0)^{1/2}} dx_0 dt_0 \tag{4.4}$$

Note that this equation assumes that all available energy is instantaneously converted into heat during slip and no energy is used for the modification of the microstructure. The equation governing heat generation per unit volume with the assumption that heating is uniform across the width w of the fault can be written as:

$$Q(x_0, t_0) = \frac{\tau D}{w t_{slip}} \left[H\left(x_0 + \frac{w}{2}\right) - H\left(x_0 - \frac{w}{2}\right) \right]; 0 < t < t_{slip} \tag{4.5}$$

$$Q(x_0, t_0) = 0; t_0 < 0, t_0 > t_{slip} \tag{4.6}$$

where D is the fault displacement, t_{slip} is the duration of the slip and H is the Heavyside step function. Substitution of (4) into (3) and integration of the space coordinate gives according to Cardwell et al. (1978):

$$T = T_0 + \frac{\tau D}{2 \varrho c_p w t_{slip}} \int_0^t \left\{ erf\left[\frac{x + (w/2)}{(4\kappa[t - t_0])^{1/2}} \right] - erf\left[\frac{x - (w/2)}{(4\kappa[t - t_0])^{1/2}} \right] \right\} dt_0; 0 < t < t_{slip} \tag{4.7}$$

$$T = T_0 + \frac{\tau D}{2 \varrho c_p w t_{slip}} \int_0^{t_{slip}} \left\{ erf\left[\frac{x + (w/2)}{(4\kappa[t - t_0])^{1/2}} \right] - erf\left[\frac{x - (w/2)}{(4\kappa[t - t_0])^{1/2}} \right] \right\} dt_0; t > t_{slip} \tag{4.8}$$

A characteristic length for heat conduction is given by $(\kappa t_{slip})^{1/2}$ which is the distance heat is conducted during faulting. Two end-members appear - if $w/(\kappa t_{slip})^{1/2} \ll 1$ the maximum temperature increase at the end of faulting on a fault of zero width is given by:

$$\Delta T = \frac{\tau D}{\varrho c_p \sqrt{\pi \kappa t_{slip}}} \tag{4.9}$$

and yields the highest temperatures (Cardwell et al., 1978). If $w/(\kappa t_{slip})^{1/2} \gg 1$ then the following equation applies:

$$\Delta T = \frac{\tau D}{\varrho c_p w} \tag{4.10}$$

In this scenario heat conduction is not important and the heat is uniformly distributed across the width of the fault.

We can now calculate the term $w/(\kappa t_{slip})^{1/2}$ for the whole width of the shear zone (~ 0.5 mm) and for the thinnest observed amorphous layer (~ 100 nm). For t_{slip} we take the time from peak strength to the end of the experiments (Tab. 4.2) and for κ we use the published values for the minerals forming the Verzasca gneiss summarized by Di Toro and Pennacchioni (2004) (see Tab. 4.3). This yields $\sim 1.8 - 4.8 \times 10^{-3}$ for a fault thickness of 0.5 mm and $\sim 3.6 - 9.7 \times 10^{-7}$ for a fault thickness of 100 nm. Thus the condition $w/(\kappa t_{slip})^{1/2} \ll 1$ is satisfied.

We note that the condition $w/(\kappa t_{slip})^{1/2} \gg 1$ would only be fulfilled if all the measured fault displacement (measured in apparatus record as well as in thin sections) in the sample took $\ll 1$ s or the thermal diffusivity, κ, would be more than 6 orders of magnitude lower than usual values for rock forming minerals. Calculated temperature increase lies between $\sim 0.4 - 2.5\,°C$ (Tab. 4.2). The assumption that no energy is consumed during grain breakage down to nanometer scales is conservative and furthermore, it has to be pointed out that the absolute values of stress are likely overestimated by $\sim 30\%$ (Holyoke and Kronenberg, 2010). Taking these factors into account would yield an even lower temperature increase. Furthermore, the values of κ, ϱ and c_p used here might not be appropriate for the nano-crystalline partly amorphous material within the slip zones which is expected to have different thermodynamic properties than bulk minerals (e.g. Helgeson et al., 1978; Dick et al., 2002; Sun and Simon, 2007; Farrell and Siclen, 2007; Levitas and Samani, 2011), however an error in the temperature calculation by ~ 2 orders of magnitude would not change the conclusion that the rock did not reach thermodynamic bulk melting temperatures.

#	Pc (MPa)	$\Delta\sigma^1$	τ^1 (MPa)	σ_n^1	μ^1	$\dot{v}_{dz_{simple}}$ (m s^{-1})	q^2 (W m^{-2})	t$^3_{slip}$ (s)	dz$^3_{simple}$ (mm)	ΔT (°C)
279MP	490	2510	1255	1750	0.72	1.80×10^{-8}	28.39	46700	0.84	0.7
317MP	498	2300	1150	1650	0.70	1.89×10^{-8}	26.93	14258	0.27	0.4
288MP	535	2520	1260	1795	0.70	1.69×10^{-7}	322.60	6510	1.10	2.5
291MP	510	2550	1275	1785	0.71	1.86×10^{-7}	352.71	4190	0.78	2.2

Table 4.2: Summary of mechanical data of experiments in quasi steady state and shear heating calculation based on equation (4.9). [1] - mean value of quasi steady state, corrected for piston overlap, [2] - mean value of quasi steady state, [3] - from peak strength

	ϱ (kg m^{-3})	c_p (J kg^{-1} K^{-1})	κ (10^{-6} m^2 s^{-1})	norm.% in Verzasca gneiss
Quartz	2650	1186	2.23	37
Plagioclase	2650	1184	1.75	24
K-feldspar	2600	1153	1.1	33
Mica (Biotite)	2950	1090	0.31	6
Verzasca gneiss	2651.50	1168.87	1.63	

Table 4.3: Physical properties of minerals (after Di Toro and Pennacchioni, 2004 and references therein) and calculated properties for Verzasca gneiss based on modal composition (after Keulen et al., 2007).

Semi-brittle flow of granitoid fault rocks under a broad range of
temperatures, confining pressures and displacement rates

5.1 Introduction

The strength of the lithosphere is expected to reach its maximum around the so-called "frictional - viscous" transition (also called "brittle-plastic" transition) where the rocks are likely to deform by semi-brittle flow (e.g. Kohlstedt et al., 1995; Stöckhert et al., 1999; White, 2001). This load-bearing layer is thus expected to have the largest potential for nucleating major earthquakes if the stored elastic energy is abruptly released.

Traditionally, the "frictional - viscous" transition, is viewed as a transition from frictional sliding on pre-existing surfaces (brittle faults) to volume flow (viscous mylonites). It has been recognized that this transition defined as one sharp point where the Byerlee's rule for frictional sliding intersects a flow law for volume flow (for a given geothermal gradient and bulk strain-rate), is a result of extrapolating both Byerlee's rule as well as steady-state flow laws to physical conditions outside their range of validity (e.g. Carter and Tsenn, 1987). Numerous variations to remedy this problem have been proposed (e.g. Shimada, 1993; Ohnaka, 1995; Blanpied et al., 1995; Kohlstedt et al., 1995; Bos and Spiers, 2002b), (Fig. 5.1).

Despite efforts to reconcile empirical rate-and-state friction rules with steady state flow laws (e.g. Noda and Shimamoto, 2010, 2012; Bos and Spiers, 2002b) no widely acknowledged flow or friction law is available to date for deformation in the semi-brittle field. Perhaps most insight into the semi-brittle flow regime comes from experiments exploring the "brittle - ductile" transition (i.e. from localized failure to distributed cataclastic flow) in porous rocks (Hirth and Tullis, 1989; Wong and Baud, 2012; Schubnel et al., 2005) as fracturing and hence development of (transient) porosity always accompanies semi-brittle flow (e.g. Keulen et al., 2007, 2008; Pec et al., 2012a; Hirth and Tullis, 1994). First we will briefly review the frameworks in which viscous and frictional deformation are treated and then we point
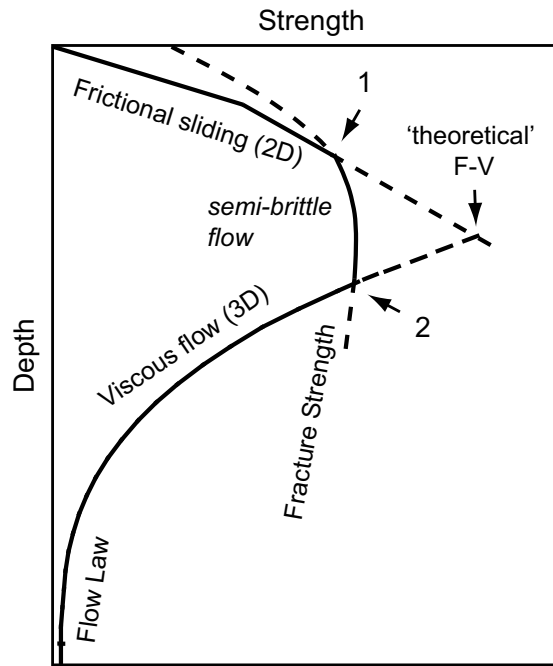
Figure 5.1: Simplified rheological profile of the lithosphere (modified after Kohlstedt et al., 1995 and Shimada, 1993). Full lines show processes limiting the strength at a given depth (for a fixed strain rate). Depth contains pressure, temperature, chemical effects etc. Semi-brittle flow is expected at depths where the strength of country rock is equal or lower to its frictional strength (Byerlee's rule) on a pre-existing fault surface (point 1, "brittle - ductile" transition sensu Kohlstedt et al., 1995). Crystal-plastic deformation is expected to dominate once the differential stress supported by the rock is equal or lower than the confining pressure (Goetze's criterion, point 2, "brittle - plastic" transition sensu Kohlstedt et al., 1995). "Theoretical Frictional - Viscous" transition is the point where 2D and 3D concepts meet (see text).

out a simple difference between both frameworks which, in our point of view, hampers our understanding of rheological behavior of faults in the semi-brittle field.

5.2   Viscous flow and frictional sliding frameworks

5.2.1   Viscous flow

Under high temperature (HT), high pressure (HP) conditions and slow bulk strain rates rocks deform by viscous flow. Strain compatibility is maintained by dislocation glide and climb, diffusion and dissolution-precipitation creep, which are in essence mass-transfer processes dependent on atomic mobility and kinetics, i.e. temperature and time. Therefore, viscous deformation is in the first order dependent on temperature and strain rate. Rocks under these conditions generally do not support high stresses as the build up of stress is counteracted by material flow relaxing the stress. The rheological response of a material is modeled in terms of various flow laws which connect the rate at which the material flows to the applied stress in the form of:

$$\dot{\varepsilon} = A\sigma^n d^m exp\left(-\frac{Q + pV}{RT}\right) \tag{5.1}$$

Where $\dot{\varepsilon}$ is the strain rate (units: s^{-1}), A the pre-exponential constant, σ the differential stress, n the stress exponent (~ 1 for diffusion creep, 3-5 for dislocation creep), d the grain size, and m the grain size exponent, Q is the activation energy, p is the pressure, V is the activation volume, R the gas constant and T the temperature. Hence viscous flow is described in a continuum-mechanic framework where the stress, strain and strain rate tensors under given temperature, pressure and microstructural conditions define how the material will deform.

In other words it is a 3D concept dealing with volumes and time. Therefore, the results of experiments in the viscous field are reported in terms of stress-strain curves at a given more or less constant piston displacement rate inducing bulk strain rates ($\dot{\epsilon}$ = displacement rate / deforming volume, units: s^{-1}) in the sample, or alternatively, at a given constant load (or better constant stress). Piezometric relationships connecting the recrystallized grain size to differential stress (e.g. Stipp et al., 2006, 2010) and "paleowattmeters" (Austin and Evans, 2007; Austin et al., 2008; Austin and Evans, 2009) relating mechanical work to the microstructure exist and are used to evaluate the strength of faults i.e. the supported differential stress. Viscously deformed rocks (mylonites) are usually viewed as aseismic despite the fact that torsion experiments at HT-HP conditions to high strain lead to abrupt sample failure due to "ductile fracture" (e.g. Dimanov et al., 2007; Piane et al., 2009; Rybacki et al., 2010, 2008) indicating that the material cannot flow indefinitely under the applied P-T-$\dot{\gamma}$ conditions and ultimately fractures and looses cohesion.

5.2.2 Frictional sliding

Under low temperature (LT), low pressure (LP) conditions and fast bulk strain rates rocks fracture and loose cohesion along a gouge-filled zone. This zone develops under a certain orientation with respect to the applied stress field as a result of coalescence of mode I cracks (Patterson and Wong 2005) or mode II/III cracks at higher confining pressures (Hirth and Tullis, 1994, Renshaw and Schulson 2007). Once this failure zone is developed frictional sliding on the existing failure surface limits the rock strength and is defined by the friction coefficient, μ (unitless):

$$\mu = \frac{\tau}{\sigma_n} \tag{5.2}$$

which is calculated by resolving the stress tensor into a normal stress component, σ_n acting perpendicular to the surface and shear stress, τ, acting parallel to the surface. The surface has a certain orientation, θ, with respect to σ_1 (see Fig. 5.2). This ratio is remarkably constant over a wide range of rock types, temperatures, confining pressures and displacement rates (from $< 10^{-9}$ m s^{-1} up to ~ 0.1 m s^{-1}) and is called the "Byerlee's rule" (Byerlee, 1978). Hence frictional sliding is inheritably a 2D concept dealing with surfaces. Frictional sliding is primarily normal stress dependent due to the inherited need for dilatancy when individual fragments slide past each other and have to do work against the normal stress (e.g. Marone, 1998). Nevertheless, the friction coefficient is linearly dependent on normal stress only over certain P-T conditions and at elevated confining pressure the rocks reach a maximal compressive strength, i.e. the shear stress becomes independent on normal stress (Renshaw and Schulson, 2007; Ohnaka, 1995).

Empirical rate-and-state dependent friction laws (Ruina, 1983; Dieterich, 1978) are success-

fully used to model the mechanical response of simulated fault surfaces (gouge-filled as well as rock-on-rock contact) under moderate normal stresses (usually < 500 MPa) to velocity steps. In their simplest form rate-and-state friction laws are described by the following equation:

$$\frac{\partial \mu^{ss}}{\partial [ln(\dot{d})]} = a - b \tag{5.3}$$

Where μ^{ss} is the steady state friction coefficient, $\dot{d}$ is the displacement rate (i.e. velocity, units: m s^{-1}) and two empirical variables, a and b are material properties and quantify the "direct" and "indirect" response to a velocity step. If a-b is positive the material is "velocity strengthening" and if a-b is negative the material is "velocity weakening" i.e. the shear stress needed to slide on the surface is lower at higher velocity compared to a slower velocity, which results in unstable sliding, i.e. stick-slip. "Velocity-weakening" is thought to be a necessary pre-requisite for the nucleation of earthquakes.

As the concept of volume does not - strictly speaking - exist, so neither strain nor strain rate are defined in the frictional sliding framework. Therefore, results of frictional experiments are mostly reported in friction coefficient vs. displacement at a given displacement rate. Earthquakes are viewed as frictional stick-slip processes.
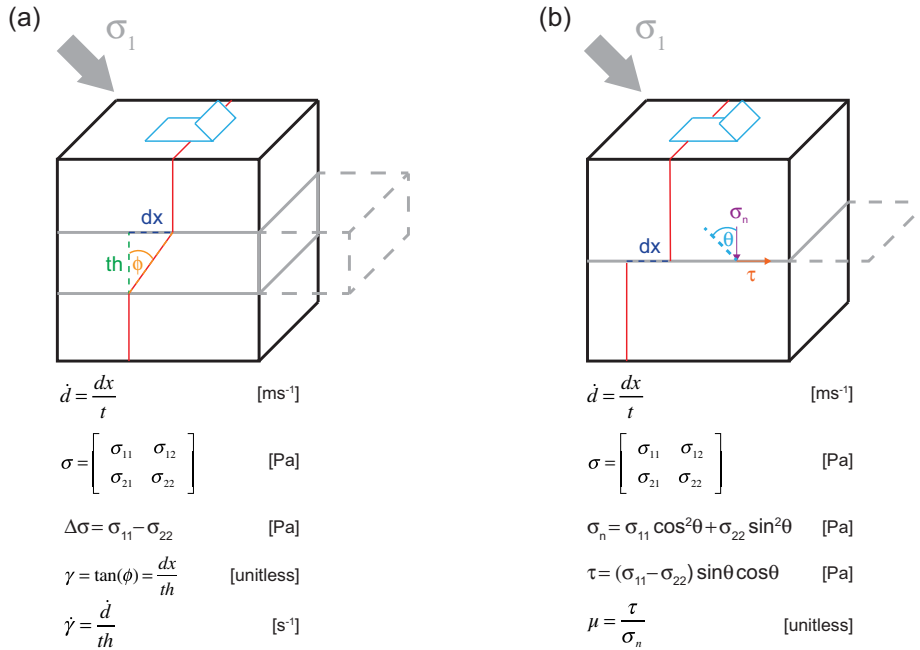
Figure 5.2: Volumes and surfaces. a) continuum-mechanics approach. dx - displacement, th - thickness, ϕ - angle of rotation of a passive line, γ - shear strain, σ- stress tensor, σ_{22} - confining pressure, $\Delta\sigma$ - differential stress, σ_{12} & σ_{21} - shear stress. Simplified 2D notation. b) surface approach. dx - displacement, σ- stress tensor, σ_n - normal stress acting perpendicular to the surface, τ - shear stress acting parallel to the surface, θ - orientation of the surface, μ - friction coefficient. Simplified 1D notation. Displacement rate, $\dot{d}$, is equally defined in both frameworks.

5.2.3 The "frictional - viscous" transition as a conceptual change

As discussed above one of the complications when dealing with the flow-to-friction transition is the conceptual change from 3D to 2D in frameworks that are used to describe material response

to stress (Fig. 5.2). Clearly the decision weather surfaces or volumes deform is observation scale dependent and therefore arbitrary. In other words, somewhere in the "frictional-viscous" transition faults stop being treated as deforming volumes and start to be treated as deforming surfaces (Fig. 5.2).

Normal stress is often treated as being an equivalent of confining pressure which is only true if no shear stress is resolved on the surface (and hence the fault does not move, Fig. 5.2). Furthermore in the 3D view material behavior seems to be strain rate dependent (strain rate = displacement rate/volume, units: s^{-1}) e.g. rocks fracture at fast strain rates and flow at slow strain rates. In the 2D view displacement rates (i.e. velocity, units: m s^{-1}) are having an effect on the frictional sliding resistance, with all rocks weakening at velocities > 0.1 m s^{-1} (e.g. Di Toro et al., 2011, 2006; Goldsby and Tullis, 2011, 2002). The comparison of strain rates to displacement rates is coupled through the deforming volume and no simple connection can be drawn. A material can deform at slow displacement rates yet very fast strain rates if the deformation is strongly localized. Work rate in the 3D approach is defined as $\dot{W} = \sigma\dot{\varepsilon} + \dot{\sigma}\varepsilon$ (units: W) (Austin and Evans, 2007, 2009) where σ is the differential stress and ε is the strain and dots signify the time derivatives (i.e. stress- and strain-rate). Whereas in the 2D approach as instantaneous power density, $\dot{\phi} = \tau\dot{d}$ (units: W/m^2) (Di Toro et al., 2011) where τ is the shear stress and $\dot{d}$ is the displacement rate (velocity). To conclude, both frameworks treat forces acting on a material (which is a physical common ground) in different fashions, which are not always straightforward to compare.

This seemingly trivial difference has important impact on the cause-and-effect relationships when interpreting natural fault zones. In the frictional field, the existence of a pre-existing surface is assumed and therefore the less deformed wall rock surrounding a fault is viewed as a "damage zone", i.e. it *post-dates* the fault core. Similarly a pseudotachylite is interpreted as a result of fast motion on the pre-existing surface (e.g. Bestmann et al., 2012). On the contrary, in the viscous field the less deformed wall rock surrounding a fault is viewed as a pre-cursor to the development of a high strain shear zone and therefore it *pre-dates* the fault. Corespondingly, a pseudotachylite is seen as a result of localization in the viscous field (e.g. John et al., 2009). Clearly, both are end member possibilities, which are often difficult to keep apart in mature fault zones, nevertheless imply either delocalization or localization within the fault zone.

In this manuscript we present new data from rock-deformation experiments performed under a wide range of conditions on granitoid cataclasites where the rocks deform by semi-brittle flow. We complement those data with previously reported microstructural data (Pec et al., 2012a) to reconstruct the evolution of the fault rocks.

5.3   Experimental methods

5.3.1   Starting material

To produce the starting material, a fine-grained granitoid boulder from Val Verzasca, Switzerland (see Keulen et al., 2007 for coordinates) was crushed to a powder by pounding on it once or twice in a steel container. The intact rock consists of $\sim 35\%$ quartz (Qtz), 29% plagioclase (Plg), 27% potassium-feldspar (Kfs) and 6% of micas and contains almost no alteration minerals (e.g. clays) (Keulen et al., 2007). After each crushing the material was sieved through

a 200 μm mesh and the coarse fragments which did not pass through the mesh were crushed again until enough material with a grain size $\leq$ 200 μm was produced. Weight loss after heating the powder for 1 h at 1000°C was $\sim$ 0.1 wt%.

5.3.2   Sample preparation

To prepare the sample, $\sim$ 0.101 g (st. dev. $= 6 \times 10^{-4}$ g) of the crushed powder with 0.2 μl ($\sim$ 0.2 wt%) water added was placed in between alumina forcing blocks pre-cut at 45°. The forcing blocks were roughened with a silicon carbide powder (grain size $\sim$ 150 μm) to assure good grip. This assembly is then weld-sealed into annealed ($\sim$ 2 h at 900°C) platinum jackets (wall thickness of 0.15 mm) with a thin nickel foil insert (thickness of 0.025 mm) using a Lampert precision welding apparatus and a cooled brass heat sink to assure good control of the added water content.

5.3.3   Sample assembly

On top and bottom of the weld-sealed sample, alumina pistons ($\varnothing$ = 6.33 mm) are attached and, together with the sample, are fitted into potassium iodide (KI) inner salt liners (Fig. 5.3). Around the sample and the inner salt cell a graphite resistivity furnace (length = 35.7 $\pm$ 0.02 mm) is inserted which is surrounded by the outer salt liners made of sodium chloride (NaCl). The temperature is controlled with a proportional-integral-derivative (PID) controller (Eurotherm) attached to a k-type thermocouple touching the centre of the shear zone (Fig. 5.3). KI has a melting point, T_m, of 681°C and a flow stress which is about 3$\times$ lower than that of commonly used sodium chloride (NaCl) at room temperature (Inoue, 1957) therefore giving a superior stress resolution. Experiments on jacketed KI placed between pre-cut alumina forcing blocks were performed to assess the influence of the confining medium and jacket on the recorded sample strength.

At a confining pressure, Pc, of $\sim$ 500 MPa, displacement rates, $\dot{d}$, of $\sim 10^{-7}$ m s^{-1} and temperatures of 300°C and 500°C, the strength of the jacketed KI samples is below the detection limit of the apparatus ($\sim$ 30 MPa, Holyoke and Kronenberg, 2010) hence the influence of the confining medium and jacket strength can be neglected (Pec et al., 2012a). Due to the short furnace length (relative to sample length) a high heat conduction in the sample assembly is present - turning of the furnace causes a rapid temperature decrease to $\sim$ 30°C in much less than 30 s.

The vertical temperature gradient from the center of the sample towards the upper part of the sample assembly was measured in two experiments using two thermocouples (TC) at different distances from each other (distance between TC$_1$ and TC$_2$ was $\sim$ 6 and $\sim$ 12 mm, with TC$_1$ being always in the middle of the sample, i.e. standard position during every experiment). Interpolation of the measured values gives a temperature gradient from the centre of the shear zone to its upper tip (distance = 3.165 mm) of $\sim$ 10%. The vertical temperature gradient in the sample assembly is $\sim 0.5 \times 10^4$ °C m^{-1} at 300°C and 1.7×10^4 °C m^{-1} at 600°C.
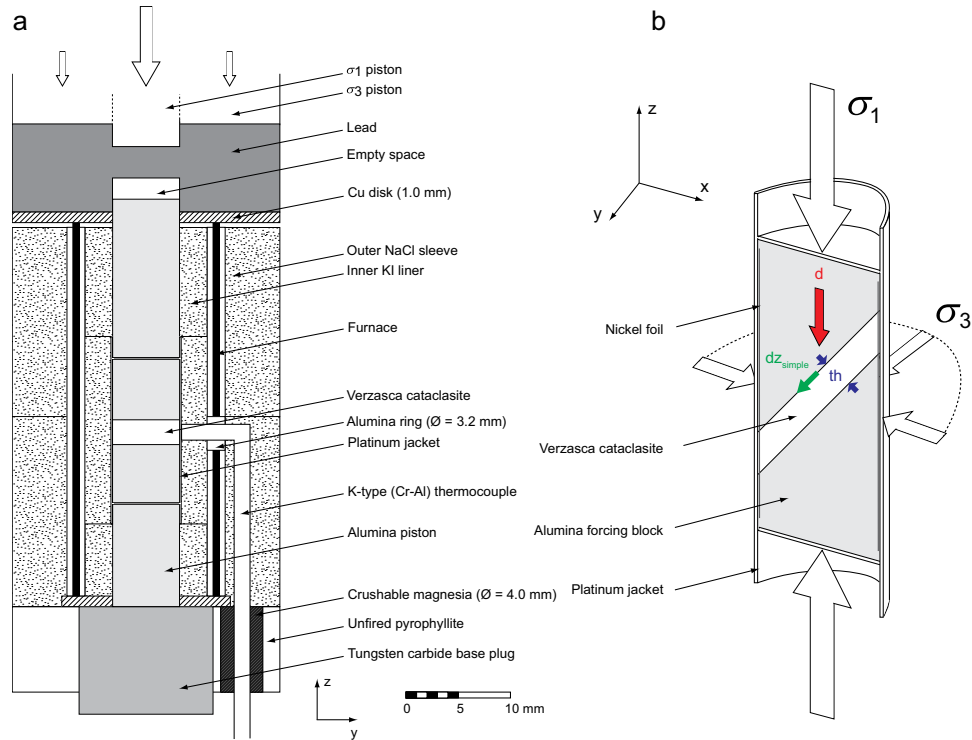
Figure 5.3: Sample assembly. a) Sample assembly and b) sample used for experiments, d = vertical displacement, th = shear zone thickness, dz_{simple} = simple shear component. (Modified after Tarantola et al., 2010)

5.3.4 Experiment execution

The sample assembly is placed in a water-cooled pressure vessel and loaded into the deformation apparatus. Confining pressure is monitored via oil pressure in the hydraulic pumping system and the force is recorded with an external load cell. Displacement of the σ_1 piston is measured externally with two devices – a direct current displacement transducer (DC-DT, resolution ~ 1 μm) and a noiseless digital linear transformation measurement (LTM) system (resolution = 0.1 μm). Advancing the confining pressure ram leads to salt collapse around the sample which builds up the confining pressure. Heating is performed in 100°C steps at a rate of 0.33°C s^{-1}. Once the desired P-T conditions are reached (typically in 5 - 8 hours) the σ_1 motor is started at a approx. constant displacement rate of $\sim 10^{-6}$, 10^{-7} or 10^{-8} m s^{-1} (or 3000 - 30 cm/year) approximating plate tectonic velocities (see Tab. 5.1). During the experiment the temperature is held constant with the PID controller. After reaching the desired amount of vertical piston displacement the samples are quenched to 200°C within 90 s resulting in varying quenching rates of 1.1 °C s^{-1}, 2.2 °C s^{-1}, 3.3 °C s^{-1}, 4.4 °C s^{-1} for samples deformed at 300, 400, 500 and 600°C, respectively. Simultaneously with quenching the load is removed from the sample and an initial differential stress of ~ 100 MPa is kept on the sample at the end of quenching to minimize unloading cracks. Temperature is then lowered to cooling water temperature (~ 14°C) in 15 – 30 minutes and load as well as confining pressure are progressively removed during depressurization to room conditions (within $\sim 2 – 4$ hours). The whole experiment (pressurization – deformation – depressurization) takes between $\sim 8 –$ 100 hours depending on the applied displacement rate.

#	T (°C)	Pc (MPa)	Peak τ (MPa)	Steady-state τ (MPa)	τ relaxed (MPa)	Peak σ_n (MPa)	peak μ	mean $\dot{\gamma}$ (s^{-1})	mean $\dot{d}$ (m s^{-1})	water (wt%)	th$_f$ (mm)	γ_{meas}	γ_{calc}
282MP	300	505	1427	N/A	N/A	1933	0.74	2.2×10^{-3}	1.30×10^{-6}	0.2	0.707	2.04	2.59
311MP	300	510	1441	N/A	N/A	1951	0.74	2.9×10^{-3}	1.60×10^{-6}	0.2	0.565	3.73	3.78
310MP	300	310	1049	970	79	1356	0.77	2.32×10^{-4}	1.25×10^{-7}	0.2	0.502	4.92	3.75
251MP	300	515	N/A	N/A	N/A	N/A	N/A	1.97×10^{-4}	1.38×10^{-7}	0.2	0.79	1.49	2.34
261MP	300	515	N/A	N/A	N/A	N/A	N/A	1.75×10^{-4}	1.41×10^{-7}	0.2	0.359	2.58	1.95
288MP	300	535	1271	1260	11	1805	0.70	3.04×10^{-4}	1.42×10^{-7}	0.2	0.440	4.00	3.90
291MP	300	510	1319	1275	44	1833	0.72	2.80×10^{-4}	1.44×10^{-7}	0.2	0.513	3.66	3.84
260MP	300	1010	1524	1455	69	2533	0.60	1.90×10^{-4}	1.33×10^{-7}	0.2	0.646	1.64	2.12
262MP	300	1475	1597	1515	82	3071	0.52	1.64×10^{-4}	1.19×10^{-7}	0.2	0.715	1.52	1.93
279MP	300	490	1279	1255	24	1770	0.72	2.08×10^{-5}	1.24×10^{-8}	0.2	0.622	3.10	3.78
287MP	300	510	N/A	N/A	N/A	N/A	N/A	1.79×10^{-5}	1.27×10^{-8}	0.2	0.646	1.94	1.96
317MP	300	500	1237	1135	102	1735	0.71	2.25×10^{-5}	1.39×10^{-8}	0.2	0.599	2.90	3.28
328MP	300	980	1413	1325	88	2394	0.59	2.27×10^{-5}	1.19×10^{-8}	0.2	0.468	3.61	3.42
315MP	400	510	1218	1195	23	1728	0.71	2.1×10^{-3}	1.20×10^{-6}	0.2	0.588	4.01	3.64
313MP	400	520	1162	1033	129	1681	0.69	2.19×10^{-4}	1.25×10^{-7}	0.2	0.496	3.08	3.28
306MP	400	485	1112	970	142	1599	0.70	2.11×10^{-5}	1.31×10^{-8}	0.2	N/A	N/A	4.12
284MP	500	530	1171	1085	86	1699	0.69	2.1×10^{-3}	1.20×10^{-6}	0.2	0.586	2.82	3.38
247MP	500	495	N/A	N/A	N/A	N/A	N/A	1.25×10^{-4}	9.40×10^{-8}	0.2	0.676	2.32	1.85
253MP	500	530	1034	N/A	N/A	1565	0.66	1.78×10^{-4}	1.35×10^{-7}	0.2	0.659	2.08	1.85
289MP	500	520	1111	943	168	1633	0.68	2.72×10^{-4}	1.40×10^{-7}	0.2	0.490	4.10	3.98
290MP	500	520	1057	966	91	1575	0.67	3.13×10^{-4}	1.57×10^{-7}	0.2	0.468	4.30	4.01
255MP	500	1010	1247	N/A	N/A	2259	0.55	1.65×10^{-4}	1.30×10^{-7}	0.2	0.690	1.59	1.69
256MP	500	1020	1250	1138	112	2272	0.55	1.97×10^{-4}	1.38×10^{-7}	0.2	0.606	2.56	2.18
263MP	500	1555	1443	1255	188	2997	0.48	2.07×10^{-4}	1.44×10^{-7}	0.2	0.745	N/A	2.44
266MP	500	1515	1369	1215	154	2885	0.47	1.85×10^{-4}	1.34×10^{-7}	0.2	0.626	2.44	2.00
278MP	500	500	1069	948	121	1571	0.68	2.42×10^{-5}	1.46×10^{-8}	0.2	N/A	N/A	3.96
286MP	500	490	907	N/A	N/A	1676	0.54	1.62×10^{-5}	1.20×10^{-8}	0.2	0.504	2.14	2.78
329MP	500	965	1048	859	190	2015	0.52	2.49×10^{-5}	1.50×10^{-8}	0.2	0.628	2.40	3.18
314MP	600	520	994	910	84	1512	0.66	2.8×10^{-3}	1.60×10^{-6}	0.2	0.589	3.91	3.92
312MP	600	495	937	790	147	1951	0.48	2.14×10^{-4}	1.26×10^{-7}	0.2	0.573	3.73	3.48
307MP	600	500	567	480	87	1065	0.53	1.69×10^{-5}	1.25×10^{-8}	0.2	0.742	2.14	1.93
316MP	600	505	728	650	78	1233	0.59	2.77×10^{-5}	1.56×10^{-8}	0.2	0.547	3.08	3.24
330MP	600	1000	858	668	190	1855	0.46	2.28×10^{-5}	1.35×10^{-8}	0.2	0.617	3.27	3.41

Table 5.1: Summary of experimental conditions. T - temperature, Pc - confining pressure, τ - shear stress, τ relaxed - shear stress relaxed from peak strength to mean value of quasi steady-state, σ_n - normal stress resolved on 45° pre-cut, μ - friction coefficient resolved on 45° pre-cut, $\dot{\gamma}$ - shear strain rate, $\dot{d}$ - displacement rate, th$_f$ - final thickness measured in thin sections, γ_{meas} - shear strain measured in thin sections, γ_{calc} - shear strain calculated from apparatus record

5.3.5 Data acquisition and treatment

Confining pressure, load and axial piston displacement are recorded in parallel with an analogue chart recorder (sampling frequency 50 Hz) and a digital data logging system (LabView 7.1) sampling at 1 or 2 Hz (one record point equals $\sim$ 0.01, 0.1 or 0.5 μm of piston displacement depending on the applied displacement rate). The data are evaluated with a MATLAB program ("rig", http://sites.google.com/site/rigprogram). The digital record is smoothed with a zero phase shift forward-reverse running average filter over 10 μm of piston displacement to filter digital input steps. The smoothing is constrained through comparison with analogue records and special care is taken that no artifacts are introduced. The mechanical data are then corrected for decreasing forcing blocks overlap with increasing slip, for apparatus compliance, for changes in confining pressure relative to hit-point ($\pm$10 MPa or less, i.e. $\sim$ 4% at 500 MPa confining pressure) and "friction" associated with driving the tungsten carbide piston into the sample assembly (1.3 kN/mm), Tarantola et al. (2012).

During deformation, thickness of the fault rock layer decreases continuously to $\sim$ 45% of its original thickness. Therefore the recorded vertical displacement is resolved into a thinning component ($\Delta\ th$) and a simple shear component (Δdz_{simple}). The starting thickness of the fault rock layer (th_0) was measured on post-mortem thin sections of two samples pressurized to Pc $\sim$ 500 MPa and heated to 300°C and 500°C without applying any differential stress. The decrease in thickness is slightly non-linear and continues progressively up to a $\gamma \sim 5$ (Fig. 5.4). No systematic dependence on temperature (Fig. 5.4), confining pressure or displacement rate can be detected in the thickness of the shear zones. To simplify the calculation of shear strain, we assume that the thinning rate is constant and that the total amount of $\Delta\ th$ ($= th_0$ - th_{final}) occurs linearly during the entire duration of the experiment (the data can be also reasonably fitted with a linear fit with an R^2 of $\sim$ 0.8 over the studied shear strain range). As no lateral escape of the material is observed (perpendicular to the shearing direction), we conclude that thinning occurs as the material is being pushed out at the ends of the forcing blocks (parallel with the shearing direction). The progressive thinning causes an increase in bulk instantaneous shear strain rate, $\dot\gamma$, of $\sim$2$\times$, thus reaching mean bulk shear strain rates of $\sim 10^{-3}$, 10^{-4} and 10^{-5} s^{-1} at displacement rates of $\sim 10^{-6}$, 10^{-7} and 10^{-8} m s^{-1}, respectively (see Tab. 5.1 for accurate values). In this manuscript we prefer to report the applied displacement rate as strain partitioning and localization leads to a strongly heterogeneous strain-rate distribution in the samples. Also, this quantity is commonly reported in friction experiments allowing easy comparison.

The calculated amount of finite shear strain from the apparatus record was compared to that measured on thin sections because the amount of finite shear strain may vary slightly form experiment to experiment due to compaction during the building up of the confining pressure. A good correlation is achieved with the data lying in a range of $\gamma \pm 0.7$. No systematic dependence on temperature (Fig. 5.4), displacement rate or confining pressure is observed with the exception of the experiment performed at 300MPa confining pressure which are conditions sub-optimal for the use of the solid medium deformation apparatus. The measured finite strain in thin sections is taken as more representative and therefore the data is re-calculated by the following equation:

$$\gamma_{(t)} = \frac{\gamma_{rigData(t)}}{max(\gamma_{rigData})} \times \gamma_{measured} \qquad (5.4)$$
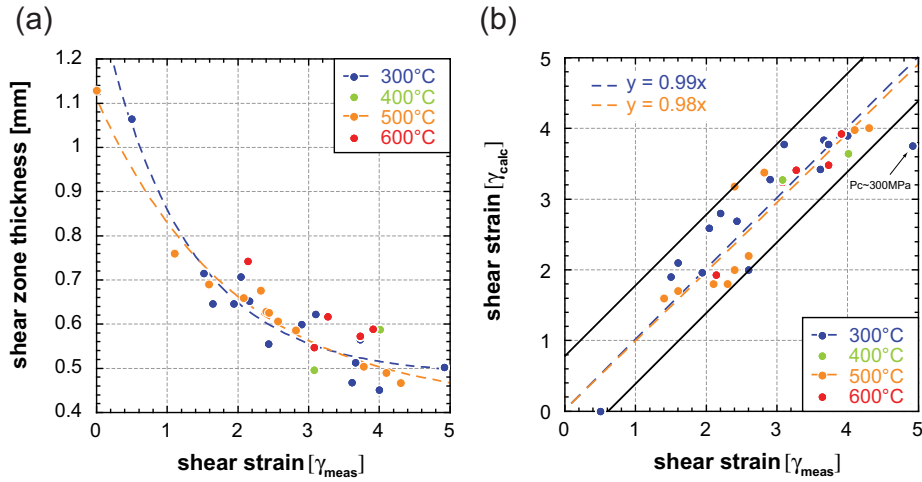
Figure 5.4: Sample thinning and finite shear strain. a) thickness vs. measured shear strain b) calculated vs. measured shear strain. Black lines contain all data from experiments at Pc > 300 MPa.

where $\gamma_{(t)}$ = shear strain at t record time, $\gamma_{rigData}$ = shear strain calculated from machine data and $\gamma_{measured}$ = shear strain measured on thin sections. All reported values of shear strain refer to the shear strain measured in thin sections unless explicitly stated otherwise.

The accuracy of the Grigg's type solid medium deformation apparatus was recently compared to a more accurate gas deformation apparatus (Holyoke and Kronenberg, 2010). It seems that the solid medium deformation apparatus reproducibly and systematically overestimates the absolute measured stress and a simple linear correction in the form:

$$\tau_{(GasApparatus)} = 0.73 \times \tau_{(GriggsApparatus)} - 24 MPa \tag{5.5}$$

Can be applied to our data to obtain more accurate stress estimates if necessary.

5.4   Mechanical data

5.4.1   Influence of temperature and displacement rate in samples deformed at Pc ∼ 500 MPa

High peak strength ($580 < \tau < 1420$ MPa) occurs around a γ of ∼ 0.8 - 2.1. Samples deformed at higher temperatures are systematically weaker compared to samples deformed at lower temperatures (Fig. 5.5). At 300°C tiny stick-slip events appear shortly before reaching peak strength (stress drop of 2 - 5 MPa, i.e. < 0.5%). The weakening occurs over ∼5 - 450 minutes depending on the applied displacement rate and no further stick-slip events can be detected. A correlation of how much stress is relaxed with temperature is seen. The 300 °C experiments weaken - if at all - only about ∼40-50 MPa on average. Samples deformed at 400-500°C weaken ∼ 130 - 140 MPa on average and samples deformed at 600°C weaken around 95 MPa on average. This prolonged weakening is accompanied by a transient increase in the measured vertical piston displacement rate by ∼ 20% (see chapter 4). Further a weak displacement rate dependence on the amount of post-peak weakening is seen with fast experiments
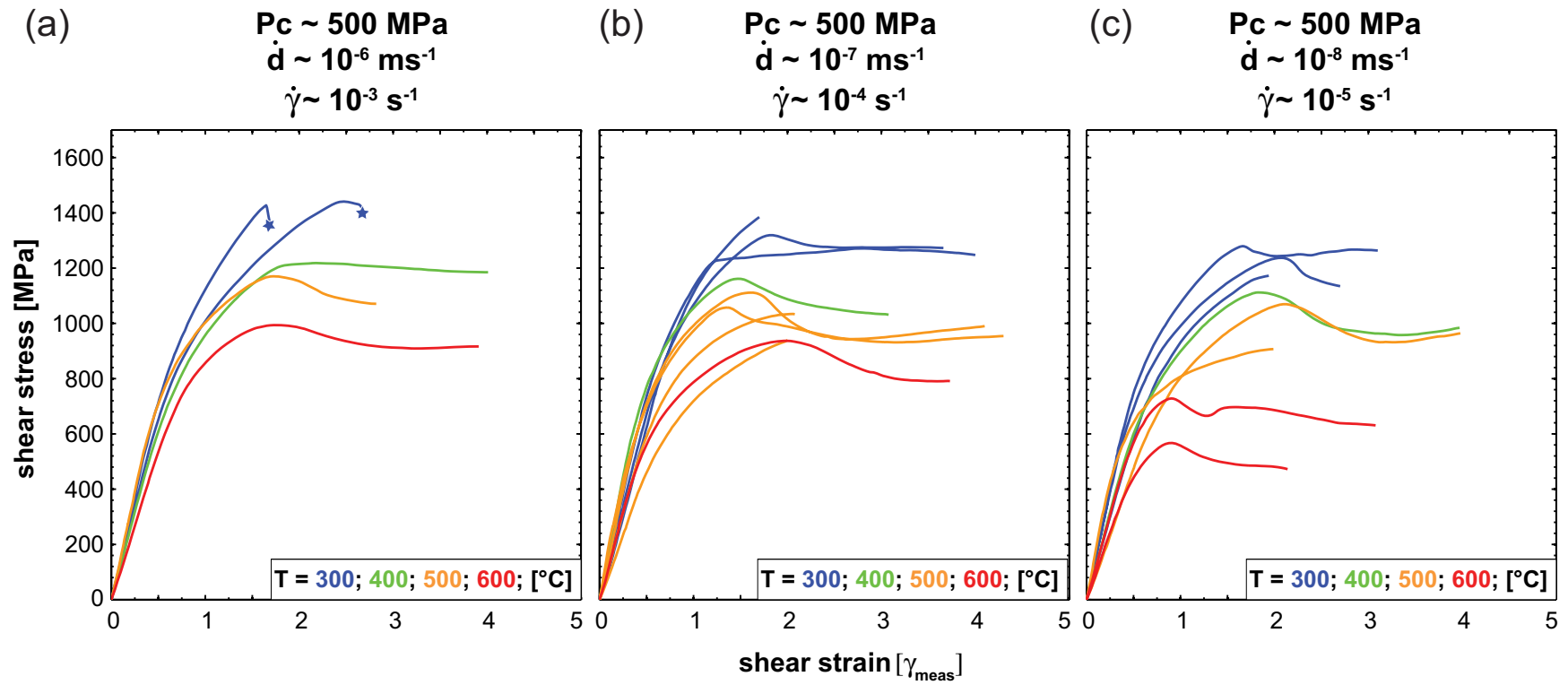
Figure 5.5: Stress - strain curves from medium to high-strain experiments. a-c) grouped by temperature and displacement rate at identical confining pressure. Stars indicate abrupt failure.

weakening < 100 MPa (for T $> 400°$C) and slower experiments weakening usually > 100 MPa (for T $> 300°$C) (Tab. 5.1). After the weakening, the samples continue to deform at a quasi steady-state shear stress up to a shear strain of ~ 4. The steady state stress level is weakly displacement rate dependent and this dependence gets more pronounced at higher temperatures (Fig. 5.5). Only samples deformed at T $= 300°$C, Pc ~ 500 MPa and displacement rates of 10^{-6} m s^{-1} fail abruptly around peak strength. The cracking is audible and is accompanied by a stress drop of ~ 800 MPa and a vertical piston displacement of 60 - 200 μm.

If plotted in the strain rate – shear stress space, we find that the fault rocks behave as a bingham body, i.e. a threshold stress is present before the material starts to flow (visco-plastic behavior). If this data would be fitted on a power-law creep equation, very high stress exponents (n ~ 17 - 48) and low activation energies (Q ~ 15-125 kJ/mol) would be obtained indicating a "power-law breakdown" regime. Furthermore it is interesting to note that the peak strength of experiments deformed at $400°$C is only ~ 60 MPa higher than at $500°$C, whereas the difference between $400°$C and $300°$C is ~ 130 MPa and between $500°$C and $600°$C is ~ 160 MPa (Figs. 5.5 and 5.6).
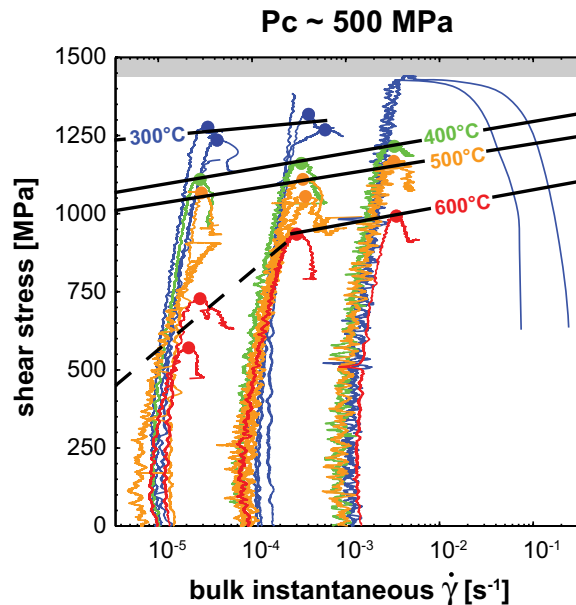
Figure 5.6: Bulk instantaneous shear strain rate vs. shear stress. The slowest experiments at $600°$C are microstructurally distinct and other physical processes are operative. Fastest experiments at $300°$C fail abruptly, the sampling rate is not high enough to resolve details during failure.

5.4.2 Influence of confining pressure and displacement rate

Experiments performed at T$=300°$C and displacement rate $\dot{d} \sim 10^{-7}$ m s^{-1} at different confining pressures (Pc ~ 300, 500, 1000 and 1500 MPa) show that the strength of the fault rock increases with increasing confining pressure and reaches higher peak stresses at lower shear strains (Fig. 5.7). The increase in strength is most pronounced between 300 and 1000 MPa confining pressure (~ 475 MPa) whereas only very little increase (~ 75 MPa) takes place between 1000 and 1500 MPa confining pressure (Fig. 5.7a) indicating that the rocks reach their maximum compressive strength. Furthermore at displacement rates of 10^{-7} m s^{-1} the samples at 1000 MPa are always systematically stronger than at 500 MPa confining pressure

irrespective of the temperature. This systematic behavior is lost at displacement rates of 10^{-8} m s^{-1} where samples deformed at T $\geq$ 500°C tend to reach similar or even lower flow stresses during steady state deformation than samples deformed at 500 MPa confining pressure (Fig. 5.8). Slow displacement rates (10^{-8} m s^{-1}) at 1000 MPa confining pressure yield well behaving steady-state deformation (Fig. 5.7b and Fig. 5.8) and the weakening slope (in strain – stress space) after peak strength is steeper and relaxes more stress (90-185 MPa) compared to lower confining pressure experiments.
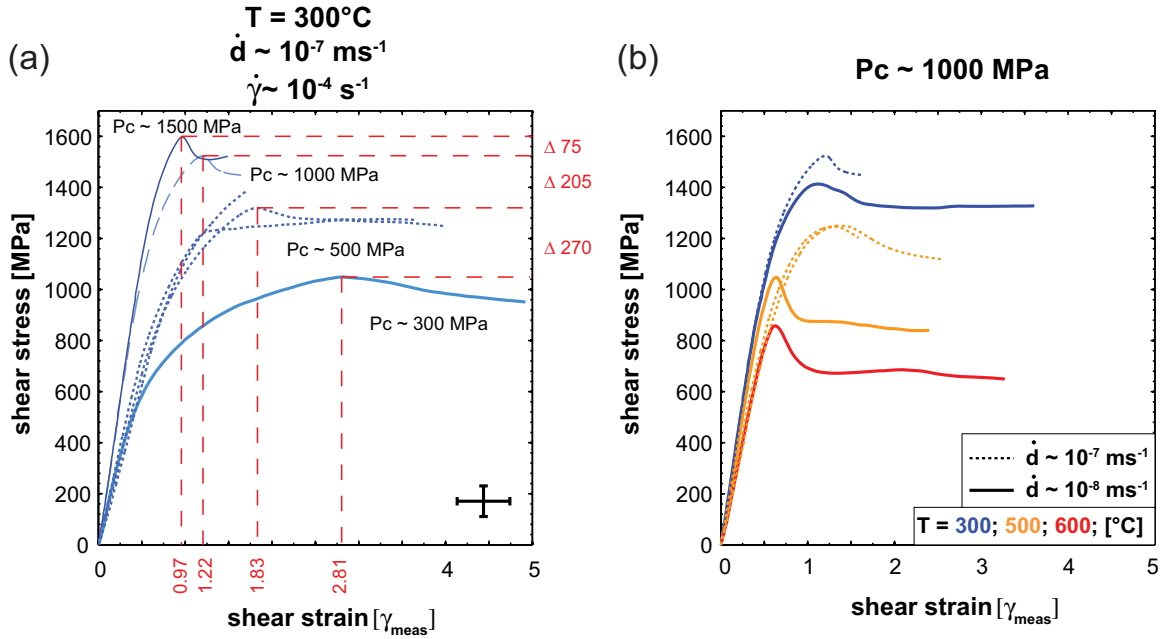
Figure 5.7: Influence of confining pressure. a) samples deformed at identical (T,$\dot{d}$) conditions at 300-1500 MPa confining pressure. Cross shows approximate error bar. b) displacement rate dependence at Pc $\sim$ 1000 MPa. $\dot{d} \sim 10^{-7}$ m s^{-1}, i.e. $\dot{\gamma} \sim 10^{-4}$ s^{-1}, $\dot{d} \sim 10^{-8}$ m s^{-1}, i.e. $\dot{\gamma} \sim 10^{-5}$ s^{-1}
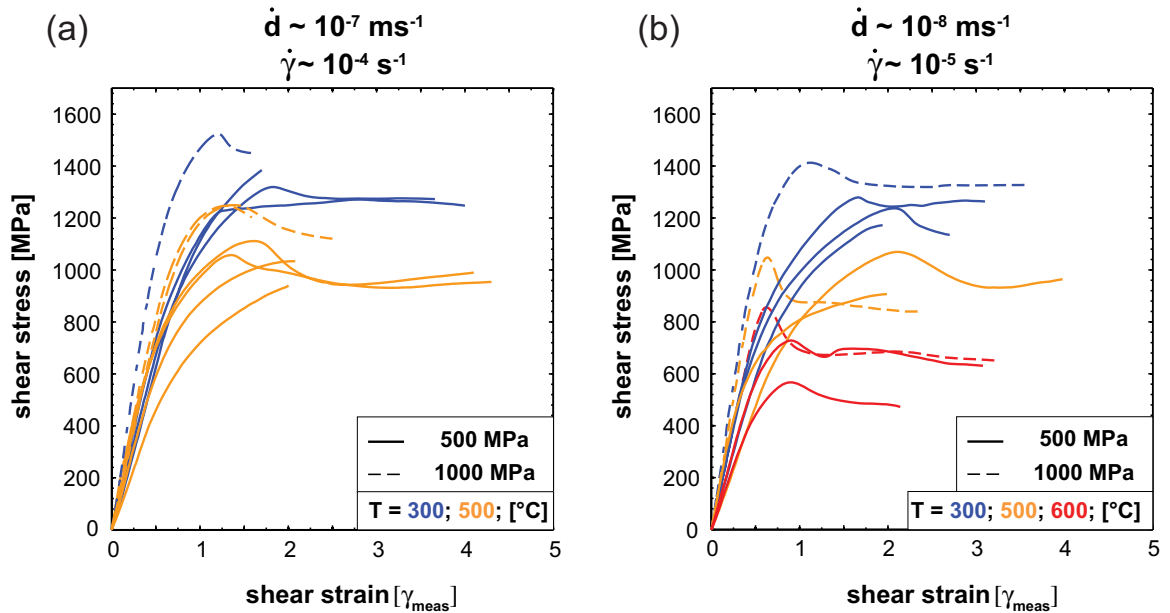
Figure 5.8: Influence of displacement rate and confining pressure. a) displacement rate $\sim 10^{-7}$ m s^{-1}, i.e. shear strain rate $\sim 10^{-4}$ s^{-1}. b) displacement rate $\sim 10^{-8}$ m s^{-1}, i.e. shear strain rate $\sim 10^{-5}$ s^{-1}.

5.4.3   Friction

In the previous section we have treated the fault rocks in a 3D continuum-mechanics framework (stress, strain) however strength of faults is usually described in terms of friction as a surface process (2D approach). We calculate the peak friction coefficient (i.e. at peak stress) on the 45° pre-cut surface as $\mu = \tau/\sigma_n$. A clear temperature dependence (~0.05 difference between 300°C and 500°C experiments) and a weak displacement rate dependence is seen (Fig. 5.9). Furthermore, the friction coefficient of the fault rock decreases with increasing confining pressure as the shear stress has reached a maximum value (maximal compressive strength) whereas the normal stress further increases in proportion to confining pressure. The friction coefficient μ is in the range typical for rock materials (Byerlee, 1978) at $300 - 500$ MPa confining pressure (~ 0.8 - 0.6) except for samples deformed at 600°C and $\dot{d} \sim 10^{-8}$ m s^{-1}. At confining pressures above 1000 MPa the friction coefficient is lower (< 0.6) at all studied temperatures (Fig. 5.9).
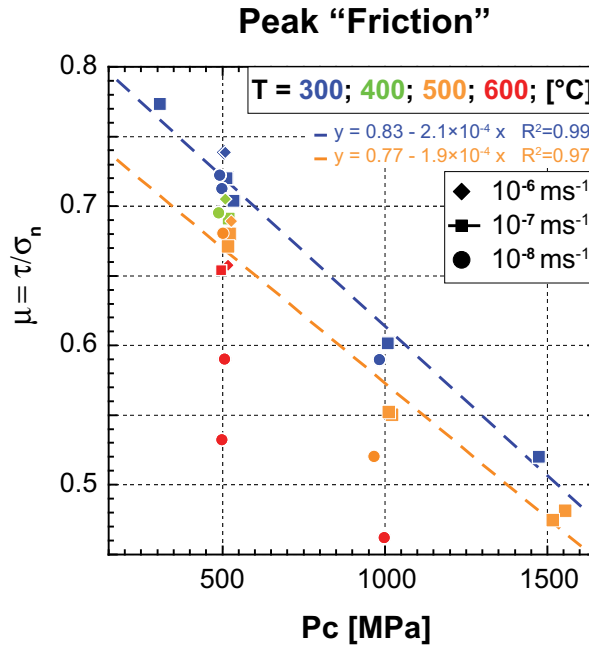
Figure 5.9: Friction coefficient resolved at the 45° pre-cut at peak stress. Best fit lines are obtained from experiments performed at $\sim 10^{-7}$ m s^{-1} i.e. shear strain rate $\sim 10^{-4}$ s^{-1}

5.5   Analytical methods

5.5.1   Sample preparation and image acquisition

After the experiment samples are vacuum impregnated with a low viscosity epoxy and doubly polished thin sections ($\sim 30 \ \mu$m thick) parallel to the compression axis, z, and the displacement direction, x, were prepared. A set of complementary thin sections parallel to the compression axis and perpendicular to the displacement (z-y) direction was made to resolve the strain distribution in the samples. The samples were carbon-coated and analyzed with field-emission gun (FEG) scanning electron microscopes (SEM) equipped with energy-dispersive spectrometers (EDS) (Philips XL 30 ESEM and FEI Nova Nano SEM 230) under 5 - 20 kV acceleration

voltage. At selected sites, transmission electron microscope (TEM) sections were prepared with a FEI NanoLab 600 FIB-SEM using Ga-ion beam for milling. TEM sections ($\sim$ 50-100 nm thick) were analyzed in a FEI Technai 20 FEG TEM with an EDS detector under 200 kV acceleration voltage. Cold CL images were obtained with a Technosys 8200 MkII at 20 kV acceleration voltage.

5.5.2 Image analysis methods

To evaluate the bulk microstructural development, areas from the middle of the shear zone – where slip is transferred from one forcing block to the other – and parallel to the forcing block – fault rock boundary were analyzed (Fig. 5.10). The length of the analyzed image was 1666 μm (i.e. $\sim$ 18% of the forcing block length) and covered the entire thickness of the shear zone. Images were consistently analyzed with a top-to-the right sense of shear and angles are measured counterclockwise from 0° (positive x-direction) to 180°. The shear zone boundary is always horizontal, i.e. at 0°. Grain size refers to the equivalent diameter of a circle calculated from the measured area of individual grains. We take the common stereological assumption that the measured area% $\sim$ volume% (for proof see Underwood, 1970). In the analyzed areas following parameters were quantified:

1. Volume% of individual mineral phases (Quartz – Qtz, Plagioclase – Plg, Potassium feldspar – Kfs, Biotite – Bt, White mica – Wm). SEM-BSE and CL images were combined to separate individual mineral phases via gray level thresholding and manual tracing in imageSXM (http://www.liv.ac.uk/$\sim$sdb/ImageSXM/) and Photoshop^{TM}.

2. Axial ratio (b/a) and orientation (ϕ) of individual phase aggregates (Qtz, Plg, Kfs) obtained via autocorrelation function (ACF) which was thresholded at two different levels, 8000 μm^2 and 400 μm^2 which roughly correspond to typical cross-sectional areas of bigger and smaller aggregates. (for full procedure see Heilbronner (1992) and Pec et al. (2012a), software at: http://pages.unibas.ch/earth/micro/).

3. Volume% of "survivor grains" (well identifiable grains at a magnification of 100$\times$, i.e. 1px = 833 nm) and "fragmented mantles" (finely crushed material with a grain size < 100 nm where no individual grains but porosity can be observed at a magnification of 100$\times$). "Survivor grains" (V_s) and "fragmented mantles" (V_m) together form an "aggregate" (V_a) delimited by phase to phase contacts. The ratio between vol% of "survivor grains" to vol% of "aggregate" quantifies comminution and is calculated by the following equation:

$$V_s/V_a = \frac{A_s}{A_a} \times 100; (\%) \qquad (5.6)$$

Where A_s is the area fraction of "survivor grains", A_a is the area fraction of "aggregates". It spans from 100% (entire aggregate formed by survivor grains) to 0% (entire aggregate formed by fragmented mantle) (Pec et al., 2012a; Boutareaud et al., 2012).

4. Volume% of "slip zones" that were manually traced based on a) unloading cracks which concentrate in the cohesive material, b) different CL signal and c) no resolvable porosity up to a magnification of 20 000$\times$ (1 pixel = 4 nm) in the FEG-SEM.

5. Volume% of individual mineral phases within the slip zones, which were obtained by combining the manually traced slip zones with phase maps of individual aggregates obtained by thresholding.
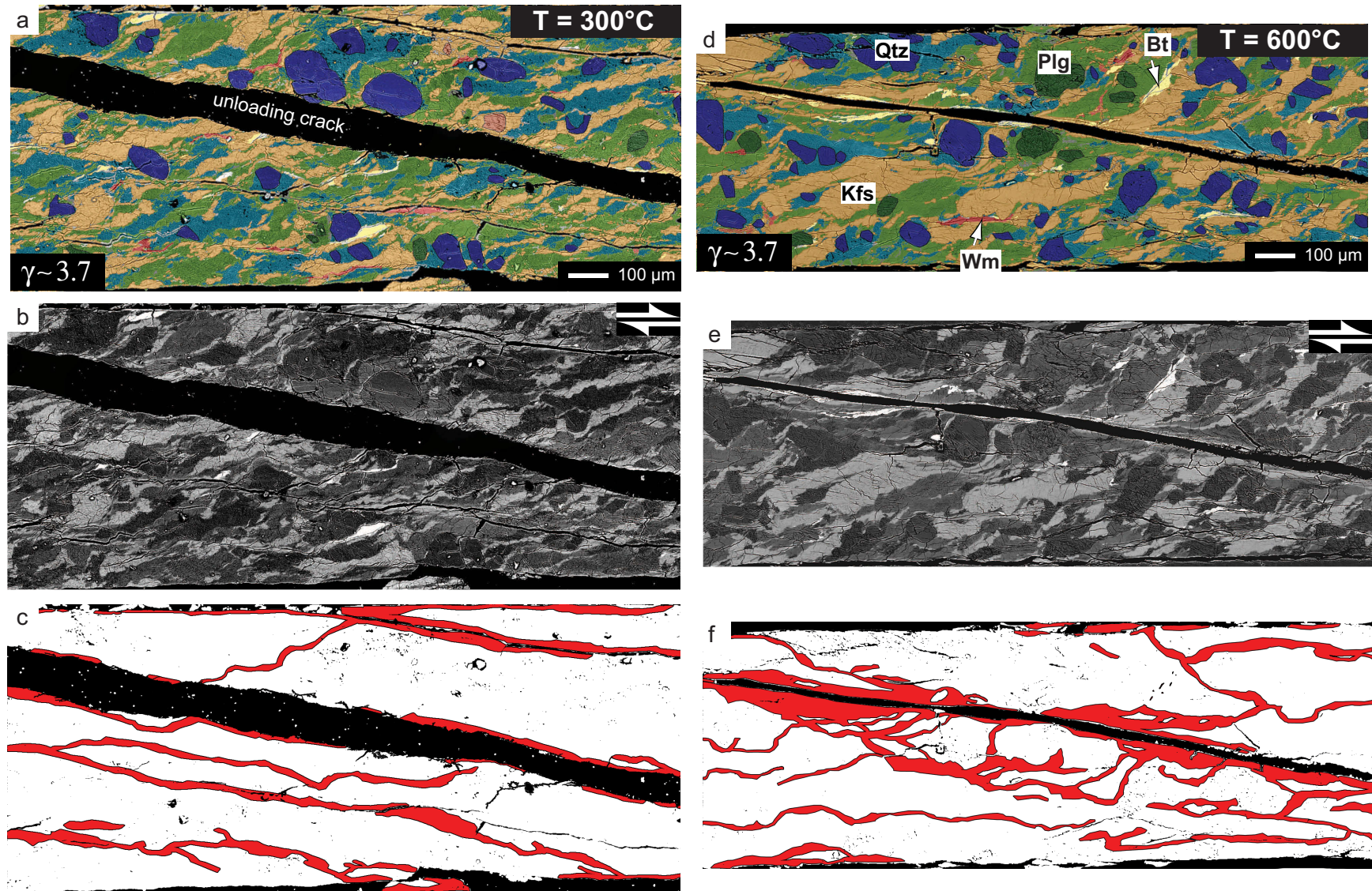
Figure 5.10: Representative microstructures used for image analysis. Both experiments performed at identical conditions (Pc $\sim$ 500 MPa, $\dot{d} \sim 10^{-7}$ m s^{-1}) to the same amount of finite strain ($\gamma \sim 3.7$) at 300°C (a-c) and 600°C (d-f). a,d) segmented images used for image analysis. blue – Qtz, orange – Kfs, green – Plg, yellow – Bt, red – Wm. Darker colors – survivor grains, lighter colors – fragmented mantle. b,e) SEM-BSE z-contrast images. Minerals in order of increasing brightness – Qtz, Plg, Wm, Kfs, Bt. c,f) manual tracings of slip zones (red), black are unloading cracks.

5.5.3 V_s/V_a ratio

Comminution occurs during the entire range of bulk shear strains explored (up to a γ_{bulk} of $\sim$ 5). Qtz always fractures the least and both feldspars fracture the most. A weak but systematic dependence of the amount of qtz survivor grains can be seen with stress and/or temperature (as we performed constant displacement rate experiments stress and temperature are coupled). V_s/V_a ratio of Qtz deformed at lower stresses at 500°C is about 10% higher than at higher stresses at 300°C (Fig. 5.11). The V_s/V_a ratio can be fitted with an exponential decay function for all conditions, it decreases most abruptly in the early stage of the experiments with a reduction by $\sim$ 60% of qtz survivor grains between bulk shear strains of 0 and 2. Further increase in the bulk shear strain from 2 to $\sim$ 4 decreases the amount of qtz survivor grains only slightly by further $\sim$15%. No clear dependence on stress or temperature can be detected in both feldspars due to the little amount of survivor grains (V_s/V_a is close to 0% at γ_{bulk} of > 2.5, Fig. 5.11) and further, no clear dependence can be observed with confining pressure or displacement rate with the exception of samples deformed at 600°C and displacement rates of 10^{-8} m s^{-1} which comminute the least and where also stresses were the lowest.
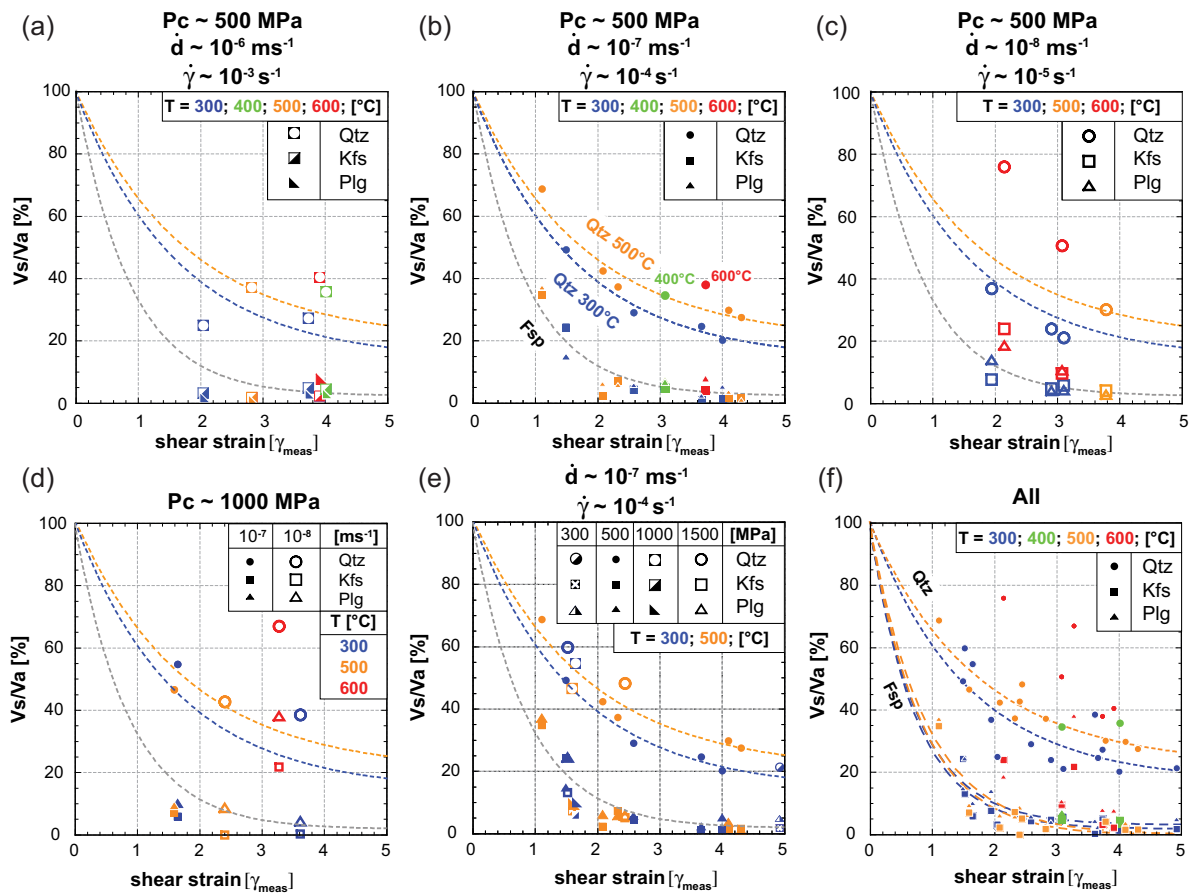
Figure 5.11: Comminution defined as the ratio of survivor grains (V_s) to the aggregate (V_a). a-c) grouped by temperature and displacement rate at Pc $\sim$ 500 MPa. Best-fit lines were obtained at 10^{-7} m s^{-1} and are kept for reference. d) grouped by temperature and displacement rate at Pc $\sim$1000 MPa e) grouped by confining pressure and temperature at a displacement rate of $\sim$10^{-7} m s^{-1} f) all experiments grouped by temperature.

5.5.4   Bulk fabric anisotropy and shape preferred orientation (SPO)

Anisotropy of the fabric obtained by the autocorrelation function (ACF) thresholded at two areas (8000 μm^2 and 400 μm^2, corresponding to larger and smaller aggregates, respectively) increases with the axial ratio b/a decreasing progressively from $\sim$ 0.7 to $\sim$ 0.4 at bulk shear strains of $\sim$ 4. A kink around a bulk shear strain of $\sim$2.5 can be detected. The fabric anisotropy increases with b/a decreasing from $\sim$ 0.7 to $\sim$ 0.5 for small aggregates and to $\sim$ 0.4 for big aggregates up to bulk shear strains of $\sim$2.5 (Fig. 5.12). The anisotropy increase is much less pronounced during higher strain deformation after a γ_{bulk} of 2.5. A weak but systematic dependence on temperature and/or stress is seen with high temperature samples being less anisotropic (i.e. less flattened) than low temperature samples (Fig. 5.10). Qtz aggregates are systematically less anisotropic than both feldspar aggregates at all shear strains. Furthermore the anisotropy of the big aggregates (8000 μm^2) is larger compared to small aggregates (400 μm^2) (Fig. 5.12). The orientation of the ACF ellipse shows a large scatter however tends to rotate antithetically to the induced sense of shear up to a γ_{bulk} of $\sim$ 2 in 500°C experiments. After a γ_{bulk} of $\sim$ 2 the orientation gets progressively more boundary parallel and scatters around 10° with respect to the shear zone boundary. Large Qtz aggregates tend to be more boundary parallel than both feldspar aggregates at high bulk strains (Fig. 5.12).
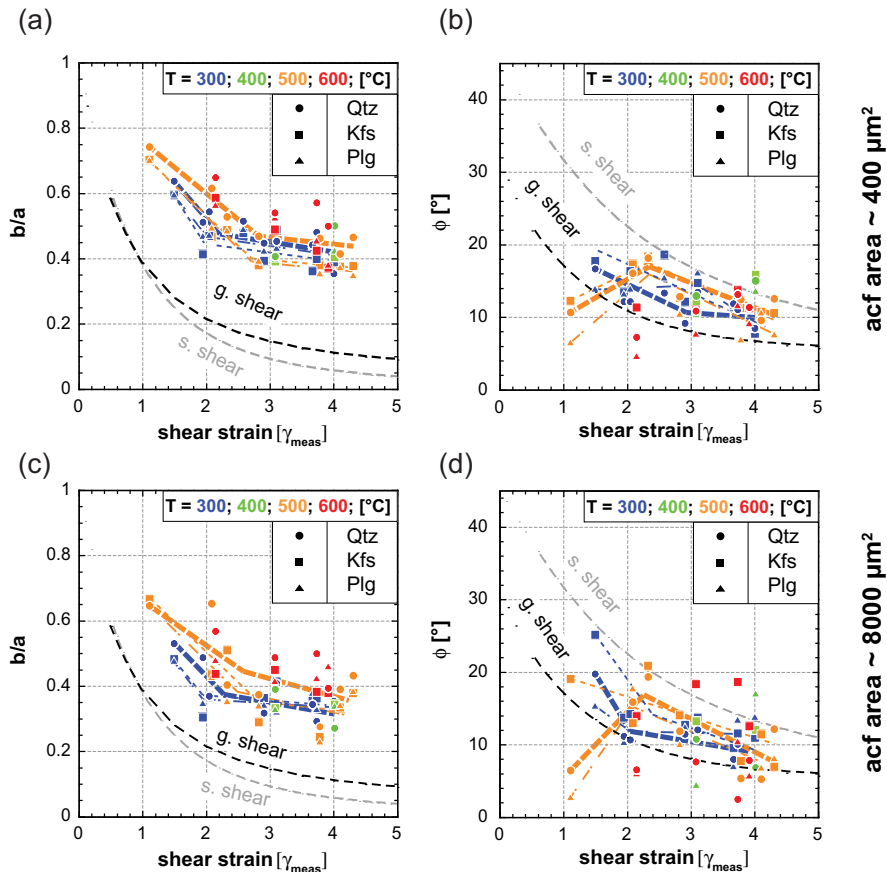
Figure 5.12: Bulk fabric anisotropy and orientation determined by the autocorrelation function (acf). Only experiments performed at Pc $\sim$ 500 MPa are shown. Dashed lines show the evolution of anisotropy and orientation calculated for a passive marker in pure simple shear (gray) and general shear (black) derived from the thinning data (see Fig. 5.4) a) anisotropy and b) orientation of small aggregates ($\sim$400 μm^2). c) anisotropy and d) orientation of the large aggregates ($\sim$8000 μm^2). Lines highlight the general trend for 300°C (blue) and 500°C (orange) experiments. Thick lines – Qtz, thin lines – Fsp.

5.5.5 Slip zones

Around a γ_{bulk} of ~ 1.5 first incipient slip zones can be detected as non-porous, cohesive zones where unloading cracks concentrate. First, they form isolated patches at high stress / strain sites adjacent to bigger quartz grains and micas, usually in a C' orientation, where extremely fine-grained feldspar material forming the "fragmented mantle" is abundant (Fig. 5.13), (Pec et al., 2012a). With increasing finite strain these zones become interconnected and form an anastomozing network around peak strength. The interconnectivity of the layers increases with increasing temperature and finite strain (Fig. 5.10). At high bulk shear strains (>2.5), the layers tend to fold in the C' orientation and slip zones in a C orientation (boundary parallel) become well developed (Fig. 5.13). Estimates of shear strain accommodated in the slip zones are around a γ of $\sim 5 - 10$ at γ_{bulk} of ~ 2 and even higher ($\gamma > 20$) at higher bulk strains ($\gamma_{bulk} \sim 4$) however markers to measure offset are hard to reliably detect at high bulk shear strains. The total volume of the slip zones increases steadily with increasing bulk finite strain and increasing temperature except for samples deformed at 600°C and displacement rates of 10^{-8} m s^{-1} (Fig. 5.14). A weak but systematic dependence of the amount of slip zones can further be seen with confining pressure and displacement rate where the slip zones are more abundant at higher confining pressures and faster displacement rates (Fig. 5.14). The slip zone microstructures change pronouncedly with increasing strain and their evolution is treated in section 5.6 in detail.
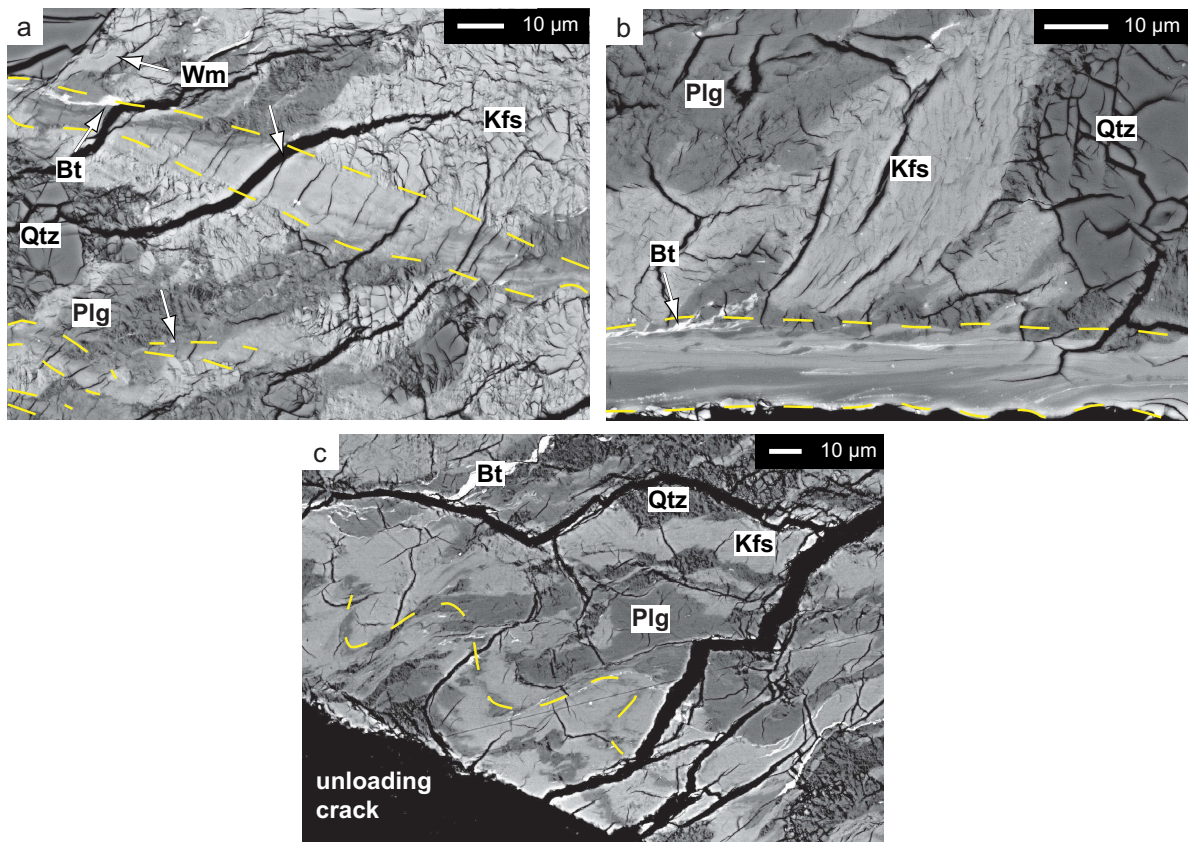
Figure 5.13: Low strain slip zones. a) Incipient slip zones in a C' orientation (between dashed lines) derived from the extremely fine grained fragmented mantles. Note the concentration of unloading cracks (arrows) in the cohesive material. b) a well developed slip zone in a C - orientation. Note the flow structures and distinct z-contrast in the slip zone (below the dashed line). Further note the thin seams of biotite-like material adjacent as well as in the slip zone (bright seams). c) Folding of a slip zone in the C' orientation.
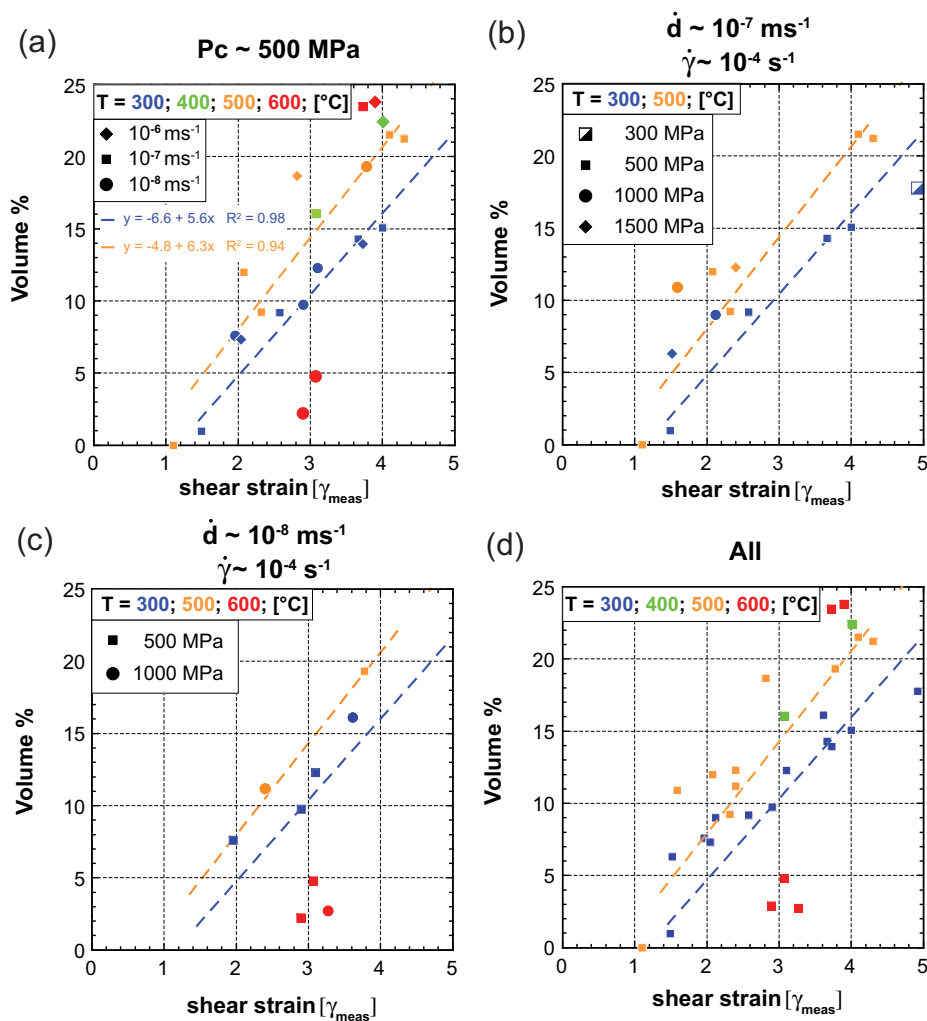
Figure 5.14: Volume% of slip zones vs. finite shear strain. a) grouped by temperature and displacement rate at Pc ~ 500 MPa. Only experiments performed at 10^{-7} m s^{-1} are used for the linear fit which is kept in all subsequent graphs as reference. b) grouped by confining pressure and temperature at a displacement rate of $\sim 10^{-7}$ m s^{-1}. c) grouped by confining pressure and temperature at a displacement rate of $\sim 10^{-8}$ m s^{-1}. d) all experiments grouped by temperature.
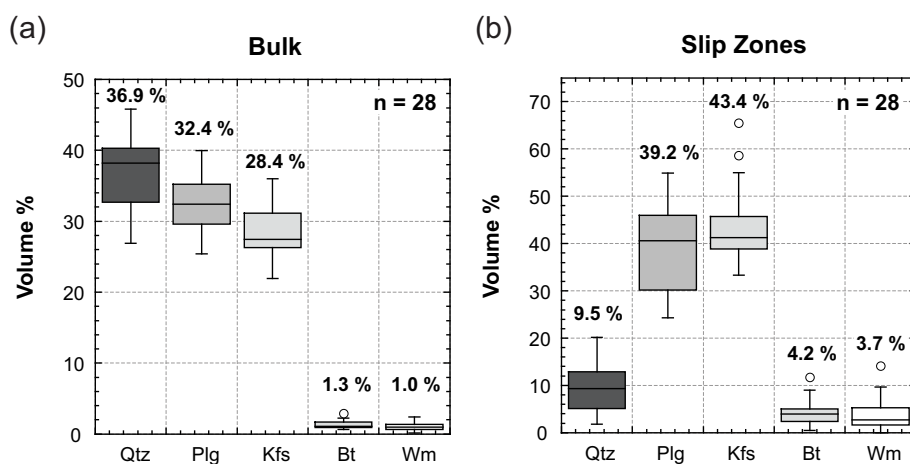
Figure 5.15: Composition of 28 analyzed experiments. a) mineral content of the whole analyzed areas b) mineral composition of the slip zones. Circles show outliers. Numbers are mean values. See text for details.

5.5.6 Bulk and slip zone volume% of individual phases

The bulk fault rock composition in 28 analyzed experiments where also slip zones were developed is: Qtz $\sim$ 36.9%, Plg $\sim$ 32.4%, Kfs $\sim$ 28.4%, Bt $\sim$ 1.3% and Wm $\sim$ 1%. In the slip zones the quartz content drops to $\sim$ 9.5% and feldspar as well as mica content increases significantly (Fig. 5.15). The ratio between Plg and Kfs as well as Bt and Wm content is around 1:1 in both bulk samples as well as slip zones. It has to be added that Kfs, Plg, Bt and Wm in the slip zones is partly amorphous material derived from their crystalline counterparts (see section 5.6).

5.5.7 Samples deformed at 600°C, $\dot{d} \sim 10^{-8}$ m s^{-1} and Pc $\sim 500 - 1000$ MPa

A notable exception to this general microstructural trend described above are samples deformed at 600°C, slow displacement rates (10^{-8} m s^{-1}) and both confining pressures (500 and 1000 MPa). These samples support the lowest shear stresses (580 - 860 MPa), have low amounts of slip zones ($< 5\%$), low fabric anisotropy (b/a $\sim$0.5 - 0.6) and all minerals seem to fracture considerably less ($>$50% qtz survivor grains, or alternatively the small grains get quickly cemented together) than at all other explored conditions. In these experiments, delicate pores are preserved between fine-grained clasts with interconnected, lobate grain boundaries which are common in the whole sample (Fig. 5.16).
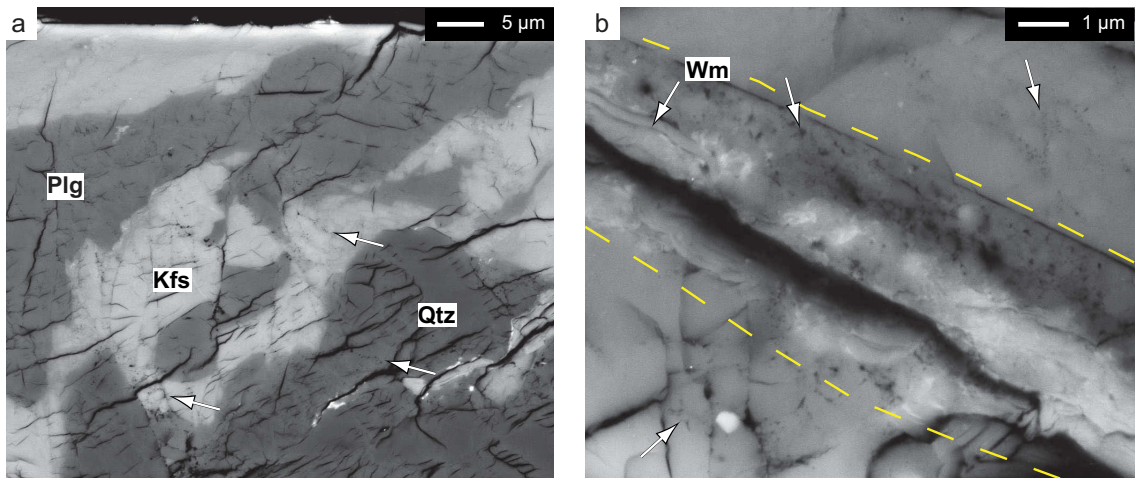
Figure 5.16: Microstructures at 600°C and slow displacement rates (10^{-8} m s^{-1}). a) typical microstructure, notice the delicate porosity (arrows) and "healed" appearance of the cataclasite. b) high magnification image of a slip zone, note the delicate pores (arrows) and interconnected lobate grain boundaries.

5.6 Microstructural evolution in slip zones with increasing strain

5.6.1 Low strain slip zones (peak strength microstructures)

The slip zones develop from extremely fine-grained feldspar mantles (grain size $<$ 100 nm) adjacent to micas and quartz aggregates (Pec et al., 2012a). This material has a bright SEM-CL signal (see chapter 4) and shows almost no luminescence in cold CL. Flow structures are observed in the slip zones and up to $\sim$ 90% of this material is amorphous to the TEM

beam and stays homogenously gray in both dark and bright field images in every tilt angle. The smallest individual crystalline fragments detectable by a FEG-TEM embedded in the amorphous matrix have a grain size of $\sim$ 8 nm, and the mean grain size of all fragments is $\sim$ 34 nm (Fig. 5.17). Crystalline grains are angular, often elongated (mean axial ratio, b/a $\sim$ 0.6) and show bent crystal planes. Locally a strong shape preferred orientation (SPO) is developed (Fig. 5.18c) and no porosity can be resolved in a FEG-TEM. Selected area diffraction patterns show weak spots and arcs as well as a broader band of diffuse intensity consistent with poorly crystalline to amorphous material (Viti, 2011). The broader band of diffuse intensity is more pronounced in regions where more strain was accommodated (Figs. 5.18 and 5.19).

Chemical changes take place in the slip zones and the material is an alumosilicate containing alkalis (Na,Ca,K) (Pec et al., 2012a; Yund et al., 1990). Further, thin ($\sim$ 0.1 μm) high-z contrast seams are present inside as well as adjacent to the slip zones (Figs. 5.13 and 5.18, Pec et al., 2012a). Theses seams have approximately a biotite composition (determined by TEM-EDS), however are amorphous to the TEM beam with individual diffracting crystals smaller than 5 nm (Fig. 5.18f). We refer to the material in the slip zones as "nanocrystalline, partly amorphous material" (PAM). The infiltration of iron and presence of tiny broken biotite crystals into the slip zones (Figs. 5.18e-g, 5.19) is typical of slip zones that accommodated more strain and is one of the characteristic features connected to the transition from PAM to amorphous material (AM). The transition as seen from SAED patterns is gradual with two end members: individual clearly delimited diffraction spots and a ring of diffuse intensity (see section 5.6.2).

The nanocrystalline feldspar and quartz fragments within the PAM are unstable at high magnifications in the TEM and amorphized quickly. To assure that the amorphous material observed in the TEM was not produced by beam damage, selected area electron diffraction (SAED) patterns where first obtained at low magnifications and higher magnification images and SAEDs were taken as quickly as possible. At magnifications up to 62 000$\times$ (1 pixel = 1.1 nm) SAED patterns as well as images could reliably be obtained without influencing the microstructure (as compared to lower magnification images), however high-resolution TEM (HRTEM) imaging was not possible. Another indication of the highly reactive nature of the PAM is that storing of a TEM foil for $\sim$ 1 year at room conditions leads to the development of surface contamination restricted to the PAM material (see Fig. 5.18) as was previously observed by Yund et al. (1990) indicating that the PAM is metastable.
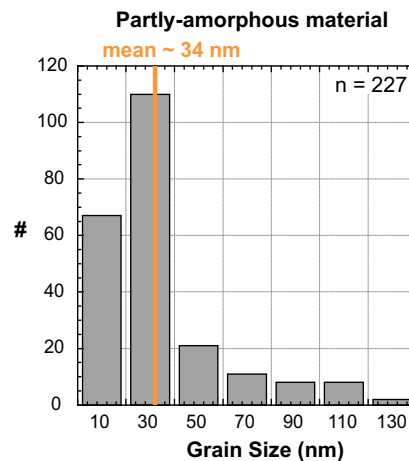
Figure 5.17: Grain size histogram of crystalline particles in the feldspar-derived PAM.
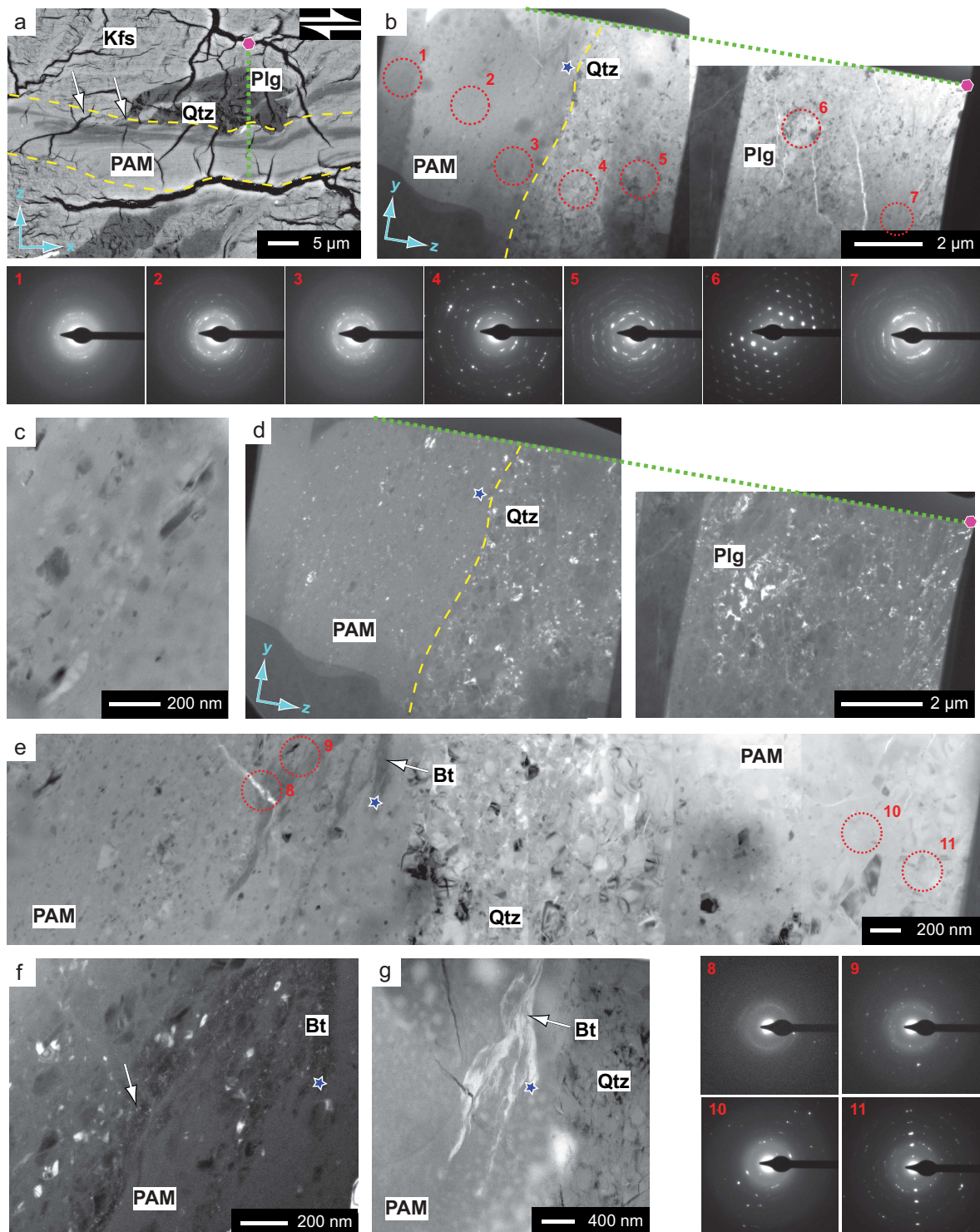
Figure 5.18: Low strain slip zone micro- and nanostructures. Hexagon and green dashed line shows the position and orientation of the transmission electron microscopy (TEM) foil. Star shows identical positions on images. Selected area electron diffraction (SAED) patterns were collected in the numbered dashed circles. a) SEM-BSE z-contrast image. Slip zone is between dashed lines. Arrows show unloading cracks. b) TEM – bright field (BF) image of the foil c) high magnification TEM-BF image of the PAM. Notice elongation and SPO of individual crystalline particles d) TEM dark field (DF) image of the foil. More than 90% of the PAM (left from the dashed line) stays homogenously gray, i.e. is amorphous to the TEM beam e) TEM – BF image of the nanocrystalline partly amorphous material and nanocrystalline quartz band where porosity is still present (white streaks). f) TEM - conical DF image of the biotite-like seam. The biotite is amorphous to the TEM beam with local tiny crystalline regions (arrow). g) Scanning transmission electron microscopy (STEM) high-angle annular dark-field image (HAADF). The brighter spots are on the surface and were produced during ~ 1 year storing of the foil at room conditions indicating that the PAM is highly reactive. No other microstructural changes were detected by comparing the older and newer TEM images.
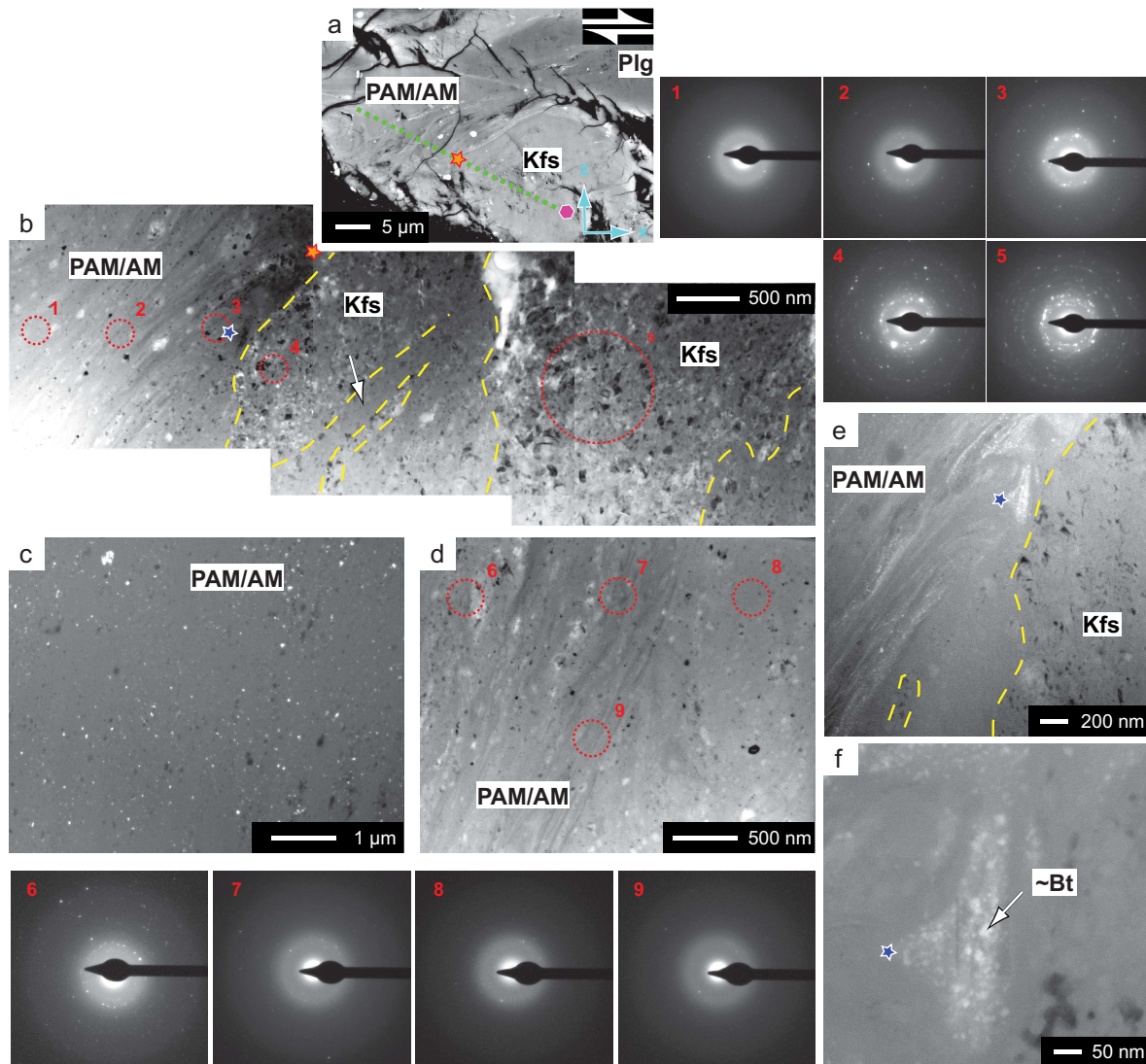
Figure 5.19: Low to medium strain slip zone. Hexagon and green dashed line shows the position and orientation of the transmission electron microscopy (TEM) foil. Stars shows identical positions on images. SAED patterns were collected in numbered dashed circles. a) SEM-BSE z-contrast image, b) TEM-BF image. Note the lenses of more coarse grained feldspar (between dashed lines) surrounded by the PAM/AM. Note that the ring of diffuse intensity is more pronounced to the left (i.e. high strain domain) c) TEM-DF image of the feldspar-derived PAM/AM. More than 90% stay homogenously gray, i.e. are amorphous to the TEM beam. d) TEM-BF image of the PAM/AM showing mostly amorphous material. e) STEM-HAADF image showing the enrichment in heavy elements (Fe) in the PAM/AM (upper left) and porosity in the coarser grained Kfs (black). f) high-magnification STEM-HAADF image. Tiny ($\sim$ 5 nm) fragments of a mineral with a biotite-like composition.

5.6.2   High strain slip zones (after quasi-steady state deformation)

After peak strength some of the low strain slip zones continue to accumulate strain and further change their microstructure. Turbulent flow structures, very thin layering and a heterogeneous chemical composition (shown by a heterogeneous z-contrast in SEM-BSE, SEM-EDS and STEM-HAADF) develops (Fig. 5.20, see also chapter 4). Within the slip zones, thin (50 nm - 2 μm thick) layers of a material with a similar z-contrast as biotite are often present. However, on the SEM scale they have a "flat" appearance and do not show any laths which are typical for still crystalline biotite (e.g. Fig. 5.21a). On the TEM scale these layers are amorphous ($\gg$ 99%) as shown by rings of diffuse intensity in SAED patterns (Fig. 5.21b,d) with very few diffracting crystals (grain size $\sim$ 6 nm, d-spacing $\sim$ 10 ångstöm) (Fig. 5.21h,i). The chemical composition of the crystalline fragments is identical to the chemical composition of the amorphous matrix on a small scale (Fig. 5.22d). The feldspar derived PAM within the high-strain slip zones has fewer diffracting grains compared to low strain PAM (compare SAED patterns and TEM-BF images of Figs. 5.18 and 5.21), gets enriched in iron close to the biotite-derived amorphous material (AM) (Fig. 5.21g) and locally only a ring of diffuse intensity without any bright spots can be detected (Fig. 5.21f).

Further lenses of PAM, polycrystalline qtz as well as single qtz grains can be observed within the AM (Figs. 5.20, 5.21b,c, 5.22a,b,i). Quartz forms σ- and δ-clasts, which are often surrounded by a darker z-contrast material which makes them appear "corroded" (Fig. 5.20). Further, very small laths of biotite-like mineral (length $\sim$ 100 - 700 nm, thickness $\sim$ 20 - 60 nm, axial ratio, b/a $\sim$ 0.1) can be observed (e.g. Fig. 5.20). The high-strain slip zones have often intrusive relationships to the surrounding crystalline aggregates and form "injection veins" (see chapter 4) (Fig. 5.20a).

These microstructures are observed in all high-strain experiments irrespective of the temperature, confining pressure or displacement rate applied. In experiments conducted at 300°C this material also forms locally very small bubbles ($\sim$ 15 nm – 1 μm, Figs.5.20d, 5.22) which are stretched and follow the local flow pattern (see chapter 4). These bubbles occur exclusively along slip zones in C' orientation. Both the AM as well as PAM layers are discordantly cut by an unloading crack which develops in experiments deformed to high finite strains, thus they must have formed before the quenching and unloading procedure (see chapter 4).

The biotite-derived amorphous material is much more stable under the TEM beam compared to nanocrystalline feldspar-derived PAM and HRTEM imaging of individual grains was possible. The individual grains often show bend contours and no idiomorphic grains were ever detected (5.22c,e,f).
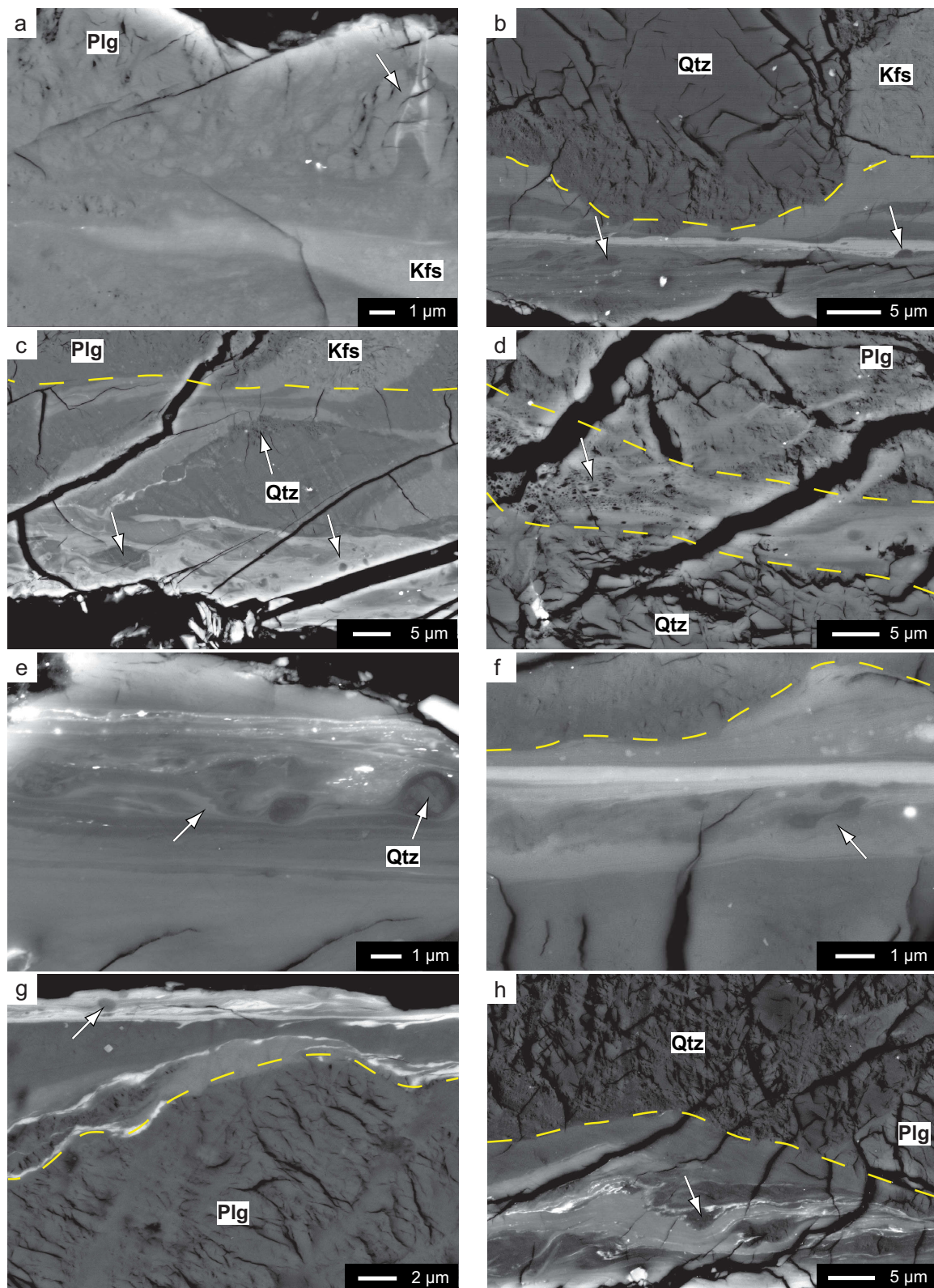
Figure 5.20: Microstructures of high strain slip zones. SEM-BSE z-contrast images after steady-state creep a-d) T=300°C, Pc ~ 500MPa. a) A small injection vein with a similar z-contrast as biotite where unloading cracks concentrate (arrow). Further, note the high mobility of the kfs-material. b) well developed slip zone (below the dashed line). Note the presence of qtz clasts (arrows), highly heterogeneous z-contrast on a small scale and the presence of a thicker layer of a material with a similar z-contrast as biotite. c) Thick slip zone containing quartz clasts (arrows). d) feldspar derived AM with bubbles (arrow) between dashed lines. e) T=300°C, Pc~1000 MPa, note the turbulent flow structures (arrow) and a qtz clast surrounded by a different z-contrast material. Further note tiny high-z contrast laths of a Fe rich material f) T= 400°C Pc~500MPa. Note the stretched qtz clast (arrow) and highly heterogeneous z-contrast. g) T=500°C, Pc~500MPa, Note the qtz clast (arrow) in the bright, heterogeneous material h) T=600°C, Pc ~ 500 MPa. Note the presence of qtz aggregates (arrow) in the slip zone (below dashed line), turbulent flow structures and fine seams of a high z-contrast mineral.
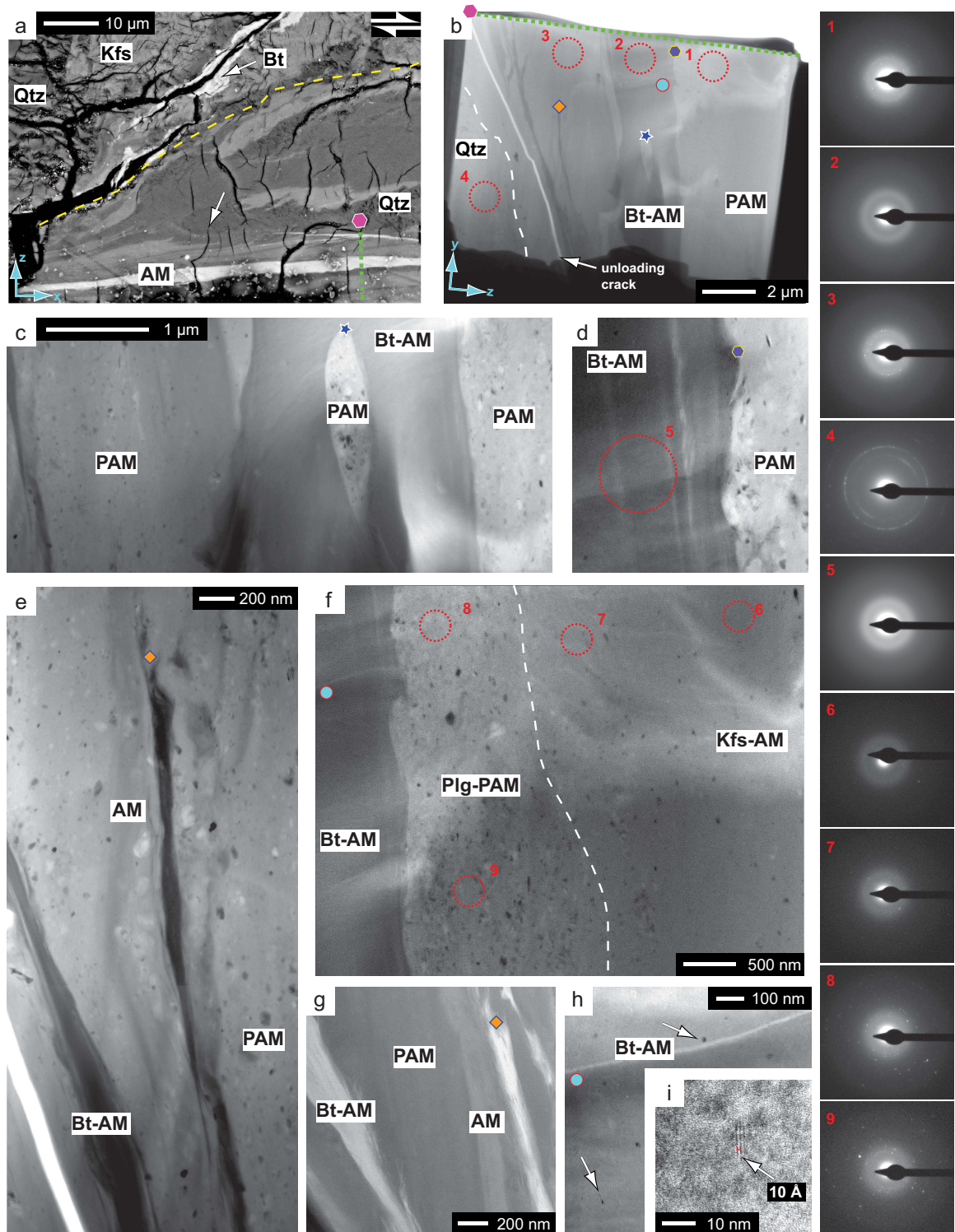
Figure 5.21: Micro- and nanostructures of high strain slip zone. Hexagon and green dashed line shows the position and orientation of the transmission electron microscopy (TEM) foil. Star, circle and lozenge show identical positions on images. Selected area electron diffraction (SAED) patterns were collected in the numbered dashed circles. Slight, continuous variations in brightness are due to foil bending. a) SEM-BSE z-contrast image. Notice the distinct appearance of crystalline Bt (up) and the Bt-derived AM (bottom). b-f) TEM-BF, b) Image of the entire foil, note the lack of any diffracting spots in the Bt-derived AM (SAED pattern 2) c) high magnification image showing an aggregate of nanocrystaline PAM surrounded by the AM material. d) high magnification image of the contact between AM and PAM. No strain-free annealed grains are observed on the contact. e) Mosaic showing the highly heterogeneous nature of PAM and AM. f) Note the differences between Plg-derived and kfs-derived PAM/AM where the kfs-derived material has fewer diffracting crystals. g) STEM-HAADF image showing the enrichment in Fe close to the biotite-like AM. h) TEM-BF of individual diffracting crystals (arrow) in the Bt-derived AM. i) HRTEM of a diffracting crystal surrounded by amorphous material. The d-spacing is ~10 ångstöm.
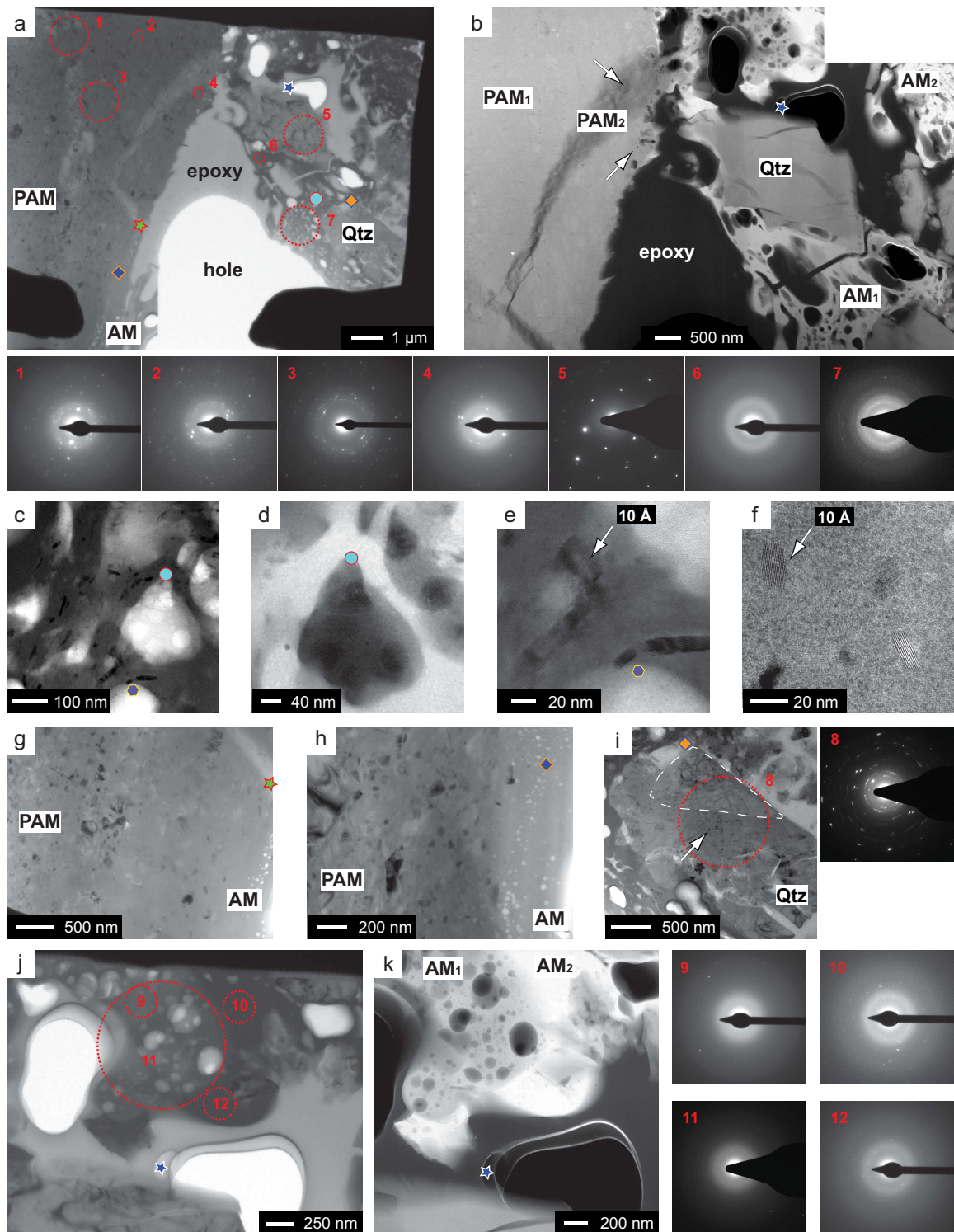
Figure 5.22: Micro- and nanostructures of high strain slip zone containing bubbles. Stars, lozenges and circle show identical positions on different images. Selected area electron diffraction (SAED) patterns were collected in the numbered dashed circles. a) TEM-BF of the foil. The epoxy-filled hole developed during the unloading procedure and thin-section preparation. Note the presence of qtz clasts in the bubbly AM and high heterogeneity of the amount of crystalline particles (e.g. SAED 7 and 6) on a micron scale. b) STEM-HAADF showing the highly heterogeneous chemical composition of the material with two distinct AM and PAM compositions (AM1, AM2, PAM1 and PAM2) note a bubble in the PAM2 (arrow) and a piece of AM in direct contact with PAM (arrow) c) HRTEM of the tiny diffracting crystals from area 7. d) STEM-HAADF showing a homogenous contrast, i.e. a homogenous chemical composition of both the amorphous matrix as well as crystals indicating that the crystalline-to-amorphous transition is iso-chemical on a small scale. e-f) HRTEM images of the individual crystalline particles, notice the bent crystal planes and absence of euhedral shapes. g-h) TEM-BF image showing a grain size reduction in the PAM towards the bubbly AM. i) TEM-BF image of a composite qtz clast made of nanocrystalline fragments (arrow) and bigger, highly strained qtz single crystals (in dashed line). j) TEM-BF image of a bubbly and non-bubbly AM. k) STEM-HAADF image showing the different chemical composition of the non-bubbly and bubbly AM.

5.6.3 Slip zones after abrupt failure

Samples deformed at T $= 300°$C, Pc ~ 500 MPa and displacement rates of 10^{-6} m s^{-1} reach the highest shear stresses ($\tau \sim 1.4$ GPa) and fail abruptly around peak strength. In these samples bubbles are mostly well developed. Preferential sites where bubbles appear are within micas adjacent to larger quartz survivor grains, i.e. where the material is subjected to high local stresses (Fig. 5.23). The bubble trains can be usually followed only over short distances (~ 10 μm) and show turbulent flow structures (Fig. 5.23c).

Another site where bubbles are observed is in some cracks which were probably low-pressure sites. The layers of a material with a similar z-contrast as biotite tend to be thinner than in samples which did not fail abruptly, however this qualitative observation is difficult to quantify. Microstructures are very similar to samples which did not fail abruptly (compare Figs. 5.23 and 5.20).
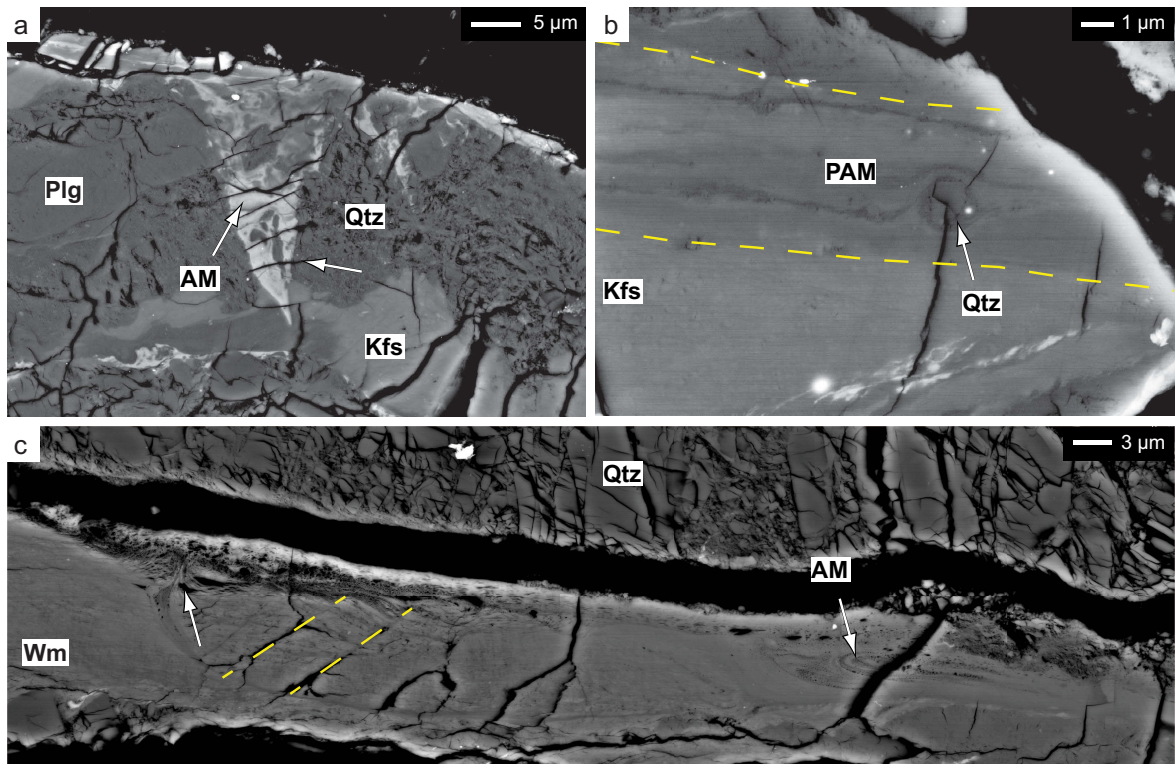
Figure 5.23: SEM-BSE z-contrast images of amorphous layers observed after abrupt failure. a) best developed injection vein. Note the highly heterogeneous z-contrast, presence of a qtz clast and turbulent flow structures. b) Slip zone with porphyroclasts of qtz (arrow). Note the variation of z-contrast within the feldspar-derived PAM c) a bookshelf structure in a Wm undergoing the crystalline-amorphous transition. Note the tiny bubbles following the local flow pattern over short distances (arrows).

5.6.4 Observations in SEM-SE

Three samples were separated along a well-developed unloading crack in the C' orientation. The broken surfaces of these samples were gold coated (thickness ~ 20 nm) and analyzed in secondary electron mode without any further preparation.

The surface of the unloading crack shows well-developed striations in both 400°C and 500°C

experiments (Fig. 5.24a-c). It has to be noted that based on microstructural observations the unloading crack develops after the deformation part of the experiment along well-developed slip zones. Hence, during the experiment, these "surfaces" were welded together by the high stresses and deformation was accommodated in the slip zone volume. Therefore the observed surface is a result of an unloading process along a severely strained PAM/AM material where significant strains were accommodated.
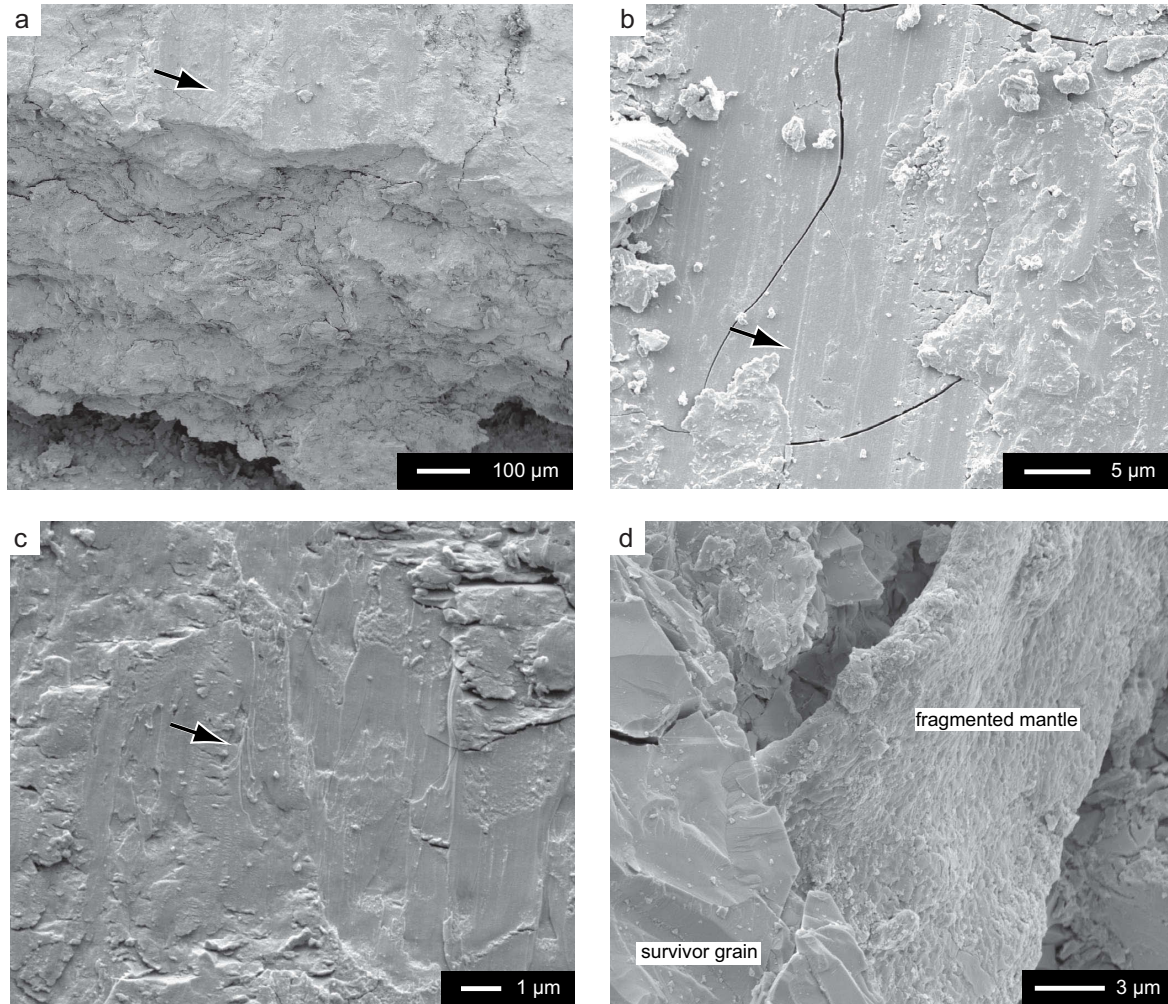
Figure 5.24: SE images of surfaces revealed along unloading cracks. a-b) T=500°C Pc $\sim$ 500 MPa. a) view into the volume of deformed cataclasite. Arrow shows striations on the unloading surface. b) high magnification image of the striations from a). Striations are parallel to the sliding direction. c) High magnification image of striations developed at T=400°C and Pc $\sim$ 500 MPa along an unloading crack. d) T = 500°C, Pc $\sim$ 500 MPa image of a fractured survivor grain and finely fractured fragmented mantle.

5.7 Discussion

5.7.1 Mechanical data

In the mechanical record a clear temperature dependence and a weak bulk strain rate dependence is seen which gets more pronounced with increasing temperature. Such behavior was observed previously at temperatures > 300 - 350 °C in granitoids if (even little) water

is present (Blanpied et al., 1995, 1998; Keulen et al., 2007, 2008; Tullis and Yund, 1980; Pec et al., 2012a), and is also commonly observed in experimentally deformed fault rocks analogues under "hydrothermal" conditions (Niemeijer et al., 2008b; Niemeijer and Spiers, 2006, 2007; Bos and Spiers, 2002a; Bos et al., 2000a; Bos and Spiers, 2000). Furthermore, the difference in peak as well as steady state stress between the 400°C and 500°C experiments is remarkably less pronounced than at all other conditions explored. Either two different mechanisms with different activation energies operate in the low (300 - 400°C) and high temperature (500 - 600°C) experiments or the fault rock exhibits a non-arrhenian temperature dependence over the explored temperature range. No microstructural evidence was found that could be linked to different physical processes acting in this range of temperatures, however more experiments at 400°C would be necessary to test this hypothesis more thoroughly. The long weakening after peak strength ($\sim$5 - 450 minutes depending on the applied displacement rate and temperature) is probably not a result of apparatus stiffness. The samples also fail abruptly under the experimental conditions and similar behavior was described by Giger et al. (2008) in quartz gouges deformed in general shear in a gas deformation apparatus indicating that this behavior is caused by the sample, not the apparatus. In the following section we will summarize the microstructural observations and discuss the possible physical processes which cause the observed mechanical response.

5.7.2   Microstructural data

5.7.2.1   Compaction

During early stages of deformation ($0 < \gamma < 1.5$) compaction of the powder is achieved by short ($\sim$160 μm) closely spaced (10 - 50 μm) R$_1$-shears. Porosity is progressively reduced along these shears and extremely fine-grained material (< 100 nm) is produced during fracturing of larger grains forming the fragmented mantle (Pec et al., 2012a). The slightly non-linear thinning indicates that the porosity reduction occurs mostly in the early stages of the experiments ($\gamma \geq 1.5$) well before the peak strength. Once the compaction is finished, the strength of the initial powdered sample is similar or higher to that of an intact rock of the same material at the elevated confining pressures employed in this study (Pec et al., 2012a) indicating that fracturing leads to strain hardening (e.g. Scholz, 2007). Comparing the amount of thinning in our experiments to experiments performed in the same sample geometry and deformation apparatus type to the same finite strains on slabs of quartz poly and single crystals (Heilbronner and Tullis, 2006; Muto et al., 2011), we find that our values are about 10% higher. As the starting material has a porosity of about 10% (Pec et al., 2012a) the reported values are in excellent agreement indicating that the thinning is a pure geometric necessity imposed by the boundary conditions present in this experimental set-up.

5.7.2.2   Strength of individual mineral phases

In all experiments, quartz fractures the least (as it does not have a cleavage and has strong covalent bonds) and forms porphyroclasts at all scales. Its anisotropy is always lower compared to both feldspars. Further it tends not to be incorporated into the slip zones and the slip zones find their way "around" larger Qtz survivor grains. The ratio between Plg and Kfs as well as Bt and Wm stays roughly the same in both bulk shear zones as well as slip zones ($\sim$1:1) indicating that the slip zones get depleted in quartz in agreement with the qualitative

observations. Observations therefore indicate that Qtz is the rheologically strongest phase at the employed experimental conditions.

Feldspars are much weaker than quartz because of one (plagioclase) and two (k-feldspar) perfect cleavages and micro-porosity (Brace et al., 1972; Tajčmanová et al., 2012), which allow efficient fracturing (Yund et al., 1990). Further, the bond strength is lower compared to quartz (ionic-covalent bonds in feldspars and Van der Waals bonds between TOT layers in micas). Very few feldspar survivor grains can be observed after finite strains of ∼2 and most of the feldspar material is transformed into fine grained (< 100 nm) fragmented mantle and PAM. Kfs aggregates tend to flatten slightly more, be more steep with respect to the shear zone boundary and often appear to be more "mobile" than Plg aggregates (Fig. 5.20a). Both feldspars form together ∼60 vol% of the samples and form a less viscous interconnected matrix.

Abundance of quartz in the Verzasca powder (∼ 37 vol%) facilitates probably the build up of high shear stresses as observed in the mechanical record (τ ∼ 0.6 - 1.4 GPa). Rigid inclusions in a softer matrix transfer load between each other increasing the bulk strength of the rock in proportion to their volume (e.g. quartz-calcite mixtures, Renner et al., 2007; Xiao and Evans, 2003; Rybacki et al., 2003). Quartz grains form high stress sites in the adjacent feldspar aggregates and as a consequence partly amorphous material (PAM) is formed there. Similarly, favorably oriented micas (basal slip along the perfect cleavage in the C' direction) tend to concentrate strain and initiate slip zones.

At low temperatures the amount of slip zones is systematically lower and the flattening of the fabric (derived from b/a ratios of ACF) is more pronounced compared to higher temperature experiments. This probably suggests that at 300°C the phase strength (or viscosity) contrast between the individual phases is the highest leading to simple shear component localization in the thin slip zones and pure shear component in the less deformed lenses (Holyoke and Tullis, 2006b,a).

An exception of this miscrostructural development are experiments deformed at 600°C and slow displacement rates (10^{-8} m s^{-1}) which are always substantially weaker (τ ∼580 - 850 MPa) than samples deformed at lower temperatures or faster displacement rates. Interconnected, lobate grains are observed typical of "healing" microstructures during dissolution-precipitation creep (Keulen et al., 2007, 2008; Tenthorey and Cox, 2006) both in the shear zone as well as in the C' oriented slip zones (Fig. 5.16). Furthermore, the low amount of fabric flattening, fragmented mantles and slip zones indicates that the grain size reduction necessary to produce the PAM is counteracted by grain growth and efficient material transport during dissolution-precipitation creep inhibiting the build up of high stresses.

Nevertheless partitioning and localization of strain into the slip zones at all explored conditions implies that they are weaker (i.e. accommodate more strain) than the surrounding material and are thus expected to have a pronounced effect on the rheological behavior as a weak interconnected layer (Handy, 1994).

5.7.2.3   Development of nanocrystalline partly amorphous material (PAM)

Microstructural observations document widespread comminution first fracturing larger survivor grains (d_{equ} > 100 μm) into fine-grained (d_{equ} < 100 nm) fragmented mantles. The frag-

mented mantle is further transformed into a cohesive, non-porous, highly strained nanocrys-
taline (mean grain size $\sim$ 34 nm) to TEM-amorphous (up to 90%) material (PAM) with
abundant flow structures. The small grains present in the amorphous matrix have locally
strong a SPO. Within the PAM in slip zones and on phase-to-phase contacts fine seams
($\sim$ 100 nm) of an amorphous/nanocrystalline material (Fig. 5.18e-g) with approximately a
biotite composition develop. These seams seem not to be connected to any larger micas and
could be a result of a chemical reaction during the experiment at all explored P-T conditions.
Furthermore, the feldspar-derived PAM often contains Ca, Na and K in proportions never
observed in original Plg or Kfs grains (despite original Plg grains are often richer in Na &
Ca and original Kfs grains are richer in K compared to the PAM) indicating a high mobil-
ity of alkalis in the PAM (Yund et al., 1990; Pec et al., 2012a). Fine but distinct layering
is observed within the slip zones and intimate intermixing of individual Kfs and Plg grains
which could explain such an composition was not observed down to the TEM scale (e.g. Fig.
5.21). The high surface-to-mass ratio and the high defect density in the nanocrystalline,
partly amorphous material is expected to enhance solid state diffusion (Chakraborty, 2008;
Suryanarayana, 2001) and could explain the observed chemical composition of the PAM.

The volumes affected by the slip zones are $\sim$ 15 - 25% depending on the temperature at a finite
shear strain of $\sim$ 4 and more than 80% of the slip zone material is formed by feldspar-derived
PAM/AM. If a quartz aggregate is present it usually forms a σ- and δ-clast geometry.

Weakening after peak strength likely occurs once the PAM is abundant enough to form an
interconnected, anastomozing network of slip-zones ($\sim$7 - 12 volume%) where the strain par-
titions. If a mineral grain is cut by a slip zone and can be used to estimate strain, local shear
strains in the slip zones are always higher compared to bulk finite strains (e.g. $\gamma_{slipzone} > 5$
at $\gamma_{bulk} \sim 2$). Localization of strain implies that the PAM material is weaker (i.e. accom-
modates more strain) than the surrounding aggregates. The fact that the volumes of slip
zones increase with increasing strain indicates that either the PAM strain hardens or that the
slip zones do not operate continuously during the whole experiment or become inactive once
their orientation is not favorable for further slip (Holyoke and Tullis, 2006c). As folding of
the slip zones is observed at high strains it seems that once a slip zone is well developed, the
flattening component imposed by geometrical constraints of the experimental set-up, does not
allow continuous operation of the slip zone.

What process causes comminution down to nanometer range? Microstructural studies show,
that extremely small grains (≤ 0.1 μm) form during breaking of grains and a whole range
of grain sizes is formed instantaneously during fracturing of a single grain (Keulen et al.,
2007; Stünitz et al., 2010; Heilbronner and Keulen, 2006; Davies et al., 2012). Extreme cases
of grain size reduction can even lead to "pulverization" of rocks (e.g. Wilson et al., 2005).
Nevertheless, breaking of grains becomes increasingly difficult with decreasing grain size due
to smaller flaw sizes and densities (Prasher, 1987). This is thought to cause the so-called
grinding limit which was determined by grain size distributions (GSD) to be around $\sim$ 1 μm
for quartz and $\sim$ 2 μm for feldspars (Keulen et al., 2007). Further grain size reduction is
thought to be achieved by shearing and attrition and the smallest observable grain sizes in
both natural as well as experimentally produced fault rocks are on the order of few tens of
nanometers (Janssen et al., 2010; Ozawa and Takizawa, 2007; Keulen et al., 2007; Wilson
et al., 2005; Yund et al., 1990; Olgaard and Brace, 1983; Weiss and Wenk, 1983; Pec et al.,
2012a; Viti, 2011).

The smallest still crystalline feldspar-like grains in the amorphous matrix have a grain size of

$\sim$8 nm i.e. have volume of $\sim$ 270 nm^3 and a surface area of $\sim$200 nm^2 if recalculated as a sphere. Considering an albite unit cell ($\sim$0.8 x 1.3 x 0.7 nm, Prewitt et al., 1976) these grains consist of $\sim$ 370 unit cells of which at least $\sim$200 are forming the grain boundary. Atoms on a grain boundary are always relaxed (as a free surface exists) i.e. have a lower long-range order than atoms fully confined within a grain. It appears that crystallinity (long-range order) cannot be maintained and the crystal structure collapses below $\sim$8 nm grain size. How these grains reach such small grain sizes in the first place is unknown (breaking, attrition?), however the preferential appearance of the PAM on high stress/strain sites suggests that high stresses and strains are necessary to produce this small grain sizes.

Another peculiar feature of the PAM is the absence of porosity. Porosity is known to get eliminated during sintering of nanocrystalline aggregates (Lo et al., 2003) and porous gels used to synthesize glass at low temperatures (Scherer et al., 1985). Sintering is a temperature dependent process as it necessitates diffusion of atoms for which the reduction of surface energy is the driving force (Scherer et al., 1985). This process is a good candidate for the production of PAM as we observe that the amount of slip zones is temperature dependent (i.e. most slip zones are at 600°C and 10^{-6} m s^{-1} despite lower stresses compared to lower T experiments). Furthermore during densification of the sintered material an SPO can develop and the viscosity of the sintered material increases (Lo et al., 2003; Scherer et al., 1985) which could explain why the volume of slip zones keeps increasing with increasing strain in addition to geometrical arguments. It is also important to point out that the PAM in the low strain slip zones is formed mostly from feldspars which contain Si and Al which are network builders and alkalis (Na, K, Ca) which are network modifiers in glasses and geopolymers (e.g. Scholze, 1977; Duxson et al., 2007). Further they are best developed around micas, which probably dehydrate during kinking and fracturing enhancing viscous processes in the surrounding material.

Sintering of silicate glass-ceramic materials leads to growth of detritic crystals and often show delicate intergrowth microstructures if treated at elevated temperatures but still below the melting point (e.g. Pinckney and Beall, 2008). However in the PAM material no microstructures which would indicate crystal growth were ever observed and all crystals appear to be highly strained (shown by bent crystal planes) and angular down to sub-10 nm scale.

Similar amorphous material was observed by Yund et al. (1990) in an extensive TEM study of high-strain rotary friction experiments on granitoids under low normal stresses (50-75 MPa) and confining pressures of $\sim$21MPa (T. Tullis, pers. comm.) at room temperature. They observed large amounts of amorphous material ($\sim$ 5 - 60%) in all experiments with a composition commonly between K-rich and Na,Ca-rich feldspars as seen in our experiments. Yund et al. (1990) estimated a temperature increase of $\sim$0.02°C on the sliding surface and convincingly argued that the amorphous material did not form by frictional melting (as the sliding velocities were slow $\sim$ 10^{-9} - 10^{-3} m s^{-1}) but by comminution of mostly feldspar grains in agreement with our observations.

5.7.2.4   Development of the fragment loaded amorphous material

The PAM transforms progressively into a more and more amorphous material (AM) as it accommodates strain. It is interesting to notice that while the PAM is mostly formed of feldspars the more amorphous AM has often a mica pre-cursor material. Micas form $\sim$ 8% of the slip zones and the most amorphous layers have a similar z-contrast as biotites ($\gg$ 99%

of non-diffracting material with very few grains around $\sim$ 5 nm big). Biotite-like material also often forms extremely small angular grains ($\sim$ 5 nm, Fig. 5.19f) within the high strain slip zones. The unit cell of biotite is $\sim$0.53 x 0.92 x 2.02 nm large (Bohlen et al., 1980), i.e. $\sim$1.4 times larger than the unit cell of feldspars and is likely therefore easier amorphized than feldspars. On the other hand as micas have a perfect basal cleavage they likely can accommodate more strain by crystal-plastic deformation and get probably comminuted later in the experiment than feldspars. The crystalline grains of biotite or feldspars embedded in the amorphous matrix are always strained (show bent crystal planes) and never form euhedral shapes. Taking into account the fact that the precursor material was already largely amorphous (see section 5.7.2.3) it seems that the AM is just a more strained stage of the PAM.

SAED patterns also show a rather homogenous transition from nanocrystalline to TEM-amorphous material with the smallest still crystalline grains being $\sim$ 5 nm in diameter and a grain size reduction is observed towards the fully amorphous layers (Fig. 5.22g,h). Furthermore, from a thermodynamic point of view, nanocrystalline materials exhibit similar behavior as amorphous glasses (Wolf et al., 1995) so no clear line between nanocrystalline materials and amorphous glasses can be drawn. No microstructural observations could be linked to a local increase in temperature (i.e. strain free, euhedral grains on the contacts with AM or detritic crystal growth) and furthermore, it appears that the transition from nanocrystalline, partly amorphous bitotites to fully amorphous AM is isochemical (as seen in STEM-HAADF images) which would not be expected of crystals crystallizing from a high-temperature melt. Very fine layers of different chemical composition are present in the AM which would also be expected to anneal quickly if the amorphous material was a high temperature melt (as melting needs the temperature for self-diffusion to be reached in the liquid phase, (Wolf et al., 1990).

The AM layers are best developed in the C-direction along the fault rock / forcing block boundary and get transferred from one forcing block to the other along one or two C' layers in the centre of the sample (see chapter 4). The layers close to the forcing block boundaries are the most depleted in crystalline material, i.e. most amorphous. They cover $\sim$1% of the whole sample and estimates of locally accommodated shear strain are $\gamma_{slipzone} > 20$ at $\gamma_{bulk} \sim 4$ implying further strain rate increase within the AM. Localization along such C-C' features is commonly observed in general shear experiments (e.g. Holyoke and Tullis, 2006b,c,a; Holtzman et al., 2005; Kohlstedt and Holtzman, 2009) and is therefore likely following the highest stress sites dictated by the general shear geometry. Shear strain rate varies by approx. 1 order of magnitude within our samples due to strain partitioning and localization, however this does not imply an increase in slip velocity ($\dot{\gamma} = \dot{d}$/deforming volume), i.e. high strain rates can be achieved at slow displacement rates given that the deforming volume is small (see chapter 4).

Nevertheless comminution (as seen by the V_s/V_a ratio) as well as fabric flattening continues even at highest explored strains indicating that not all deformation occurs in the AM layers. Manual 2D tracings on high-magnification mosaics have estimated that the AM material most likely forms a multiply-connected topology with about $\sim$ 30 volume% left for gaps in the film (see chapter 4), however it has to be pointed out that this is a rough estimate as the unloading crack tends to obscure the exact topology. Nevertheless the samples support high shear stresses ($\tau \sim$ 0.8 - 1.2 GPa) also when the deformation is mostly localized in the AM layers indicating that despite the PAM and AM have a relatively lower viscosity than the granular aggregates (as seen in the microstructural record), they probably can support

significant shear stresses at high strain rates.

Failure of the sample occurs only at the fastest displacement rates (10^{-6} m s^{-1}) at T=300°C and Pc $\sim$ 500 MPa where similar AM is present as observed in all other experiments which did not fail, therefore the fragment loaded amorphous material cannot be a result of abrupt failure.

5.7.2.5 Summary of microstructural implications

All our observations suggest that the microstructural development is primarily controlled by the amount of finite strain accommodated by the sample (see Fig. 5.25 for summary). Secondary controlling parameters are temperature/stress, confining pressure and displacement rate. Deformation partitions into lenses of fragmented material and slip zones of PAM/AM. Deformation in the lenses is mostly accommodated by fracturing, granular flow and probably also dissolution precipitation creep in the extremely fine grained material (< 100 nm) as a result of geometrical necessity when the lenses slide past each other (Pec et al., 2012a). Clear microstructural evidence for dissolution precipitation creep is common only in slowly deformed experiments at 600°C and in experiments performed under lower temperature conditions (300 and 500°C) during longer time scales (Keulen et al., 2007, 2008).
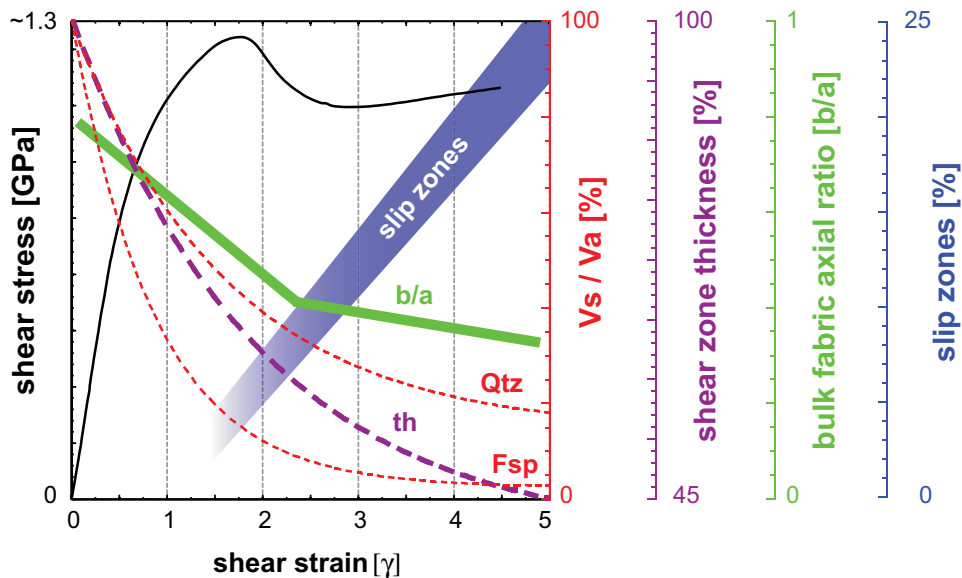
Figure 5.25: General trends of microstructural and mechanical evolution with increasing strain. Color coded y-axis on the right-hand side show the general trend observed in comminution (red), thinning (purple), fabric anisotropy (green) and vol% of slip zones (blue). th – thickness, Qtz – quartz, Fsp – feldspar

Partitioning of strain into the slip zones implies than they are weaker than the surrounding lenses. Nevertheless as fracturing and strain hardening occurs on the sample scale (Pec et al., 2012a), together with preferential appearance on high stress sites, it seems that high stresses are necessary for the production of PAM and AM. It appears that the PAM and AM in the slip zones behave as viscous, fragment loaded turbulent fluids and are therefore a likely candidate to explain the observed mechanical response (temperature and rate dependence). The continuity of the observed microstructures indicates that these layers developed continuously during the experiment and cannot be explained by the accumulation of many successive events. In the microstructural record, we did not find any clear evidence for high

temperatures and therefore, we explore other possibilities how to destroy a crystal lattice.

As discussed above, it seems that the amorphous-crystalline system is not binary (Wolf et al., 1995) and a wide range of various materials with poor long-range order exist in between these two end-member states. Therefore the transition from PAM to AM is rather arbitrary. Nevertheless some indicative microstructures for the AM which are not observed in the PAM are: a) turbulent flow structures b) bubbles in experiments performed at 300°C c) high z-contrast laths of iron-rich material d) "corroded" appearance of some, especially quartz, clasts within the AM.

In chapter 4, we compared the amorphous material formed at 300°C, Pc $\sim$ 500 MPa and $\dot{d}$ 10^{-8} - 10^{-7} m s^{-1}, i.e. 7-8 orders of magnitude slower than seismic slip ($\sim$1 m s^{-1}) to naturally occurring pseudotachylites and found a number of similarities. We notice that many of the microstructures occur also under conditions explored in this study (T=300 – 500°C, Pc $\sim$ 300 – 1000 MPa, $\dot{d}$ $\sim$ 10^{-6} – 10^{-8} m s^{-1} and T=600°C, Pc $\sim$ 500 – 1000 MPa and $\dot{d}$ > 10^{-8} m s^{-1} at high (>2.5) bulk shear strains, Fig. 5.20) with bubbles being the only unique microstructure to experiments performed at 300°C. In chapter 4 we estimated the temperature increase and came to a value of max. $\sim$2.5°C increase indicating that this amorphous material was not formed by melting at bulk thermodynamic temperatures of the rock or the individual minerals.

5.7.3 Crystalline-to-amorphous transition

While our observations down to the TEM scale prove that the material is amorphous, they do not give us any direct information about the processes which caused the crystalline-to-amorphous transition in our fault rocks.

The crystalline-to-amorphous transition is achieved by four processes a) heterogeneous melting b) homogeneous melting, c) heterogeneous amorphization and d) homogeneous amorphization (Wolf et al., 1990; Yip et al., 2005). All these processes seem to have a common physical cause which is volume expansion leading to progressive decrease of the shear modulus (Born criterion, Wolf et al., 1990; Yip et al., 2005). The temperature increase during the formation of these layers is inferred to be negligible (as the slip velocities are slow and heat conduction high) and therefore we favor an amorphization process.

Amorphization occurs for example during sever deformation below bulk thermodynamic melting temperatures (see Suryanarayana, 2001 and references therein, chapter 4). Processes responsible for amorphization can be seen as a result of increasing the Gibbs free energy of the material (Fig. 5.26). The Gibbs free energy is defined as $\Delta G = \Delta H - T\Delta S$ where ΔH is the change in enthalpy, ΔS is the change in entropy and T is the thermodynamic temperature. It can be further divided into $\Delta G_{tot} = \Delta G_{chem} + \Delta G_{elastic} + \Delta G_{surface} + \Delta G_{strain}$ where ΔG_{chem} is the influence of substitutional order (e.g. chemical composition), $\Delta G_{elastic}$ is the influence of elastic strain, $\Delta G_{surface}$ is the influence of grain boundaries and ΔG_{strain} is the influence dislocations and crystallinity (Stünitz, 1998).

Our microstructural observations confirm that the PAM and AM present in the slip zones is a metastable, far from thermal equilibrium material, because it consists of chemically heterogeneous, nanocrystalline, partly-amorphous to amorphous layers.
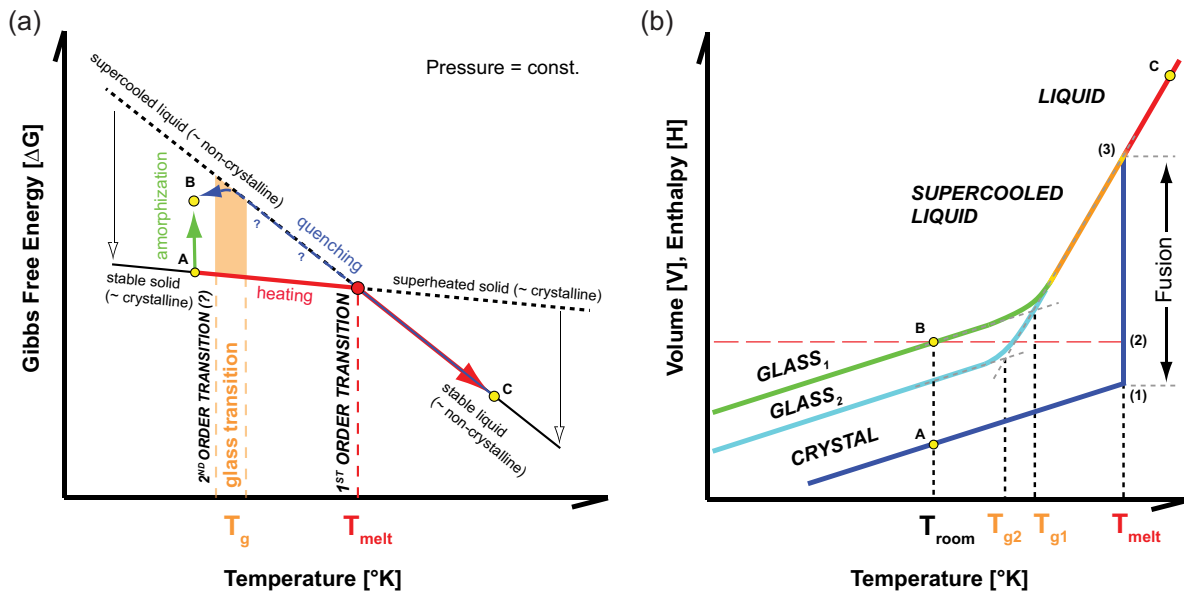
Figure 5.26: Conceptual model. a) Gibbs free energy vs. temperature. Path from crystalline to amorphous state is either through heating, melting and quenching (path A - C - B) or through amorphization/vitrification in the absence of temperature increase due to increase in Gibbs free energy (path A - B). modified after Philpotts and Ague (2009). The position of the glass transition temperature is unknown during the experiment. b) Volume or Enthalpy vs. temperature. A, B and C correspond to (a). T_m shows the melting point of an equilibrium crystal (blue line). At the melting point, input of energy into the system does not result in a temperature increase but allows the change of bond lengths and angles disordering the crystal lattice into a liquid (Fusion, 1 - 3). T_{g1} and T_{g2} show the position of the glass transition temperature if a glass forming liquid is supercooled (i.e. below T_m and above T_g, orange line). With decreasing temperature the liquid structure is kinetically locked in and the position of the glass transition depends on the previous history of the (supercooled)liquid. Glass$_1$ was quenched more quickly then Glass$_2$. As the glass transition temperature is history-dependent, several conventions exist how it is defined, nevertheless all of them are arbitrary and agree at best within a couple of °K. The glass shown by point B at room temperature (observation conditions) contains some portion of the enthalpy or volume of fusion (red dashed line, point 2) compared to a crystalline solid (point A) and is in a metastable state. Modified after Debenedetti and Stillinger (2001).

5.7.4   Implied rheological behavior of PAM and AM

Amorphous materials exhibit a wide range of rheological behavior from solid-like to fluid-like and are hence described in terms of visco-elastic rheology (Malkin, 2009; Duxson et al., 2007). Depending on many parameters (the amount of short-, medium- and long-range order, presence of second-phase particles (Haw, 2004), chemical composition, bond strength, degree of polymerization, observation time scales and temperature with respect to the glass transition temperature, T_g) amorphous materials can be either very "weak" (i.e. accommodate strain at low shear stresses) or very "strong" (i.e. support high shear stresses without straining), (e.g. Cordonnier et al., 2012; Hess et al., 2008; Lavallée et al., 2008; Falk and Langer, 2011; Suryanarayana, 2001; Duxson et al., 2007; Malkin, 2009). The superposition of elastic deformation on irreversible viscous flow causes complex behavior. Elastic energy is accumulated during deformation due to the distortion of individual atoms in the material by an externally applied stress. This build up of elastic energy is counteracted by material reorganization due to diffusion (e.g. Chakraborty, 2008) which maintains strain compatibility and allows flow. Therefore amorphous materials exhibit a temperature and time (strain rate) dependent rheology, similar to crystalline solids. Depending on the P-T-$\dot{\gamma}$ conditions the material will either flow or fracture which is given by the dimensionless Deborah number (Reiner, 1964), $De = tc/tp$ where tc is the stress relaxation time and tp is the observation time, and $De = 0 - \infty$.

If the build up of stress is slow enough that the material can efficiently relax the stress under given P-T conditions, the material will flow i.e. behave as a fluid (low De). On the other hand if the build up of stress is fast, and the relaxation processes can not keep pace at given P-T conditions with the imposed loading, the material will accumulate elastic energy until – ultimately – it fractures, i.e. behaves as a solid (high De).

One of the fundamental differences between an ideal solid and an ideal fluid is the response to applied (small) shear strain (e.g. Mason and Weitz, 1995). An ideal solid stores all mechanical energy and its response is elastic (given by the shear modulus, $G = \tau/\gamma$, where τ is the shear stress and γ is the shear strain, i.e. stress depends on strain) whereas an ideal fluid dissipates all mechanical energy and its response is viscous (viscosity, $\eta = \tau/\dot{\gamma}$ where τ is the shear stress and $\dot{\gamma}$ is the shear strain rate, i.e. stress depends on strain rate). Visco-elastic materials exhibit an intermediate behavior. It should be pointed out that this distinction between a solid and a fluid is purely rheological, i.e. purely based on the materials response to strain. In everyday experience the rheological behavior also corresponds to thermodynamical states of matter, i.e. thermodynamical liquids are fluid and thermodynamical solids are solid, however this does not have to be always the case. Fluidized gouges and cataclazites are a good example of a non-molten material exhibiting fluid-like behavior in natural fault zones (Rowe et al., 2005; Kirkpatrick and Shipton, 2009; Brodsky et al., 2009; Otsuki et al., 2003).

During deformation, the work rate, $\dot{W}$ and the competition between energy dissipation rate, $\dot{\theta}$, including heat production and other irreversible increases in entropy and the rate of increase in internal energy, $\dot{E}$, should control the microstructural development (Austin and Evans, 2007 and references therin). If a large amount of mechanical energy is stored in the microstructure, this energy can not be dissipated and can not do any work. Or in other words, if mechanical energy was used to break atomic bonds and produce a nanocrystalline or amorphous material, it will not be available to increase the temperature.

Keeping in mind that the slip zones form an interconnected layer which concentrate significant amounts of strain within the fault rock, we suggest that the observed rate and temperature dependence is mainly caused by the viscous component of the visco-elastic rheology of the PAM and AM. As the temperature increases and strain rate decreases the viscous component becomes more pronounced which could explain the observed mechanical response (Figs. 5.5, 5.6, 5.7, 5.8).

On a more speculative level, the observed non-arrhenian dependence of temperature in the range between 400 - 500°C might be an expression of the PAM and AM undergoing a glass transition. Nevertheless as only bulk rheological behavior of the sample is known (i.e. slip zones + deforming lenses) micro-indentation tests or differential scanning calorimetric measurements would have to be performed to constrain the glass transition temperature. Further, based on microstructural observations, it seems that the PAM/AM acted as a considerable sink of energy during deformation resulting in a metastable, far from thermal equilibrium material storing some portion of the volume/enthalpy of fusion (Fig. 5.26, e.g. Suryanarayana, 2001).

This material is not a result of abrupt failure as it is observed in both samples that crept continuously over several days as well as in samples that failed catastrophically. Therefore, it is possible to speculate that the AM might cause failure under certain P-T-$\dot{\gamma}$ conditions, i.e. at a given Deborah number, De $\gg$ 0, the AM cannot flow anymore and abruptly fractures. Amorphous materials are likely to be produced under high-stress low-temperature conditions

and might thus trigger earthquakes under a broad range of conditions. Typical conditions where amorphization would be expected is on fault asperities, which increase in size in proportion to the applied force so that the material is stressed just to its yielding point (e.g. Scholz, 2007).

5.7.5   Implications for natural fault zones

In our experiments the simulated fault rock microstructure scales primarily with finite strain (Fig. 5.25). Fault surfaces with slicken slides appear during unloading along the highly strained PAM and AM in the slip zones (Fig. 5.24). However, considering the high normal stresses acting on this surface, and the fact that the unloading crack always cuts discordantly through slip zones (Fig. 5.10, chapter 4), we would argue that during deformation the local strain rates in the deforming volumes controlled how the material deforms. In the mechanical record, we see that the fault rocks do not fail abruptly (except for experiments performed at 300°C and 10^{-6} m s^{-1}) but reach a high quasi-steady state stress level and continue to deform up to a γ of $\sim$5.

The bulk strain rate and temperature dependence are indicative of viscous deformation suggesting that the rock flows. Nevertheless the "flow" is accommodated by a combination of granular flow accompanied by fracturing of the coarser grained aggregates and laminar / turbulent flow of the PAM / AM on the sample scale.

The AM/PAM is inferred to be a metastable, far from thermal equilibrium material and therefore is expected to crystallize and/or devitrify over geological time-scales as an attempt to lower its Gibbs free energy. It is worth noting that the feldspar derived PAM/AM has a composition, which is suitable for growing white micas and clay minerals (Wintsch et al., 1995). The growth of metamorphic minerals from amorphous pre-cursors is well documented (e.g. Eggleton and Buseck, 1980) and such process could lead to development of a mica foliation following the former slip zones.

5.7.6   The "frictional-viscous" transition

In the introduction we pointed out difficulties in comparing friction to flow due to the dimensional miss-match of the two theories. Studies trying to reconcile the rate-and-state dependent friction laws with steady state flow laws often approach the "frictional-viscous" transition from the Earth's surface, i.e. from the frictional field. However, as plate tectonic movement is probably driven by powerful convective motions in the mantle (e.g. Bercovici, 2003), it is interesting to approach the "frictional-viscous" transition from below, i.e. from the viscous flow field.

First, what boundary conditions should we assume? An approximately constant velocity boundary condition seems as the most appropriate because plate tectonic velocities are best constrained (in contrast to stresses and strain rates which are less well constrained), and faults *have* to accommodate tectonic plate movement.

Yield strength of the lithosphere will increase with decreasing depth in the viscous field (because the temperature and confining pressure decrease, Fig. 5.1). For a given constant velocity boundary condition two end member possibilities appear. Either the shear zone width

changes (and hence strain rate at given velocity) so that the fault rocks operate at stresses which equal the yield strength of the undeformed country rocks ("constant stress" approach, the strength of the lithosphere is dictated by the undeformed rocks, Platt and Behr, 2011) or the fault rocks are weaker than the country rocks and operate at lower stresses than the surrounding country rock ("constant strain rate" approach, the strength of the lithosphere is dictated by the shear zones e.g. Kohlstedt et al., 1995) with any intermediate situation possible.

In both cases the strength of the lithosphere will be at its peak in the semi-brittle field i.e. around the "frictional-viscous" where the rocks can no longer accommodate the imposed displacement by viscous flow and start to build up elastic energy until they fracture. Fracture can be seen as the result of materials inability to flow at given P-T-$\dot{\gamma}$ conditions (given by the Deborah number). Pervasive fracturing will on the other hand increase mass-transfer processes facilitating viscous flow in the fault rocks (due to the increased surface-to-mass ratio and increase in permeability and fluid flow etc., e.g. Faulkner et al., 2010) thus a feedback process develops. In fact, there is wide spread evidence that both fracturing and viscous flow often operate in concert to accommodate plate tectonic movement at all crustal levels (e.g. Fusseis et al., 2006; Fusseis and Handy, 2008; Menegon et al., 2011; Mancktelow and Pennacchioni, 2005; Pennacchioni and Mancktelow, 2007; Pennacchioni et al., 2006; Závada et al., 2007, 2012; Gratier et al., 1999, 2011; Gratier and Gamond, 1990; Hadizadeh et al., 2012) rising the possibility that rather than a sharp transition from one deformation process to an other the "frictional-viscous" transition is a transition influenced by our observation scale (i.e. when we view a fault as a surface and as a volume) and frameworks in which we think about the processes. In other words, the "frictional-viscous" transition should not be regarded as a layer occurring at a certain given depth in the crust. This is sometimes assumed based on the "constant strain rate" approach to rheological profiles (Fig. 5.1). The fact that Byerlee's rule intersects with a steady-state flow law for wet quartzite deformed at "geological" strain rates of $\sim 10^{-15}$ s^{-1} around greenschist-facies conditions might be more a lucky coincidence than a fundamental change in deformation processes (as it is based on the assumption that an average plate tectonic velocity of 1 cm/year is homogenously and continuously accommodated by a 320 km wide zone and an heat flow of 60 mW m^{-1} on Earth's surface, e.g. Kohlstedt et al., 1995).

In the upper crust above the "brittle-ductile transition" (i.e. the transition from frictional sliding to cataclastic and semi-brittle flow, Fig. 5.1) the yield strength will likely be limited by the Byerlee's rule and decrease towards the Earth's surface where no shear stresses can be supported (as a free surface exists). However as fracture strength is size dependent (e.g. Bhattacharyya and Chakrabarti, 2006; Scholz, 2007) it is difficult to say at what depth the transition from frictional sliding to distributed semi-brittle or cataclastic flow should occur.

Nevertheless, rheological profiles are very useful due to their simplicity. The general evolution of crustal strength predicted by these profiles matches field observations very well and its use in models also yields good results. The fact that most faults obey andersonian mechanics in the upper crust (e.g. Sibson and Xie, 1998; Collettini and Sibson, 2001; Scholz, 2007) demonstrates that Byerlee's rule for friction is often valid. Field observations in the viscous field also document a general trend of strength decrease with increasing depth (Stipp et al., 2002a,b; Jerabek et al., 2007; Kilian et al., 2011a,b; Behr and Platt, 2011). The occurrence of amphibolite facies to green schist facies viscous shear zones which are associated with contemporaneous brittle deformation (e.g. Fusseis et al., 2006; Fusseis and Handy, 2008; Mancktelow and Pennacchioni, 2005; Pennacchioni and Mancktelow, 2007; Pennacchioni et al.,

2006) as well as pseudotachylites occurring around depths corresponding to the base of the seismogenic layer fit the picture well (Bestmann et al., 2011, 2012; Di Toro et al., 2005; Di Toro and Pennacchioni, 2004; Di Toro et al., 2006; Sibson, 1975; Cowan, 1999; Spray, 2010; Wenk et al., 2000; Lin, 2007). These field observations indicate that around greenschist faciest conditions viscous deformation processes struggle to accommodate the displacement, dilatation becomes possible and the fault rocks begin to fracture.

However, some observations do not fit this picture. Recently discovered family of "slow earthquakes" (Beroza and Ide, 2011), occurrence of pseudotachylites below seismogenic depths (e.g. Austrheim and Boundy, 1994), together with the ongoing debate where the strength of the lithosphere resides (e.g. Maggi et al., 2000; Bürgmann and Dresen, 2008) shows that the implications of rheological profiles should not be over interpreted.

There is an long-standing debate whether faults are "weak" or "strong" i.e. what friction coefficient is needed to operate the fault in a given stress field. The most puzzling examples are low angle normal faults (LANF) which operate at very shallow dips not allowed for in the classical Andersonian point of view (e.g. Wernicke, 1981). Another well studied example is the San Andreas fault (SAF) which seams to be misoriented with respect to the local stress field (even though this interpretation was questioned, e.g. Scholz, 2000). The orientation of such faults is "paradoxical" if we assume the universality of Byerlee's rule, and these apparent paradoxes are being often explained within the frame-work that caused them by searching for low friction minerals in the fault rocks.

For example, the apparent weakness of the creeping SAF segment was recently "explained" by the presence of saponite which is one of the minerals with the lowest friction coefficient known (Lockner et al., 2011). Just a couple of years earlier talc with a slightly higher friction coefficient was the proposed solution (Moore and Rymer, 2007). These studies were approaching the problem from the frictional point of view. However, Gratier and co-workers (Gratier et al., 2011) have demonstrated that the imposed plate tectonic movement can be entirely accommodated by penetrative pressure-solution creep accompanied by microfracturing (viscous point of view).

The friction coefficient as a simple ratio of shear stress to normal stress with no natural concept of strain, time or temperature dependence is to crude to capture fault behavior. Similarly steady-state flow laws break down at high stresses which accompany fracturing (see 5.4) and are of limited use at the base of the seismogenic layer where interseismic, seismic and post seismic processes accommodate the plate tectonic motion. As mentioned above, microstructural studies document that the interplay between fracturing and mass-transfer processes is rather the rule than exception in natural fault rocks over a broad range of pressures and temperatures. Fault rocks can be viewed as low- to medium-grade metamorphic rocks and are not simple granulated equivalents of the protolith (Faulkner et al., 2010). Therefore, a viscous component seems to be often present in natural fault rocks.

Maybe a more useful question to ask is what is the most efficient way to accommodate the imposed displacement resulting from plate tectonic motions?

For example large scale extension, from a geometrical point of view, is much more efficiently accommodated on a low angle normal fault compared to andersonian high-angle normal faults. Both frictional as well as viscous theories are useful in their range of validity, however faults exhibit a broad range of behavior which is not necessarily well described by any of them alone. It seems necessary to search for an underlying rheological behavior which is consistent with

both flow and friction and would be equally useful in the "frictional-viscous" field. And at last, but not least would be simple enough to be useful.

5.8   Conclusions

We conducted an experimental study on granitoid fault rocks under a broad range of temperatures, displacement rates and confining pressures where the rocks deform by semi-brittle flow and conclude the following:

- Microstructural evolution is primarily controlled by finite strain and secondarily by stress/temperature, confining pressure and bulk strain rate.

- The presence of quartz as the strongest rheological phase probably facilitates the build up of high stresses.

- High stresses cause pervasive comminution and crystal lattice destruction in the weaker minerals (feldspars and micas) and form the nanocrystalline partly amorphous material (PAM).

- Peak strength is reached once an interconnected anastomozing network of slip zones formed of PAM where the strain partitions is formed.

- Some slip zones continue to accumulate strain and the PAM is progressively transformed into an amorphous material (AM) which shares many similarities with naturally occurring pseudotachylites.

- Both PAM and AM represent high-energy, far from thermal equilibrium microstructures.

- Slicken-slides formed by PAM / AM appear along unloading cracks on the exposed surfaces.

- The "frictional-viscous" transition should not be regarded as a layer occurring at a fixed depth. "Frictional-viscous" behavior is probably common in natural fault rocks.

Concluding remarks

This study focused on the rheological behaviour and mircrostructural development of granitoid fault rocks in the semi-brittle flow regime. The physical processes operating under these conditions were identified and their influence on the rheolgoical behaviour was assessed. This chapter summarizes the main observations of this study, presents the reached conclusions and discusses its implications for natural fault zones. Further research possibilities are being suggested.

Deformation apparatus

The sample assembly was optimized for acquiring precise and reproducible results at low temperatures by using potassium iodide as a weak confining salt. Good reproducibility can be achieved ($\ll 5\%$) if all the pieces of the assembly are as similar as possible, and the deformation geometry is well constrained (by the pre-cut forcing blocks). At the elevated isotropic confining pressures, it is necessary to use forcing blocks of significantly harder material (e.g. alumina) than the deforming powder as the strength of the powder is identical or higher to that of an intact rock once the porosity has been eliminated. The detection limit, accuracy, precision and resolution of the apparatus was assessed. The apparatus performs well if the strength contrast between the sample and the parts constituting the solid medium sample assembly is high. The slope of the run-in segment of the force curve used to asses the friction correction is dependent only on the distance to hit point and not the experimental conditions (pressure, temperature and displacement rate) as previously thought. A force of 1.3 kN/mm is necessary to advance the tungsten carbide piston into the pressure vessel and should be subtracted from sample strength. Further, during general shear deformation to high strains, the thinning imposed by the geometric constraints of the experimental set-up needs to be well quantified. Care has to be taken when re-calculating the raw data to stress - strain curves as the assumptions (friction correction and forcing block overlap correction) become progressively more important the higher the strains are.

Microstructural development

Microstructural observations document wide spread comminution first fracturing larger survivor grains (> 100 μm) into fine grained fragmented mantles (< 100 nm) along R_1 - Riedel shears. Quartz fractures the least and both feldspars the most indicating that quartz is the rheologicaly strongest phase. Adjacent to favourably oriented micas (basal slip in the C' direction) and on high-stress sites next to larger quartz survivor grains the fine grained feldspar material (< 100 nm) is progressively transformed into a cohesive, nanocrystalline, partly amorphous material (PAM) showing (laminar) flow structures. The chemical composition of this PAM is commonly intermediate between potassium-feldspar and plagioclase. The amount of this material increases with increasing strain and micas get incorporated into the PAM. This material forms roughly 4 - 6 thicker, anastomozing interconnected layers in the C-C' direction with a simply connected topology covering up to around 7-12 vol% of the whole shear zone around peak strength. The slip zones accommodate 2.5 - 5 times more strain compared to the strain in the bulk rock indicating strain partitioning and localization.

With increasing bulk strain, the deformation localizes further and the PAM in the slip zones becomes progressively more amorphous ($> 90\%$ - 99%) containing very few crystalline fragments with a grain size on the order of ~ 5 nm. Within this matrix, larger clasts of PAM as well as quartz single crystals and composite clasts are present. Some of these clasts are surrounded by a layer of a different z-contrast material. The fragment loaded, TEM-amorphous material (AM) has a more heterogeneous chemical composition compared to the feldspar derived PAM and is in general more ferromagnesian and less silicic than the bulk rock. The most amorphous layers have a biotite as a pre-cursor. These layers show turbulent flow structures, occupy roughly 1% of sample volume exploiting 1 or 2 pre-existing slip zones and – most likely – form a multiply-connected topology. This AM material often shows intrusive relationships with the crystalline fragmented aggregates forming injection veins. Grain size reduction is observed towards the fully TEM-amorphous layers and all still crystalline fragments are highly strained. On a small scale, the chemical composition of nano-crystalline fragments and amorphous material is identical, indicating that the crystalline-to-amorphous transition is iso-chemical.

The exception to this microstructural development are experiments deformed at 600 °C, confining pressures of 500 and 1000 MPa and slowest displacement rates (10^{-8} m s^{-1} inducing strain rates, $\dot{\gamma}$, of $\sim 10^{-5}$ s^{-1}). Fine grained material has often interconnected, lobate grain boundaries indicative of dissolution-precipitation creep and PAM is rarely observed in these experiments. These experiments also show the lowest degree of fabric flattening.

If an unloading crack from high strain experiments is inspected in SE-SEM, fine striations are observed. These striations are made of the PAM and AM which formed in the slip zones where the strain localized.

Mechanical development

Strain hardening occurs up to high peak shear strength ($\tau \sim 0.6$ - 1.4 GPa). The peak strength is strongly temperature dependent (300°C experiments are the strongest, 600°C the weakest) and weakly bulk strain rate dependent (faster experiments are stronger than slower ones). After the peak strength the samples weaken slightly (by 40 - 140 MPa) and continue to deform at a high stress level ($\tau \sim 0.8$ - 1.2 GPa) without abrupt failure up to a shear strain, γ of ~ 5. Only samples deformed at 300°C and the fastest displacement rates fail abruptly around peak strength. The failure is audible and accompanied by a stress drop by 800 MPa

shear stress and a 60 - 200 μm vertical piston displacement.

Increasing the confining pressure from 300 MPa to 1500 MPa causes the fault rock to reach higher shear stresses at lower shear strains. The increase is most pronounced from 300 - 1000 MPa (475 MPa), whereas only little increase (75 MPa) takes place between 1000 and 1500 MPa confining pressure. The calculated friction coefficient, μ, reflects this behaviour and as the normal stress keeps increasing in proportion to confining pressure while the shear stress has reached its peak and does not increase any further, it decreases from 0.8-0.65 at 300 - 500 MPa confining pressure to $\sim$ 0.5 at 1500 MPa confining pressure.

Experiments performed at 600 °C, confining pressures of 500 and 1000 MPa and slowest displacement rates (10^{-8} m s^{-1}, inducing strain rates, $\dot{\gamma}$, of $\sim$ 10^{-5} s^{-1}) reach the lowest shear stresses (450 - 600 MPa). Higher confining pressure experiments performed at slower displacement rates weaken slightly more after peak strength compared to experiments performed at 500 MPa confining pressure and yield well behaving steady state stress levels.

If plotted in the shear strain rate vs. shear stress space a high shear stress threshold is present (0.8 - 1.2 GPa) before the cataclasite begins to flow. The flow is weakly strain rate dependent (i.e. faster shear strain rates are reached at higher stresses, behaviour of a Bingham body). If the data is fitted to standard power-law constitutive equations, very high stress exponents (n $\sim$ 17 - 48) and low activation energies (Q $\sim$ 15 - 125 kJ/mol) are obtained indicating a "power law break down" regime. Due to the large shear stresses (on the order of 1 GPa) a large elastic/frictional component is present rendering the use of power law creep equations difficult (or rather meaningless).

Boundary conditions present in the experimental set-up

Measurement of sample thickness indicates that a thinning component of $\sim$ 55% occurs up to shear strains of $\sim$ 5. The thinning is slightly non-linear indicating that most of the compaction takes place early in the experiment ($\gamma < 1.5$). The samples thin roughly 10% more compared to published values on low porosity rocks which is in agreement with the observation that the starting material has $\sim$ 10% porosity. A significant pure shear component is always present in general shear experiments.

Measured simple shear displacement in thin sections ($\sim$ 2.5 mm at shear strains of $\sim$ 5) constrains how much deformation the fault rock sustained over the time period of deformation independently on mechanical data obtained from the deformation apparatus. This displacement has to be accommodated in the shear zone over 0.5 - 50 hours of deformation (depending on the applied displacement rate). If the deformation would be accommodated homogeneously in the whole fault rock volume, strain rates of $\sim$ 10^{-3} - 10^{-5} s^{-1} would be reached. Microstructural record documents strong strain partitioning in the polyphase rock where 2.5 - 5 times more strain is accommodated in the slip zones compared to the bulk rock, however it has to be noted that this is a rough estimate as strain estimates are difficult to perform in high strain slip zones. However a local strain rate increase has to be compensated by a strain rate decrease in the low strain domains as the total displacement is fixed, or in other words increase in strain rate does not imply an increase in slip velocity.

For a constant velocity boundary condition (induced by the σ_1 piston) two end member possibilities for strain partitioning in a rheologically polyphase material (and any combination thereof) exist: either a iso-stress boundary condition exists and the weaker zones accommodate more strain at identical stresses as the stronger domains (i.e. strain-rate varies), or an iso-

strain boundary conditions exists and the weaker zones deform at lower stresses than the stronger domains (i.e. stress varies). Microstructures imply strong strain and strain-rate partitioning and therefore a iso-stress boundary condition seems as the most probable.

Temperature considerations

The temperature increase above set experimental temperatures was calculated to be small ($\sim 2.5°$C). The high temperature flux in the sample assembly ($\sim 10^4$ °C m^{-1}) renders the possibility of high temperature increase unlikely, especially by $\sim 1400°$C which would be necessary to interpret the observed microstructures in current state-of-the-knowledge. Further, the range of accessible conditions in displacement rates (velocities) varies significantly more than the range of accessible shear stresses during laboratory experiments (10^{-8} m s^{-1} to 1 m s^{-1} vs. 1500 MPa to 1 MPa, if we compare our data to typical values where frictional melting is observed) and therefore the influence of speed on the temperature increase is expected to be more important. Stick-slip events were also proposed as an mechanism for temperature increase leading to thermodynamic melting, however they would need enormous accelerations (A. Niemeijer, pers. comm.). We can reliably detect sample failure and piston movement by 60 - 200 μm and also can measure the cumulative displacement over several minutes to days of deformation (around 2 mm). This places an upper bound on displacement jogs that could go undetected in our experimental set up. We can assume that the sample sticks (velocity 0 m/s) and then slips at a seismic velocity (1 m s^{-1}) thus reaching high temperatures (at least in theory according to the shear heating equation) within say 1 μm (needing 1 μs for the displacement) an acceleration of 10^6 m s^{-2} would be necessary. A slip of say 1000 μm in 1000 μs (a substantial part of displacement measured in thin sections) would result in an acceleration of 10^3 m s^{-2}. These are conservative estimates because we neglect the fact that such stick slip events would also have to break to 0 m/s again (back to stick). Such accelerations correspond to approx. $100 - 100\,000$ g-force rendering such possibility unlikely as well.

Inferring the origin and rheological behaviour of PAM and AM

The high strength contrast between individual minerals forming the granitoid rock (Qtz - strongest, Fsp and micas - weakest) and high qtz content ($\sim 40\%$) facilitates the build up of high differential stresses necessary to destroy the crystal lattice of the weaker minerals at the employed experimental conditions. The nanocrystalline partly amorphous material probably strain hardens as a result of porosity reduction during temperature-activated sintering (as the vol% of slip zones keeps increasing with increasing finite strain and temperature) and geometric necessity. As a result of strain localization during high bulk strain ($\gamma > 2.5$) quasi steady-state creep, zones of amorphous material form exploiting some of the pre-existing slip zones. These zones contain clasts of partly amorphous material and quartz single crystals as well as composite clasts, have intrusive relationship towards the surrounding rock, show turbulent flow structures, and at 300°C forms bubbles. The continuity of the flow structures and deformed bubbles indicate that they formed continuously during the experiment. Based on comparison to published microstructures of natural pseudotachylites, we conclude that the fragment loaded amorphous material could be identified as a pseudotachylite in nature. However, neither the mechanical record nor the microstructures indicate that this material has reached high temperatures.

As the pre-cursor material is already largely amorphous, it seems that the fragment loaded amorphous material is just a higher strain stage of the nanocrystalline, partly amorphous material. Crystalline to amorphous transition is achieved by four different processes (ho-

mogenous and heterogeneous amorphization and melting), two of which do not need any temperature increase. Therefore, the presence of XRD- or TEM-amorphous material should not be used to imply thermodynamic melting. Furthermore, the transition from crystalline to amorphous material seems to be continuous and attention should be paid to the fact that nanocrystalline materials might posses very different thermodynamical properties compared to their (micro)crystalline counterparts.

The amorphous material is formed mostly of feldspars and micas which contain both network modifiers (alkalis etc.) as well as builders (Si, Al) found in glasses. Further, they have a relatively large unit cell and weaker weakest-link inter-atomic bonds (feldspars unit cell ~ 0.8 nm^3, ionic bonds; micas unit cell ~ 1.0 nm^3, Van der Waals bonds) compared to quartz (unit cell ~ 0.13 nm^3, covalent bonds). Once the material approaches nanocrystalline grain sizes, it seems to be difficult to maintain long-range order as many atoms form the surface where the lattice is distorted.

Amorphous materials do not melt but undergo a glass transition over a broader temperature range if heated. Based on mechanical data showing similar strengths at 400°C and 500°C over 3 orders of magnitude variations in bulk strain rates, together with the basic and ferromagnesian composition of the amorphous material lets us speculate that the glass transition occurs somewhere around $\sim$500°C. We imply that the amorphous material will exhibit a visco-elastic rheology and, as it occurs in experiments that crept continuously for several days as well as in experiments that failed abruptly, we conclude that the amorphous material cannot be the result of abrupt failure.

Rheological behaviour of amorphous materials depends on many parameters (the amount of short-, medium- and long-range order, presence of second-phase particles, chemical composition, bond strength, degree of polymerization, observation time scales and temperature with respect to the glass transition temperature, T_g) and amorphous materials can be either very "weak" (i.e. accommodate strain at low shear stresses) or very "strong" (i.e. support high shear stresses without straining). In other words the presence of amorphous material should not be used to imply weakness of the material.

Turbulent microstructures observed in the amorphous material indicate that it exhibits a fluid-like behaviour, i.e. shear stress will be proportional to shear strain rate. Turbulence occurs generally at high Reynolds number in newtonian fluids, in non-newtonian fluids the relationship is even more complex and no good understanding of turbulence is currently available.

We speculate that this material might under certain P-T-$\dot{\gamma}$ strain rate conditions be the cause of failure if its Deborah number reaches high values and the material fractures as a solid quickly dissipating accumulated elastic energy. Amorphization would be expected to occur in nature under low temperature, high pressure or stress conditions in a material which has a high phase strength contrast necessary to build up high stresses and destroy the crystal lattice of the weaker mineral(s). Such process could trigger earthquakes under a broad range of conditions.

Future research possibilities

1. We have documented that the rocks fail under fast displacement rates and T=300°C. It would be interesting to explore the lower temperature range. If our predictions are true, we would expect that rocks at lower temperatures (e.g. 200°C) will fail abruptly after a certain finite strain also at slower displacement rates (e.g. 10^{-7} ms^{-1}). Furthermore, the microstructures at T=600°C and slowest displacement rates are strikingly different from all other conditions indicating that the production of the nanocrystalline as well as amorphous material might be inhibited at higher temperatures and/or lower stresses. It therefore seems that the amorphous material resembling a pseudotachylite can form only over a narrow P-T-$\dot{\gamma}$ space.

2. The higher confining pressure range was hardly covered. Experiments operating at higher confining pressure benefit more from the design of the deformation apparatus (i.e. the results are more reproducible). Such experiments could provide important insights into processes responsible for earthquake generation at greater depth (i.e. in a subducting slab). Current theories for earthquake nucleation (rate-and-state dependent friction) are only applicable to the upper crust as frictional sliding will be inhibited at the "brittle-ductile" transition. On the contrary, very deep earthquakes are simulated in laboratory and probably connected to phase transitions. Currently, most earthquakes between the shallow and deep ones are explained in terms of dehydration embrittlement, i.e. high pore pressures. However these models are purely mechanical, i.e. do not take in account chemical effects of the fluids at high pressures.

3. The thermodynamic properties of the amorphous and nanocrystalline partly amorphous material could be measured by differential scanning calorimetry if enough material could be obtained for example at a FIB. In combination with nanoindentation methods the glass transition temperature could be assessed and the amount of energy stored in the metastable microstructure could be estimated. However due to the inherited heterogeneity of the material, it is expected that many measurements would have to be performed to obtain a statistically relevant picture.

4. Longer experiments could asses whether the nanocrystalline, partly-amorphous to amorphous material devitrifies or undergoes a metamorphic reaction, forming e.g. micas or clay minerals. This could provide an important clue on how major lithosphere scale faults initiate and mature. Many fault cores are commonly phylosillicate-rich and the metastable material might be a good candidate for metamorphism.

5. Ball milling of the Verzasca gneiss powder could reproduce microstructures observed in this study. As the temperature during milling is well constraint it could test whether the amorphous material can form by a purely mechanical effect.

6. Is there a connection between strain rate and displacement rate for shear heating? Based on microstructural observations and employed experimental conditions, we inferred that the amorphous material did not form by melting at high temperatures. The induced displacement rates were slow however, due to strain localization the local strain rates were possibly up to 1 order of magnitude higher than the bulk induced strain rates (as high as $\sim 10^{-2}$ s^{-1} in the fastest experiments). Shear heating studies in the viscous field work usually purely with bulk strain rates, however they are connected to the displacement rate through the deforming volume. On the contrary, frictional studies working on frictional heating use displacement rates (i.e. velocities) rendering the data hardly

comparable. It seems plausible that a critical volume for a given thermal boundary condition needs to be deformed at a high strain rate so that the temperature can increase and is not conducted away. It seems that a strain rate without a displacement rate and vice-versa are meaningless.

7. A theoretical framework which would allow the description of the phenomenology observed during semi-brittle flow is a necessary pre-requisite to develop constitutive equations. Application of current frictional as well as viscous flow approaches seems not to be useful in the semi-brittle flow regime.

RIG: a Matlab^{TM} program for evaluation of mechanical data from experimental apparatuses

Installation: Unpack RIG.zip into any convenient directory. Add the RIG directory including subdirectories ("rig analogue chart", "rig digital chart" and "files") to your MATLAB path (file → set path → add folder with subfolders → RIG). After this you either have to restart MATLAB or update your toolbox path cache (file → preferences → general → update toolbox cache)

Uninstallation: Delete the RIG directory and remove the path from your MATLAB

Contact: Any bug reports, suggestions etc. are welcome on:

matej.pec@unibas.ch or *matej.pec@seznam.cz*

www: http://sites.google.com/site/rigprogram

A.1   Quick guide

Before you start, it is useful to close any open figures and clear all variables on the workspace with the commands "close all" and "clear all" (write this into the command window). Then you have to import your data into MATLAB. The most convenient format to import is a text file with column headers corresponding to the variables in the column. Use the standard import function of MATLAB (file → import data...) a dialogue window like this will appear after you choose your file:
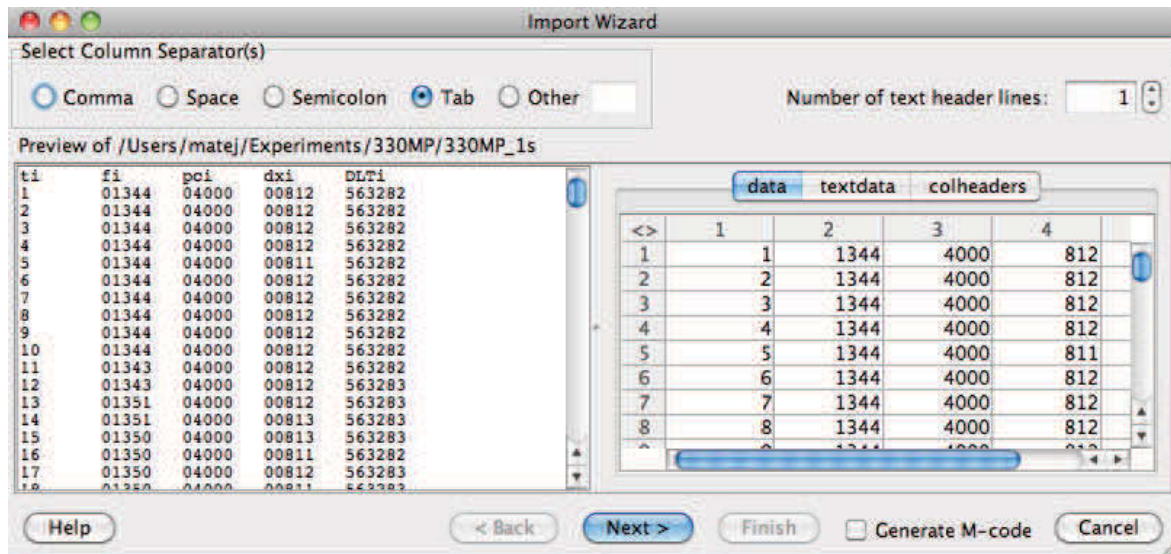
Select the appropriate separator and click "Next >"
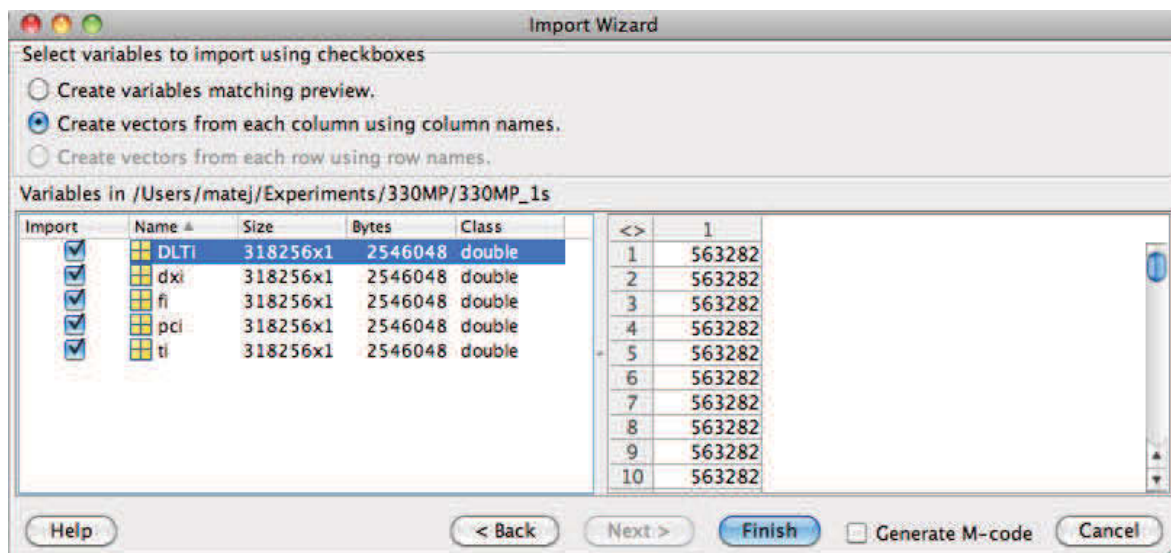
select "Create vectors from each column using column names" and click "Finish". Now the desired variables are on your workspace.

Note: the variables HAVE to be called **ti** (time input), **fi** (force input) **pci** (confining pressure input) **dxi** (displacement input) and optionally **DLTi** (digital length transducer input – installed on rig2 in Tromsø). An example text file is included in the "files" folder for tests.

To run the program just type "rig" for evaluation of digital chart data or "rigA" for evaluation of "classical" chart data into the MATLAB command window and follow the instructions on the screen...that's it!

Once the analysis is finished, in addition to MATLAB workspace variables, three text files will be created in the working directory ($name-of-your-experiment-log.txt$ containing information about your input during the evaluation of data, calibrations used etc.; $name-of-your-experiment-fits.txt$ containing the data about linear fits created during hit-point definition and three differently defined hit-point values (kN) (for details see Fig. A.4) and $name-of-your-experiment-coax.txt$ or $shear.txt$ with the results for further processing using i.e spreadsheet editors.

If you want more help see section A.3 or type "help rig" into the MATLAB command window or any other function name (see Fig. A.1 for names of used functions) – a simple help will be displayed.

A.2   Detailed manual

A.2.1   Introduction

An open platform MATLAB program for the evaluation of mechanical data from experiments is introduced. The program performs stress-strain, strain rate (and many more) calculations for samples deformed a) in coaxial compression b) in shear (induced by sliding of pre-cut blocks in coaxial compression). Further, it allows quantitative evaluation of the run-in and "elastic" curves. The program has been developed with special emphasis on the evaluation of data from solid medium Griggs deformation apparatuses but can be used for any other deformation apparatus working with the same sample geometry. Easily modifiable rig calibrations ensure that no deep knowledge of MATLAB is needed for the operation of this program. All calibrations are for the Tromsø rigs.

This program is based on the fortran programs rigPrep, rigC4 and rigS4 developed by Renée Heilbronner (http://pages.unibas.ch/earth/micro/) which were in turn developed from various precursors (RIGX etc.) written for the Griggs apparatus at Brown University and from another one (RIG) written for the Heard apparatus at ETH Zürich.

A.2.2   Motivation

During rock deformation experiments one usually records only the elapsed time, confining pressure ($\sigma_3=\sigma_2$), force recorded on the σ_1 piston and displacement of the σ_1 piston. These input measurements, combined with the measured sample dimensions are used for calculating the final strain rate, stress-strain curves etc. It is clear that different numerical approaches can lead to significant differences in the final output data. Since usually experimental studies are not specific about the exact calculating procedure, we find it useful to
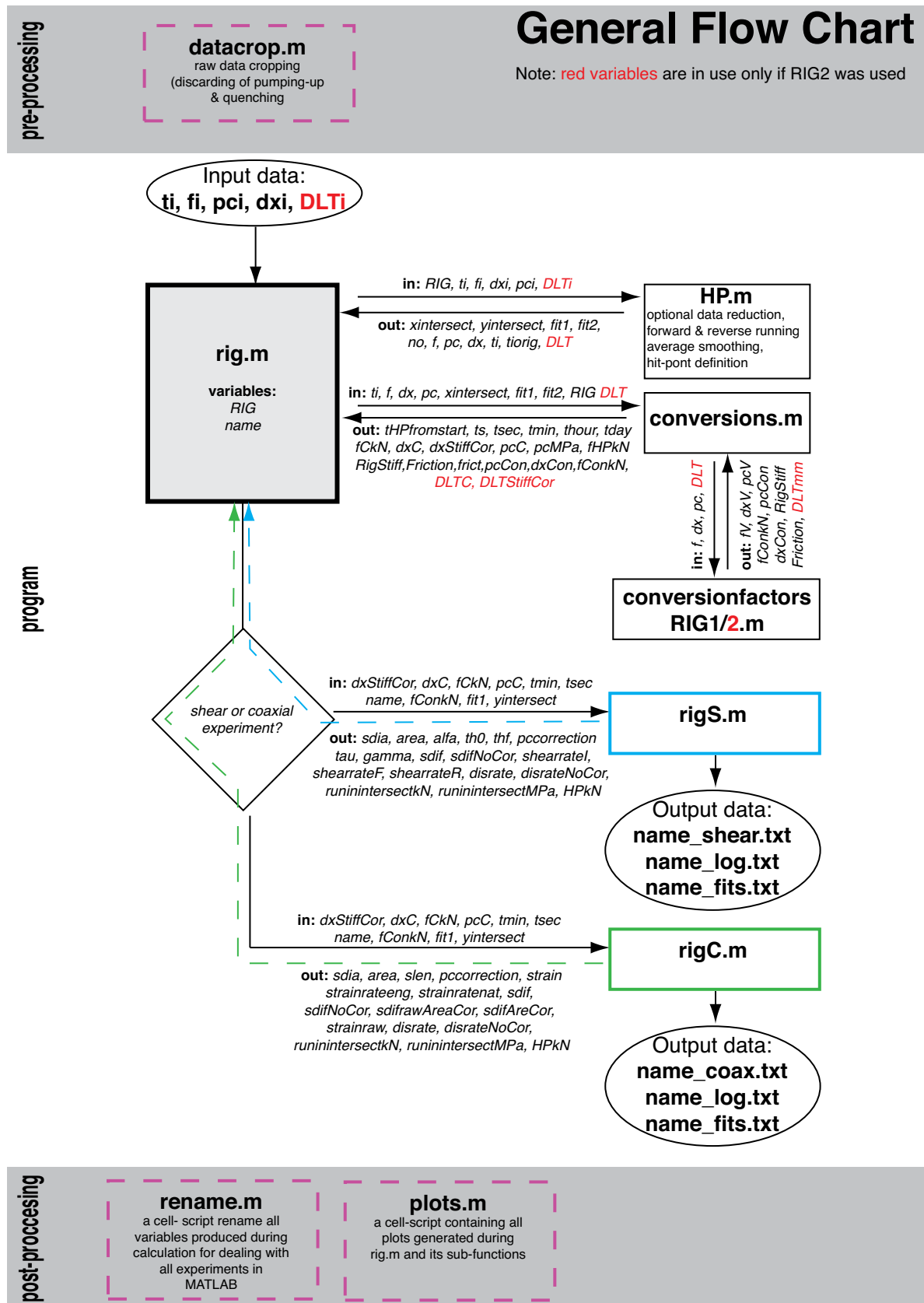
Figure A.1: RIG flow chart

introduce a program, which explicitly states how the raw data is evaluated. MATLAB was chosen because it is widely available on universities, allows easy plotting and the source code is easily readable. The program is divided into two main sections: "rig analogue chart" and "rig digital chart". The major difference is in the input data (chart units vs. volts) and conversion factors used. Otherwise is the calculating procedure identical. Rig-digital-chart includes some extra functions designed to deal with digital chart records and is described in detail here.

A.2.3   RIG

The main function $rig.m$ calls the following functions which will be described in the following sections: a) $HP.m$ b) $conversions.m$ c) $conversion factors RIG1/2.m$ d) $rigC.m$ e) $rigS.m$. Additional scripts used are f) $txtwrite.m$ g) $getpoly.m$ from the GNU polyLX toolbox and h) $filtfilt.m$ from the noise-proccessing toolbox (not described here). The program is by default written for two rigs but can be easily expanded to any desired number. These functions have to be in the same folder, which must be in the MATLAB search path (see installation). Further scripts for more advanced MATLAB users are dealing with the raw and final data include i) datacrop.m j) rename.m k) plots.m. A flow chart summarizes the program structure in Fig. A.1, a brief description of variables is in section A.4.

A.2.3.1   datacrop.m

Script to crop data; used to cut away pumping up of the experiment and quenching. Plots fi, pci, dxi against ti. Allows zooming to the area of interest and selecting of data via $getpoly.m$. Discards data outside of user-selected region. This script is not included in the $rig.m$ and has to be called by typing $datacrop$ (or $datacrop2$ if rig2 data is used) into the MATLAB command window.

Note: since the vectors have to have the same size for further evaluation it is necessary that the cut data start and stop on a common ti, i.e. the selection has to be rectangular. Otherwise an error *??? Error using ==> plot Vectors must be the same lengths* will occur.

A.2.3.2   rig.m

This script is used to call all the other functions, plot recalculated data (force (kN), displacement (mm) and confining pressure (MPa) vs. time (min)) and to write the output text files. Function $txtwrite.m$ is used for writing the $log.txt$ and $fits.txt$ file. Standard c-language command fprintf is used to write the $shear.txt$ and $coax.txt$ files due to large amounts of data written into these files ($fprintf$ is about one order of magnitude faster than $txtwrite.m$).

A.2.3.3   HP.m

This script is used to define the hit-point and basic data treatment. For large files ($>$100 000 records per variable) a data reduction option is offered to maintain computing speed. The data reduction takes every X^{th} point according to user input (i.e. entering "2" results in a file half the original size). Data smoothing by a forward and reverse running average is offered.
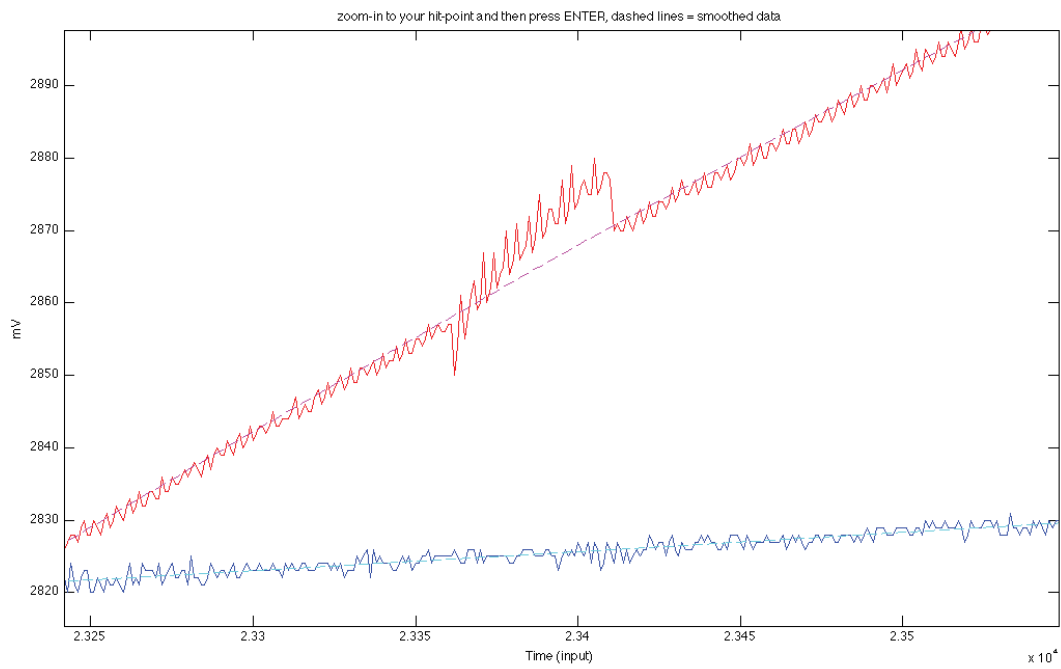
Figure A.2: Raw data (solid lines), smoothed data (dashed lines)
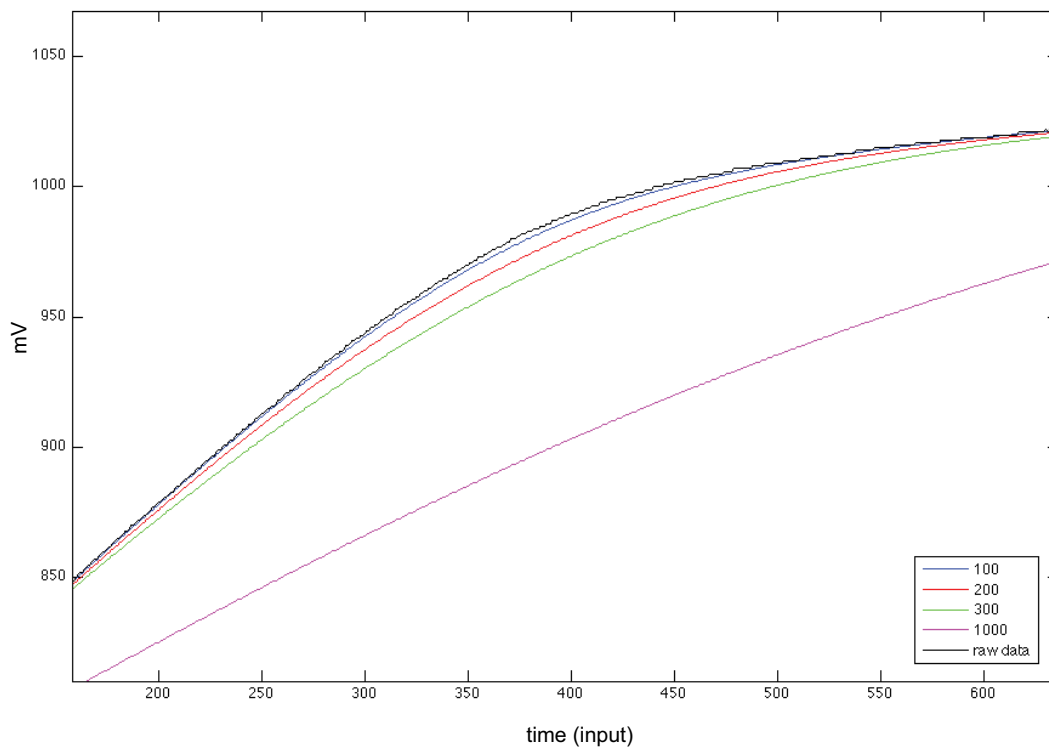
Figure A.3: Effect of different filter range (purple = 1000, green = 300, red = 200, blue = 100, black are raw input data)

This filter has the advantage that it does not introduce any phase shift, effectively filters out digital input steps and high frequency noise, if present (Fig. A.2). The minimum possible filter range is 3, too high filter range results in poor fits in regions with an abrupt change in slope (Fig. A.3).

Afterwards a plot of the raw force (mV), displacement data (mV), confining pressure (mV) and its smoothed counterparts vs. time (input) is generated (Fig. A.4). Zooming into the individual curves allows verifying the quality of the data fit.

Note: by pressing "ctrl + c" you can abort the program if smoothing is not good and start the program again to choose a more appropriate filter range for smoothing.

Once you are satisfied with the data fit you can zoom into the region of the hit-point so that the run-in as well as "elastic" part of the curve can be seen.

Note: Appropriate zooming (i.e. a long and narrow rectangle) also allows to vertically exaggerate the curves for better identification of the hit-point in weak samples.

After hitting "enter" the plot is updated and allows selecting of a region on the run-in curve and the "elastic" part of the force curve (using the *getpoly.m* script). These regions are fitted with a linear regression curve and their intersection is calculated (actual hit-point).

Note: start with the run-in curve in order to get the right numbers in the "fits.txt" text file – otherwise the slopes and y-intersects of the run-in and elastic curves will be switched.

Output is the smoothed data, the linear fit thru the run-in & "elastic" curves in the form $fit = [a, b]$ where a is the slope of the run in curve and b its intersect with the y-axis (y=ax + b) and their intersect (hit-point). In the end the script discards all data before the hit-point.
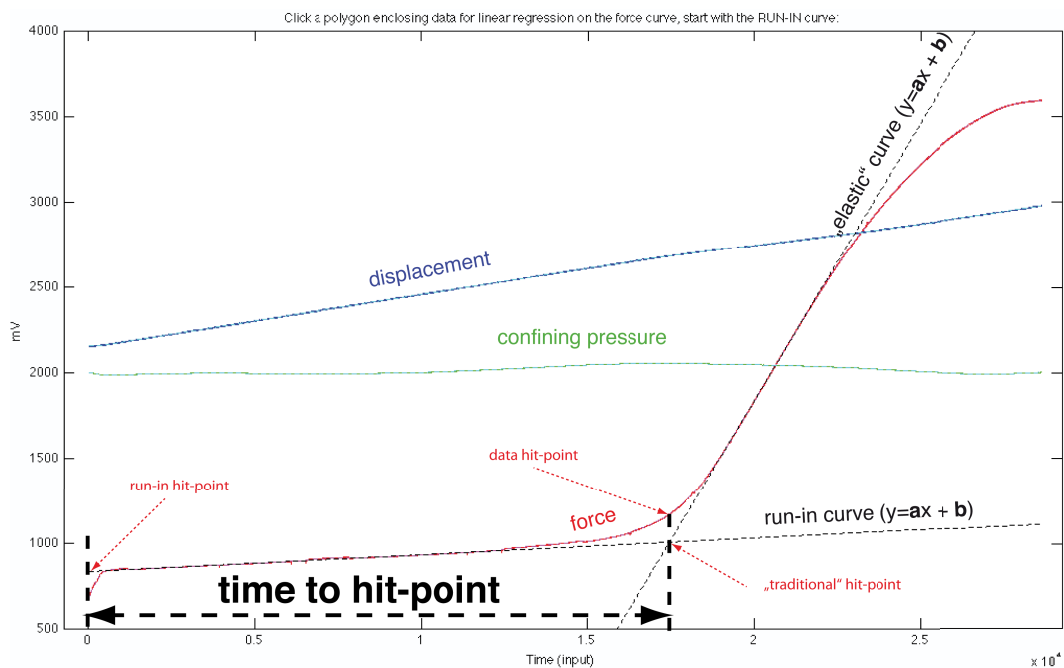
Figure A.4: Raw and smoothed data, three different hit point definitions and definition of time to hit-point are shown (part of the $name − of − your − experiment fits.txt$ output)

A.2.3.4   conversions.m

This script recalculates the input time to time in seconds, minutes, hours and days and calculates the time at hit-point.

Note: the time at hit point is calculated assuming that the analyzed file starts in the moment where the σ_1 motor has been started (Fig. A.4). (use *datacrop.m* to cut away the pumping-up of the experiment if it has been recorded into the same file as actual deformation). The run-in hit-point is defined as the y-axis intersect of the run in curve, therefore user attention is needed to verify the quality of the fit (good for well behaving run-in curves, gets worse in weak samples and/or steep run-in curves)

Further, it calls the function *conversionfactorsRIG*1.*m* (or *conversionfactorsRIG*2.*m*) where the appropriate conversion factors are stored and recalculates the raw data to (kN) for force, (MPa) for confining pressure and (mm) for displacement. Displacement corrected for rig stiffness and force (kN) corrected for friction is calculated as well. It plots the uncorrected displacement (mm) vs. time (min) and the least squares fit forced through zero to check the linearity of motor speed (deviates from linear by strong samples)

A.2.3.5   conversionfactorsRIG1/2.m

A short function that stores the conversion factors (Volts to (kN),(MPa),(mm) for force, confining pressure and displacement, respectively) for individual rigs so that it can be easily modified. It also contains the rig stiffness correction factor (rigStiff), i.e. how much "longer" does the rig get with applied load (mm/kN) and rig friction (Friction). The rig stiffness is typically obtained by loading some very stiff material (i.e. tungsten carbide rods) at conditions close to the experimental ones. One assumes that all the measured displacement is due to the compliance of the rig. The values for friction can be obtained from salt dummy runs that simulate the real experiment. In the case of a Griggs rig, one obtains a bulk correction factor including the confining media strength, jacket strength and any friction in the apparatus itself (see chapter 5.3). Both of these corrections can be ignored (i.e set to 0).

A.2.3.6   rigC.m

This script evaluates coaxial experiments. All corrections and assumptions are plotted so that the user can immediately see their effect. The script reads the measured sample length and diameter (Fig. A.5). Strain is calculated by assuming that the sample retains a right cylinder shape during deformation by the following equation:

$$\epsilon = \frac{1 - (l_0 - dx)}{l_0} \times 100 \tag{A.1}$$

where ϵ is the finite strain (units: %) dx is the displacement of σ_1 piston (units: mm) and l_0 is the original sample length (units: mm).
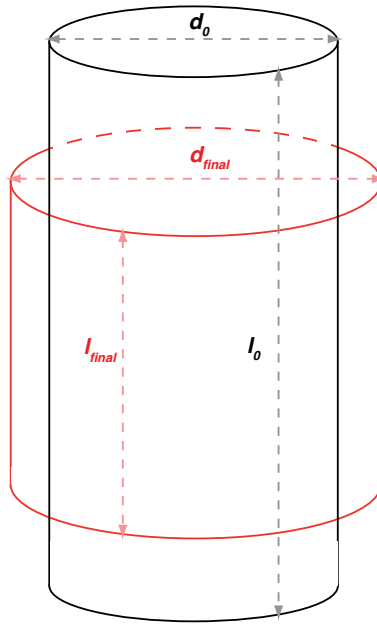
Figure A.5: Sample in coaxial compression before (black) and after deformation (red) assuming no volume change

Displacement rate of the σ_1 piston is calculated from displacement (uncorrected as well as corrected for rig stiffness) as:

$$\dot{d} = \frac{\partial dx}{\partial t} \tag{A.2}$$

Where $\dot{d}$ is the displacement rate (units: mm s^{-1}) and t is time (units: s)

Natural (finite) strain rate is then calculated as:

$$\dot{\epsilon}_{nat.} = \frac{\dot{d}}{l_0} \tag{A.3}$$

(units: s^{-1})

and engineering (instantaneous) strain rate as:

$$\dot{\epsilon}_{eng.} = \frac{\dot{d}}{l_0 - (l_0 - dx)} \tag{A.4}$$

(units: s^{-1})

The applied stress on the sample is calculated assuming that the sample retains a constant volume (i.e. cross-sectional area expands at the same rate as the sample is being shortened) (Fig. A.5) by the following equation:

$$\sigma_1 = \frac{F \times \left(\frac{l_0 - dx}{l_0}\right)}{area} \tag{A.5}$$

(units: MPa)

Where F is the force (units: N) and $area$ is the cross sectional area of the cylinder (units: mm^2)

Note: This correction can lead to significant changes in the trend of the data in high strain experiments (Fig.A.6) and should be reviewed with caution by the user.
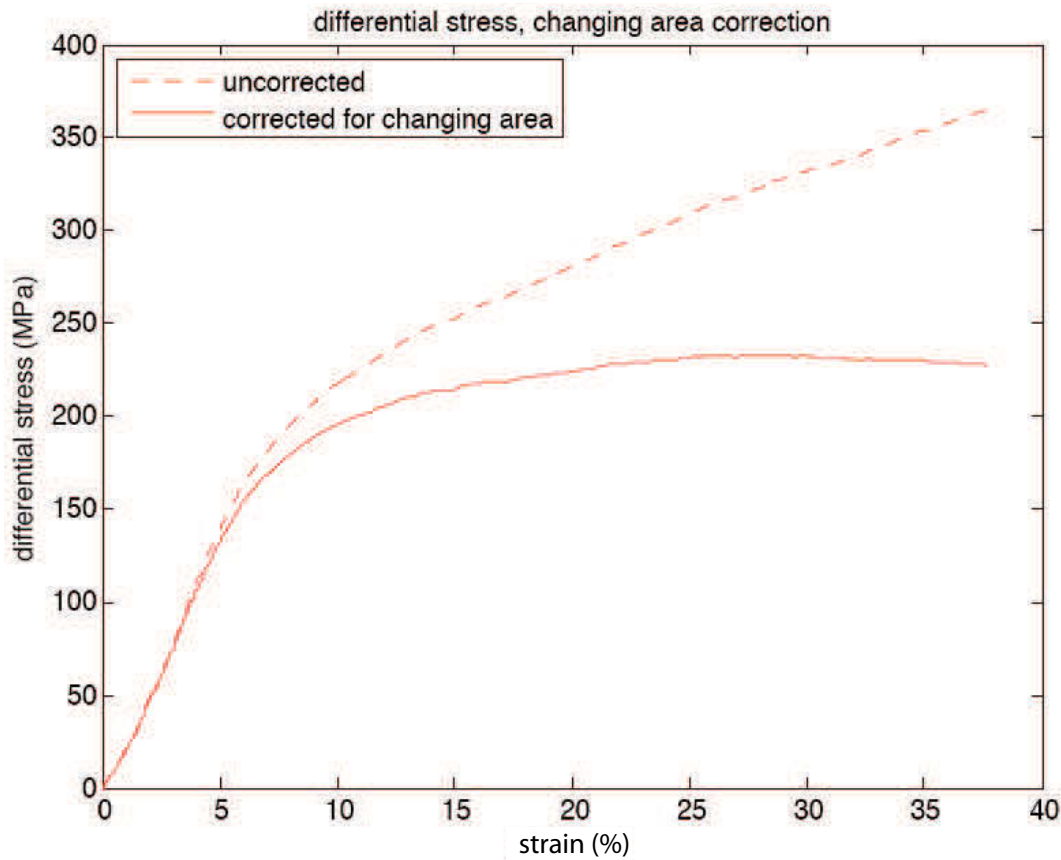
Figure A.6: strain hardening or steady state? The effect of constant volume assumption

Change in the confining pressure (σ_3) with time (t) occurs during Griggs rig experiments. Since the differential stress, $\Delta\sigma$, is calculated as σ_1 - σ_3 at the time of the hit-point one might prefer to calculate the differential stress taking in account the change of the confining pressure with time.

$$\Delta\sigma_{(t)} = \sigma_{1(t)} - \sigma_{3(t)} \tag{A.6}$$

(units: MPa)

The script plots raw stress (uncorrected for area change) and stress (corrected for area change) (MPa) vs. strain (%). Further it plots the displacement rate of σ_1 piston (corrected as well

as uncorrected for rig stiffness) (mm s^{-1}) vs. time (min) and, at last, natural and engineering strain rates (s^{-1}) vs. time (min). If the user has chosen the confining pressure correction it also plots the differential stress (uncorrected and corrected for changing confining pressure) (MPa) against time (min).

A.2.3.7 rigS.m

This script evaluates general shear experiments. All corrections and assumptions are plotted so that the user can immediately see their effect. The script reads the measured sample diameter; initial and final thickness of the shear zone (mm) and the angle of the pre-cut in the forcing blocks (°) (Fig. A.7 and A.8). The initial thickness of the shear zone has to be measured e.g in a hydrostatic experiment. We assume that no change in area of forcing blocks occurs (i.e d_0 stays constant during the deformation, the forcing blocks do not accomodate strain).
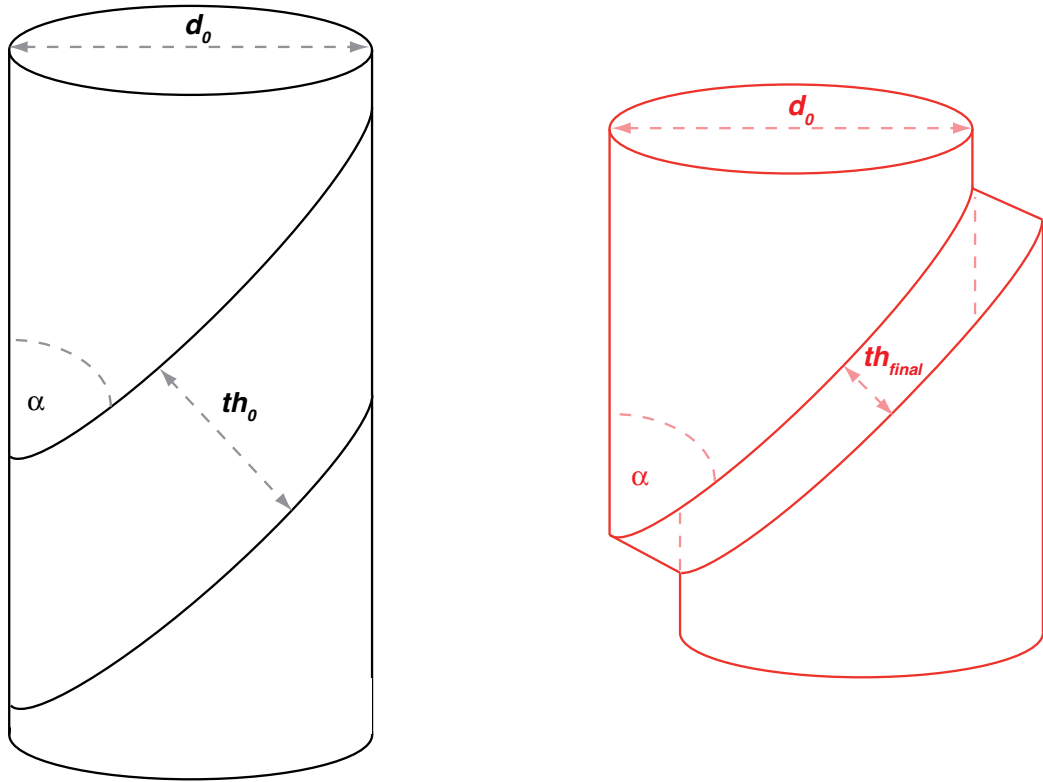
Figure A.7: Sample geometry for shear experiments before (black) and after (red) deformation.

Shear strain is calculated by resolving the vertical displacement (dx) into a pure-shear component (Δth) i.e. thinning of the shear zone and simple-shear component (dz_{simple}). We assume that the thinning of the shear zone occurs continuously during the whole run and that maximal piston overlap occurs in the beginning of the experiment (Fig. A.8). First the proportion (i.e. how much vertical displacement does account for the compaction of the shear zone) is calculated by the following equation:

$$proportion = \frac{dz_1 tot}{dx} \tag{A.7}$$
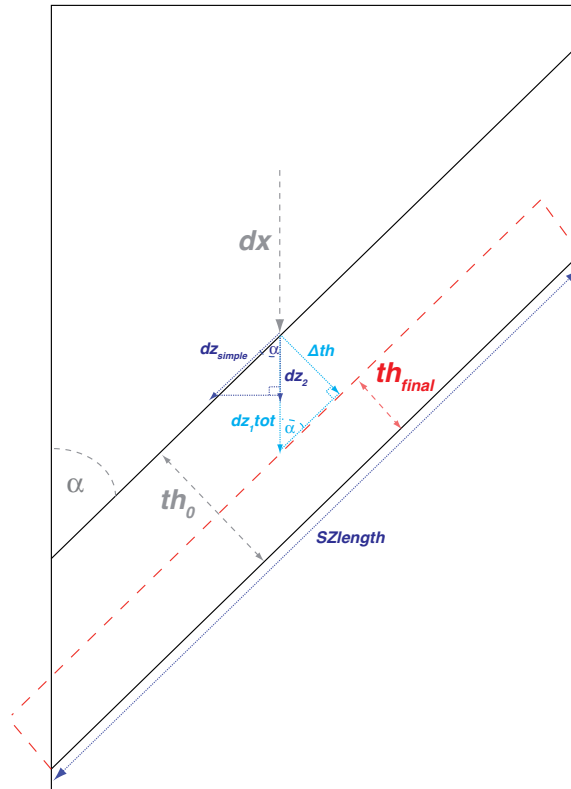
Figure A.8: Resolving of vertical displacement (dx) into pure shear (Δth) and simple shear (dz$_{simple}$)

Then the vertical displacement component is calculated as:

$$dz_{1(t)} = proportion \times dx_{(t)} \tag{A.8}$$

$$dz_{2(t)} = dx_t - dz_{1(t)} \tag{A.9}$$

(units: mm)

The thickness of the shear zone at a given time (t) is calculated as (Fig. A.8):

$$th_{(t)} = th_0 - dz_{1(t)} \times sin(\alpha) \tag{A.10}$$

(units: mm)

And the simple shear component is calculated as:

$$dz_{simple(t)} = \frac{dz_{2(t)}}{cos(\alpha)} \tag{A.11}$$

(units: mm)

Shear strain (γ) at given time (t) is then calculated as:

$$\gamma_{(t)} = \frac{dz_{simple(t)}}{th_{(t)}} \qquad (A.12)$$

(unitless)

Stress (σ_1) is calculated as (assuming no forcing block deformation):

$$\sigma_1 = \frac{F}{area} \qquad (A.13)$$

(units: MPa)

Where F is the force in (N) and $area$ is the cross sectional area of the cylinder in (mm^2)

Again a correction for changing confining pressure is offered (see equation A.6).

Assuming that the piston overlap (area of contact) gets smaller with increasing slip, we calculate the changing area by the following equations:

$$contact_{(t)} = \frac{dz_{simple(t)}}{\frac{d_0}{sin(\alpha)}} \qquad (A.14)$$

(unitless)

Where $\frac{d_0}{sin(\alpha)}$ is the length of the shear zone (Fig. A.8). The area overlap is calculated using auto correlation function of a circle. A cubic fit to one half of the auto correlation function profile is used (Fig. A.9). Note that the solution is identical also for an ellipse. For more information on ACF see e.g. Heilbronner (2002).

$$acfArea_{(t)} = 1 - 1.2082 \times contact_{(t)} - 0.19134 \times contact_{(t)}^2 + 0.39461 \times contact_{(t)}^3 \quad (A.15)$$

Note: This assumption has exactly the opposite effect as the constant volume assumption in coaxial experiments evaluation (i.e. force steady state turns into shear stress hardening because of the diminishing area on which the force acts) and should be reviewed carefully by the user.
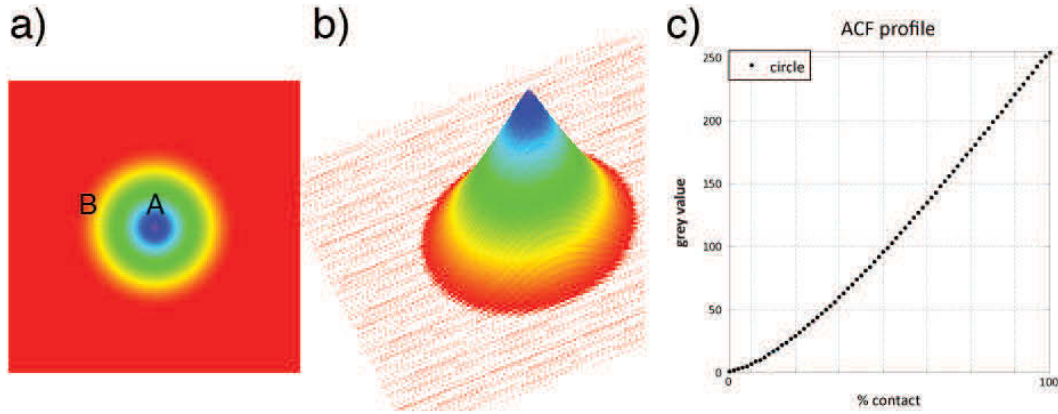
Figure A.9: Piston overlap calculation a) auto correlation function of a circle, purple corresponds to 100% correlation (i.e. maximal piston overlap), red corresponds to no correlation (i.e. no piston overlap); b) surface plot of a); c) profile B-A of a), cubic fit of this curve is used to calculate acfArea

Shear stress (τ) is calculated for 45° precut forcing blocks as:

$$\tau_{(t)} = \frac{0.5 \times \Delta\sigma_{(t)}}{acfArea} \tag{A.16}$$

(units: MPa)

Note: The calculated shear stress is ONLY valid for the case of 45° pre-cut forcing blocks – this will be fixed in some future release.

Vertical piston displacement rate is calculated with equation A.2 and natural (finite) shear strain rate is then calculated as (Twiss and Moores, 2007):

$$\dot{\gamma}_{nat.(t)} = \frac{\frac{0.5 \times \Delta dz_{simple}}{\Delta t}}{th_0} \tag{A.17}$$

(units: s^{-1})

Engineering (instantaneous) shear strain rate is calculated as (Twiss and Moores, 2007):

$$\dot{\gamma}_{eng.(t)} = \frac{\frac{0.5 \times \Delta dz_{simple}}{\Delta t}}{th_{(t)}} \tag{A.18}$$

(units: s^{-1})

Shear strain rate compatible with the one calculated in rigS4.f (http://pages.unibas.ch/earth/micro/) is calculated as:

$$\dot{\gamma}_{R(t)} = \frac{\Delta\gamma}{\Delta t} \tag{A.19}$$

(units: s^{-1})

The program plots shear stress (MPa) vs. shear strain and all three strain rates (s^{-1}) vs. time (min). If the user has chosen the confining pressure correction it also plots the differential stress (uncorrected and corrected for changing confining pressure) (MPa) against time (min).

A.2.3.8   rename.m

A simple cell script that can be used to rename and clear all variables from MATLAB workspace. It is separated into three cells, which can be executed by the "evaluate cell" button. The first one renames DLT variables (use only if RIG2 was used), the second one is used to rename all variables used during the calculation of a shear experiment and the last one is used for renaming variables used during the calculation of coaxial experiments. Afterwards, you can save your workspace for further data treatment with MATLAB. To access this script just type "edit rename" into the command window. Then you can do "find & replace" and replace all "255" with the number or name of your experiment.

A.3   Troubleshooting

If you can not import a file into MATLAB open it in Textwrangler or any other text editor end select the option "show invisibles" usually there are some extra symbols after the 4th/5th column - just select one line and do "search and replace" to delete them. Make sure that every line is terminated by "enter"' (and not "tab enter")
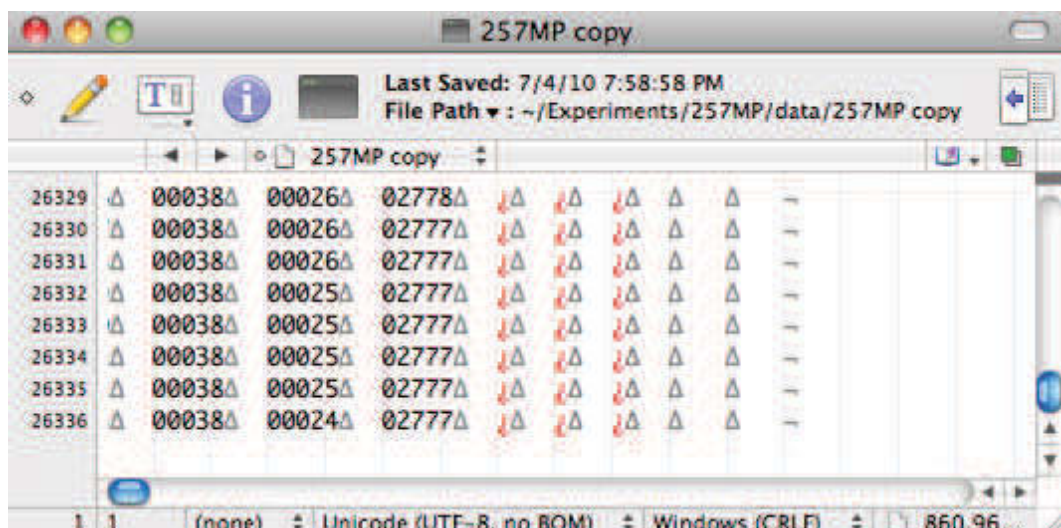
If your file imported into MATLAB is not complete check the line at which the import stops in textwrangler ("apple + J" is "go to line") if the data is not recorded due to buffer owerflow etc. MATLAB stops importing at this point. Delete the lines without data and try once again.

A.4   Output variables

ACFcontactDLT – forcing block overlap calculated form digital length transducer (DLT) displacement data

ACFcontact – forcing block overlap calculated form direct-current displacement transducer (DC-DT) displacement data

DLTC – DLT data recalculated to mm from the hit-point (i.e displacement at hit-point = 0)

DLTStiffCor – DLT data recalculated to mm and corrected for rig stiffness

DLT – digital length transducer smoothed by forward & reverse running average filter (used for all calculations instead of DLTi)

Friction – friction correction factor (kN mm^{-1})

HPkN – "traditional" hit-point value in kN (see Fig. A.4)

RIG – number/name of the rig used

RigStiff – correction factor for rig stiffness for the individual rig (kN mm^{-1})

alfa – angle (°) of the shear zone with respect to σ_1

area – cross sectional area of the sample (mm^2)

disrateDLTNoCor – displacement rate calculated from DLT data not corrected for rig stffness (mm s^{-1})

disrateDLT – displacement rate calculated from DLT data corrected for rig stffness (mm s^{-1})

disrateNoCor – displacement rate calculated from DC-DT data not corrected for rig stiffness (mm s^{-1})

disrate – displacement rate calculated from DC-DT data corrected for rig stiffness (mm s^{-1})

dxC – DC-DT data recalculated to mm from the hit point (i.e displacement at hit-point = 0).

dxCon – conversion factor to recalculate volts to mm for DC-DT

dxStiffCor – DC-DT data recalculated to mm and corrected for rig stiffness

dx – displacement in milivolts smoothed by the forward and reverse running average filter (used for all calculations instead of dxi)

dzsimpleDLT – Simple shear displacement calculated from DLT data (see Fig. A.8)

dzsimple – Simple shear displacement calculated from DC-DT data(see Fig. A.8)

extype – coaxial experiment (1) or shear experiment (2)

fCkN – force in kN from the hit-point (i.e force at hit-point = 0)

fConkN – conversion factor to recalculate volts to kN for the load cell

fHPkN – force at data hit-point in kN (see Fig. A.4)

f – force in milivolts smoothed by the forward and reverse running average filter (used for all calculations instead of fi)

fit1 – a and b parameters (y=ax + b) for the run-in curve

fit2 – a and b parameters (y=ax + b) for the "elastic" curve

frictDLT – force corrected for friction (using DLT not corrected for rig stiffness)

frict – force corrected for friction (using dx not corrected for rig stiffness)

gammaDLT – shear strain calculated from DLT data

gamma – shear strain calculated from DC-DT data

name – name/number of the experiment

no – number of points used for the forward and reverse running average filter

pcC – change in confining pressure (in MPa) with respect to "traditional" hit-point (i.e confining pressure at hit-point = 0)

pcCon – conversion factor to recalculate volts to MPa for the confining pressure

pcMPa – confining pressure in MPa

pc – confining pressure in milivolts smoothed by the forward and reverse running average filter (used for all calculations instead of pci)

pccorrection – has the correction for changing confining pressure been used? (y/n)

runinintersectMPa – run-in hit-point in MPa (using initial area of the sample) (see Fig. A.4)

runinintersectkN – run-in hit-point in kN (see Fig. A.4)

sdia – sample diameter in mm

sdifFrictDLT – differential stress (MPa) calculated from DLT data corrected for apparatus friction

sdifFrict – differential stress (MPa) calculated from DC-DT data corrected for friction

sdif – sdifNoCor corrected for changing confining pressure (if the user has chosen not to apply the changing confining pressure correction it will be identical to sdifNoCor) (MPa)

sdifAreaCor – differential stress corrected for changing area and changing confining pressure (if the user has chosen not to apply the changing confining pressure correction it will be identical to sdifrawAreaCor) (MPa)

sdifNoCor – differential stress assuming that the sample has retained the original area throughout the deformation (i.e. no changing area correction) (MPa).

sdifrawAreaCor – differential stress corrected for changing area (MPa)

slen – samle length (mm)

shearrateFDLT – finite shear rate (s^{-1}) calculated from DLT data

shearrateF – finite shear rate (s^{-1}) calculated from DC-DTdata

shearrateIDLT – instantaneous shear rate (s^{-1}) calculated from DLT data

shearrateI – instantaneous shear rate (s^{-1}) calculated from DC-DT data

shearrateRDLT – shear rate compatible with rigS4.f (s^{-1}) calculated from DLT data

shearrateR – shear rate compatible with rigS4.f (s^{-1}) calculated from DC-DT data

strain – coaxial strain (%)

strainrateeng – engineering (instantaneous) strain rate (s^{-1})

srainratenat – natural (finite) strain rate (s^{-1})

strainraw – (sample length – displacement) / sample length

tHPfromstart – time to hit-point from the beginning of recording (s^{-1})

slopeMPa – first derivative of σ_1 by time input

slopedx – first derivative of DC-DT displacement (V) by time input

slopef – first derivative of force input by time input

slopekN – first derivative of force (kN) by time input

slopemm – first derivative of DC-DT displacement (mm) by time input

slopepc – first derivative of confining pressure (MPa) by time input

tHPfromstart – time (input) to hit-point from beginning of the deformation part of the experiment

tauDLT – shear stress (MPa) calculated from DLT data

tauFrictDLT – shear stress (MPa) corrected for apparatus friction calculated from DLT data

tauFrict – shear stress (MPa) corrected for apparatus friction calculated from DC-DT data

tau – shear stress (MPa) not corrected for apparatus friction

th0 – original thickness of the shear zone (mm)

thf – final thickness of the shear zone (mm)

tday – time in days

thour – time in hours

tmin – time in minutes

tsec – time in seconds

ts – time input record interval (s)

tiorig – saves the original time (including pumping if it was recorded in the same file) (s)

xintersect – position of intersection of the run-in and elastic curves on the x-axis (ti)

yintersect – position of intersection of the run-in and elastic curves on the y-axis (mV)

Summary of performed experiments

#	Name	Exp. type	Rig	P.V.	T [°C]	Pc [MPa]	$\dot{d}$ [mm s^{-1}]	$\dot{\gamma}$ [s^{-1}]	plug material	inner sleeves	powder weight [g]	water [μl]	water [wt%]	jacket	sample $\varnothing$ [mm]	F.B.
1	142JO	shear	2	?	24	500	10^{-4}	10^{-4}	Pb + Sn	NaCl	~ 0.1	2	0.2	Au	6.5	VZ
2	145JO	shear	2	?	24	500	10^{-4}	10^{-4}	Pb + Sn	NaCl	~ 0.1	2	0.2	Au	6.5	VZ
3	138JO	hydrostatic	2	?	300	500	N/A	N/A	Pb + Sn	NaCl	~ 0.1	2	0.2	Au	6.5	VZ
4	147JO	shear	2	?	300	500	10^{-4}	10^{-4}	Pb + Sn	NaCl	~ 0.1	2	0.2	Au	6.5	VZ
5	150JO	shear + relax creep	2	?	300	500	10^{-4}	10^{-4}	Pb + Sn	NaCl	~ 0.1	2	0.2	Au	6.5	VZ
6	177MP	shear	2	old	300	560	10^{-4}	10^{-4}	Pb + Sn	NaCl	0.1005	2	0.2	Au	6.55	VZ
7	178MP	shear + const. load creep	2	old	300	500	10^{-4}	10^{-4}	Pb + Sn	NaCl	0.0997	2	0.2	Au	6.56	VZ
8	194MP	shear + relax creep	1	new	300	510	10^{-4}	10^{-4}	Pb	NaCl	0.1007	2	0.2	Pt	6.538	VZ
9	195MP	test of alumina FB	2	old	300	500	10^{-3}	10^{-3}	Pb	NaCl	0.0997	2	2.0	Pt	6.33	Al$_2$O$_3$
10	210MP†	const. load creep	1	new	300	488	10^{-4}	10^{-4}	Pb	NaCl	0.1012	2	2.0	Pt+Ni	6.33	Al$_2$O$_3$
11	211MP	shear + relax creep	2	old	300	500	10^{-4}	10^{-4}	Pb	NaCl	0.1	2	2.0	Pt+Ni	6.33	Al$_2$O$_3$
12	229MP	shear, Al$_2$O$_3$ FB	1	hercules	300	496	10^{-4}	10^{-4}	Pb	KI	0.1003	2	2.0	Pt+Ni	6.33	Al$_2$O$_3$
13	237MP	Verzasca FB, no gouge	2	old	300	493	10^{-4}	10^{-4}	Pb	KI	0	2	0.2	Pt+Ni	6.54	VZ
14	251MP	shear	1	new?	300	515	10^{-4}	10^{-4}	Pb	KI	0.1007	0.2	0.2	Pt+Ni*	6.33	Al$_2$O$_3$
15	257MP	shear	1	old	300	495	10^{-4}	10^{-4}	Pb	KI	0.1001	dry	0.0	Pt+Ni*	6.33	Al$_2$O$_3$
16	260MP	shear	1	old	300	1010	10^{-4}	10^{-4}	Pb	KI	0.101	0.2	0.2	Pt+Ni*	6.33	Al$_2$O$_3$
17	261MP	shear	2	new	300	515	10^{-4}	10^{-4}	Pb	KI	0.101	0.2	0.2	Pt+Ni*	6.33	Al$_2$O$_3$
18	262MP	shear	2	new	300	1475	10^{-4}	10^{-4}	Pb	KI	0.1015	0.2	0.2	Pt+Ni*	6.33	Al$_2$O$_3$
19	279MP	shear - high strain	2	old	300	490	10^{-5}	10^{-5}	Pb	KI	0.1013	0.2	0.2	Pt+Ni*	6.33	Al$_2$O$_3$
20	280MP†	shear	2	new	300	500	10^{-3}	10^{-3}	Pb	KI	0.1	0.2	0.2	Au+Ni*	6.33	Al$_2$O$_3$
21	282MP	shear	2	new	300	505	10^{-3}	10^{-3}	Pb	KI	0.101	0.2	0.2	Pt+Ni*	6.33	Al$_2$O$_3$
22	287MP	shear	1	old	300	510	10^{-5}	10^{-5}	Pb	KI	0.101	0.2	0.2	Pt+Ni*	6.33	Al$_2$O$_3$
23	288MP	shear - high strain	1	old	300	535	10^{-4}	10^{-4}	Pb	KI	0.1017	0.2	0.2	Pt+Ni*	6.33	Al$_2$O$_3$
24	291MP	shear - high strain - BaCl	1	old	300	510	10^{-4}	10^{-4}	Pb	KI	0.1008	0.2	0.2	Pt+Ni*	6.33	Al$_2$O$_3$
25	310MP	shear - high strain	2	old	300	310	10^{-4}	10^{-4}	In	KI	0.1001	0.2	0.2	Pt+Ni*	6.33	Al$_2$O$_3$
26	311MP	shear - high strain	2	old	300	510	10^{-3}	10^{-3}	Pb	KI	0.1	0.2	0.2	Pt+Ni*	6.33	Al$_2$O$_3$
27	317MP	shear - high strain	2	old	300	500	10^{-5}	10^{-5}	Pb	KI	0.0997	0.2	0.2	Pt+Ni*	6.33	Al$_2$O$_3$
28	318MP	shear - high strain	2	old	300	500	10^{-6}	10^{-6}	Pb	KI	0.1008	0.2	0.2	Pt+Ni*	6.33	Al$_2$O$_3$
29	328MP	shear - high strain	2	new	300	980	10^{-5}	10^{-5}	Pb	KI	0.1006	0.2	0.2	Pt+Ni*	6.33	Al$_2$O$_3$

Table B.1: Summary of performed experiments at $\leq 300^{\circ}$C. * – annealed jacket, P.V. – pressure vessel, $\dot{d}$ - displacement rate, $\dot{\gamma}$ - shear strain rate, F.B. - forcing blocks.

#	Name	Exp. type	Rig	P.V.	T [°C]	Pc [MPa]	$\dot{d}$ [mm s^{-1}]	$\dot{\gamma}$ [s^{-1}]	plug material	inner sleeves	powder weight [g]	water [μl]	water [wt%]	jacket	sample $\varnothing$ [mm]	F.B.
30	179MP	hydrostatic	1	new	395	350	N/A	N/A	Pb	NaCl	0.0999	2	0.2	Au	6.56	VZ
31	240MP	shear + const. load creep	2	new	400	500	10^{-4}	10^{-4}	Pb	KI	0.101	2	2.0	Pt+Ni	6.33	Al$_2$O$_3$
32	306MP	shear - high strain	2	old	400	485	10^{-5}	10^{-5}	Pb	KI	0.1007	0.2	0.2	Pt+Ni*	6.33	Al$_2$O$_3$
33	313MP	shear - high strain	2	old	400	520	10^{-4}	10^{-4}	Pb	KI	0.101	0.2	0.2	Pt+Ni*	6.33	Al$_2$O$_3$
34	315MP	shear - high strain	2	old	400	510	10^{-3}	10^{-3}	Pb	KI	0.1007	0.2	0.2	Pt+Ni*	6.33	Al$_2$O$_3$
35	154JO	shear + relax creep	2	?	500	500	10^{-4}	10^{-4}	Pb + Sn	NaCl	~ 0.1	2	0.2	Au	6.5	VZ
36	155JO	shear + const. load creep	2	?	500	500	10^{-4}	10^{-4}	Pb + Sn	NaCl	~ 0.1	2	0.2	Au	6.5	VZ
37	156JO	shear	2	?	500	500	10^{-4}	10^{-4}	Pb + Sn	NaCl	~ 0.1	2	0.2	Au	6.5	VZ
38	176MP	shear	2	old	500	590	10^{-4}	10^{-4}	Pb + Sn	NaCl	0.1017	2	0.2	Au	6.56	VZ
39	180MP	shear + const. load creep	1	new	500	540	10^{-4}	10^{-4}	Pb	NaCl	0.1005	2	0.2	Au	6.56	VZ
40	188MP	shear + relax creep	2	old	500	535	10^{-4}	10^{-4}	Pb	NaCl	0.1	2	0.2	Pt	6.509	VZ
41	191MP	shear test of C instead Pb	2	old	500	500	10^{-3}	10^{-3}	C	NaCl	0.1008	2	0.2	Pt	6.54	VZ
42	193MP	shear + relax creep	2	old	500	550	10^{-3}	10^{-3}	C	NaCl	0.1012	2	0.2	Pt	6.537	VZ
43	200MP	KI test, C	2	old	500	500	10^{-3}	10^{-3}	C	KI	0.1076	2	2.0	Pt+Ni	6.33	Al$_2$O$_3$
44	202MP	Hydrostatic, double TC	2	old	550	500	N/A	N/A	C	NaCl	0.0999	2	2.0	Pt+Ni	6.33	Al$_2$O$_3$
45	208MP	shear	2	old	500	500	10^{-4}	10^{-4}	Pb	NaCl	0.1004	2	2.0	Pt+Ni	6.33	Al$_2$O$_3$
46	209MP	shear	1	new	500	539	10^{-4}	10^{-4}	Pb	NaCl	0.1	2	2.0	Pt+Ni	6.33	Al$_2$O$_3$
47	239MP	Verzasca FB, no gouge	2	old	500	499	10^{-4}	10^{-4}	Pb	KI	0	2	0.2	Pt+Ni	6.54	VZ
48	243MP	shear	2	old	500	500	10^{-4}	10^{-4}	Pb	KI	0.1001	2	2.0	Pt+Ni	6.33	Al$_2$O$_3$
49	245MP	shear	2	new	500	510	10^{-4}	10^{-4}	Pb	KI	0.101	dry	0.0	Pt+Ni*	6.33	Al$_2$O$_3$
50	247MP	shear	2	new	500	495	10^{-4}	10^{-4}	Pb	KI	0.101	0.2	0.2	Pt+Ni*	6.33	Al$_2$O$_3$
51	253MP	shear + const. load creep	2	new	500	530	10^{-4}	10^{-4}	Pb	KI	0.1	0.2	0.2	Pt+Ni*	6.33	Al$_2$O$_3$
52	255MP	shear	2	old	500	1010	10^{-4}	10^{-4}	Pb	KI	0.1007	0.2	0.2	Pt+Ni*	6.33	Al$_2$O$_3$
53	256MP	shear + const. load creep	2	new	500	1020	10^{-4}	10^{-4}	Pb	KI	0.1008	0.2	0.2	Pt+Ni*	6.33	Al$_2$O$_3$
54	263MP	shear	2	old	500	1555	10^{-4}	10^{-4}	Pb	KI	0.1013	0.2	0.2	Pt+Ni*	6.33	Al$_2$O$_3$
55	266MP	shear	2	old	500	1515	10^{-4}	10^{-4}	Pb	KI	0.1012	0.2	0.2	Pt+Ni*	6.33	Al$_2$O$_3$
56	278MP	shear - high strain	1	new	500	500	10^{-5}	10^{-5}	Pb	KI	0.1014	0.2	0.2	Pt+Ni*	6.33	Al$_2$O$_3$
57	284MP	shear	2	new	500	530	10^{-3}	10^{-3}	Pb	KI	0.101	0.2	0.2	Pt+Ni*	6.33	Al$_2$O$_3$
58	286MP	shear	2	new	500	520	10^{-5}	10^{-5}	Pb	KI	0.1013	0.2	0.2	Pt+Ni*	6.33	Al$_2$O$_3$
59	289MP	shear - high strain	2	new	500	520	10^{-4}	10^{-4}	Pb	KI	0.1013	0.2	0.2	Pt+Ni*	6.33	Al$_2$O$_3$
60	290MP	shear - high strain - BaCl	2	new	520	500	10^{-4}	10^{-4}	Pb	KI	0.1018	0.2	0.2	Pt+Ni*	6.33	Al$_2$O$_3$
61	329MP	shear - high strain	1	old	500	965	10^{-5}	10^{-5}	Pb	KI	0.0998	0.2	0.2	Pt+Ni*	6.33	Al$_2$O$_3$

Table B.2: Summary of performed experiments at 400°C and 500°C. * – annealed jacket, P.V. – pressure vessel, $\dot{d}$ - displacement rate, $\dot{\gamma}$ - shear strain rate, F.B. - forcing blocks.

#	Name	Exp. type	Rig	P.V.	T [°C]	Pc [MPa]	$\dot{d}$ [mm s^{-1}]	$\dot{\gamma}$ [s^{-1}]	plug material	inner sleeves	powder weight [g]	water [μl]	water [wt%]	jacket	sample $\varnothing$ [mm]	F.B.
62	307MP	shear - high strain	2	old	600	500	10^{-5}	10^{-5}	Pb	KI	0.0999	0.2	0.2	Pt+Ni*	6.33	Al$_2$O$_3$
63	312MP	shear - high strain	2	old	600	495	10^{-4}	10^{-4}	Pb	KI	0.1012	0.2	0.2	Pt+Ni*	6.33	Al$_2$O$_3$
64	314MP	shear - high strain	1	new	600	520	10^{-3}	10^{-3}	Pb	KI	0.1019	0.2	0.2	Pt+Ni*	6.33	Al$_2$O$_3$
65	316MP	shear - high strain	1	new	600	505	10^{-5}	10^{-5}	Pb	KI	0.1005	0.2	0.2	Pt+Ni*	6.33	Al$_2$O$_3$
66	330MP	shear - high strain	2	old	600	1000	10^{-5}	10^{-5}	Pb	KI	0.1007	0.2	0.2	Pt+Ni*	6.33	Al$_2$O$_3$
67	206MP	Carrara marble	2	old	600	500	10^{-4}	10^{-4}	C	NaCl	N/A	0	0	Pt	6.5	N/A
68	234MP	Shear - Vogelsberg basalt	2	old	500	500	10^{-4}	10^{-4}	Pb	KI	0.1011	2	2	Au + Ni	6.33	Al$_2$O$_3$
69	235MP	Shear - Vogelsberg basalt	2	old	300	500	10^{-4}	10^{-4}	Pb	KI	0.1004	2	2	Au + Ni	6.33	Al$_2$O$_3$
70	197MP	NaCl salt insert test	2	old	300	500	10^{-4}	10^{-4}	Pb	NaCl	N/A	0	0	Pt	6.33	Al$_2$O$_3$
71	198MP	NaCl salt insert test	2	old	500	500	10^{-4}	10^{-4}	Pb	NaCl	N/A	0	0	Pt	6.33	Al$_2$O$_3$
72	204MP	KI salt insert test	2	old	300	500	10^{-4}	10^{-4}	Pb	KI	N/A	0	0	Pt	6.33	Al$_2$O$_3$
73	226MP	NaCl salt insert test	1	old	300	500	10^{-4}	10^{-4}	Pb	NaCl	N/A	0	0	Pt	6.33	Al$_2$O$_3$
74	227MP	KCl salt insert test	2	old	500	500	10^{-4}	10^{-4}	Pb	KI / KCl	N/A	0	0	Pt	6.33	Al$_2$O$_3$
75	231MP	KI salt insert test	2	old	500	500	10^{-4}	10^{-4}	Pb	KI	N/A	0	0	Pt	6.33	Al$_2$O$_3$

Table B.3: Summary of performed experiments at 600°C. Calibration experiments on salt as well as different materials are included. * – annealed jacket, P.V. – pressure vessel, $\dot{d}$ - displacement rate, $\dot{\gamma}$ - shear strain rate, F.B. - forcing blocks.

Bibliography

Andersen, T. B. and Austrheim, H. k. (2006). Fossil earthquakes recorded by pseudotachylytes in mantle peridotite from the Alpine subduction complex of Corsica. *Earth and Planetary Science Letters*, 242(1–2):58–72.

Angell, C. A., Ngai, K. L., McKenna, G. B., McMillan, P. F., and Martin, S. W. (2000). Relaxation in glassforming liquids and amorphous solids. *Journal of Applied Physics*, 88(6):3113–3157.

Austin, N. and Evans, B. (2009). The kinetics of microstructural evolution during deformation of calcite. *J. Geophys. Res.*, 114(B9):B09402.

Austin, N., Evans, B., Herwegh, M., and Ebert, A. (2008). Strain localization in the Morcles nappe (Helvetic Alps, Switzerland). *Swiss Journal of Geosciences*, 101(2):341–360.

Austin, N. J. and Evans, B. (2007). Paleowattmeters: A scaling relation for dynamically recrystallized grain size. *Geology*, 35(4):343–346 DO – 10.1130/G23244A.1.

Austrheim, H. and Boundy, T. M. (1994). Pseudotachylytes Generated During Seismic Faulting and Eclogitization of the Deep Crust. *Science*, 265(5168):82–83.

Beeler, N., Lockner, D. A., Kilgore, B. D., and Moore, D. E. (2011). In *AGU Fall meeting*, volume T54A-01.

Behr, W. M. and Platt, J. P. (2011). A naturally constrained stress profile through the middle crust in an extensional terrane. *Earth and Planetary Science Letters*, 303(3–4):181 – 192.

Bercovici, D. (2003). The generation of plate tectonics from mantle convection. *Earth and Planetary Science Letters*, 205(3–4):107 – 121.

Beroza, G. C. and Ide, S. (2011). Slow earthquakes and nonvolcanic tremor. *Annual Review of Earth and Planetary Sciences*, 39(1):271–296.

Berthé, D., Choukroune, P., and Jegouzo, P. (1979). Orthogneiss, mylonite and non coaxial deformation of granites: the example of the South Armorican Shear Zone. *Journal of Structural Geology*, 1(1):31–42.

Bestmann, M., Pennacchioni, G., Frank, G., Göken, M., and de Wall, H. (2011). Pseudo-tachylyte in muscovite-bearing quartzite: Coseismic friction-induced melting and plastic deformation of quartz. *Journal of Structural Geology*, 33(2):169–186.

Bestmann, M., Pennacchioni, G., Nielsen, S., Göken, M., and de Wall, H. (2012). Deformation and ultrafine dynamic recrystallization of quartz in pseudotachylyte-bearing brittle faults: A matter of a few seconds. *Journal of Structural Geology*, 38(0):21–38.

Bhattacharyya, P. and Chakrabarti, B. (2006). *Modelling Critical and Catastrophic Phenomena in Geoscience: A Statistical Physics Approach*. Lecture Notes in Physics. Springer.

Blanpied, M. L., Lockner, D. A., and Byerlee, J. D. (1991). Fault stability inferred from granite sliding experiments at hydrothermal conditions. *Geophysical research letters*, 18(4):609–612.

Blanpied, M. L., Lockner, D. A., and Byerlee, J. D. (1995). Frictional slip of granite at hydrothermal conditions. *Journal of Geophysical Research-Solid Earth*, 100(B7).

Blanpied, M. L., Marone, C., Lockner, D. A., Byerlee, J. D., and King, D. P. (1998). Quantitative measure of the variation in fault rheology due to fluid-rock interactions. *Journal of Geophysical Research-Solid Earth*, 103(B5).

Bohlen, S. R., Peacor, D. R., and Essene, E. J. (1980). Crystal chemistry of a metamorphic biotite and its significance in water barometry. *American Mineralogist*, 65(1-2):55–62.

Borch, R. S. and Green, H. W. (1989). Deformation of peridotite at high pressure in a new molten salt cell: Comparison of traditional and homologous temperature treatments. *Physics of the Earth and Planetary Interiors*, 55(3-4):269–276.

Bos, B., Peach, C. J., and Spiers, C. J. (2000a). Frictional-viscous flow of simulated fault gouge caused by the combined effects of phyllosilicates and pressure solution. *Tectonophysics*, 327(3-4):173–194.

Bos, B., Peach, C. J., and Spiers, C. J. (2000b). Slip behavior of simulated gouge-bearing faults under conditions favoring pressure solution. *Journal of Geophysical Research-Solid Earth*, 105(B7).

Bos, B. and Spiers, C. J. (2000). Effect of phyllosilicates on fluid-assisted healing of gouge-bearing faults. *Earth and Planetary Science Letters*, 184(1):199–210.

Bos, B. and Spiers, C. J. (2001). Experimental investigation into the microstructural and mechanical evolution of phyllosilicate-bearing fault rock under conditions favouring pressure solution. *Journal of Structural Geology*, 23(8):1187–1202.

Bos, B. and Spiers, C. J. (2002a). Fluid-assisted healing processes in gouge-bearing faults: Insights from experiments on a rock analogue system. *Pure and Applied Geophysics*, 159(11):2537–2566.

Bos, B. and Spiers, C. J. (2002b). Frictional-viscous flow of phyllosilicate-bearing fault rock: Microphysical model and implications for crustal strength profiles. *Journal of Geophysical Research-Solid Earth*, 107(B2):2028.

Boutareaud, S., Hirose, T., Andréani, M., Pec, M., Calugaru, D.-G., Boullier, A.-M., and Doan, M.-L. (2012). On the role of phyllosilicates on fault lubrication: Insight from micro- and nanostructural investigations on talc friction experiments. *J. Geophys. Res.*, 117(B8):B08408.

Brace, W. F. and Kohlstedt, D. L. (1980). Limits on Lithospheric Stress Imposed by Laboratory Experiments. *J. Geophys. Res.*, 85(B11):6248–6252.

Brace, W. F., Silver, E., Hadley, K., and Goetze, C. (1972). Cracks and Pores: A Closer Look . *Science*, 178(4057):162–164 DO – 10.1126/science.178.4057.162.

Brantut, N., Schubnel, A., and Guéguen, Y. (2011). Damage and rupture dynamics at the brittle-ductile transition: The case of gypsum. *J. Geophys. Res.*, 116(B1):B01404.

Brodsky, E. E., Rowe, C. D., Meneghini, F., and Moore, J. C. (2009). A geological fingerprint of low-viscosity fault fluids mobilized during an earthquake. *J. Geophys. Res.*, 114(B1):B01303.

Byerlee, J. D. (1978). Friction of Rocks. *Pure and Applied Geophysics*, 116:615–626.

Bürgmann, R. and Dresen, G. (2008). Rheology of the lower crust and upper mantle: Evidence from rock mechanics, geodesy, and field observations. *Annual Review of Earth and Planetary Sciences*, 36(1):531–567.

Bürgmann, R., Rosen, P. A., and Fielding, E. J. (2000). Synthetic aperture radar interferometry to measure earth's surface topography and its deformation. *Annual Review of Earth and Planetary Sciences*, 28(1):169–209.

Cardwell, R. K., Chinn, D. S., Moore, G. F., and Turcotte, D. L. (1978). Frictional heating on a fault zone with finite thickness. *Geophysical Journal of the Royal Astronomical Society*, 52(3):525–530.

Carter, N. L. and Tsenn, M. C. (1987). Flow properties of continental lithosphere. *Tectonophysics*, 136(1–2):27–63.

Chakraborty, S. (2008). Diffusion in Solid Silicates: A Tool to Track Timescales of Processes Comes of Age. *Annual Review of Earth and Planetary Sciences*, 36(1):153–190.

Cherns, D., Hutchison, J. L., Jenkins, M. L., Hirsch, P. B., and White, S. (1980). Electron irradiation induced vitrification at dislocations in quartz. *Nature*, 287(5780):314–316.

Chester, F. M. and Chester, J. S. (1998). Ultracataclasite structure and friction processes of the Punchbowl fault, San Andreas system, California. *Tectonophysics*, 295(1-2):199–221.

Chester, F. M., Evans, J. P., and Biegel, R. L. (1993). Internal structure and weakening mechanisms of the San Andreas fault. *J. geophys. Res*, 98:771–786.

Chester, F. M. and Higgs, N. G. (1992). Multimechanism friction constitutive model for ultrafine quartz gouge at hypocentral conditions. *Journal of Geophysical Research*, 97(B2):1859–1870.

Chester, F. M. and Logan, J. M. (1987). Composite planar fabric of gouge from the Punchbowl Fault, California. *Journal of Structural Geology*, 9(5-6):621 – 634, IN5–IN6.

Collettini, C. and Sibson, R. H. (2001). Normal faults, normal friction? *Geology*, 29(10):927–930.

Cordonnier, B., Schmalholz, S. M., Hess, K.-U., and Dingwell, D. B. (2012). Viscous heating in silicate melts: An experimental and numerical comparison. *J. Geophys. Res.*, 117(B2):B02203.

Cowan, D. (1999). Do faults preserve a record of seismic slip? A field geologist's opinion. *Journal of Structural Geology*, 21(8-9):995–1001.

Davies, T. R. and McSaveney, M. J. (2009). The role of rock fragmentation in the motion of large landslides. *Engineering Geology*, 109(1-2):67–79.

Davies, T. R. H., McSaveney, M. J., and Boulton, C. J. (2012). Elastic strain energy release from fragmenting grains: Effects on fault rupture. *Journal of Structural Geology*, 38(0):265–277.

De Ronde, A. A., Heilbronner, R., Stünitz, H., and Tullis, J. (2004). Spatial correlation of deformation and mineral reaction in experimentally deformed plagioclase-olivine aggregates. *Tectonophysics*, 389(1-2):93–109.

Debenedetti, P. G. and Stillinger, F. H. (2001). Supercooled liquids and the glass transition. *Nature*, 410(6825):259–267.

Di Toro, G., Goldsby, D. L., and Tullis, T. E. (2004). Friction falls towards zero in quartz rock as slip velocity approaches seismic rates. *Nature*, 427(6973):436–439.

Di Toro, G., Han, R., Hirose, T., De Paola, N., Nielsen, S., Mizoguchi, K., Ferri, F., Cocco, M., and Shimamoto, T. (2011). Fault lubrication during earthquakes. *Nature*, 471(7339):494–498.

Di Toro, G., Hirose, T., Nielsen, S., Pennacchioni, G., and Shimamoto, T. (2006). Natural and Experimental Evidence of Melt Lubrication of Faults During Earthquakes . *Science*, 311(5761):647–649.

Di Toro, G. and Pennacchioni, G. (2004). Superheated friction-induced melts in zoned pseudotachylytes within the Adamello tonalites (Italian Southern Alps). *Journal of Structural Geology*, 26(10):1783–1801.

Di Toro, G., Pennacchioni, G., and Teza, G. (2005). Can pseudotachylytes be used to infer earthquake source parameters? An example of limitations in the study of exhumed faults. *Tectonophysics*, 402(1–4):3–20.

Dick, K., Dhanasekaran, T., Zhang, Z., and Meisel, D. (2002). Size-Dependent Melting of Silica-Encapsulated Gold Nanoparticles. *Journal of the American Chemical Society*, 124(10):2312–2317.

Dieterich, J. H. (1978). Time-dependent friction and the mechanics of stick-slip. *Pure and Applied Geophysics*, 116(4):790–806.

Dieterich, J. H. (1979). Modeling of Rock Friction 1. Experimental Results and Constitutive Equations. *J. Geophys. Res.*, 84(B5):2161–2168.

Dimanov, A., Rybacki, E., Wirth, R., and Dresen, G. (2007). Creep and strain-dependent microstructures of synthetic anorthite–diopside aggregates. *Journal of Structural Geology*, 29(6):1049–1069.

Dingwell, D. B., Hess, K.-U., and Romano, C. (1998). Extremely fluid behavior of hydrous peralkaline rhyolites. *Earth and Planetary Science Letters*, 158(1-2):31–38.

Dolejs, D. and Wagner, T. (2008). Thermodynamic modeling of non-ideal mineral-fluid equilibria in the system Si-Al-Fe-Mg-Ca-Na-KHO-Cl at elevated temperatures and pressures: Implications for hydrothermal mass transfer in granitic rocks. *Geochimica et Cosmochimica Acta*, 72(2):526–553.

Druiventak, A., Trepmann, C. A., Renner, J., and Hanke, K. (2011). Low-temperature plasticity of olivine during high stress deformation of peridotite at lithospheric conditions — an experimental study. *Earth and Planetary Science Letters*, 311(3–4):199 – 211.

Duxson, P., Fernández-Jiménez, A., Provis, J., Lukey, G., Palomo, A., and van Deventer, J. (2007). Geopolymer technology: the current state of the art. *Journal of Materials Science*, 42(9):2917–2933.

Eggleton, R. and Buseck, P. (1980). High Resolution Electron Microscopy of Feldspar Weathering. *Clays and Clay Minerals*, 28(3):173–178.

Evans, J. P. and Chester, F. M. (1995). Fluid-rock interaction in faults of the San Andreas system: Inferences from San Gabriel fault rock geochemistry and microstructures. *Journal of Geophysical Research-Solid Earth*, 100(B7).

Falk, M. L. and Langer, J. (2011). Deformation and failure of amorphous, solidlike materials. *Annual Review of Condensed Matter Physics*, 2(1):353–373.

Farrell, H. H. and Siclen, C. D. V. (2007). Binding energy, vapor pressure, and melting point of semiconductor nanoparticles. *JVSTB*, 25(4):1441–1447.

Farver, J. R. and Yund, R. A. (1999). Oxygen bulk diffusion measurements and TEM characterization of a natural ultramylonite: implications for fluid transport in mica-bearing rocks. *Journal of Metamorphic Geology*, 17(6):669–683.

Faulkner, D., Jackson, C., Lunn, R., Schlische, R., Shipton, Z., Wibberley, C., and Withjack, M. (2010). A review of recent developments concerning the structure, mechanics and fluid flow properties of fault zones. *Journal of Structural Geology*, 32(11):1557 – 1575.

Fecht, H. J. (1992). Defect-induced melting and solid-state amorphization. *Nature*, 356(6365):133–135.

Ferré, E. C., Geissman, J. W., and Zechmeister, M. S. (2012). Magnetic properties of fault pseudotachylytes in granites. *J. Geophys. Res.*, 117(B1):B01106.

Fitz Gerald, J. D., Boland, J. N., McLaren, A. C., Ord, A., and Hobbs, B. E. (1991). Microstructures in Water-Weakened Single Crystals of Quartz. *J. Geophys. Res.*, 96(B2):2139–2155.

Fitz Gerald, J. D. and Stünitz, H. (1993). Deformation of granitoids at low metamorphic grade. I: Reactions and grain size reduction. *Tectonophysics*, 221(3-4):269–297.

Fusseis, F. and Handy, M. R. (2008). Micromechanisms of shear zone propagation at the brittle-viscous transition. *Journal of Structural Geology*, 30(10):1242–1253.

Fusseis, F., Handy, M. R., and Schrank, C. (2006). Networking of shear zones at the brittle-to-viscous transition (Cap de Creus, NE Spain). *Journal of Structural Geology*, 28(7):1228–1243.

Gieré, R., Williams, C. T., Wirth, R., and Ruschel, K. (2009). Metamict fergusonite-(Y) in a spessartine-bearing granitic pegmatite from Adamello, Italy. *Chemical Geology*, 261(3–4):333–345.

Giger, S. B., Cox, S. F., and Tenthorey, E. (2008). Slip localization and fault weakening as a consequence of fault gouge strengthening — Insights from laboratory experiments. *Earth and Planetary Science Letters*, 276(1–2):73–84.

Goetze, C. and Evans, B. (1979). Stress and temperature in the bending lithosphere as constrained by experimental rock mechanics. *Geophysical Journal of the Royal Astronomical Society*, 59(3):463–478.

Goldsby, D. L. and Tullis, T. E. (2002). Low frictional strength of quartz rocks at subseismic slip rates. *Geophysical research letters*, 29(17):21–25.

Goldsby, D. L. and Tullis, T. E. (2011). Flash Heating Leads to Low Frictional Strength of Crustal Rocks at Earthquake Slip Rates. *Science*, 334(6053):216–218.

Gratier, J. P. and Gamond, J. F. (1990). Transition between seismic and aseismic deformation in the upper crust . *Geological Society, London, Special Publications*, 54(1):461–473 DO – 10.1144/GSL.SP.1990.054.01.42.

Gratier, J.-P., Renard, F., and Labaume, P. (1999). How pressure solution creep and fracturing processes interact in the upper crust to make it behave in both a brittle and viscous manner. *Journal of Structural Geology*, 21(8-9):1189–1197.

Gratier, J.-P., Richard, J., Renard, F., Mittempergher, S., Doan, M.-L., Di Toro, G., Hadizadeh, J., and Boullier, A.-M. (2011). Aseismic sliding of active faults by pressure solution creep: Evidence from the San Andreas Fault Observatory at Depth . *Geology*, 39(12):1131–1134 DO – 10.1130/G32073.1.

Hadizadeh, J., Mittempergher, S., Gratier, J.-P., Renard, F., Toro, G. D., Richard, J., and Babaie, H. A. (2012). A microstructural study of fault rocks from the SAFOD: Implications for the deformation mechanisms and strength of the creeping segment of the San Andreas Fault. *Journal of Structural Geology*, 42(0):246–260.

Handy, M. R. (1994). Flow laws for rocks containing two non-linear viscous phases: a phenomenological approach. *Journal of Structural Geology*, 16(3):287–302.

Handy, M. R. and Stunitz, H. (2002). Strain localization by fracturing and reaction weakening-a mechanism for initiating exhumation of subcontinental mantle beneath rifted margins. *Geological Society London Special Publications*, 200(1):387.

Haw, M. D. (2004). Jamming, Two-Fluid Behavior, and "Self-Filtration" in Concentrated Particulate Suspensions. *Physical Review Letters*, 92(18):185506.

Heilbronner, R. (2002). Analysis of bulk fabrics and microstructure variations using tesselations of autocorrelation functions. *Computers and Geosciences*, 28(4):447–455.

Heilbronner, R. and Keulen, N. (2006). Grain size and grain shape analysis of fault rocks. *Tectonophysics*, 427(1-4):199–216.

Heilbronner, R. and Tullis, J. (2006). Evolution of c axis pole figures and grain size during dynamic recrystallization: Results from experimentally sheared quartzite. *Journal of Geophysical Research*, 111.

Heilbronner, R. P. (1992). The autocorrelation function: an image processing tool for fabric analysis. *Tectonophysics*, 212(3-4):351–370.

Helgeson, H., Delany, J., Nesbitt, H., and Bird, D. (1978). Summary and critique of the thermodynamic properties of rock-forming minerals. *American Journal of Science*, 278-A:1–229.

Hemley, R. J., Jephcoat, A. P., Mao, H. K., Ming, L. C., and Manghnani, M. H. (1988). Pressure-induced amorphization of crystalline silica. *Nature*, 334(6177):52–54.

Hess, K. U., Cordonnier, B., Lavallée, Y., and Dingwell, D. B. (2008). Viscous heating in rhyolite: An in situ experimental determination. *Earth and Planetary Science Letters*, 275(1-2):121–126.

Hess, K.-U., Dingwell, D. B., Gennaro, C., and Mincione, V. (2001). Viscosity-temperature behaviour of dry melts in the Qz-Ab-Or system. *Chemical Geology*, 174(1-3):133–142.

Hirose, T. and Shimamoto, T. (2005). Growth of molten zone as a mechanism of slip weakening of simulated faults in gabbro during frictional melting. *J. Geophys. Res.*, 110(B5):B05202.

Hirth, G., Teyssier, C., and Dunlap, W. J. (2001). An evaluation of quartzite flow laws based on comparisons between experimentally and naturally deformed rocks. *International Journal of Earth Sciences*, 90(1):77–87.

Hirth, G. and Tullis, J. (1989). The effects of pressure and porosity on the micromechanics of the brittle-ductile transition in quartzite. *Journal of Geophysical Research*, 94(B12):17825.

Hirth, G. and Tullis, J. (1994). The brittle-plastic transition in experimentally deformed quartz aggregates. *Journal of Geophysical Research-Solid Earth*, 99(B6).

Holtzman, B. K., Kohlstedt, D. L., and Morgan, J.-P. (2005). Viscous Energy Dissipation and Strain Partitioning in Partially Molten Rocks. *Journal of Petrology*, 46(12):2569–2592.

Holyoke, C. W. and Kronenberg, A. K. (2010). Accurate differential stress measurement using the molten salt cell and solid salt assemblies in the Griggs apparatus with applications to strength, piezometers and rheology. *Tectonophysics*, 494(1–2):17–31.

Holyoke, C. W. and Tullis, J. (2006a). Formation and maintenance of shear zones. *Geology*, 34(2):105–108.

Holyoke, C. W. and Tullis, J. (2006b). Mechanisms of weak phase interconnection and the effects of phase strength contrast on fabric development. *Journal of Structural Geology*, 28(4):621–640.

Holyoke, C. W. and Tullis, J. (2006c). The interaction between reaction and deformation: an experimental study using a biotite + plagioclase + quartz gneiss. *Journal of Metamorphic Geology*, 24(8):743–762.

Imber, J., Holdsworth, R. E., Butler, C. A., and Strachan, R. A. (2001). A reappraisal of the Sibson-Scholz fault zone model: the nature of the frictional to viscous ("brittle-ductile") transition along a long-lived, crustal-scale fault, Outer Hebrides, Scotland. *Tectonics*, 20(5).

Inoue, K. (1957). The Strength of Single Crystals of Inorganic Salts under High Pressure, II. *The Review of Physical Chemistry of Japan*, 27(2):54–58.

Janssen, C., Wirth, R., Rybacki, E., Naumann, R., Kemnitz, H., Wenk, H.-R., and Dresen, G. (2010). Amorphous material in SAFOD core samples (San Andreas Fault): Evidence for crush-origin pseudotachylytes? *Geophys. Res. Lett.*, 37(1):L01303.

Jerabek, P., Stünitz, H., Heilbronner, R., Lexa, O., and Schulmann, K. (2007). Microstructural-deformation record of an orogen-parallel extension in the Vepor Unit, West Carpathians. *Journal of Structural Geology*, 29(11):1722–1743.

John, T., Medvedev, S., Rupke, L. H., Andersen, T. B., Podladchikov, Y. Y., and Austrheim, H. (2009). Generation of intermediate-depth earthquakes by self-localizing thermal runaway. *Nature Geosci*, 2(2):137–140.

Jones, K. S. and Santana, C. J. (1999). Amorphization of elemental and compound semiconductors upon ion implantation. *Journal of Materials Research*, 6(05):1048–1054.

Kanamori, H. (1994). Mechanics of earthquakes. *Annual Review of Earth and Planetary Sciences*, 22(1):207–237.

Kato, A., Ohnaka, M., Yoshida, S., and Mochizuki, H. (2003). Effect of strain rate on constitutive properties for the shear failure of intact granite in seismogenic environments. *Geophysical research letters*, 30(21):2108.

Keulen, N. (2006). Grain scale processes in fault rock - a comparison between experimental and natural deformation. *PhD thesis*, pages 1–245.

Keulen, N., Heilbronner, R., Stünitz, H., Boullier, A.-M., and Ito, H. (2007). Grain size distributions of fault rocks: A comparison between experimentally and naturally deformed granitoids. *Journal of Structural Geology*, 29(8):1282–1300.

Keulen, N., Stünitz, H., and Heilbronner, R. (2008). Healing microstructures of experimental and natural fault gouge. *Journal of Geophysical Research*, 113(B06205):1–52.

Kilian, R., Heilbronner, R., and Stünitz, H. (2011a). Quartz grain size reduction in a granitoid rock and the transition from dislocation to diffusion creep. *Journal of Structural Geology*, 33(8):1265–1284.

Kilian, R., Heilbronner, R., and Stünitz, H. (2011b). Quartz microstructures and crystallographic preferred orientation: Which shear sense do they indicate? *Journal of Structural Geology*, 33(10):1446 – 1466.

Kirkpatrick, J. D. and Shipton, Z. K. (2009). Geologic evidence for multiple slip weakening mechanisms during seismic slip in crystalline rock. *J. Geophys. Res.*, 114(B12):B12401.

Kirkpatrick, J. D., Shipton, Z. K., and Persano, C. (2009). Pseudotachylytes: Rarely Generated, Rarely Preserved, or Rarely Reported? *Bulletin of the Seismological Society of America*, 99(1):382–388.

Kohlstedt, D. L., Evans, B., and Mackwell, S. J. (1995). Strength of the lithosphere: Constraints imposed by laboratory experiments. *J. geophys. Res*, 100(17):517–587.

Kohlstedt, D. L. and Holtzman, B. K. (2009). Shearing Melt Out of the Earth: An Experimentalist's Perspective on the Influence of Deformation on Melt Extraction. *Annual Review of Earth and Planetary Sciences*, 37(1):561–593.

Koizumi, Y., Otsuki, K., Takeuchi, A., and Nagahama, H. (2004). Frictional melting can terminate seismic slips: Experimental results of stick-slips. *Geophys. Res. Lett.*, 31(21):L21605.

Kronenberg, A. K. and Shelton, G. L. (1980). Deformation microstructures in experimentally deformed Maryland diabase. *Journal of Structural Geology*, 2(3):341–353.

Kronenberg, A. K. and Tullis, J. (1984). Flow Strengths of Quartz Aggregates: Grain Size and Pressure Effects due to Hydrolytic Weakening. *J. Geophys. Res.*, 89(B6):4281–4297.

Lavallée, Y., Meredith, P. G., Dingwell, D. B., Hess, K. U., Wassermann, J., Cordonnier, B., Gerik, A., and Kruhl, J. H. (2008). Seismogenic lavas and explosive eruption forecasting. *Nature*, 453(7194):507–510.

Levitas, V. I. and Samani, K. (2011). Size and mechanics effects in surface-induced melting of nanoparticles. *Nat Commun*, 2:284.

Lin, A. (1999). S- C cataclasite in granitic rock. *Tectonophysics*, 304(3):257–273.

Lin, A. (2001). S-C fabrics developed in cataclastic rocks from the Nojima fault zone, Japan and their implications for tectonic history. *Journal of Structural Geology*, 23(6-7):1167–1178.

Lin, A. (2007). *Fossil Earthquakes: The Formation and Preservation of Pseudotachylytes.* Springer, Berlin Heidelberg New York.

Lo, C. L., Duh, J. G., and Chiou, B. S. (2003). Low temperature sintering and crystallisation behaviour of low loss anorthite-based glass-ceramics. *Journal of Materials Science*, 38(4):693–698.

Lockner, D. a., Morrow, C., Moore, D., and Hickman, S. (2011). Low strength of deep San Andreas fault gouge from SAFOD core. *Nature*, 472(7341):82–5.

Lockner, D. A., Summers, R., and Byerlee, J. D. (1986). Effects of temperature and sliding rate on frictional strength of granite. *Pure and Applied Geophysics*, 124:445–469.

Lumpkin, G. R., Leung, S. H. F., and Ferenczy, J. (2012). Chemistry, microstructure, and alpha decay damage of natural brannerite. *Chemical Geology*, 291(0):55–68.

Lund, A. C. and Schuh, C. A. (2003). Atomistic simulation of strain-induced amorphization. *Applied Physics Letters*, 82(13):2017–2019.

Maggi, A., Jackson, J. A., McKenzie, D., and Priestley, K. (2000). Earthquake focal depths, effective elastic thickness, and the strength of the continental lithosphere. *Geology*, 28(6):495.

Mair, K. and Marone, C. (2000). Shear Heating in Granular Layers. *Pure and Applied Geophysics*, 157(11):1847–1866.

Mair, K., Renard, F., and Gundersen, O. (2006). Thermal imaging on simulated faults during frictional sliding. *Geophys. Res. Lett.*, 33(19):L19301.

Malkin, A. (2009). The state of the art in the rheology of polymers: Achievements and challenges. *Polymer Science Series A*, 51(1):80–102.

Mancktelow, N. S. and Pennacchioni, G. (2005). The control of precursor brittle fracture and fluid-rock interaction on the development of single and paired ductile shear zones. *Journal of Structural Geology*, 27(4):645–661.

Marone, C. (1998). Laboratory-derived friction laws and their application to seismic faulting. *Annual Review of Earth and Planetary Sciences*, 26(1):643–696.

Mason, T. G. and Weitz, D. A. (1995). Optical measurements of frequency-dependent linear viscoelastic moduli of complex fluids. *Phys. Rev. Lett.*, 74:1250–1253.

Melosh, H. J. (2005). The Mechanics of Pseudotachylite Formation in Impact Events. In Koeberl, C. and Henkel, H., editors, *Impact Tectonics*, Impact Studies, pages 55–80. Springer Berlin Heidelberg.

Menegon, L., Nasipuri, P., Stünitz, H., Behrens, H., and Ravna, E. (2011). Dry and strong quartz during deformation of the lower crust in the presence of melt. *J. Geophys. Res.*, 116(B10):B10410.

Menegon, L. and Pennacchioni, G. (2010). Local shear zone pattern and bulk deformation in the Gran Paradiso metagranite (NW Italian Alps). *International Journal of Earth Sciences*, 99(8):1805–1825.

Menegon, L., Pennacchioni, G., Heilbronner, R., and Pittarello, L. (2008). Evolution of quartz microstructure and c-axis crystallographic preferred orientation within ductilely deformed granitoids (Arolla unit, Western Alps). *Journal of Structural Geology*, 30(11):1332–1347.

Mishima, O. (1996). Relationship between melting and amorphization of ice. *Nature*, 384(6609):546–549.

Moore, D. E. and Rymer, M. J. (2007). Talc-bearing serpentinite and the creeping section of the San Andreas fault. *Nature*, 448(7155):795–797.

Muto, J., Hirth, G., Heilbronner, R., and Tullis, J. (2011). Plastic anisotropy and fabric evolution in sheared and recrystallized quartz single crystals. *J. Geophys. Res.*, 116(B2):B02206.

Nakayama, H., Tsuchiya, K., and Umemoto, M. (2001). Crystal refinement and amorphisation by cold rolling in tini shape memory alloys. *Scripta Materialia*, 44(8–9):1781–1785.

Niemeijer, A., Di Toro, G., Nielsen, S., and Di Felice, F. (2011). Frictional melting of gabbro under extreme experimental conditions of normal stress, acceleration, and sliding velocity. *J. Geophys. Res.*, 116(B7):B07404.

Niemeijer, A., Elsworth, D., and Marone, C. (2009). Significant effect of grain size distribution on compaction rates in granular aggregates. *Earth and Planetary Science Letters*, 284(3-4):386–391.

Niemeijer, A., Marone, C., and Elsworth, D. (2008a). Healing of simulated fault gouges aided by pressure solution: Results from rock analogue experiments. *J. Geophys. Res*, 113.

Niemeijer, A., Toro, G. D., Griffith, W. A., Bistacchi, A., Smith, S. A. F., and Nielsen, S. (2012). Inferring earthquake physics and chemistry using an integrated field and laboratory approach. *Journal of Structural Geology*, (0):–.

Niemeijer, A. R. and Spiers, C. J. (2006). Velocity dependence of strength and healing behaviour in simulated phyllosilicate-bearing fault gouge. *Tectonophysics*, 427(1-4):231–253.

Niemeijer, A. R. and Spiers, C. J. (2007). A microphysical model for strong velocity weakening in phyllosilicate-bearing fault gouges. *Journal of Geophysical Research-Solid Earth*, 112(B10):B10405.

Niemeijer, A. R., Spiers, C. J., and Peach, C. J. (2008b). Frictional behaviour of simulated quartz fault gouges under hydrothermal conditions: Results from ultra-high strain rotary shear experiments. *Tectonophysics*, 460(1-4):288–303.

Noda, H. and Shimamoto, T. (2010). A rate- and state-dependent ductile flow law of polycrystalline halite under large shear strain and implications for transition to brittle deformation. *Geophysical research letters*, 37(9):L09310.

Noda, H. and Shimamoto, T. (2012). Transient behavior and stability analyses of halite shear zones with an empirical rate-and-state friction to flow law. *Journal of Structural Geology*, 38(0):234–242.

Odedra, A., Ohnaka, M., Mochizuki, H., and Sammonds, P. (2001). Temperature and pore pressure effects on the shear strength of granite in the brittle-plastic transition regime. *Geophysical research letters*, 28(15):3011–3014.

Ohnaka, M. (1995). A shear failure strength law of rock in the brittle-plastic transition regime. *Geophysical research letters*, 22(1):25–28.

Ohnaka, M. (2003). A constitutive scaling law and a unified comprehension for frictional slip failure, shear fracture of intact rock, and earthquake rupture. *J. Geophys. Res*, 108(B2):2080.

Ohnaka, M., Akatsu, M., Mochizuki, H., Odedra, A., Tagashira, F., and Yamamoto, Y. (1997). A constitutive law for the shear failure of rock under lithospheric conditions. *Tectonophysics*, 277(1-3):1–27.

Olgaard, D. L. and Brace, W. F. (1983). The microstructure of gouge from a mining-induced seismic shear zone. *International Journal of Rock Mechanics and Mining Sciences & Geomechanics Abstracts*, 20(1):11–19.

Onuma, K., Muto, J., Nagahama, H., and Otsuki, K. (2011). Electric potential changes associated with nucleation of stick-slip of simulated gouges. *Tectonophysics*, 502(3–4):308–314.

Otsuki, K., Monzawa, N., and Nagase, T. (2003). Fluidization and melting of fault gouge during seismic slip: Identification in the Nojima fault zone and implications for focal earthquake mechanisms. *J. Geophys. Res.*, 108(B4):2192.

Ozawa, K. and Takizawa, S. (2007). Amorphous material formed by the mechanochemical effect in natural pseudotachylyte of crushing origin: A case study of the Iida-Matsukawa Fault, Nagano Prefecture, Central Japan. *Journal of Structural Geology*, 29(11):1855–1869.

Panozzo, R. (1983). Two-dimensional analysis of shape-fabric using projections of digitized lines in a plane. *Tectonophysics*, 95(3-4):279–294.

Panozzo, R. (1984). Two-dimensional strain from the orientation of lines in a plane. *Journal of Structural Geology*, 6:215–221.

Pec, M., Stünitz, H., and Heilbronner, R. (2012a). Semi-brittle deformation of granitoid gouges in shear experiments at elevated pressures and temperatures. *Journal of Structural Geology*, 38(0):200–221.

Pec, M., Stünitz, H., Heilbronner, R., Drury, M., and de Capitani, C. (2012b). Origin of pseudotachylites in slow creep experiments. *Earth and Planetary Science Letters*, 355:299–310.

Pennacchioni, G. and Mancktelow, N. S. (2007). Nucleation and initial growth of a shear zone network within compositionally and structurally heterogeneous granitoids under amphibolite facies conditions. *Journal of Structural Geology*, 29(11):1757–1780.

Pennacchioni, G., Toro, G. D., Brack, P., Menegon, L., and Villa, I. M. (2006). Brittle-ductile-brittle deformation during cooling of tonalite (Adamello, Southern Italian Alps). *Tectonophysics*, 427(1-4):171–197.

Philpotts, A. and Ague, J. (2009). *Principles of Igneous and Metamorphic Petrology*. Cambridge University Press.

Piane, C. D., Wilson, C. J. L., and Burlini, L. (2009). Dilatant plasticity in high-strain experiments on calcite–muscovite aggregates. *Journal of Structural Geology*, 31(10):1084–1099.

Pinckney, L. R. and Beall, G. H. (2008). Microstructural Evolution in Some Silicate Glass–Ceramics: A Review. *Journal of the American Ceramic Society*, 91(3):773–779.

Platt, J. and Behr, W. (2011). Lithospheric shear zones as constant stress experiments. *Geology*, 39(2):127–130.

Prasher, C. L. (1987). *Crushing and Grinding Process Handbook*. John Wiley & Sons Inc, New York.

Prewitt, C. T., Sueno, S., and Papike, J. J. (1976). The crystal structures of high albite and monalbite at high temperatures. *American Mineralogist*, 61(11-12):1213–1225.

Price, N. A., Johnson, S. E., Gerbi, C. C., and Jr., D. P. W. (2012). Identifying deformed pseudotachylyte and its influence on the strength and evolution of a crustal shear zone at the base of the seismogenic zone. *Tectonophysics*, 518–521(0):63–83.

Rahier, H., Mele, B., Biesemans, M., Wastiels, J., and Wu, X. (1996). Low-temperature synthesized aluminosilicate glasses. *Journal of Materials Science*, 31(1):71–79.

Rahier, H., Simons, W., Van Mele, B., and Biesemans, M. (1997). Low-temperature synthesized aluminosilicate glasses: Part III Influence of the composition of the silicate solution on production, structure and properties. *Journal of Materials Science*, 32(9):2237–2247.

Reichelt, M., Gunst, U., Wolf, T., Mayer, J., Arlinghaus, H. F., and Gold, P. W. (2010). Nanoindentation, TEM and ToF-SIMS studies of the tribological layer system of cylindrical roller thrust bearings lubricated with different oil additive formulations. *Wear*, 268(11–12):1205–1213.

Reimold, W. (1995). Pseudotachylite in impact structures — generation by friction melting and shock brecciation?: A review and discussion. *Earth-Science Reviews*, 39(3-4):247–265.

Reiner, M. (1964). The Deborah Number. *Physics Today*, 17(1):62.

Renard, F., Gratier, J.-P., and Jamtveit, B. r. (2000). Kinetics of crack-sealing, intergranular pressure solution, and compaction around active faults. *Journal of Structural Geology*, 22(10):1395–1407.

Renner, J. (1996). Experimentelle Untersuchungen zur Rheologie von Coesit. *PhD thesis*, pages 1–178.

Renner, J., Siddiqi, G., and Evans, B. (2007). Plastic flow of two-phase marbles. *J. Geophys. Res.*, 112(B7):B07203.

Renshaw, C. E. and Schulson, E. M. (2007). Limits on rock strength under high confinement. *Earth and Planetary Science Letters*, 258(1–2):307–314.

Rowe, C. D., Moore, J. C., Meneghini, F., and McKeirnan, A. W. (2005). Large-scale pseudotachylytes and fluidized cataclasites from an ancient subduction thrust fault . *Geology*, 33(12):937–940.

Ruina, A. (1983). Slip Instability and State Variable Friction Laws. *J. Geophys. Res.*, 88(B12):10359–10370.

Rybacki, E., Paterson, M. S., Wirth, R., and Dresen, G. (2003). Rheology of calcite-quartz aggregates deformed to large strain in torsion. *J. Geophys. Res.*, 108(B2):2089.

Rybacki, E., Wirth, R., and Dresen, G. (2008). High-strain creep of feldspar rocks: Implications for cavitation and ductile failure in the lower crust. *Geophys. Res. Lett.*, 35(4):L04304.

Rybacki, E., Wirth, R., and Dresen, G. (2010). Superplasticity and ductile fracture of synthetic feldspar deformed to large strain. *Journal of Geophysical Research*, 115(B8):B08209.

Scherer, G. W., Brinker, C., and Roth, E. (1985). Sol → gel → glass: III. Viscous sintering. *Journal of Non-Crystalline Solids*, 72(2–3):369–389.

Scholz, C. H. (2000). Evidence for a strong san andreas fault. *Geology*, 28(2):163–166.

Scholz, C. H. (2007). *The Mechanics of Earthquakes and Faulting*. Cambridge University Press, Cambridge.

Scholze, H. (1977). *Glas: Natur, Struktur und Eigenschaften*. Springer-Verlag.

Schubnel, A., Fortin, J., Burlini, L., and Guéguen, Y. (2005). Damage and recovery of calcite rocks deformed in the cataclastic regime. *Geological Society, London, Special Publications*, 245(1):203–221.

Shimada, M. (1993). Lithosphere strength inferred from fracture strength of rocks at high confining pressures and temperatures. *Tectonophysics*, 217(1-2):55–64.

Shimamoto, T. (1986). Transition Between Frictional Slip and Ductile Flow for Halite Shear Zones at Room Temperature. *Science*, 231(4739):711–714.

Sibson, R. H. (1975). Generation of Pseudotachylyte by Ancient Seismic Faulting. *Geophysical Journal of the Royal Astronomical Society*, 43(3):775–794.

Sibson, R. H. and Xie, G. (1998). Dip range for intracontinental reverse fault ruptures: Truth not stranger than friction? *Bulletin of the Seismological Society of America*, 88(4):1014–1022.

Spray, J. G. (1987). Artificial generation of pseudotachylyte using friction welding apparatus: simulation of melting on a fault plane. *Journal of Structural Geology*, 9(1):49–60.

Spray, J. G. (1995). Pseudotachylyte controversy: Fact or friction? *Geology*, 23(12):1119–1122.

Spray, J. G. (2010). Frictional Melting Processes in Planetary Materials: From Hypervelocity Impact to Earthquakes. *Annual Review of Earth and Planetary Sciences*, 38(1):221–254.

Stewart, M., Holdsworth, R. E., and Strachan, R. A. (2000). Deformation processes and weakening mechanisms within the frictional-viscous transition zone of major crustal-scale faults: insights from the Great Glen Fault Zone, Scotland. *Journal of Structural Geology*, 22(5):543–560.

Stipp, M., Stünitz, H., Heilbronner, R., and Schmid, S. M. (2002a). Dynamic recrystallization of quartz: correlation between natural and experimental conditions . *Geological Society, London, Special Publications*, 200(1):171–190.

Stipp, M., Stünitz, H., Heilbronner, R., and Schmid, S. M. (2002b). The eastern Tonale fault zone: a 'natural laboratory'for crystal plastic deformation of quartz over a temperature range from 250 to 700 C. *Journal of Structural Geology*, 24(12):1861–1884.

Stipp, M., Tullis, J., and Behrens, H. (2006). Effect of water on the dislocation creep microstructure and flow stress of quartz and implications for the recrystallized grain size piezometer. *J. Geophys. Res.*, 111(B4):B04201.

Stipp, M., Tullis, J., Scherwath, M., and Behrmann, J. H. (2010). A new perspective on paleopiezometry: Dynamically recrystallized grain size distributions indicate mechanism changes. *Geology*, 38(8):759–762.

Stöckhert, B., Brix, M. R., Kleinschrodt, R., Hurford, A. J., and Wirth, R. (1999). Thermochronometry and microstructures of quartz-a comparison with experimental flow laws and predictions on the temperature of the brittle-plastic transition. *Journal of Structural Geology*, 21(3):351–369.

Stünitz, H., Fitz Gerald, J. D., and Tullis, J. (2003). Dislocation generation, slip systems, and dynamic recrystallization in experimentally deformed plagioclase single crystals. *Tectonophysics*, 372(3-4):215–233.

Stünitz, H., Keulen, N., Hirose, T., and Heilbronner, R. (2010). Grain size distribution and microstructures of experimentally sheared granitoid gouge at coseismic slip rates - Criteria to distinguish seismic and aseismic faults? *Journal of Structural Geology*, 32(1):59–69.

Stünitz, H. (1998). Syndeformational recrystallization – dynamic or compositionally induced? *Contributions to Mineralogy and Petrology*, 131:219–236. 10.1007/s004100050390.

Sun, J. and Simon, S. (2007). The melting behavior of aluminum nanoparticles. *Thermochimica Acta*, 463(1-2):32–40.

Suryanarayana, C. (2001). Mechanical alloying and milling. *Progress in Materials Science*, 46(1–2):1–184.

Tajčmanová, L., Abart, R., Wirth, R., Habler, G., and Rhede, D. (2012). Intracrystalline microstructures in alkali feldspars from fluid-deficient felsic granulites: a mineral chemical and TEM study. *Contributions to Mineralogy and Petrology*, pages 1–15.

Takagi, H., Takahashi, K., Shimada, K., Tsutsui, K., Miura, R., Kato, N., and Takizawa, S. (2012). Integrated estimates of the thickness of the fault damage zone in granitic terrain based on penetrative mesocracks and XRD analyses of quartz. *Journal of Structural Geology*, 35(0):64–77.

Tarantola, A., Diamond, L., and Stünitz, H. (2010). Modification of fluid inclusions in quartz by deviatoric stress I: experimentally induced changes in inclusion shapes and microstructures. *Contributions to Mineralogy and Petrology*, 160(6):825–843.

Tarantola, A., Diamond, L., Stünitz, H., Thust, A., and Pec, M. (2012). Modification of fluid inclusions in quartz by deviatoric stress. III: Influence of principal stresses on inclusion density and orientation. *Contributions to Mineralogy and Petrology*, 164(3):537–550.

Tenthorey, E. and Cox, S. F. (2006). Cohesive strengthening of fault zones during the interseismic period: An experimental study. *Journal of Geophysical Research-Solid Earth*, 111(B9):B09202.

Thatcher, W. (2009). How the continents deform: The evidence from tectonic geodesy*. *Annual Review of Earth and Planetary Sciences*, 37(1):237–262.

Trepmann, C. A. and Stöckhert, B. (2002). Cataclastic deformation of garnet: a record of synseismic loading and postseismic creep. *Journal of Structural Geology*, 24(11):1845–1856.

Trepmann, C. A. and Stöckhert, B. (2003). Quartz microstructures developed during non-steady state plastic flow at rapidly decaying stress and strain rate. *Journal of Structural Geology*, 25(12):2035–2051.

Trepmann, C. A., Stöckhert, B., Dorner, D., Moghadam, R. H., Küster, M., and Röller, K. (2007). Simulating coseismic deformation of quartz in the middle crust and fabric evolution during postseismic stress relaxation – An experimental study. *Tectonophysics*, 442(1-4):83–104.

Tullis, J. and Yund, R. (1992). Chapter 4 The Brittle-Ductile Transition in Feldspar Aggregates: An Experimental Study. *International Geophysics*, 51:89–117.

Tullis, J. and Yund, R. A. (1977). Experimental deformation of dry Westerly granite. *J. Geophys. Res.*, 82(36):5705–5718.

Tullis, J. and Yund, R. A. (1980). Hydrolytic weakening of experimentally deformed Westerly granite and Hale albite rock. *Journal of Structural Geology*, 2(4):439–451.

Tullis, J. and Yund, R. A. (1987). Transition from cataclastic flow to dislocation creep of feldspar: Mechanisms and microstructures. *Geology*, 15(7):606–609.

Twiss, R. and Moores, E. (2007). *Structural Geology*. W. H. Freeman.

Ueda, T., Obata, M., Di Toro, G., Kanagawa, K., and Ozawa, K. (2008). Mantle earthquakes frozen in mylonitized ultramafic pseudotachylytes of spinel-lherzolite facies . *Geology*, 36(8):607–610 DO – 10.1130/G24739A.1.

Underwood, E. E. (1970). *Quantitative stereology*. Addison-Wesley series in metallurgy and materials. Addison-Wesley Pub. Co.

van Daalen, M., Heilbronner, R., and Kunze, K. (1999). Orientation analysis of localized shear deformation in quartz fibres at the brittle–ductile transition. *Tectonophysics*, 303(1-4):83–107.

Violay, M., Gibert, B., Mainprice, D., Evans, B., Dautria, J.-M., Azais, P., and Pezard, P. (2012). An experimental study of the brittle-ductile transition of basalt at oceanic crust pressure and temperature conditions. *J. Geophys. Res.*, 117(B3):B03213.

Viti, C. (2011). Exploring fault rocks at the nanoscale. *Journal of Structural Geology*, 33(12):1715–1727.

Weiss, L. E. and Wenk, H. R. (1983). Experimentally produced pseudotachylite-like veins in gabbro. *Tectonophysics*, 96(3-4):299–310.

Wenk, H. R. (1978). Are pseudotachylites products of fracture or fusion? *Geology*, 6(8):507–511.

Wenk, H.-R., Johnson, L. R., and Ratschbacher, L. (2000). Pseudotachylites in the Eastern Peninsular Ranges of California. *Tectonophysics*, 321(2):253–277.

Wernicke, B. (1981). Low-angle normal faults in the Basin and Range Province: nappe tectonics in an extending orogen. *Nature*, 291(5817):645–648.

Wheeler, J. (1992). Importance of pressure solution and Coble creep in the deformation of polymineralic rocks. *Journal of Geophysical Research*, 97(B4):4579–4586.

White, J. C. (2012). Paradoxical pseudotachylyte – Fault melt outside the seismogenic zone. *Journal of Structural Geology*, 38(0):11–20.

White, S. (2001). Textural and microstructural evidence for semi-brittle flow in natural fault rocks with varied mica contents. *International Journal of Earth Sciences*, 90(1):14–27.

Wilson, B., Dewers, T., Reches, Z., and Brune, J. (2005). Particle size and energetics of gouge from earthquake rupture zones. *Nature*, 434(7034):749–752.

Wintsch, R. P., Christoffersen, R., and Kronenberg, A. K. (1995). Fluid-rock reaction weakening of fault zones. *Journal of Geophysical Research-Solid Earth*, 100(B7):13021–13032.

Wolf, D., Okamoto, P. R., Yip, S. amd Lutsko, J. F., and Kluge, M. (1990). Thermodynamic parallels between solid-state amorphization and melting. *Journal of Materials Research*, 5(2):286 – 301.

Wolf, D., Wang, J., Phillpot, S. R., and Gleiter, H. (1995). On the thermodynamic relationship between nanocrystalline materials and glasses. *Physics Letters A*, 205(4):274–280.

Wong, T.-f. and Baud, P. (2012). The brittle-ductile transition in porous rock: A review. *Journal of Structural Geology*, (0):–.

Xiao, X. and Evans, B. (2003). Shear-enhanced compaction during non-linear viscous creep of porous calcite–quartz aggregates. *Earth and Planetary Science Letters*, 216(4):725–740.

Yamasaki, J., Takeda, S., and Tsuda, K. (2002). Elemental process of amorphization induced by electron irradiation in Si. *Physical Review B*, 65(11):115213.

Yip, S., Phillpot, S. R., and Wolf, D. (2005). Crystal Disordering in Melting and Amorphization. pages 2009–2023. Springer Netherlands.

Yund, R. A. (1986). Interdiffusion of NaSi—CaAl in peristerite. *Physics and Chemistry of Minerals*, 13(1):11–16.

Yund, R. A., Blanpied, M. L., Tullis, T. E., and Weeks, J. D. (1990). Amorphous material in high strain experimental fault gouges. *J. geophys. Res*, 95:15589–15602.

Závada, P., Desbois, G., Schwedt, A., Lexa, O., and Urai, J. L. (2012). Extreme ductile deformation of fine-grained salt by coupled solution-precipitation creep and microcracking: Microstructural evidence from perennial Zechstein sequence (Neuhof salt mine, Germany). *Journal of Structural Geology*, 37(0):89–104.

Závada, P., Schulmann, K., Konopásek, J., Ulrich, S., and Lexa, O. (2007). Extreme ductility of feldspar aggregates - Melt-enhanced grain boundary sliding and creep failure: Rheological implications for felsic lower crust. *J. Geophys. Res.*, 112(B10):B10210.

Publications:

Pec, M., Stünitz, H.,Heilbronner, R., Drury, M.R., De Capitani, C. (2012).
Origin of pseudotachylites in slow creep experiments.
Earth and Planetary Science Letters
doi: 10.1016/j.epsl.2012.09.004.

Pec, M., Stünitz, H.,Heilbronner, R. (2012).
Semi-brittle deformation of granitoid gouges in shear experiments at elevated pressures and temperature.
Journal of Structural Geology
38, 200-221. doi: 10.1016/j.jsg.2011.09.001.

Boutareaud, S., Hirose, T., Andréani, M., **Pec, M.**, Calugaru, D.-G., Boullier, A.-M., Doan, M.-L. (2012).
On the role of phyllosilicates on fault lubrication: Insight from micro- and nanostructural investigations on talc friction experiments.
Journal of Geophysical Research
117, B08408. doi: 10.1029/2011JB009006.

Tarantola, A., Diamond, L., Stünitz, H., Thust, A. and **Pec, M.** (2012).
Modification of fluid inclusions in quartz by deviatoric stress. III: Influence of principal stresses on inclusion density and orientation.
Contributions to Mineralogy and Petrology
164, 537-550. doi: 10.1007/s00410-012-0749-1.

Conference abstracts:

Kohlstedt, D. L., **Pec, M.**, Holtzman, B. (2014) Influence of stress on melt topology in viscously deforming, partially molten rocks. Goldschmidt Conference, Sacramento, USA. **(invited talk)**

Pec, M., Stünitz, H., Heilbronner, R., Drury, M.R. (2013) Fault-related amorphous materials and their influence on the rheological behavior of fault zones. AGU, T23J-03, San Francisco, USA. **(invited talk)**

Pec, M., Kohlstedt, D. L., Zimmerman, M. E., Holtzman, B.K. (2013) Reactive melt migration in mantle rocks: an experimental study. AGU, T53B-2588, San Francisco, USA.

Pec, M., Kohlstedt, D. L., Zimmerman, M. E., Holtzman, B.K. (2013) An experimental study of reactive melt migration in mantle rocks. DRT, abstract volume pp 79, Leuven, Belgium.

Pec, M., Stünitz, H., Heilbronner, R., Drury, M.R., De Capitani, C. (2012) Origin of pseudotachylites during slow creep experiments. EGU, Vienna, Geophysical Research Abstracts, Vol. 14, EGU2012-10812

Pec, M., Stünitz, H., Heilbronner, R. (2011) Slow pseudotachylites. AGU San Francisco, USA, T13A-2364

Heilbronner, R., **Pec, M.**, Stünitz, H. (2011) Microstructure evolution of fault rocks at the 'brittle-to-plastic' transition. AGU San Francisco, USA, T13A-2345

Pec, M., Stünitz, H., Heilbronner, R. (2011) Slow pseudotachylites. SGM Zürich, Switzerland, Symposium 1, pp 24

Pec, M., Stünitz, H., Heilbronner, R. (2011) Rheology of granitoid fault rocks at the "brittle-to-plastic" transition: an experimental study. DRT Oviedo, Spain. pp 97

Pec, M., Stünitz, H., Heilbronner, R. (2011) Semi-brittle deformation in shear experiments at elevated pressures and temperatures: Implications for crustal strength profiles. CETeG 2011, Lisek, Czech Republic. ISSN 0231-5548

Pec, M., Stünitz, H., Heilbronner, R. (2011) Brittle deformation in shear experiments at elevated pressures and temperatures. EGU 2011, Vienna, Geophysical Research Abstracts, Vol. 13,

Boutareaud, S., Hirose, T., Doan, M.L., Andréani, M., Calugaru, D.G., **Pec, M.**, Boullier A.M., Kunze, K., Cordonnier, B., (2011) Talc lubrication of faults at seismic velocities: an experimental approach. EGU 2011, Vienna, Geophysical abstracts volume, Vol. 13,

Pec, M., Stünitz H., Heilbronner R., (2010) The brittle-viscous transition in granitoid fault rocks. Workshop on Physico-chemical processes in seismic faults, abstracts volume pp 21-22, Padova, Italy

Boutareaud, S., Hirose, T., Doan, M.L., Andréani, M., Calugaru, D.G., **Pec, M.**, Boullier A.M., Cordonnier, B., (2010) Talc lubrication of faults at seismic velocities. Workshop on Physico-chemical processes in seismic faults, abstracts volume pp 21-22, Padova, Italy

Pec, M., Stünitz, H., Heilbronner, R. (2010) Localization and Partitioning of Deformation in Experimentally Produced Granitoid Fault Rocks. EGU 2010, Vienna, Geophysical Research Abstracts, Vol. 12, EGU2010-14206

Pec, M., Stünitz, H., Heilbronner, R. (2010) Semi-brittle Flow in Granitoid Fault Rocks. EGU 2010, Vienna, Geophysical Research Abstracts, Vol. 12, EGU2010-14088

Goyette, J., John, B., Campbell-Stone, E., Stünitz, H., Heilbronner, R., **Pec, M.** (2009) Architecture of a low-angle normal fault zone, southern Basin and Range (SE California), AGU San Francisco, T53C-1592

Pec, M., Stünitz, H., Heilbronner, R. (2009) Compaction and creep in experimentally deformed cataclasites. DRT Liverpool, UK

Pec, M., Stünitz, H., Heilbronner, R. (2009) Transition from frictional to viscous deformation in granitoid fault gouges. SGM Neuchâtel, Symposium 2: Structural Geology, Tectonics and Geodynamics abstracts, pp 102-103

Pec, M., Heilbronner, R., Stünitz, H. (2009) Transition from frictional to viscous deformation in granitoid fault rocks. EGU 2009, Vienna, Geophysical Research Abstracts, Vol. 11 EGU2009-9776

Invited talks:

American Geophysical Union, San Francisco, USA, December 2013, "Fault-related amorphous materials and their influence on the rheological behavior of fault zones"

University of Minnesota, Minneapolis, USA, February 2013, "Semi-brittle flow of fault rocks: On the origin of pseudotachylites in slow creep experiments"

Charles University, Prague, Czech Republic, October 2012, "Rheology of fault rocks in semi-brittle flow regime"

University of Strathclyde, Glasgow, U.K., October 2012, "Semi-brittle flow of fault rocks: On the origin of pseudotachylites in slow creep experiments"

Utrecht University, Utrecht, The Netherlands, July 2012, "Behaviour of granitoid fault rocks in semi-brittle flow: Origin of pseudotachylites in slow creep experiments"

Ruhr-University Bochum, Bochum, Germany, April 2012, "Origin of pseudotachylites in slow creep experiments"

ETH Zürich, Zürich, Switzerland, March 2012, "Origin of pseudotachylites in slow creep experiments"

PGP Oslo, Oslo, Norway, November 2011, "Slow Pseudotachylites"

Geophysical Institute, Czech Academy of Sciences, Prague, Czech Republic, April 2010, "Transition from frictional to viscous deformation in granitoid fault rocks"

ETH Zürich, Zürich, Switzerland, December 2009 "Transition from frictional to viscous deformation in granitoid fault gouges"

Workshops:

MTEX workshop, San Francisco, California, USA, December 2013

Gordon Research Conference - Rock Deformation, Andover, New Hampshire, USA, August 2012

Workshop on Advancing Experimental Rock Deformation Research: Scientific and Technical Needs, Harvard University, Massachusetts, USA, August 2012

Experimental Petrology and Rock Deformation, EURISPET, ETH-Zürich, Switzerland. 20-27 November 2010

Gordon Research Conference - Rock Deformation, Tilton, New Hampshire, USA, 8-13 August 2010

Texture analysis and orientation imagining, Tromsø University, Norway, 2012, 2011, 2010 (assistant)

Image analysis in Geosciences, Basel University, Switzerland, 2012, 2011, 2010, 2009, 2008 (assistant)

Swiss Tectonic Group Excursion, The Alps, 2011, 2010, 2009, 2008

Awards:

"Journal of Structural Geology: Student Author of the Year 2012 Award"

"Best students oral presentation"
Central European Tectonic Group (CETeG), 2011, Lisek, Czech Republic.

Curriculum Vitae

Name:	Matěj Peč
Nationality:	Czech
Date of Birth:	1.3.1984
City of Birth:	Prague

Appointments:

2012 - now
Post-doc researcher at the **University of Minnesota**, Department of Earth Sciences, Minneapolis, USA

Education:

2008 - 2012
Ph.D. studies at the **University of Basel**, Geological Institute, Basel, Switzerland
(advisors: Prof. Renée Heilbronner , Prof. Holger Stünitz)
graduated *summa cum laude*

2006 - 2008
Master studies in Structural geology and Petrology at the **Charles University**, Faculty of Natural Sciences, Prague, Czech Republic

Master thesis:
"Tectono-metamorphic Evolution of the Aulus Basin Metasediments in the Vicinity of the Lherz Peridotite Massif, North Pyrenean Metamorphic Zone"
(advisor: Dr. Stanislav Ulrich)

2006 - 2007
ERASMUS scholarship at **Université Montpellier 2**, Montpellier, France

2003 - 2006
Bachelor studies in Geology at the **Charles University**, Faculty of Natural Sciences, Prague, Czech Republic

1999 - 2003
Secondary school in Prague, **Gymnázium Jaroslava Seiferta**